CRANFIELD UNIVERSITY

Pau Lluis Orts-Gonzalez

Reheated Humid Air Turbine Thermo-Economic Analysis for Power Generation and Marine Propulsion Applications

School of Aerospace, Transport and Manufacturing

Ph.D. Thesis
Academic Year: Nov 2014 - Feb 2018

Supervisor: Dr. P. K. Zachos

February 2018

CRANFIELD UNIVERSITY

School of Aerospace, Transport and Manufacturing

Full time Ph.D.

Academic Year: Nov 2014 - Feb 2018

Pau Lluis Orts-Gonzalez

Reheated Humid Air Turbine Thermo-Economic Analysis for Power Generation and Marine Propulsion Applications

Supervisor: Dr. P. K. Zachos

February 2018

Abstract

The increasing demand in the marine and energy sectors, the pursuit of more efficient designs and reducing the emissions, specially in the marine sector due to the new IMO regulation, and the deregulation of the energy sector opens a window of opportunity for the research in new advanced gas turbine based power plants for mid-scale applications.

Previous studies have identified humid air turbines as promising gas turbine models, capable to compete diesel and combined cycles in terms of thermal efficiency, currently dominating the marine and energy sectors respectively. Among the different architectures, the reheated humid air turbine presents the largest potential.

This thesis evaluates the thermodynamic performance and the design of a reheated humid air turbine across its design envelope. A comparison in terms of efficiency and dimensions against reference marine engines, and an economic comparison against reference power generation plants is conducted to analyse the potential of such cycle. The performance effects of the component degradation are studied to obtain the expected decay in efficiency and power.

The research outcomes prove the higher thermal efficiency of the reheated humid air turbine, with a maximum value of 61.35%, compared to reference marine engines. The economic analysis for power generation applications confirms the better economic performance of the cycle compared to the combined cycle plants. In addition, the degradation of the intercooler is identified to produce several penalties in the efficiency and power output. However, these penalties could be avoided with a reduced extra investment targeted to redesign the intercooler.

Overall, this research constitutes a step forward in understanding the design of the reheated humid air turbines and appreciates its potential for applications where high efficiency and density of power are of competitive advantage.

Acknowledgements

First and foremost I want to thank my supervisor Dr. Pavlos K. Zachos. Your knowledge, guidance, support, and your infinite patience had been crucial for me in the fulfilment of this challenging task.

I would also like to acknowledge the valuable contribution of my industrial supervisor during the early stages of this project, Mr. Paul Fletcher.

My colleges at Cranfield University, who have made of this experience a pleasant journey, also deserve my gratitude. A special thanks goes to Luis Estefano Ferrer-Vidal, Giovanni Brighenti, and the Erans for the endless conversations we had across these three years.

I could not forget to thank the Txoko and my friends in Valencia, for the support, laughs, and great times they have provided me. Nevertheless, I must express my gratitude to Xuso and Dani for sharing this experience and stand with me this whole time. You have become more than friends.

Last, and most important, I have to thank my parents for all the support and opportunities they have given in the course of my entire life. Without them, none of this would have been possible. Furthermore, I do not forget about my brother, whose technical and none technical advice had been of great help in and outside the PhD.

To all of them, thank you.

Contents

List of Figures

List of Tables

Nomenclature

Abbreviations

AAHX	Air-Air Heat Exchanger
AC	Aftercooler
ADJ	Adjustment
AE	Annual Expenses
AHAT	Advanced Humid Air Turbine
AWHX	Air-Water Heat Exchanger
BBY	Balance Beginning of each Year
BD	Book Depreciation
CC	Combustion Chamber
CCGT	Combined Cycle Gas Turbine
CHAT	Cascade Humid Air Turbine
COE	Cost Of Electricity
CRF	Capital Recovery Factor
DC	Degraded Coefficient
DCo	Direct Costs
DITX	Deferred Income Taxes
DP	Design Point
EC	Economiser
ECA	Emission Controlled Area
EGCS	Exhaust Gas Cleaning System
EGR	Exhaust Gas Recirculation
EPRI	Electric Power Research Institute
ESDU	Engineering Sciences Data Unit
EvGT	Evaporative Gas Turbine

FC	Fuel Cost
FCI	Fixed Capital Investment
FI	Fixed Investment
FPT	Free Power Turbine
GT	Gas Turbine
HAT	Humid Air Turbine
HAWIT	Humid Air Water Injection Turbine
HFO	Heavy Fuel Oil
HPC	High Pressure Compressor
HPT	High Pressure Turbine
HX	Heat eXchanger
IC	Intercooler
ICo	Indirect Costs
IEA	International Energy Agency
IMO	International Maritime Organisation
ITX	Income Taxes
LHV	Low Heat Value
LNG	Liquid Natural Gas
LPC	Low Pressure Compressor
LPT	Low Pressure Turbine
M	Mixer
MARPOL	Maritime Pollution
MGO	Maritime Gas Oil
NTU	Number of Transfer Units
OM	Operation and Maintenance
OMC	Operation and Maintenance Cost
OPR	Overall Pressure Ratio
OTXI	Other Taxes and Insurance
OUT	Outlet
PEC	Purchase Equipment Cost
pp	percentage point
PR	Pressure Ratio
RC	Recuperator
RCE	Return of the Common Equity
RD	Return of the Debt
Rel. PR	Relative Pressure Ratio

RH	Reheater
RHAT	Reheated Humid Air Turbine
RPS	Return of the Preferred Stock
RWI	Recuperated Water Injected
SAT	Saturator
SCR	Selective Catalytic Reduction
SP	Selection Parameter
SPEC	Specific Purchase Equipment Cost
STIG	Steam Injection Gas Turbine
T	Turbine
TCI	Total Cost of Investment
TCR	Total Capital Recovery
TDI	Total Depreciable Investment
TET	Turbine Entry Temperature
TNDI	Total Non Depreciable Investment
TNI	Total Net Investment
TNO	Total Net Outlay
TRL	Technology Readiness Level
TRR	Total Revenue Requirement
TXD	Tax Depreciation
WAC	Water Atomisation Cooling

Symbols

A_c	Contact area per volume
A_{cross}	Cross sectional area
A_f	Fins area
A_{free}	Free flow area
A_{fro}	Frontal area
A_{header}	Header area
A_{HX}	Heat transfer area
$A_{\max}$	Maximum ESDU heat transfer area
A_t	Outer tube area
A_{wl}	Wall area
B	Packing dimension

C	Heat capacity
C^*	Heat exchanger heat capacity ratio
c_p	Specific heat capacity
d_e	External diameter of the tubes
d_{eq}	Equivalent diameter
D_h	Hydraulic diameter
d_i	Inner diameter of the tubes
d_o	Outer diameter of the tubes
d_p	Diameter of the packing
D_{wg}	Water-gas diffusion coefficient
De	Geometric parameter
$\dot{E}x$	Exergy
F	Packing factor
f	Friction factor
F_f	Correction factor
$F_i(x)$	Fitness of the individual
fc	Fraction coefficient
fc_{1st}	Fraction coefficient of first payment
fc_{2nd}	Fraction coefficient of second payment
$\dot{G}$	Mass flux
g	Gravitational constant
Gz	Graetz number
H	Packing dimension
h	Specific enthalpy
h_f^*	Height of the flow
h_f	Height of the fins
h_{fg}	Specific enthalpy of evaporation
H_p	Height of the packing
i	Annual rate of return
j	Chilton-Colburn factor
k	Thermal conductivity
L	Length
L_f	Length of the fins
L_{flow}	Length of the flow passage
L_{Nf}	Width / No flow length
L_p	Width of the flow passage

L_s	Spacing between fins
L_t	Length of the tubes
M	Molar mass
$\dot{m}$	Mass flow
n	Book life
n_{con}	Construction period
n_{des}	Design period
N_f	Density of fins
N_{HX}	Number of heat exchangers
N_l	Number of hot layers
N_p	Number of passes
N_{p_d}	Number of dry passes
N_r	Number of rows
N_t	Number of tubes
n_{tax}	Taxable period
Nu	Nusselt number
P	Pressure
ΔP	Pressure losses
ΔP_f	Pressure drop fouling penalty
p_r	Pitch between rows
p_t	Pitch between tubes
Per	Perimeter
Pr	Prandtl number
$\dot{Q}$	Heat flow
R	Specific gas constant
R_f	Fouling resistance
r_f	Fuel inflation rate
r_i	Global inflation rate
R_{wl}	Wall resistance
Re	Reynolds number
RX	Relaxation factor
S	Packing dimension
s	Specific entropy
Sc	Schmidt number
Sh	Sherwood number
T	Temperature

t_f	Thickness of the fins
t_{film}	Thickness of the fouling film
ΔT_{lm}	Logarithmic mean temperature
t_p	Thickness of the plate
ΔT_{sp}	Saturator pinch point temperature difference
t_t	Thickness of the tube
t_w	Thickness of the water film
t_{wl}	Thickness of the wall
U	Overall heat transfer
u	Velocity
v	Diffusion volume
$\dot{W}$	Power
W	Weight
z	Height of the packing section

Greek letters

α	Heat transfer coefficient
β	Bypass ratio
Γ	Mass flow per unit length
γ	Heat capacity ratio
ϵ	Void fraction
ε	Effectiveness of the heat exchanger
ε_{pass}	Effectiveness of a single pass of the heat exchanger
η_f	Fin efficiency
η_o	Extended surfaces efficiency
η_{pol}	Polytropic efficiency
η_{th}	Thermal efficiency
Θ	Packing dimension
κ	Constant
κ_{CO_2}	Specific CO_2 emission's cost
κ_f	Specific fuel's cost
κ_i	Coefficient
κ_{pf}	Plate-fin cost function
κ_{tf}	Tube-fin cost constant
λ	Mass transfer coefficient

μ	Dynamic viscosity
Ξ	Cost
ρ	Density
τ	Yearly operating time
Φ_M	Ackerman's correction factor
χ	Income tax rate
ψ	Specific flow exergy
Ω	Geometric parameter
ω	Water to air ratio

Subscripts

a	dry air
c	cold
ce	common equity
$clean$	clean conditions
$comp$	compressor
$cond$	condensed water
d	debt
deg	degraded conditions
$dest$	destroyed
eff	effective
el	electric
f	interface
g	gas / humid air
gen	generator
h	hot
Int	interests
in	inlet
out	outlet
$p-f$	plate-fin
ps	preferred stock
Ref	reference
sat	saturated
Sim	simultaneous

t	tube
$t-f$	tube-fin
tot	total
$turb$	turbine
v	vapour
w	water
wet	wet part of economiser
wl	wall

Chapter 1

Introduction

1.1 Background

As part of the Cranfield research, new powering alternatives for the marine and energy markets are being studied. Both markets present similar operational characteristics, the power plants spend most of their time at design point load. In addition, both sectors are now focused on the pursuit of more efficient and less polluting engines to satisfy the increment in the demand. Advanced gas turbine based power plants are among the most suitable alternatives to accomplish such objectives. Their low emission levels and high efficiency position them as strong candidates. Nevertheless, before analysing in detail the possible candidates it is necessary to first understand the current situation of the marine and the energy markets.

1.1.1 Marine market scenario

Nowadays, more than 80% of the international trade is made by sea [1]. The international seaborne commerce has been steadily growing for the past decades, as shown in Figure 1.1, mainly driven by the global rise of the gross domestic product [2]. In addition, over the past two decades, the market scenario has changed in favour of the marine transportation. The developing countries have shifted their positions from being mere suppliers of raw materials to start being also meaningful importers of processed products. This transformation has contributed

to expand the maritime trade market and has permitted it to grow a few percentage points faster than the global economy. Most importantly, this trend is expected to continue at a moderate rate over the next years [3].

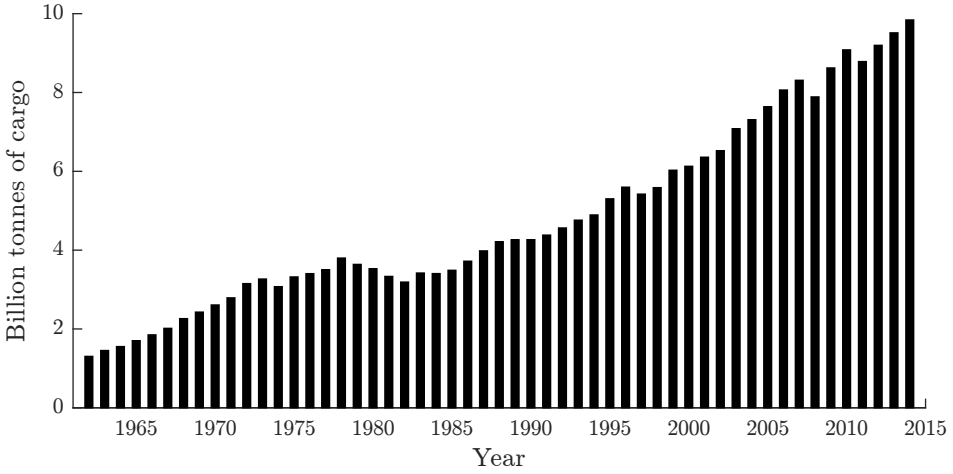

FIGURE 1.1: International seaborne trade, 1960-2015.
Source: International Energy Agency [2].

The main reason of such success lies on the cost advantages the marine trade presents against other alternatives, being a 97% more energy efficient than air trade, or 69% more efficient than track transportation [4]. The vast majority of the commercial vessels are currently powered by large two-stroke diesel engines. Their low specific investment cost, high reliability, simplicity, low fuel price, and high thermal efficiency, exceeding in some cases 55%, has allowed these power plants to clearly establish themselves as the principal option when powering commercial vessels.

However, the rising awareness about the impact of the global ship emissions on the ocean environment and, especially, in the coastal areas has arisen some concerns about the sustainability of the sector considering the current growth. Ship emissions account for a 16% of all sulfur from petroleum-derived fuels [5]. In addition, 70% of these emissions occur within 400 km of land, having a severe impact on the coastal communities and population health [6]. Moreover, the marine sector has also been predicted to be responsible for around 14% of the global NO_x emissions from fossil fuels [5], which produce serious respiratory diseases and act in detriment of the ozone layer.

The care about air pollution and the contribution to global warming coming from the marine sector have generated some concerns among the experts and the author-

ities. Accordingly, the International Maritime Organisation (IMO) redacted the 2008 MARPOL Annex VI amendments [7] in prevention of air pollution produced by ships. This document sets the limits on SO_x and NO_x emissions from ships, and imposes more stringent standards in the Emissions Control Areas (ECA). The objective is to globally reduce the sulphur fuel content to 0.5%, and to 0.1% in the ECA by 2020, as shown in Figure 1.2a. The amendments also pointed towards a progressive reduction of the NO_x emission limits, going from 17 g/kWh for low-speed diesel engines installed between 2000-2010 (Tier I) operating in the ECA, to 14.4 g/kWh if installed after 2010 (Tier II), and to 3.4 g/kWh if installed after 2015 (Tier III), as illustrated in Figure 1.2b.

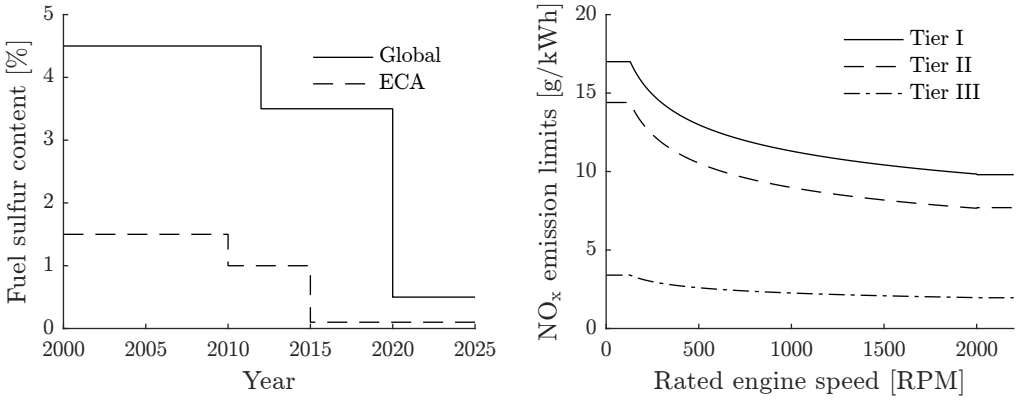

(a) Limits of sulphur concentration in fuel

(b) Limits of NO_x emissions

FIGURE 1.2: Sea emissions limits covered by MARPOL Annex VI. Source: International Maritime Organisation [7].

Different solutions are being studied, some of them have already been applied, towards the reduction of the diesel emissions. To be within in the SO_x emissions limits imposed inside the ECA, the diesel engines are adopting two solutions: either switch from Heavy Fuel Oils (HFO) to higher distillate fuels with lower sulphur content, like Marine Gas Oil (MGO), or install Exhaust Gas Cleaning Systems (EGCS), also known as scrubbers. Any of both solutions involves a serious increment in the expenses for the future years, EGCS implicates a capital expenditure of 200-400 €/kW and MGO is 240-300 $/ton more expensive than HFO. Nevertheless, there is no strong conclusion about which of both options is more economic [8]. The two most promising solutions to reduce the NO_x emissions include the installation of Selective Catalytic Reduction (SCR) systems or Exhaust Gas Recirculation (EGR) systems. Both systems have been used for decades. Hence, the technology is mature. Nevertheless, their implementation in plants with high

sulphur content increases the installation challenges due to the highly corrosive environment. The installation costs of these systems implies the payment of considerable amounts of money. For a current ship, the EGR full system addition is approx 10%-13% of the vessel price [9]. Therefore, any technique employed to stay within the limits imposed by the new IMO regulation will considerably increase the capital and the operational expenditure of the diesel plants.

In this scenario, an equalisation in the total cost of the advanced gas turbine based power plants and the diesel engines might be expected. This offers a potential window for the advanced gas turbine based power plants to finally be introduced into the marine market for a more general use, rather than just for fast ferries or military applications. Moreover, gas turbine based power plants also offer the advantages of producing less noise, lower NO_x and SO_x emissions, being lighter and more compacts, presenting a higher availability, and requiring lower workload crew [10]. On top of that, the current trend towards the electrification of the propulsion systems in the marine sector [2, 11, 12], and the new developments in more compact and efficient electric machinery [13–17] further facilitates the introduction of the gas turbines in the marine market.

1.1.2 Energy market scenario

The global economy, measured with the gross domestic product, is growing at an average rate of 3.4% a year. In addition, global population is expected to rise from 7.4 billion today to more than 9 billion by 2040, and urbanisation of the rural areas adds a city with the size of Shanghai every four months. Therefore, energy demand is expected to grow up to a 30% between the present day and 2040, with larger impact in the developing countries [18], as presented in Figure 1.3.

In this scenario, energy efficiency is a key factor to ensure a reliable, safe, sustainable, and affordable energy sector in the future. The most recent improvements towards more efficient power generation methods have permitted to augment the population with access to electricity, to hold back the rise in emissions, and to reduce bills of the energy consumers. The improvements achieved in efficiency since 2000 have been reflected in a reduction of the spendings of $50 billion in the Internal Energy Agency (IEA) member countries in 2016 [19]. Nevertheless, larger improvements in efficiency are required since the growth in CO_2 emissions is limited to a 5% between the present and 2040 [18], if the objective of an increment

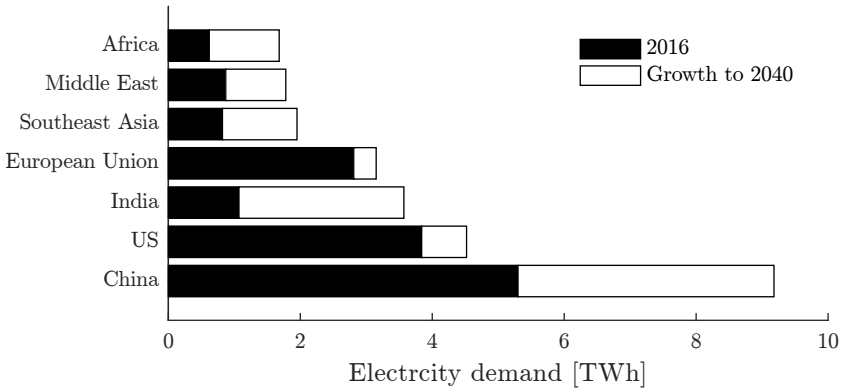

FIGURE 1.3: Electricity demand forecast.
Source: International Energy Agency [18].

lower than 2 °C in the global temperature is to be achieved, as stated in the Paris Agreement.

To achieve such objective, enormous efforts are being invested in the development of renewable energies. However, different forecasts predict a scenario where the fossil fuel based energy generation methods still account for the largest part [18, 20–22]. The price competitiveness they offer and the lack of capability of the renewable energies to cover all the new demand still justifies the viability of fossil fuels. Natural gas seems to be the most successful candidate due to the lower environmental footprint it produces when compared to its direct competitors (coal or oil) and the relative cost reduction it can offer. For example, the future predictions show that in the 2040 scenario in China it would be more economical to operate combined cycle power plants with gas rather than still burning coal for power generation [20]. Moreover, US increasing ability to produce shale gas is directly impacting the market prices, making the Liquid Natural Gas (LNG) more competitive [20]. A boom in extraction from shale deposits combined with the new US position as the world leader in LNG pricing could help to the LNG in achieving lower prices than even the crude oil. Consequently, the demand of natural gas is expected to grow a 45% by 2040 [18].

Among the different alternatives, advanced gas turbine based power plants are the most common option when generating energy based on natural gas due to their low specific investment costs, short construction periods, and high efficiency, especially the combined cycle power plants. Combined cycles have proven to achieve extraordinary efficiency levels for the large scale with the use of critical steam cycles. This has permitted them to get established as based load power generation

plant since the 80s. The latest progress has allowed building power plants exceeding the frontier of 60% of efficiency for applications in the range of 400-800 MW [23].

Nevertheless, with the deregulation of the market towards the use of mid-sized plants, a door is opened for the engineers to discover more efficient alternatives at those power levels, 10-100 MW. These plants might result perfect for covering medium power requirements with stations localised close to where the power is demanded, supplying energy during peak hours, compensating the renewable energies when not available, or simply being used as the main power source. Nevertheless, these new power plants need to offer high efficiency, low environmental impact, rapid start-up processes, low maintenance, good flexibility, and low specific investment costs.

1.1.3 Humid air turbines as an alternative

The current trends in the energy and the marine markets towards more efficient and less polluting engines opens a window of opportunity to the development of novel power plants capable of fulfilling the aforesaid demands. Both markets share similar design characteristics, which are focused on the metrics achieved at design point, where the power plants spend most of their operating time. Thus, a general design of the cycle is supposed to be fairly valid for both applications.

Such scenario, where two potential applications in different markets with similar design and operational requirements are foreseen, offers a promising landscape for the future development and implementation of advanced gas turbines. The extensive use of gas turbines has permitted to deeply evolve and mature their technology, and currently stand among the most reliable and efficient power units [24].

Nowadays, the most common practice to enlarge the performance of the gas turbine consists on the transformation into a combined cycle [25–27]. However, despite the current extensive and efficient use of the combined cycles on the power generation market, new thermodynamic cycles are being investigated. The main objective of these investigations is to discover engine configurations capable of offering a better thermal efficiency, faster start-ups, better flexibility, lower environmental impact, lower maintenance, lower specific costs, etc. A new cycle combining all the

previous ideas was born in the 80s, the so-called humid air turbine, also known as evaporative gas turbine [28, 29]. The humid air turbine is an intercooled, aftercooled, recuperated, humidified gas turbine based cycle that uses a novel and more efficient approach to recover the heat from the flue gasses. In this cycle the heat rejected in the intercooling and aftercooling processes, together with the heat available in the flue gasses after the recuperator is reinjected into the cycle through the evaporation of warm water (at temperatures below the boiling point) into the the dry air before the recuperator, considerably reducing the entropy generated compared to a process involving steam generation.

thermo-economic studies [30–32] have proven that the humid air cycles are capable of achieving a better performance than the combined cycles. The ability to evaporate the water inside the gas turbine avoids the necessity of a bottoming cycle, permitting to obtain a lower specific investment cost and footprint while keeping high-efficiency values. The different cycle analysis conducted [33–38] revealed that the humid air cycle achieves thermal efficiencies in the range of 52%-57%. In addition to a better design performance, the humid air cycle has demonstrated to have a better off-design performance. It presents a lower reduction in the thermal efficiency at part-load and a lower sensibility to the ambient temperature compared to current combined cycle power plants [39, 40]. Moreover, the humid air turbine offers a 90% reduction of the NO_x emissions in comparison to simple gas turbines [41, 42].

Despite the many existing configurations [28, 31, 36, 38], the reheated configuration analysed by Sanchez [10] shows the most promising results, being able to achieve a maximum efficiency beyond 63%. This finding, together with the presented in the previous paragraph, convert the reheated humid air cycle into a promising candidate to be integrated into the marine and energy markets.

1.2 Aims and objectives

The reheated humid air turbine has been identified as one the of the promising alternatives to confront the challenges that the marine and the energy sectors have to overcome. Nevertheless, the studies on reheated configurations of the humid air turbine performed so far have simply focused on the maximum achievable thermal efficiency.

Hence, prior its implementation in the mentioned markets, further research needs to be conducted to gain knowledge about its performance and design characteristics. A design space exploration would permit to identify the dependency of the performance of the cycle, and its physical designs, on the thermodynamic design variables. This analysis would also allow the evaluation of the feasibility of the components across its design envelope. In addition, a study of the effect of the designing ambient temperatures on the performance and designs of the power plant seems necessary. Depending on the allocation of the power plant or the selected marine route of the vessel, the designing ambient conditions might differ considerably.

To actually prove the capability of the reheated humid air turbine to be introduced inside the commercial marine and power generation markets, it would be necessary to compare the power plant against reference power plants employed nowadays for these applications.

The use of the reheated humid air turbine in commercial marine and coastal power generation applications opens the door to the direct use of seawater as coolant. However, this idea involves the necessity of materials with exceptional fouling, corrosion, and erosion resistance, which obviously would impact the acquisition cost of these components. Nevertheless, despite the use of high resistance materials, a certain amount of degradation will always be expected. A degradation analysis would permit to predict the loss in performance derived from the deterioration of these components and identify the economic impact of preventing this deterioration.

Therefore, to assess the potential of the reheated humid air turbine it is necessary to first fill the identified gaps in knowledge. With such purpose, the main aim of this thesis is to assess the economic and thermodynamic viability of the reheated humid air turbine as a prime mover for marine applications and as a power generation plant.

In order to achieve this aim, the following objectives to be achieved have been identified:

- Evaluate the thermodynamic performance of the cycle and its designs, at a component and system level, across a prescribed design envelope to compare,

in terms of thermal efficiency and dimensions, the obtained designs against reference marine prime movers.

- Use the data obtained in the design space exploration together with an economic model to compare, in terms of thermal efficiency and expenditures, the performance of the reheated humid air turbine against reference power generation plants.
- Analyse the performance deterioration caused by the degradation of the power plant's components, and evaluate the economic and performance impact of redesigning the components to reduce the degradation penalties.

1.3 Research novelty

This research introduces for the first time the design and optimisation of a part-flow reheated humid air turbine to fully analyse its thermodynamic and economic potential in marine propulsion and energy production applications. For that purpose a new component optimisation platform has been created and employed to identify the most economic, compact, and efficient design solutions. This work has permitted to compare the thermodynamic and economic performance of the analysed cycle against their prime competitors and preliminary establish the main advantages achieved. Moreover, the performed research also studies the effects derived from the degradation of the components, which was a complete unknown for humid cycles so far, using an exergetic analysis that permits to easily identify the key parts of the system that penalise the efficiency.

Nevertheless, the investigation does not deal with the part-load operation of the power plant an its effects on the efficiency, which have not yet been analysed. In addition, the analyses does not consider either the integration of the power plant with the vessel for the marine applications, which are also still unknown. Therefore, in order to complete the investigations about the reheated humid air turbine these topics further research will have to be conducted in the future.

Overall, this research constitutes a step forward in understanding the design of the reheated humid air turbines at component level and appreciates the potential of such system for applications where high efficiency in addition to low overall plant

volume and weight are of competitive advantage, which have not been studied until today.

1.4 Thesis structure

In this thesis, the physical design of the reheated humid air turbine is evaluated for marine and power generation applications. The developed work is presented in seven chapters.

Chapter 2 provides a description of the humid air turbine cycles and the most remarkable developments achieved. Important information introducing the main characteristics and design methods of the humidification system is provided as well.

Chapter 3 presents the thermodynamic architecture of the analysed reheated humid air turbine cycle, together with the description of the different components integrating the power plant. The different architectures selected for components are characterised, and the designing and cost estimation models are reported. In addition, key considerations for the design of the heat exchangers are also introduced.

Chapter 4 displays the layout of the power plant, and analyses the impact of the designing variables on the design of the components and the metrics of the power plant, focusing on the weight, volume, and cost. In addition, the power plant is compared against reference marine engines to highlight the advantages of the reheated humid air turbine.

Chapter 5 evaluates the thermo-economic performance of the reheated humid air turbine for power generation applications. The analysis includes a sensitivity study to examine the impact of the main cost drivers on the economic metrics, and the comparison of the cycle against high efficiency humid and combined cycle systems previously presented.

Chapter 6 deals with the study of the impact on the thermodynamic performance derived from the degradation of the components. The economic and thermodynamic evaluation of the implications of redesigning the air-water heat exchangers to prevent the performance deterioration closes the chapter.

Chapter 7 summarises the main findings and most relevant conclusions of this research, and provides guidelines for the future studies towards the further development of the reheated humid air turbine cycle in the marine and the power generation sectors.

Chapter 2

Literature review

This chapter introduces the humid air turbine cycle and summarises the different studies that have been conducted to understand, analyse, and improve its thermodynamic and economic performance. The cycle presentation is complemented with the description of its key component, the saturator tower, and the different existing design alternatives and methods. In addition, the literature review is completed with the explanation of some heat exchanger design considerations.

2.1 Humid air turbines

The Humid Air Turbines (HAT) or Evaporative Gas Turbines (EvGT) were initially introduced by Nakamura et al. [43] and Rao [28] in the late 80's. Both patents presented similar concepts based on a single spool intercooled gas turbine with a single expander. The air after the high pressure compressor is cooled in the aftercooler, warmed and humidified in the saturator tower, and preheated in the recuperator before being injected into the combustion chamber. The cycle uses the heat available in the exhaust gases to preheat cold gases in the recuperator. The low-quality heat (low temperature) rejected during the intercooling, aftercooling, and at the outlet of the recuperator is employed to warm the water, which is then injected into the saturator. A diagram of the standard HAT is presented in Figure 2.1.

At the saturator, the dry air coming from the aftercooler is inserted at the bottom of the tower, whereas the pressurised hot water coming from the air-water heat

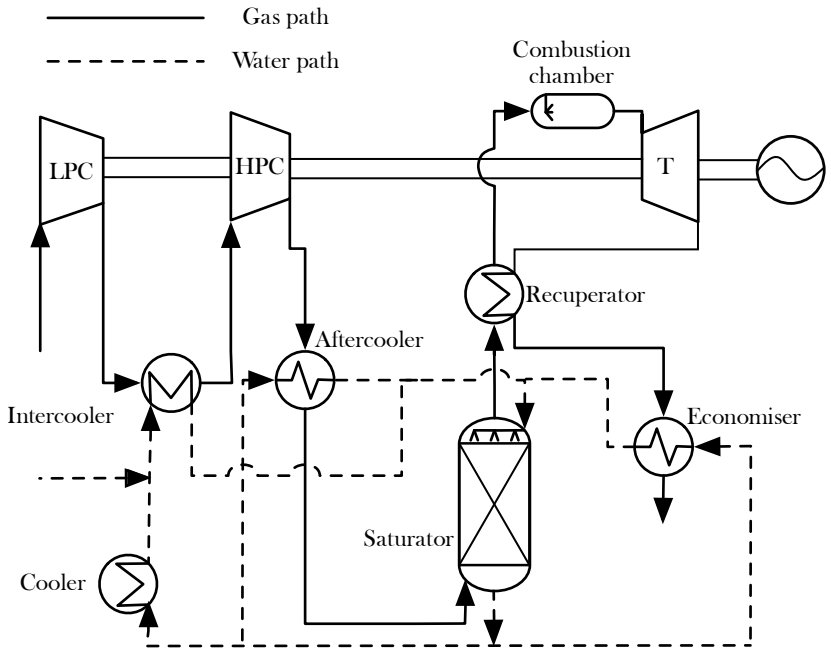

FIGURE 2.1: Schematic layout of a standard humid air turbine cycle.

exchangers is inserted at the top. The dry air flows upwards, in counter-current direction with the falling hot water. The hot water warms the dry air and gets evaporated within it, raising the temperature and the mass flow of the gas. This process permits to recover the low-quality heat with minimum losses since the temperature difference between the hot and the cold flows is minimised. The advantage of this process compared with the typical steam generation process (inside a boiler) is the capability of evaporating the water at temperatures lower than the boiling point, making possible to recover heat at lower temperatures for better thermal efficiency. In addition, the augmented mass flow of the hot section compared with the cold section permits to enlarge the specific power of the cycle.

Interest in the HAT cycle led the Electric Power Research Institute (EPRI) of the US to investigate about its potential [33, 34]. The EPRI studied the conversion of industrial (GE and ABB) and aero-derivative (Pratt and Whitney PW4000) gas turbines into HAT cycles. The performance of the obtained configurations was compared against the obtained from a triple-pressure reheated Combined Cycle Gas Turbine (CCGT) using the same core turbines. Despite the higher specific investment of the HAT cycles (11%-26%), its larger thermal efficiency (53.5%-57.4%) compared with the CCGT (4 percentage points higher in average) permitted to predict a lower cost of the electricity. The investigation also highlighted the larger turbine mass flow, 20%-30% higher than the compressor inlet mass flow, which may lead to problems in the turbine operation if no redesign or bleed was considered.

Interest in the humid air turbine also arose in Europe. Chiesa et al. [44] investigated about the thermodynamic optimisation of different gas-steam cycles to study the potential of the humidification. The compared cycles included a Recuperated Water Injected (RWI) cycle, a Steam Injection Gas Turbine (STIG), a CCGT, and a standard HAT cycle. The RWI consists of a recuperated gas turbine that includes evaporating intercooling and aftercooling, as shown in Figure 2.2. This increases the mass flow in the hot section and permits to recover heat at lower temperatures in the recuperator. The STIG cycle is based on a simple gas turbine that features a heat recovery steam generator at the exhaust to generate steam that is then injected before the combustion chamber or the recuperator in case the cycle includes one. Among the different configurations, the HAT cycle was at least 2 percentage points (pp) more efficient than the rest of the analysed configurations, with a thermal efficiency of 55.13% obtained for an Overall Pressure Ratio (OPR) of 48 and Trubine Entry Temperature (TET) equal to 1773 K. The analysis also revealed that the optimum pressure ratio split between the two compressors is the one minimising the compression work, and that the intercooler and the aftercooler should reduce as much as possible the air temperature. The exergy analysis pointed to the ability of injecting water at low temperatures as the distinctive advantage of the HAT compared with the other humid configurations. The analysis revealed that the exergy destruction due to the water evaporation in the saturator is lower than in the mixing of steam and dry air of the STIG. Last, the exergy analysis also identified the combustion chamber as the main source of the irreversibilities. To attenuate the exergy destruction in the combustion chamber, Chiesa et al. [44] proposed the addition of a reheater. This solution would permit a higher heat recuperation and, consequently, increase the inlet air temperature at the main combustion chamber.

The potential of the standard HAT was further supported by the results obtained by Gallo [35]. The study compared the performance of the HAT cycle against an intercooled-recuperated gas turbine, a CCGT, and a STIG, among other advanced configurations. The analysis showed that the HAT's maximum thermal efficiency (54.8% for an OPR=12 and TET=1573 K) was at least 1 pp superior than the CCGT's, 4 pp higher than the intercooled-recuperated gas turbine's, and almost 10 pp larger than the STIG's and the rest of the configurations. Gallo [35] also highlighted the ability to increase the specific power, up to an 84.4% for an OPR=30 and TET=1573 K (32 pp more than the STIG and 58 pp more than the CCGT), compared to a simple gas turbine of equivalent characteristics.

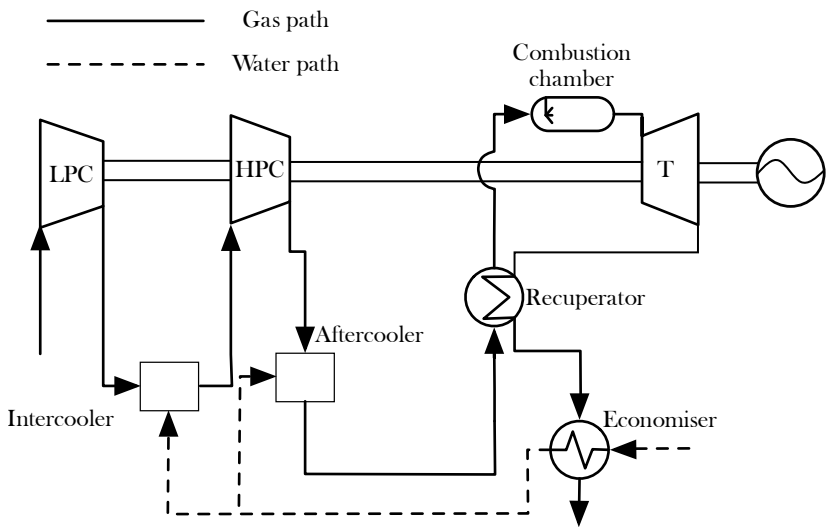

FIGURE 2.2: Schematic layout of a recuperated water injected cycle.

Lazzaretto and Segato [45] decided to optimise the performance of the HAT cycle viewing the heat exchange system as a "black-box". The model allowed to calculate the heat transfer between the hot and the cold flows regardless the layout and number of the heat exchangers. The optimal boundary conditions between the basic components and the "black-box" were calculated maximising the heat transfer in the "black-box", independently of the structure of the heat exchanger's network. The advantage of this approach consisted on the ability to evaluate the performance of the cycle regardless the selected heat exchanger's network. The analysis revealed that the pressure ratio split and the intercooling temperature maximising the thermal efficiency were the same that minimised the compression work. Moreover, the study verified that the addition of the aftercooler had a positive influence on the performance, while the overall pressure ratio had little impact on the thermal efficiency. The later design optimisation of the heat exchange system [46] showed that the optimum architecture should include an intercooler, an aftercooler, and an economiser.

The work presented by Nyberg and Thern [47] further supports the conclusions obtained by Lazzaretto and Segato [45, 46]. It focused on the influence of the heat exchangers on the performance of the HAT cycle. For that purpose different configurations were compared. Starting from a simple gas turbine, heat exchangers were added, until obtaining an intercooled-aftercooled HAT cycle with economiser. The results highlighted the importance of the economiser and the aftercooler to increase the amount of warm water injected into the saturator. Moreover, it was concluded that the intercooler should be placed in order to minimise the

compression work (splitting equally the pressure ratio) and maximise the water outlet temperature. In addition, the study emphasised the efficiency benefits of injecting the water into the saturator at a higher temperature over the benefits obtained from injecting a larger mass flow of water.

To further complete the thermodynamic analysis of the HAT cycle, Kim et al. [39] studied the effect of the designing ambient temperature on the cycle's performance. The study also included the analysis of a simple gas turbine and a CCGT. The conclusions highlighted the lower dependency of the HAT on the ambient temperature compared with the other cycles, in terms of thermal efficiency and power output.

Wang et al. [48] decided to expand the knowledge on the HAT's performance by the simulation of its off-design performance. The analysis included a comparison of the performance of a standard HAT cycle against a STIG, a RWI gas turbine, a recuperated gas turbine, and simple gas turbine. The off-design performance of all the components was fully simulated. The results showed a lower response of the HAT cycle to the variation of the ambient temperature compared with the rest of the cycles. The HAT's efficiency only dropped a 2.21% when the ambient temperature was increased from 0 °C to 35 °C. Nevertheless, the STIG and the simple gas turbine presented a lower drop in the thermal efficiency when reducing the power output (13% and 17% respectively for a 50% power reduction) compared with the HAT (22% for a 50% power reduction). However, Wang et al. [48] suggested that better results for the HAT could have been obtained by regulating the air mass flow through the saturator.

In order to further increase the performance of the HAT cycle, new architectures were proposed. To solve the problem of the mass flow imbalance between the turbines and the compressors [28, 34] without modifying the design of the turbines, Nakhamkin et al. [49] proposed the Cascade Humid Air Turbine (CHAT). This configuration permits to solve the imbalance problem using the heavy-duty gas turbines, and industrial compressor and expanders arranged in a two-spool non-coaxial architecture. The analysed cycle integrated an intercooler, a saturator tower, a recuperator, and a second combustion chamber. The low pressure shaft was composed by a W501F low pressure turbine and modified combustion chamber, and a W501D class compressor. On the other hand, the high pressure shaft was based on standard gas turbine supplied by Dresser-Rand. According to the results, the CHAT presented a 55% faster start-up process than a CCGT

of similar characteristics, lower emissions due to the humid combustion, similar thermal efficiency at full load, but considerably higher at part-load performance, and less sensibility to the ambient temperature.

An additional analysis presented by Nakhamkin et al. [50] pointed that by the elimination of the low pressure compressor it was possible to obtain a thermal efficiency of 60% with a high pressure combustor's outlet temperature of 1422 K and 1667 K in the low pressure combustor. The efficiency could be boosted up to 63% if the high pressure combustor's temperature increased up to 1755 K, which proved the potential of the addition of a second combustion chamber proposed by Chiesa et al. [44].

Higuchi et al. [36] and Hatamiya et al. [37] introduced the concept of the Advanced Humid Air Turbine (AHAT). The AHAT cycle is based on the standard HAT cycle, as illustrated in Figure 2.3. However, it substitutes the intercooling by a Water Atomisation Cooling (WAC) of the compressor. This system consists in spraying cold water prior the compressor, which then gets evaporated during the air compression process reducing the required compressor work. Higuchi et al. [36] and Hatamiya et al. [37] concluded that the AHAT was capable of achieving a thermal efficiency of 55.1% (5% larger than a mid-size CCGT) with an OPR=20 and TET=1673 K, and without the necessity of an intercooler.

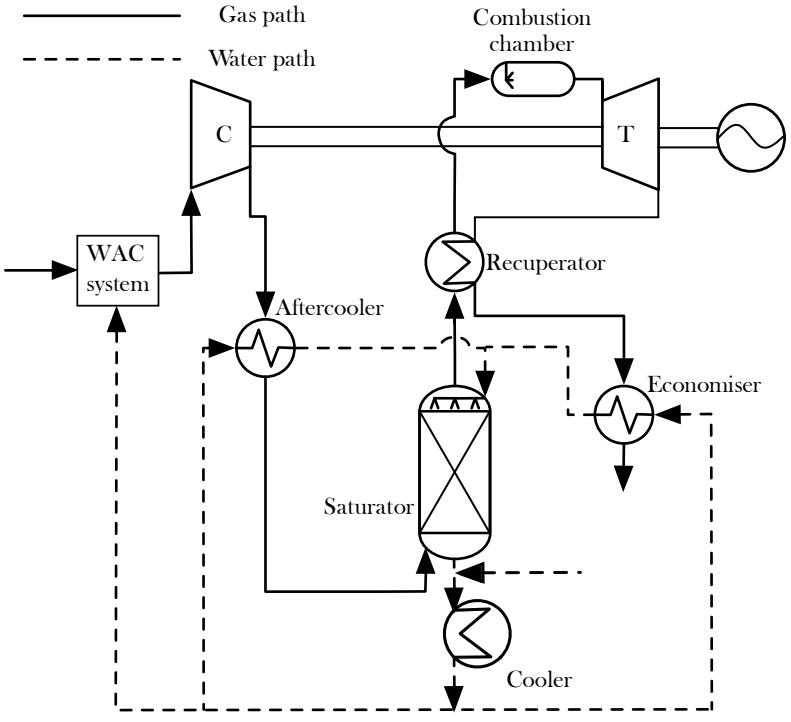

FIGURE 2.3: Schematic layout of an advanced humid air turbine cycle.

The AHAT's analysis was complemented by the off-design simulation performed by Takahashi et al. [40] and the comparison of the results against the performance of a similar CCGT. The analysis proved the 9% lower dependency of the AHAT's efficiency to the ambient temperature compared with the CCGT. The study also included the part-load performance simulation of the cycles, which showed a 15% lower reduction of the efficiency compared to the CCGT.

The work developed by Traverso and Massardo [31] compared the performance of a STIG, a RWI gas turbine, a standard HAT cycle, and a novel concept called the Humid Air Water Injection Turbine (HAWIT). The HAWIT consists in a standard HAT that substitutes the conventional intercooling process by a water injection intercooling, as depicted in Figure 2.4. The results were compared against the data of a state of the art two-pressure level CCGT. The thermodynamic analysis revealed that the HAT cycle was the most efficient alternative with a maximum thermal efficiency of 52% (OPR=30 and TET=1673 K), whereas the HAWIT showed a maximum thermal efficiency of 50.3% (OPR=30 and TET=1673 K). Nevertheless, none of the analysed cycles was able to reach the thermal efficiency of the combined cycle (52.7%). However, the HAWIT, the HAT, and the STIG overcome the specific work of the CCGT by more than a 50%.

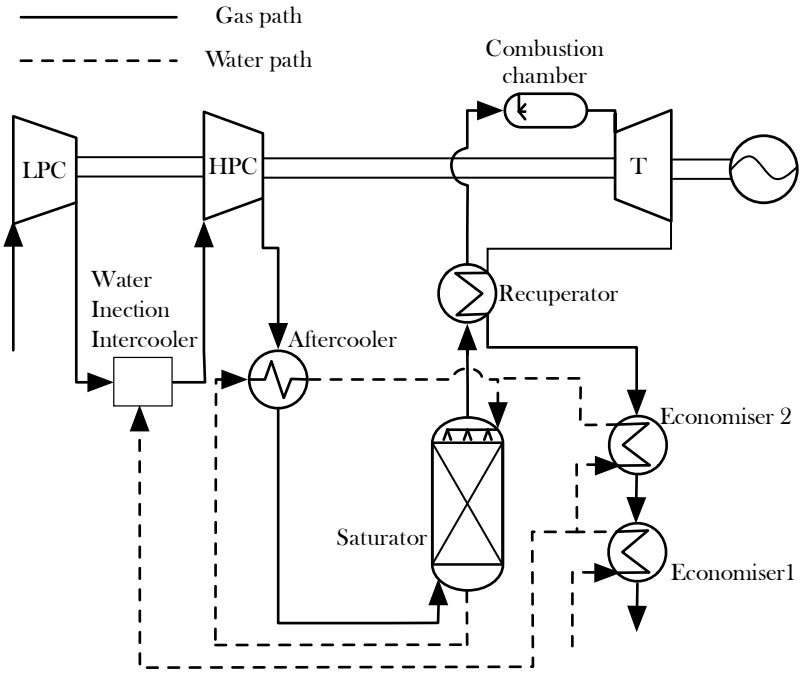

FIGURE 2.4: Schematic layout of a humid air water injection turbine cycle.

Traverso and Massardo [31] completed their study with an economic analysis of the cycles, which identified the HAWIT as the most economic option, followed by

the HAT, and the RWI (20%, 16%, and 14% lower cost of electricity compared with the CCGT respectively). The lower investment of the HAWIT (2% lower than the HAT) permits to reduce the final cost of the electricity despite its lower thermal efficiency.

Kavanagh and Parks [38] introduced the concept of the TOP-HAT, which consisted in a recuperated gas turbine with an economiser to warm water that was injected an evaporated within in the compressors, as shown in Figure 2.5. The study performed a multi-objective optimisation to maximise the thermal efficiency and the power output of the cycles. The performance of the TOP-HAT was compared to the performance of a STIG and a HAT, both optimised as well. From the three alternatives analysed, the TOP-HAT was the most promising in terms of thermodynamic performance, with a specific power of 706 kJ/kg and 53% thermal efficiency, whereas the HAT cycle achieved an efficiency of 52% and a specific power of 617 kJ/kg, and the STIG 49% and 564 kJ/kg respectively.

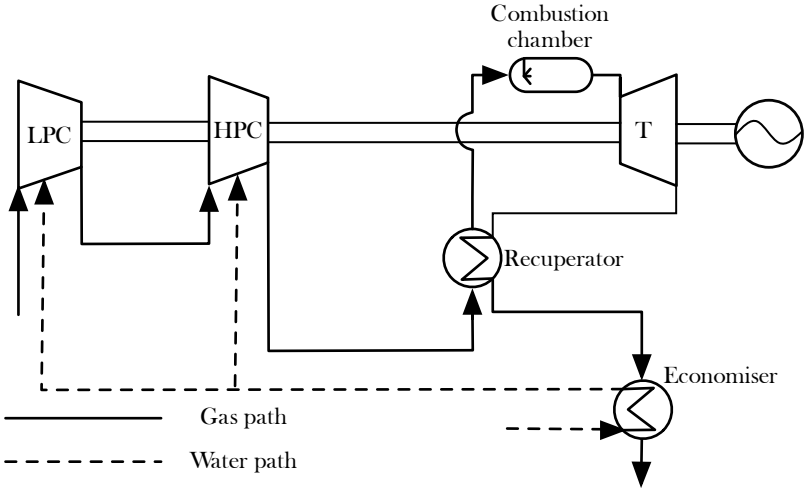

FIGURE 2.5: Schematic layout of a TOP humid air turbine cycle.

The analysis was completed with the addition of the economic metrics of the cycles [30]. The study also involved a standard CCGT to be used as reference advanced gas turbine. The TOP-HAT was identified as the most economic cycle, followed by the HAT and the STIG. The TOP-HAT was effectively a 7% more economic than a standard medium size CCGT. On the other hand, the HAT and the STIG presented a very similar cost of electricity when compared to the CCGT. Nevertheless, all three humid cycles had a lower specific purchase equipment cost than the CCGT (53% in the case of the steam injection cycle, 57% the HAT, and 75% the TOP-HAT). In addition, the results showed that the most efficient

and the most economic cycle configurations were very similar in the case of the TOP-HAT and the HAT.

Another modification of the standard HAT cycle was presented when Westermark [51] patented the idea of the part-flow humidification. In this configuration, a fraction the air coming out of the high pressure compressor bypasses the aftercooler and the saturator to later join with the humid air prior the recuperator. From a thermodynamic point of view, higher water evaporation levels can be achieved within in the saturator if only a fraction of the air is humidified. In addition, as the air coming from the compressor is usually hotter than the air going out of the saturator, a fraction of it can be directly used to warm the humid air. Moreover, humidifying a lower fraction of the air permits to reduce the size of the aftercooler and the saturator, leading to less expensive designs.

Ågren and Westermark implemented the idea of the part flow humidification in an aero-derivative (Rolls-Royce Trent) HAT [52] and in an intercooled industrial core (ABB GTX100) HAT [53]. The cycles also included high-temperature heat exchangers, placed before the aftercooler and behind the recuperator, to generate steam that was injected prior the recuperator, like in a STIG. The obtained results supported the statement of the reduction in the acquisition costs since the humidification system required a 20% lower heat exchange area. The thermodynamic benefits were clear for the aero-derivative design (the thermal efficiency was 1.4 pp higher than the full-humidified version), whereas the industrial core configuration only presented a reduction in the heat exchangers size for a small penalisation in the efficiency.

Jonsson and Yan [54, 55] conducted an exergy analysis to further study the effects and the possible benefits derived from the part-flow humidification. For this analysis, the configurations were the same as the ones studied by Ågren and Westermark [52, 53]. According to the previous results, the analysis showed that the efficiency of the industrial configuration was not altered when reducing the flow fraction passing through the saturator, while the efficiency of the aero-derivative design had an optimum for 20% humidification. The exergy analysis allowed to reveal that the largest part of the exergy was destroyed in the combustion chamber, in accordance with the results obtained by Chiesa et al. [44]. The analysis also pointed the importance of the heat recovery system in the increment of the efficiency, as it permits to recover 70% of the exhaust exergy.

Jonsson and Yan [32] also compared the techno-economic performance of the part-flow HAT cycle with the obtained by the equivalent full-humidification version and the STIG version. The cycles were based on three different gas turbines to investigate the influence of the pressure ratio. A Rolls-Royce Trent with an OPR of 35, a GTX100 with an OPR of 20, and a Cyclone with an OPR of 17. The Trent based power plants presented the lowest cost of electricity, 4% lower than the GTX100 based power plants and 11% lower than the Cyclone based power plants. Comparing the different cycles, the part-flow HAT resulted to be 1% more economic than the full-humidification HAT, and the full-humidification HAT 1% more than the STIG. Thus, the study concluded that the aero-derivative engines had a larger potential for humidification due to their higher pressure ratios, and identified the part-flow HAT as the best humidified cycle. In addition, the comparison of the part-flow Trent HAT against an equivalent CCGT showed that the HAT was able to produce electricity at a cost 3% lower while presenting an initial investment a 12% lower.

Sanchez [10] evaluated the performance of a reheated HAT with part-flow humidification, based on the Rolls-Royce MT30 core, for marine applications. The reheated HAT demonstrated theoretically to achieve a thermal efficiency around 64% (the study did not include blade cooling), what would make it competitive, in terms of thermal efficiency, against the diesel engines for marine propulsion applications. Contrary to the previously studied HAT cycles, the water was considered to be circulating in an open-loop, which simplifies the cycle and avoids the necessity of the bulky and expensive water treatment system. This is possible given the almost nonexistent droplet entrainment at the outlet of the saturator, as reported by Rosen [56] and Linquist [41], which can even act as a scrubber containing the air impurities in the non-evaporated water.

The first experimental facility to test the performance of the HAT cycle was developed at the Lund Institute of Technology in Sweden. The main objective was to prove the rise in the thermal efficiency and power output obtained when humidifying a simple gas turbine. The selected cycle [41] was simpler than the standard HAT cycle (Figure 2.1). It was composed by a 600 kW Volvo VT600 single-shaft gas turbine, one-stage centrifugal compressor and two-stage axial turbine, a counter-flow recuperator, a tube-fin economiser, and a structured packed bed saturator tower. For the sake of simplicity, the cycle did not incorporate any intercooler or aftercooler. In order not to exceed the maximum mass flow admissible

by the turbine, a bleed-off valve was positioned downstream the compressor. The combustion chamber had to be modified for combustion with humidified air.

During the first experiments [41] two different start-up strategies were followed. The fastest and less harmful strategy, initiation of the gas turbine in full integration with the humidification process, presented a start-up time of approximately 5 min from cold start to full load. The following test [41] showed that the thermal efficiency was improved from 22% to 35% due to the conversion of the VT600 into a HAT cycle. In addition, the test certified the stable combustion process with mass humidity ratios of 0.14. Moreover, undetectable levels of unburned hydrocarbons and CO were measured together with values for the NO_x emissions lower than 10 ppm. This means a 90% reduction in the NO_x emissions compared to the non-humidified version. Later on, a plate aftercooler was added to the cycle [57], which proved to enlarge the efficiency of the plant by 1 pp.

In order to prove the operability of the humid air cycles for higher power outputs, a second test house was developed in the Hitachi installation in Japan. Based on the promising results obtained by Higuchi et al. [36], Hatamiya et al. [37] and Takahashi et al. [40], the investigation focused on the research of the AHAT. Kuroki et al. [58] presented the developed technologies required for the construction of the test rig and introduced the plant architecture. The 4 MW power plant consisted on a two-stage radial compressor (OPR of 8), a two-stage axial turbine, a reverse can combustion chamber modified for high humidity combustion, a random packed saturator tower, an aftercooler, a recuperator, and an economiser.

Initially, the developed cluster nozzle burner was tested before setting the entire power plant. The research conducted by Koganezawa et al. [59] proved the correct operation of the combustion chamber for the simulated inlet combustor conditions (18% water to air ratio and 902 K) showing almost 0 ppm of CO and less than 10 ppm of NO_x. The first experimental results on the 4 MW testbed were presented by Higuchi et al. [42] and Araki et al. [60]. The tests proved the correct operation of the power plant and the flexibility of the cycle, producing a maximum power of 3.99 MW with a thermal efficiency of 40%. In addition, the NO_x emissions were confirmed to remain below 10 ppm.

After proving the correct operation of the 4 MW testbed, a 40 MW plant was developed to verify the operability of an AHAT cycle based on a heavy duty industrial turbine. In order to simplify the architecture and facilitate the construction

of the test rig [61], the aftercooler and the economiser were eliminated, and the packed bed saturator was substituted by a spray-type tower. The employed gas turbine was the H-50 single shaft with a multi-can combustion chamber. The results obtained by Yagi et al. [61] and Takeda et al. [62] proved the flame stability at high humidity ratios, presented a cold start-up of approximately 60 min, 66% faster than a conventional CCGT. Moreover, the AHAT achieved the expected power output of 40 MW. Nevertheless, no figure about the thermal efficiency was provided.

2.2 Saturator tower

In the HAT cycle, the saturator tower is the key and truly novel component of the plant. The saturator enables recovering low-quality heat into the cycle by evaporating relatively high amounts of water into the main gas path at low temperatures. That yields to minimum exergy losses since both flows present more similar temperatures all along the tower compared with the evaporation process happening in the STIG, where the water is evaporated at a constant temperature (the boiling temperature).

There exists three different configurations of saturation towers: spray, tubular, and packed bed towers. The spray tower, illustrated in Figure 2.6a, is the simplest concept. The pressurised air is driven into a shell where water is sprayed in fine droplets by a nozzle. Besides its simplicity, the model does not offer any other advantage. The main drawback of this configuration is the requirement of high water purity. When the water droplets are evaporated, the salts content within the water remains as dust in the compressed air, which may produce severe corrosion and erosion damages in the turbine blades.

The tubular tower, depicted in Figure 2.6b, proposed by Dalili and Westermark [63] is a concept that permits to integrate into one component the economiser and the saturator. Therefore, it is considered convenient for small cycles. The configuration is similar to a shell-tube heat exchanger, it consists of a vertical shell filled with a bundle of vertical tubes. The exhaust gases circulate on the shell-side crossing the tube bundle, whereas the cold air flows upwards inside the tubes in counter-current direction with the water film, which falls attached to the inner walls of the tubes. Dalili [64] suggested the introduction of fins on the

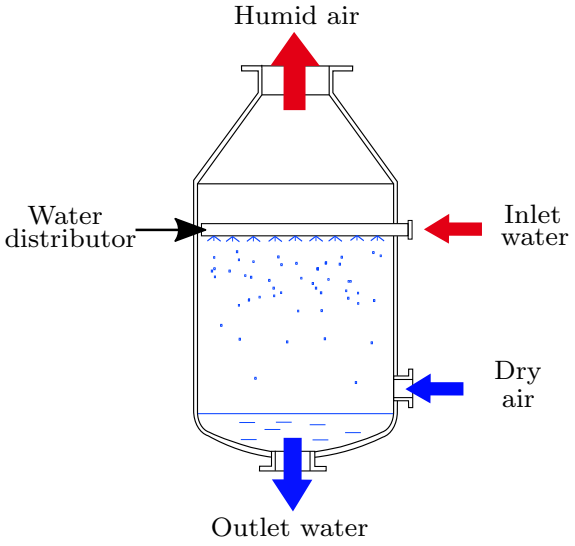

(a) Spray

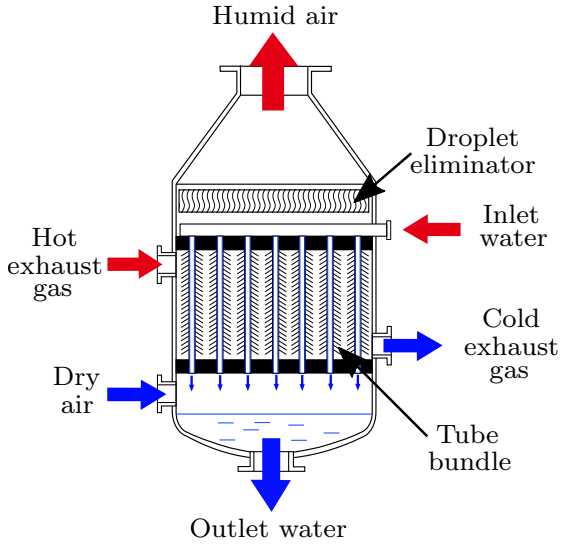

(b) Tubular

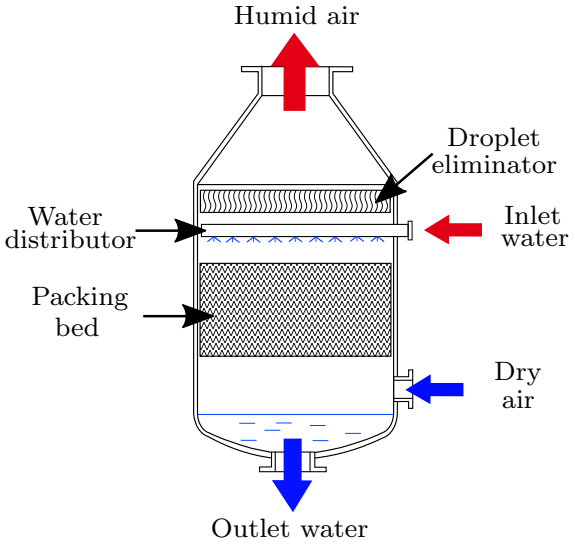

(c) Packed bed

FIGURE 2.6: Classification of saturator towers.

outer part of the tubes to increase the heat transferred. The main advantage of this model is the reduction in the required space, as it covers the function of the economiser as well. Moreover, the shell walls become thinner compared with the other two models since the exhaust gases flowing on the shell-side are not pressurised. Nevertheless, it has to be ensured that the hot air does not exceed the boiling temperature of the water to ensure a continuous water film, which limits the performance of the cycle.

The packed bed tower, represented in Figure 2.6c, is the configuration that most HAT models include. The concept consists in a shell filled wtih surface extension material, also called packing material, to enlarge the contact area between the water and the compressed air. The water is injected at the top via the water distributor, which must warranty an equal dispensation to ensure that there are no dry areas in the packing. The water falls along the packing in counter-current direction with the rising air injected at the bottom. There are two main types of packing: random dumped and structured packing. The structured packing offers a better performance for gas turbine applications due to the lower pressure drop and the better transfer properties [64]. Howerver, the cost of the structured packing per cubic meter is significantly higher than the random packing. Nevertheless, the higher efficiency of the structured packing compensates the higher cost [65].

The tubular and the packed bed saturators do not require to use purified water, contrary to the spray tower. The water always falls in a continuous film and only a fraction of the water is evaporated. Thus, the salts remain in the water. Moreover, the moisture condensates around the particles suspended in the air dragging them into the water film or being trapped in the droplet eliminator. Hence, both configurations must include a droplet eliminator to avoid any droplet entrainment into the turbomachinery [64, 66].

The performance of the saturator tower is usually characterised in an h-T diagram, illustrated in Figure 2.7. The y-axis represents the enthalpy of the gas per kilogram of dry air and the x-axis temperature. The solid line, also called the working line, correlates the enthalpy of the gas with the temperature of the falling water. The dashed line represents the correlation between the gas temperature and its enthalpy at saturated conditions.

The saturator pinch point temperature difference (ΔT_{sp}) is the minimum temperature difference between the working line and the air saturation curve (Figure 2.7).

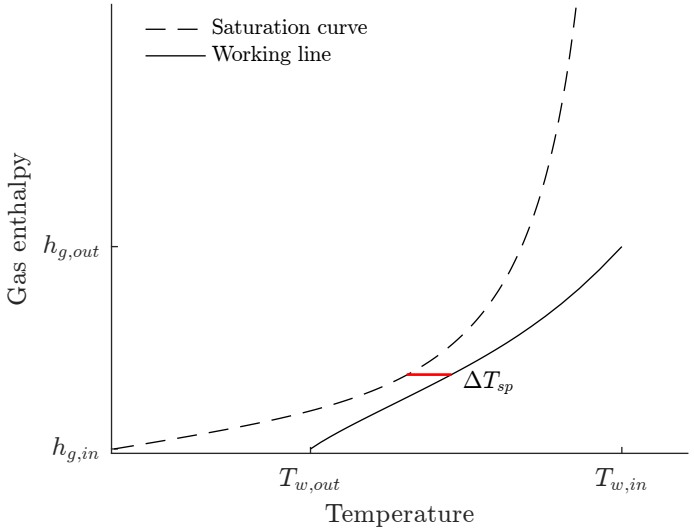

FIGURE 2.7: Saturator working line.

It represents the "technology level" of the saturator since it reflects the discrepancy of the working line from an ideal humidification process with a zero pinch point temperature difference. For higher ΔT_{sp} values, the heat recovered falls, which implies that higher amounts of exergy are dumped into the atmosphere. The pinch point represents as well the driving force of the mass transfer process. The higher the pinch point, the larger the driving force and the easier the mass transfer process occurs. This permits to associate the pinch point with the height of the tower [66]. Increasing the height reduces the ΔT_{sp} and vice versa. More information about the saturator tower's performance can be found in the literature [66–70].

One of the first models to calculate the performance of pressurised saturation towers was presented by Enick et al. [71]. The model divided the tower in sections of constant water temperature leap and assumed that the slope of the working line was constant in each section. This permitted to easily calculate the outlet conditions. Nevertheless, this assumption entailed some accuracy penalties.

In order to solve the accuracy issues of the previous model, new algorithms were developed by Lindquist et al. [66], Dalili [64], Parente et al. [72], and Araki et al. [73]. These models also discretised the tower in a finite number of small sections. The difference with the previous model is that these new algorithms directly solved the heat and mass transfer balance equations for each section, which permitted to eliminate the straight line assumption and increase the accuracy of the calculations. Nevertheless, it was necessary to employ the heat and mass

transfer coefficients to solve the complex system of equations in each section. The problem being that to properly estimate the coefficients detailed knowledge about the tower's geometry is required.

The main drawback of these models was the requirement of complex numerical methods to warranty the convergence of the systems of equations. Nevertheless, Aramayo-Prudencio and Young [69] proposed a similar model, but also included the description of a pseudo-transient numerical method to easily convergence the equations. This facilitated the implementation of the algorithm into new simulation models.

The previously introduced models have a high degree of accuracy. Nonetheless, they require several iterations to obtain the final result, which implies large computational times. Moreover, most of them require detailed information about the tower's geometry to use the complex correlations that estimate the values of the heat and mass transfer coefficients. Aramayo-Prudencio and Young [68] proposed a new model that avoided all these issues. This model required no geometrical data, but only the inlet conditions of the dry air and of the liquid water stream, as well as the design ΔT_{sp}. The model enables saturator's performance calculations by solving the thermodynamic relationship equations only at three points of the tower, instead of dividing it into a larger number of sections. Compared with the previous algorithms, this model was considerably less time consuming and required no knowledge of the tower's geometry, just the definition of its "technology level" via ΔT_{sp}. The short calculating time makes the model highly suitable for performing a large number of design point calculations. Nevertheless, the algorithm is not able to estimate the off-design performance since it is not known how ΔT_{sp} changes when altering the inlet conditions in a given saturator tower.

Sizing methods basically consist in the iterative calculations of the height of the tower using the previously presented models until convergence between the estimated and the design performance is achieved. Simpler models were presented by Lindquist et al. [66], Dalili [64], and Parente et al. [72], which assumed the working line to be straight and estimated the height based on the area between the working line and the saturation line (Figure 2.7). Nevertheless, these methods only gave accurate results for pressure lower than 10-15 bar [72].

2.3 Heat exchangers

The heat exchangers fulfil a primary function of the HAT cycles. They recuperate the heat contained in the exhaust gases, but also the heat rejected during the intercooling and aftercooling processes. Accordingly to Lazzarato and Segato [46] the optimum heat exchange system should include an intercooler, an aftercooler, a recuperator, and an economiser. Different types of heat exchangers have been employed for the construction of these devices. The Japanese test rig [73] used a tube-fin architecture for the aftercooler and a plate-fin for the recuperator, whereas the Lund University plant [57, 66] employed a brazed-plate configuration for the aftercooler and a tube-fin for the recuperator. On the other hand, Jonsson and Yan [32] suggested the use of tube-fin and smooth-tube heat exchangers for the aftercooler and the recuperator respectively, and Lindquist [66] proposed the use of a brazed-plate configuration for the intercooler. However, one of the most famous intercooled-recuperated gas turbines, the WR-21 [74], uses a plate-fin configuration for both heat exchangers. Nevertheless, all the authors [32, 66, 73] agreed on the use of tube-fin architectures for the economiser. Thus, it is concluded that there is not a unique possible solution. The selection of the heat exchanger type might depend on the design requirements and specifications.

Tube-fin and smooth-tube configurations are normally arranged in shell and tube architectures. These type of heat exchangers are the most commonly used in the industry due to its versatility and capacity to operate over a wide range of pressure and temperatures. Although they are among the least expensive types of heat exchangers, they are also known for being substantially bulky [75]. Tube-fin and smooth-tube configurations can also be arranged as economisers of a heat recovery steam generator if the air-side is not pressurised. Brazed-plate heat exchangers offer a more compact solution compared to shell and tube configurations [75] since they have a considerably larger surface area per volume unit. In addition, they are able to achieve high effectiveness in expense of a relatively high pressure drop. The main drawback of the brazed-plate architecture is the pressure limitations, as they should not be used at pressures over 16 bar [75]. Plate-fin exchangers are noted for their small size and weight. These units can offer a surface area per volume unit 45 larger than shell and tube configurations [75]. Moreover, its high structural strength permits them to operate with pressures up to 200 bar [75].

Although the type of selected heat exchanger might differ according to the different objectives of each designer, the materials to be employed for the construction of the devices are normally more standardised. Aluminium is a commonly used material in the design of heat exchangers [75] due to its high strength, and low acquisition cost. Nevertheless, for applications where high oxidation resistance is required, the aluminium is often subtitled by stainless steel [32, 75].

Materials to be employed in the design of high-temperature heat exchangers are limited by their corrosion, oxidation, and creep resistance properties. In micro-turbines, the use of stainless steel 347 is very extended for the design of recuperators [76–79]. The stainless steel 347 shows an excellent performance up to 650 °C. Moreover, the stainless steel 347 can be modified by the introduction of a higher nickel content to operate up to 750 °C, which obviously increases the price. A Cr_2O_3 layer is formed on the surface, avoiding further oxidation of the material [78]. However, above 650 °C the layer suffers from instabilities that lead to higher oxidation rates and cracking of the film, accelerating the oxidation process and leading to failure. In addition, the process can be accelerated by the water vapour produced during the combustion process [79].

For higher temperatures, it is necessary the use of nickel-based alloys, also known as superalloys, as the Inconel 625, Haynes 230, or Haynes 214 [76, 78]. The use of these superior alloys permits to enlarge the operating temperature of the recuperators up to 850 °C [77]. Among the different superalloys, the Inconel 625 is quoted as the only superalloy that has been commercially developed and extensively used in high-temperature recuperators [78]. It presents the best trade-off between acquisition cost and material properties. Inconnel 625 recuperators have already been used in the design of medium size gas turbines as the WR-21 [80] and the Mercury 50 [81].

McDonald [76] suggested the design of a multi-pass cross counterflow modular recuperator to reduce the cost for high temperature applications. The heat exchanger could use a superalloy in the first high-temperature section, and lower grade materials in the colder modules. This solution is proven [76] to reduce the acquisition cost up to a 60% compared with a unit designed entirely with superalloys.

More exotic solutions involving the design of ceramic recuperators have also been analysed [76, 79, 82] in order to extend the operability up to 1150 °C. Nonetheless,

utilisation of a ceramic recuperator in medium or large gas turbine has not yet been reported and considerable effort is still required to develop mature, reliable, and low-cost ceramic configurations.

Another important consideration that limits the spectrum of viable materials is the use of seawater as coolant. This may lead to fouling issues, and consequent deterioration of the heat exchanger's performance and integrity. The most important forms of fouling include crystalline, corrosion, particulate, and biological fouling [83]. Crystalline fouling is produced by the crystallisation of salts that have a solubility that diminishes with increasing temperature. Corrosion fouling results as consequence of the material oxidation, which produce an insulating layer. Particulate fouling is produced by the deposition of particles suspended in the water. Last, a whole range of types of biological forms grow on heat exchanger tubes in seawater, leading to biological fouling. The deposition or creation of a layer of debris, biological material, or oxides on the surface of the heat exchangers walls creates an insulating layer that reduces the overall heat transfer coefficient.

Although stainless steel is employed to avoid oxidation of the heat exchangers, it is not generally suitable for seawater duties as it suffers from stress corrosion cracking [84]. Copper alloys have demonstrated along the years to be one of the most suitable options for designs involving seawater [85]. The good corrosion resistance of these alloys is based on the formation of a protective film of corrosion products in the early period after initial exposure. The surface layer results to be toxic for most of the biofouling forms, avoiding its growth [86]. Nevertheless, copper itself has very poor erosion and impingement resistance. The addition of nickel increases its strength and its corrosion resistance, and allows higher flow velocities [84]. Alloys with up to 10% nickel content, 90-10 copper-nickel, retain a high resistance to the attachment and growth of marine organisms. Nickel content can be enlarged up to 30%, 70-30 copper-nickel, if strength and erosion-corrosion resistance wants to be further increased. The high thermal conductivity, good biofilm formation and corrosion resistance make the copper-nickel alloys excellent candidates for the design of marine heat exchangers.

Other possibilities include the use of titanium alloys [87]. Titanium alloys offer the advantage of presenting an excellent erosion and corrosion resistance, a low density and high strength compared to other metals, and lower disposal problems than copper alloys due to its lower toxicity [84]. Therefore, its excellent erosion resistance permits to design the heat exchangers with higher flow velocities to

achieve higher heat transfer coefficients, whereas its higher strength permits to achieve designs with thinner walls, facilitating the heat transfer process. Nevertheless, the biofouling resistance of the copper based alloys is still larger and their costs are significanlty lower [84].

No matter what type of heat exchanger is selected or material is employed, operation and maintenance of the seawater intake system has a profound effect on heat exchanger's performance [84]. Shipboard systems are relatively simple, as ships navigate normally in zones with large bodies of water where there are very low amounts of debris. These intake systems have a gate to avoid the entrance of floating loads or fish. In addition, stationary screens or strainers are placed between the pumps and the water box. In case of heat exchangers with narrow passages, additional screens are necessary to assure the removal of the debris.

On the other hand, the design of intakes for coastal plants is critical and more complex [84]. A frontal grate is placed to keep out large floating debris. Downstream the grates, travelling screen are employed to avoid the entrance of fish, crab claws, sea-shells, twigs, polyethylene bags and similar trash. These screens rotate to slowly discharge the accumulated rubbish. Further down, the travelling screens, stationery screens are placed to remove the last pieces of debris before the water enters the water box. Keeping the intake system in good condition is crucial for the proper operability of the heat exchangers. Frequently, heat exchanger failures which are identified as tube failures are caused by screen failures.

2.4 Summary

In this chapter, the conducted research on humid gas turbines is summarised, the characteristics and the design alternatives of the saturator towers are described, and the different architectures previously employed in heat exchangers are presented together with the material considerations and seawater-derived issues.

The HAT cycle has demonstrated in several studies to achieve a thermal efficiency within the range 52%-55%, while reducing the NO_x emissions a 90% compared to non-humidified gas turbines. Moreover, the lack of necessity of a bottoming cycle to recover the exhaust heat allows reducing the specific investment and the footprint compared with CCGT. Various analyses have concluded that the lower

specific investment of the HAT and its large efficiency permit to predict a better economic performance than CCGT.

The studies also predicted a better off-design and part-load performance of the HAT cycle compared with simple gas turbines and CCGT. The performance of the HAT is less affected by the ambient temperature and its efficiency is less penalised when decreasing the output power setting.

The performance and economic analyses focused on identifying the best layout of the cycle and heat exchanger distribution. These studies arrived at the conclusion that the most effective layout should include one intercooler, one aftercooler, and one economiser, in addition to the recuperator. Other analyses investigated the variation of the thermal efficiency and the specific power with the pressure ratio and the combustion temperature. This proved that the benefits derived from the humidification are larger for higher pressure ratios. Other investigations demonstrated the benefits of further modifying the cycle, as the part-flow humidification, the spray intercooling, and the water atomisation cooling of the compressors. Nevertheless, the largest benefit was obtained by the introduction of a second combustion chamber, which permitted to raise the efficiency up to 63%.

Three types of the tower have been presented so far, the spray tower, the packed bed tower, and the tubular tower. Among the three options, the packed bed tower appears to be the best configuration for the humidification of medium scale gas turbines due to its low-pressure losses and its large contact area. The different sizing and performance models developed so far have also been introduced.

About the heat exchangers, there is no agreement on which type of heat exchanger should be used for each device. Nevertheless, the studies agree on the necessity of using nickel-based alloys on the heat exchangers with inlet temperature above 750 °C, and copper-nickel or titanium heat exchangers for marine applications. The authors also warn about the hazards of using seawater as a cooling fluid due to the biofouling and corrosion issues it might involve, and strongly recommend the use of filtration systems.

Chapter 3

Component design models

This chapter presents the design processes followed for the sizing of the different components of the cycle. The thermodynamic configuration of the cycle is introduced to present the different systems integrating the reheater humid air turbine proposed by Sanchez [10] and the duties that they have to fulfil. The architecture selected for each component is described, together with the design models developed. In addition, the price estimation techniques employed for the calculation of the component's acquisition cost are presented. Last, the optimisation routine created for heat exchangers design process is described. The detailed design models of the heat exchangers and the saturator tower are presented in Appendix A.

3.1 Reheated humid air turbine

The Reheated Humid Air Turbine (RHAT) cycle analysed in this study is based on the configuration presented by Sanchez [10], a dual-shaft gas turbine with a free power turbine. The layout of the power plant studied is depicted in Figure 3.1. The gas turbine includes an air-water intercooler between the two compressors to reduce the compression work. The air-water aftercooler installed after the high pressure compressor is used to reduce the air temperature upstream the saturator tower, promoting the absorbance of moisture during the evaporation process and, hence, improving the thermal efficiency of the power plant [57]. In within the saturator, a heat and mass transfer process takes place from the water towards the air whose temperature and mass flow are increased. Due to the relatively low temperature of the gas at the outlet of the saturator, the addition of a recuperator significantly

benefits the thermal efficiency of the cycle. After preheating the humid air, it passes through the burner and turbines. At the outlet of the core turbines, a reheater is added in order to enlarge the thermal efficiency and the specific power, as recommended by Chiesa et al. [44] and Nakhamkin et al. [50]. The integration of the second combustion chamber will potentially reduce the exergy destroyed in the main combustion, which is the principal source of irreversibilities in the cycle [44, 55]. The addition of the reheater permits to enlarge the heat recovered in the recuperator [44], increasing the temperature of the gas at the inlet of the combustion chamber. Downstream the power turbine and the recuperator, which returns the waste heat into the core stream, an economiser is introduced to recover the low-quality heat remaining in the bulk gas and transfer it to the water.

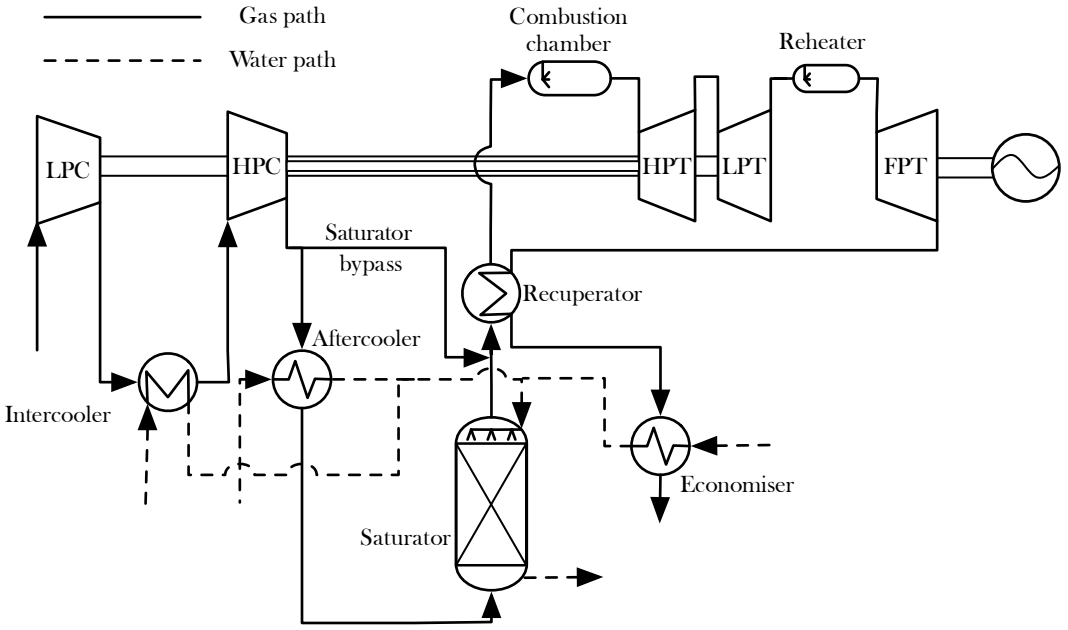

FIGURE 3.1: Schematic layout of the reheated humid air turbine cycle.

The RHAT uses an intercooler, an aftercooler, and an economiser to warm the saturator's feeding water, as suggested by Lazzaretto and Segato [46], and Nyberg and Thern [47]. The water is pressurised before passing through the heat exchangers to promote the natural convection from these devices to the saturator tower. The combination of the air-water heat exchange system with the saturator allows recovering the low-quality energy, otherwise dumped into the atmosphere. Therefore, the combination of these components is what permits to enlarge the efficiency of the cycle compared to a conventional gas turbine.

As suggested by Ågren and Westermark [52, 53], and Jonsson and Yan [32], a saturator bypass duct is included in the design. This duct joins the outlet of the

high pressure compressor and the inlet of the recuperator, allowing a fraction of the dry air to bypass the aftercooler and the saturator, and simply be mixed with the humid air prior it enters the recuperator. Therefore, the required transfer area of the saturator and the aftercooler is reduced.

The water is considered to be circulating in an open loop, simplifying the system. The evaporation process and the high efficiency of the droplet eliminator placed at the outlet of the saturator make the component a water-treatment device per se, as explained by Rosen [56] and Lindquist [41]. This enables the use of seawater in the heat exchange system, which is substantially beneficial for marine applications and energy plants located in coastal areas.

Although the transformation of the RHAT into a reheated HAWIT or a reheated TOP-HAT might increase the thermal efficiency of the cycle and result in a more economic configuration [30, 31, 38], these systems would not have permitted the use of seawater as coolant due to the requirement of demineralised water. Therefore, it is preferred to employ a conventional intercooling system and avoid the use of demineralised water.

3.2 Saturator

The saturator tower is the key component of the humid air turbine cycles. It enables the reinjection of the low-quality heat into the cycle by evaporating large amounts of water into the main gas path at low temperatures.

A structured packed bed tower configuration is selected for the design of this component. This configuration permits the use of untreated water [64], which is significantly beneficial for the use in marine and coastal applications. In addition, the structured packing permits to obtain a large exchange area while keeping the pressure losses to a minimum in comparison with the random packing [65], which is critical for the efficient performance of the gas turbine. Although the tubular tower might offer a more compact design, it cannot operate with gas temperatures above the boiling point in order to ensure a continuous water film [64], which is not satisfied for the RHAT. Therefore, the tubular configuration had to be discarded.

A representation of the saturator tower selected is shown in Figure 3.2. The objective of the packed bed is to maximise the contact area between the falling

liquid water and the rising air. A liquid distributor is placed to ensure the uniform dispensation of the incoming water along the cross-sectional area. In addition, a droplet eliminator is necessary to prevent any potential droplet entrainment into the turbomachinery, which would entail risk for the rotating equipment integrity.

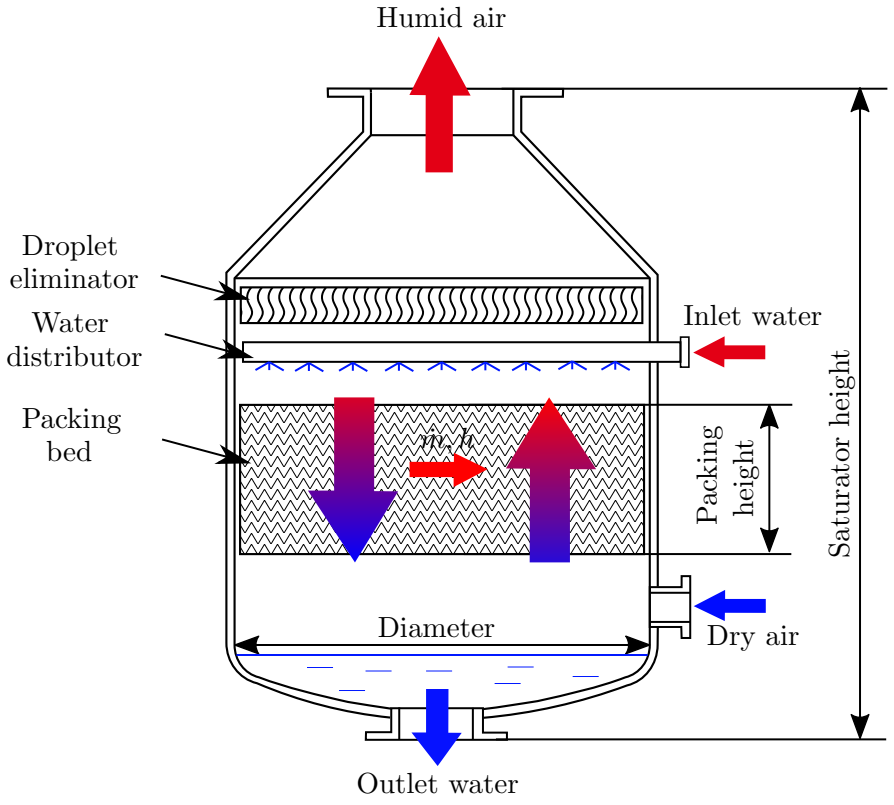

FIGURE 3.2: Architecture of the structured packed bed saturator tower.

The saturator's sizing model uses an iterative approach to calculate the height of the tower based on matching the design performance and the estimated performance for the guessed height. Although this approach is more computational demanding than the straight line working methods [64, 66, 72], it provides more accurate results [72]. The model is based on the work presented by Coulson and Richardson [65], and Aramayo-Prudencio and Young [69]. The required data includes the inlet and outlet thermodynamic properties (temperature, pressure, humidity, and mass flow) of the air and water. The outcomes are the packing's height, the total tower's height, the diameter of the packing, and the total weight of the device.

First, the model calculates the diameter of the packing from the design pressures losses and the mass flow. The packing's diameter is calculated following the correlation presented by Coulson and Richardson [65]. Based on the recomendations reported by Dalili [64], the selected pressure losses per length unit selected are

300 Pa/m and the maximum velocity is 60% of the flooding velocity, in order to ensure a stable operation and avoid water over-flood.

Then, knowing the diameter, the height of the packing is calculated based on the work presented by Aramayo-Prudencio and Young [69]. The calculation procedure consists in an iterative algorithm that guesses the height of the device to estimate the thermodynamic performance. The iterative procedure is repeated until convergence between the estimated performance and the design performance is reached.

The height of the liquid distributor and the droplet eliminator are assumed to be constant for all the designs. The height of the outlet cone and the inlet plenum are derived from the diameter of the packing.

Last, the weight of the tower is calculated based on the density of the material and the volume that it occupies. The material is assumed to be stainless steel, with an internal coating of copper-nickel to prevent corrosion. Although a description of the sizing methodology is provided herein, the full details of the model are described in Appendix A.

3.3 Intercooler and aftercooler

The intercooler lowers the temperature of the gas between both compressors in order to minimise the compression work. The aftercooler chills the air prior being injected into the saturator with the objective of maximising the energy absorbed by the gas within the tower and reduce the outlet temperature of the water. Both heat exchangers are assumed to use seawater as the coolant fluid to absorb the heat rejected by the gas.

Nevertheless, the objective of these heat exchangers is not only to reduce the temperature of the gas but also to warm the cooling water as much as possible to improve the performance of the saturator [47]. The requirement of warming the water and cooling the air at the same time challenges the design of the heat exchangers. To achieve a maximum temperature jump in both fluids, the heat capacities ($\dot{m}\ c_p$) of both fluids must be similar, according to Eq. 3.1. However, the specific heat capacity (c_p) of the water is four times larger than the one of the air. Thus to achieve a similar heat capacity, the mass flow of the water has to be

four times lower than the mass flow of the gas. On top of that, the density of the water is two to three orders of magnitude larger than the one of the pressurised air. Hence, the volumetric flow of the water becomes 400-1000 time lower than the volumetric flow of the gas. This challenges the design of the heat exchangers since it is really complicated to fit flows with such dissimilar volumes and achieve proper velocities for both of them.

$$\dot{Q} = (\dot{m}\ c_p)_g\ \Delta T_g = (\dot{m}\ c_p)_w\ \Delta T_w \tag{3.1}$$

A plate-fin architecture is selected for the design of both heat exchangers in order to maximise the compactness of the design while ensuring the mechanical integrity of the heat exchanger at the same time [75]. Nonetheless, the large difference between both volumetric flows makes impossible to use a counter-current configuration, the most compact, as it would involve extremely large gas velocities or extremely low water velocities due to the similar frontal areas both flows would have. The solution is to arrange the geometry in multi-pass cross counterflow configuration, as shown in Figure 3.3. The air flows in a straight path, whereas the water passages cross multiple times the air's path. The advantage of this solution consists in its flexibility. This architecture permits to design almost independently the frontal areas of both fluids, without deteriorating the performance or harming the design integrity. Finally, this configuration enables to achieve the recommended flow velocities on both fluids. The material selected for the design of the heat exchangers is 90-10 copper-nickel due to its high resistance to corrosion and fouling growth in marine enviroments [85].

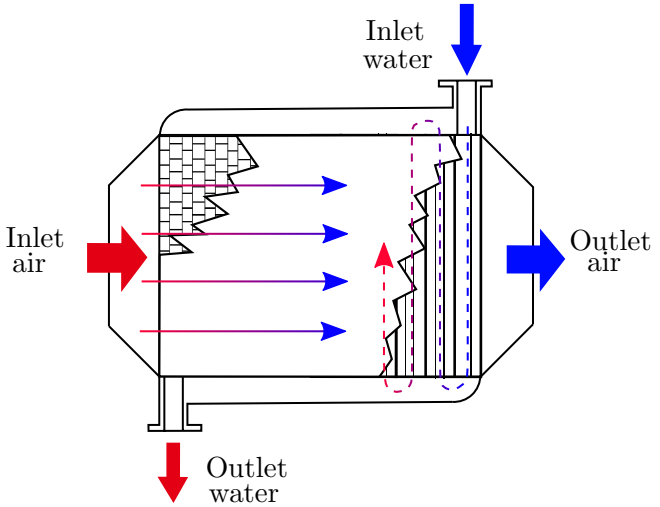

FIGURE 3.3: Architecture of the intercooler and aftercooler.

The air-side passages are designed with a serrated fin configuration. This configuration produces the highest heat transfer coefficients due to the intense turbulence created and helps strengthening the structure [88]. The water-side passages are designed with plain fins to decreases the risk of fouling and passage blocking, as well as to reduce the pumping work.

Other architectures were initially considered for the design of these heat exchangers as the brazed-plate, or the shell and tube heat exchangers. Nevertheless, the use of brazed-plate architectures with pressures exceeding 16 bar is not recommended due to leakages and structural issues [75], for that reason this configuration was discarded. The shell and tube configuration offers the advantage of its high availability in the market and a low acquisition price. However, a study performed by Tous [89] demonstrated that this architecture is not capable of achieving any feasible design for the required thermodynamic performance. Although theoretically the performance can be achieved, the obtained geometry leads to infeasible designs due to the volume flow of the two fluids being highly different. The resulting configuration had a reduced number of tubes in order to achieve normal water velocities, what caused the tubes to be excessively large.

The effectiveness-Number of Transfer Units ($\varepsilon - NTU$) method presented by Kays and London [90] is followed to estimate the heat transfer area. The number of transfer units is obtained by means of the correlations provided by the Engineering Society Data Unit (ESDU) [91]. To obtain the main heat exchanger dimensions, the heat transfer coefficient of the air-side is estimated using the expressions provided by Yang and Li [92]. For the water-side, the equations suggested by ESDU [93, 94] are employed to evaluate the heat transfer coefficient for turbulent and laminar flow respectively. The full model is explained in detail in Appendix A.

The model requires as inputs the thermodynamic conditions (temperature, pressure, humidity, and mass flow) of the air and the water at the inlet and the outlet. In addition, it also requires a significant number of geometry variables: the length of the water-channels, the width of the water-passes, the number of layers, the height of the fins, the length of the fins of the air-side, the number of fins per meter on both sides. The main outcomes of the model are the length, the width, the height, and the weight of the heat exchanger. Although it has to be mentioned that the design of the headers is not included.

3.4 Recuperator

The recuperator uses the high-quality energy contained in the power turbine exhaust gas to heat the humid air before entering the combustion chamber. This permits to reduce the fuel required to achieve the imposed turbine inlet temperature.

A plate-fin architecture is selected for the design of this heat exchanger due to its compactness, and its capability to stand large pressure differences between both fluids [75]. Two different configurations are considered, Figure 3.4, a pure counter-current configuration and a multi-pass cross counterflow configuration. In both configurations, the cold and the hot layers contain a serrated fin distribution to enhance the heat transfer coefficient and to strengthen the structure.

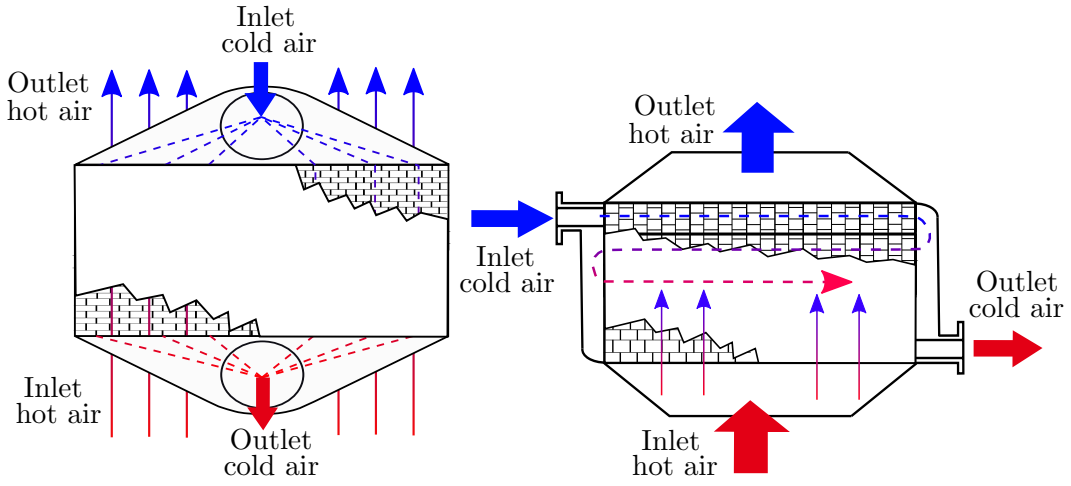

(a) Counter-current configuration (b) Multi-pass configuration

FIGURE 3.4: Architecture of the recuperator.

In the counter-current configuration the cold air flows along an upper pipeline to be distributed among the multiple layers, as depicted in Figure 3.4a. Then, it flows downwards and is collected in a tube to unify the air coming from all the multiple layers. The hot air simply flows upwards in between the cold layers without the requirement of any distributor. In the multi-pass configuration, the hot air flows upwards in a straight line path, whereas the cold air flows downwards along several passages that cross completely the hot path multiple times, as illustrated in Figure 3.4b.

The presence of the second combustor makes necessary the use of nickel alloys in the design of the recuperator, as the inlet temperature is in the range of 700-800 °C

[76, 77, 79]. The multi-pass configuration suggested by McDonald [76] allows to build only the hottest passes on nickel alloys, and the coldest ones on cheaper stainless steel. However, the pure counter-current configuration would be made entirely of nickel alloy. Hence, despite the lower heat transfer area required by the pure counter-current configuration heat exchanger, it may result in a more expensive device compared to the multi-pass configuration as the whole heat exchanger has to be made in nickel alloys.

The model developed to size the heat exchangers is equivalent to the model employed for the design of the intercooler and the aftercooler. Instead of having air and water, the fluid is air on both sides. The model is explained in detail in Appendix A.

3.5 Economiser

The economiser uses the low-quality energy remaining in the gas at the outlet of the recuperator to warm a large amount of pressurised water to feed the saturator. As the gas cools, it reaches the dew point, triggering the condensation of the gas moisture on the inner walls of the heat exchanger. The amount of water condensed can reach up to 25% of the moisture within in the gas. Thus, it is necessary to take some precautions when selecting the architecture of this heat exchanger to avoid issues derived from fouling and passage blocking.

A mixture of tube-fin and plain-tube configuration is selected for the design of the economiser, as shown in Figure 3.5. The water flows inside the tubes, while the air flows over them. The tubes are arranged in a multi-pass cross counterflow configuration in order to make possible achieving large effectiveness values. The section that is closer to the gas entrance, also called the dry part, is designed with a tube-fin configuration. The section closer to the gas exhaust, also called the wet part, is designed with a plain tube configuration to promote the flow of the condensing moisture over the tube's walls. Although the tube configuration is less compact than plate-fin, it prevents the appearance of any issue derived from passage blocking due to the presence of dirt gas and condessed water inside extremely narrow passages. The material selected for the design of the heat exchangers is 90-10 copper-nickel due to its high resistance to corrosion and fouling growth in marine enviroments [85].

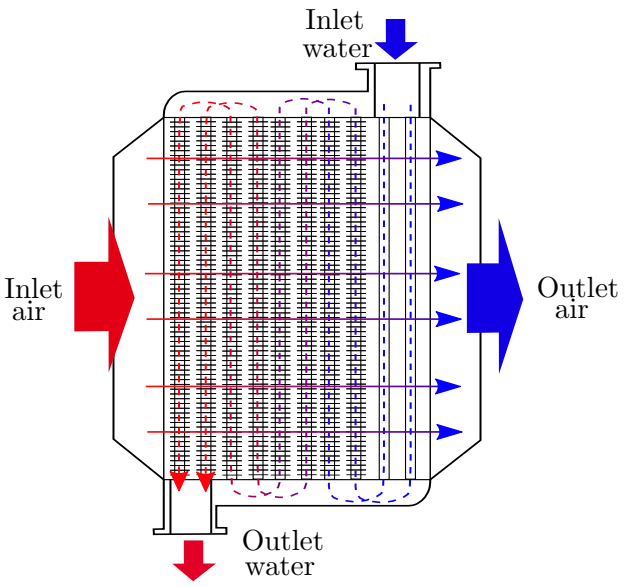

FIGURE 3.5: Architecture of the economiser.

The $\varepsilon - NTU$ method described by Kays and London [90] is followed to estimate the heat transfer area. The number of transfer units is obtained by means of the correlations provided by ESDU in [91]. To calculate the heat transfer coefficient of the dry air-side flow, the correlations given in the ESDU items [95] are utilised. However, in the wet part, the heat and mass transfer process were simulated following the model presented by Gesellschaft [96]. The heat transfer coefficient of the water was evaluated as dictated in the ESDU items [93, 94]. The full model is explained in detail in Appendix A.

In addition to the thermodynamic conditions (temperature, pressure, humidity, and mass flow) of the air and the water at the inlet and the outlet, the model also requires significant geometry data as inputs. These geometric variables include the length of the tubes, the width of the air passage, the pitch between the rows of tubes, the number of passes, the diameter of the tubes, the height of the fins, and the density of fins. The main outcomes of the model are the length, the width, the height, and the weight of the heat exchanger. It has to be mentioned that the dimensions do not account for the headers, as they are not considered in the design.

3.6 Gas turbine and generator

The gas turbine represents the core of the power plant, where the gas is compressed, the heat is added, and the work is extracted. The size of the turbomachinery is estimated by means of the scaling laws presented by Sanchez [10], derived from the work developed by Walsh and Fletcher [97]. The length, width, and height are scaled from their reference value using the square root of the inlet mass flows ratios, as presented in Eq. 3.2. The weight of the turbomachinery changes with the cube of the linear scaling factor. However, for industrial heavyweight engines, an index of 2.7 is employed as recommended by Walsh and Fletcher [97]. Thus, knowing the reference weight the scaled weight can be obtained using Eq. 3.3. This process does not account for the weight of the inlet and outlet ducts, neither of the ancillary equipment required for the operation of the gas turbine.

$$L = L_{Ref}\sqrt{\frac{\dot{m}}{\dot{m}_{Ref}}} \tag{3.2}$$

$$W = W_{Ref}\left(\sqrt{\frac{\dot{m}}{\dot{m}_{Ref}}}\right)^{2.7} \tag{3.3}$$

L represents either the length, width, or height, W the weight, $\dot{m}$ the inlet mass flow, and the subscript Ref stands for reference values.

The weight and dimension values of the reheated humid air turbine presented by Sanchez [10] are taken as a reference to scale the size of the turbomachinery. The scaling technique has some limitations, as it can not reproduce the change in sized derived from a variation of the pressure ratio. Nevertheless, for obtaining an approximated number of the overall dimensions to roughly estimate the volume occupied by the power plant, the formula is accurate enough since there are no dramatic variations in the pressure ratio.

The weight and size of the generator are obtained from a reference permanent magnet generator used in the design of prime mover systems for fully electric ships [98, 99].

3.7 Cost estimation

3.7.1 Saturator

The acquisition cost of the saturator is derived from the weight of the shell (8,800 \$/ton) and the packing volume (3,800 \$/m^3), assuming that both are made in stainless steel. To consider the cost of the droplet eliminator, water sprays, and the rest of the subcomponents, an additional \$14,000 are added on top of the baseline cost [100].

3.7.2 Heat exchangers

The acquisition cost of the plate-fin heat exchangers ($\Xi_{HX,p-f}$) is estimated by means of Eq. 3.4, presented by ESDU [75].

$$\Xi_{HX,p-f} = \kappa_{pf}\{[\dot{Q}/\Delta T_{lm}]^*\}\ [\dot{Q}/\Delta T_{lm}]^* \tag{3.4}$$

where κ_{pf} is a function of $[\dot{Q}/\Delta T_{lm}]^*$. This correlation can be found in the work presented by ESDU [75]. The parameter $[\dot{Q}/\Delta T_{lm}]^*$ is defined as:

$$[\dot{Q}/\Delta T_{lm}]^* = A_{HX}\ U_{ESDU} \tag{3.5}$$

where A_{HX} is the estimated heat transfer area and U_{ESDU} is the average heat transfer coefficient prescribed by ESDU [75], which for the air-water plate-fin heat exchangers has a value of 491 W/m^{2}K and 217 W/m^{2}K for the air-air configuration.

It has to be mentioned that the ESDU correlations are only valid within the specified limits in the documentation [75]. Thus, if the design of a heat exchanger would require a larger heat transfer area than the maximum specified in the documentation, it would have to be split in two devices with a heat transfer area lower than the maximum specified. The maximum heat transfer area for the air-water configurations is 2,000 m^2, and 4,500 m^2 for the air-air configuration.

The acquisition cost of the tube-fin heat exchangers ($\Xi_{HX,t-f}$) is calculated using the correlation presented by Casarosa et al. [101], where k_{tf} represents the cost per area of the device (58.64 \$/m^2).

$$\Xi_{HX,t-f} = \kappa_{tf} A_{HX} \tag{3.6}$$

The cost correlations of the heat exchangers are originally derived for components made of stainless steel. Consequently, the material correction factors suggested by Towler and Sinnot [102] are applied to convert the cost depending on the construction material. The coefficients for the different material are presented in Table 3.1.

TABLE 3.1: Material's cost coefficients [102].

Material	Coefficient
Stainless Steel	1.30
Copper-Nickel	1.54
Titanium	1.89
Nickel alloys	1.70

3.7.3 Gas turbine and generator

The acquisition cost of the gas turbine is composed by the price of the two compressors, the two combustion chambers, and the three turbines. The cost of each of these components and the generator is calculated accordingly to the following equations, where the values of the constants are showed in Table 3.2, based on the model developed by Traverso et al. [103].

Compressors

$$\Xi_{comp} = c_1 \left[\frac{\left(\dfrac{\dot{m}\sqrt{R\,T}}{P\,m_{cr}} \right)_{in}}{\left(\dfrac{\dot{m}\sqrt{R\,T}}{P\,m_{cr}} \right)_{Ref}} \right]^{c_2} \frac{PR^{c_4}\,\ln(PR)}{(1-\eta_{pol})^{c_2}} \tag{3.7}$$

$$m_{cr} = \frac{\sqrt{\gamma}}{((\gamma+1)/2)^{\gamma+1/(2(\gamma-1))}} \tag{3.8}$$

Combustion chambers

$$\Xi_{CC} = cc_1 \left[\frac{\left(\frac{\dot{m}}{\rho}\right)_{out}}{\left(\frac{\dot{m}}{\rho}\right)_{Ref}} \right]^{cc_5} \left[1 + \exp^{cc_3\left(\frac{T_{out}}{T_{Ref}}\right)-cc_4} \right] \frac{1}{\Delta P^{cc_2}} \tag{3.9}$$

Turbines

$$\Xi_{turb} = t_1 \left[\frac{\left(\frac{\dot{m}}{\rho}\right)_{out}}{\left(\frac{\dot{m}}{\rho}\right)_{Ref}} \right]^{t_5} \left[1 + \exp^{t_3\left(\frac{T_{in}}{T_{Ref}}\right)-t_4} \right] \frac{\ln(PR)}{(1-\eta_{pol})^{t_2}} \tag{3.10}$$

Generator

$$\Xi_{gen} = g_1 \left(\frac{\dot{W}_{el}}{\dot{W}_{el_{Ref}}} \right)^{g_2} \tag{3.11}$$

$\dot{m}$ represents the mass flow through the component, R the gas constant, T the temperature of the gas, P the pressure, ρ the density, γ the heat capacity ratio (c_p/c_v), PR the pressure ratio across the compressor or the turbine, η_{Pol} the polytropic efficiency, ΔP the percentage pressure loss across the combustor, $\dot{W}$ the power supplied to the generator, the subscript *out* stands for outlet conditions.

TABLE 3.2: Cost factors of the gas turbine [30].

cc_1	\$ 2,385	t_1	\$ 7,680	c_1	\$ 6,500	g_1	\$ 1,324
cc_2	0.995	t_2	0.290	c_2	0.15	g_2	0.72
cc_3	5.479	t_3	4.185	c_3	0.85	P_{Ref}	101.325 kPa
cc_4	34.360	t_4	26.600	c_4	0.30	T_{Ref}	298.15 K
cc_5	0.600	t_5	0.750	$\dot{W}_{Ref}$	1.0 kW	$\dot{m}_{Ref}$	1 kg/s
						R_{Ref}	289.2 J/kg K

Once the cost of the components is obtained, the price of the bare gas turbine ($\Xi_{Bare-GT}$) is estimated as the sum of the cost of the components plus the ancillaries ($\Xi_{ancillaries}$) as shown in Eq. 3.12. The cost of the system's ancillaries is approximated as 40% the cost of the compressors, combustors, and turbines [30].

$$\Xi_{Bare-GT} = \sum \Xi_{comp} + \sum \Xi_{CC} + \sum \Xi_{turb} + \Xi_{ancillaries} \tag{3.12}$$

Last, the cost of the gas turbine (Ξ_{GT}) is the sum of the bare gas turbine and the packing ($\Xi_{packing}$), as shown in Eq. 3.13. The cost of the packiing is estimated as 40% of the cost of the bare gas turbine [30].

$$\Xi_{GT} = \Xi_{Bare-GT} + \Xi_{packing} \tag{3.13}$$

3.7.4 Power plant

The Purchase Equipment Cost (PEC) is estimated as the sum of the price of the gas turbine, the heat exchangers, and the generator.

$$PEC = \Xi_{GT} + \sum \Xi_{HX} + \Xi_{gen} \tag{3.14}$$

The Specific Purchase Equipment Cost ($SPEC$) represents the PEC per watt generated.

$$SPEC = \frac{PEC}{\dot{W}} \tag{3.15}$$

All the cost estimates are updated to 2015 by means of the Chemical Engineering Plant Cost Index [104].

3.8 Heat exchangers geometry optimisation

For a prescribed combination of the thermodynamic design variables, infinite different heat exchangers designs can be identified depending on the geometric variables selected. To reduce from the infinite designs to just one for each thermodynamic configuration, an optimisation routine has been developed. The optimiser routine requires as inputs the thermodynamic data, the geometry variables to be optimised and its boundaries, and the objectives of the optimisation. The boundaries of the geometric design variables are established depending on the type of the heat exchanger. On top of that, the optimiser routine also demands the specific heat exchanger's sizing tool for each component. Once the optimisation routine is

completed, the optimum geometry configuration is obtained. A flow chart of the optimisation environment is depicted in Figure 3.6a.

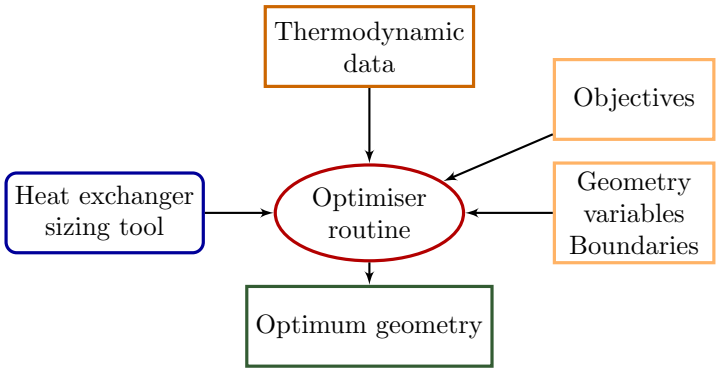

(a) Optimiser environment

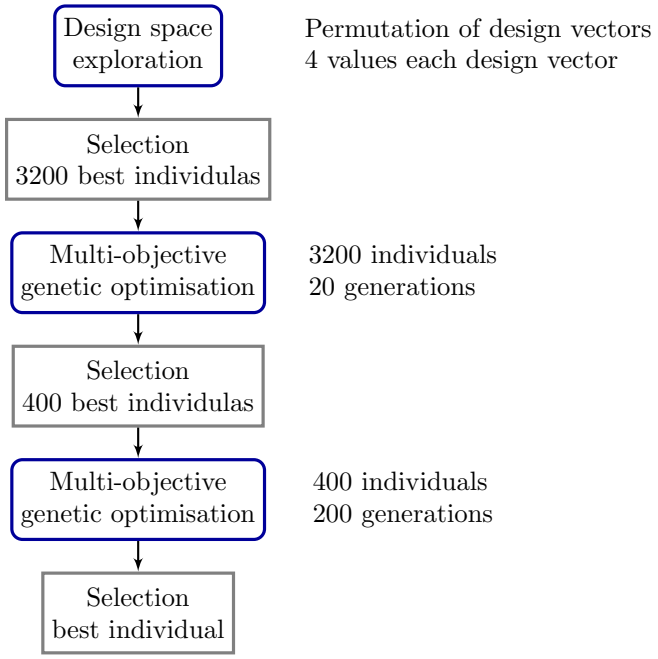

(b) Optimiser routine

FIGURE 3.6: Flowchart of the heat exchanger design optimisation.

The optimisation routine consists of a first design space exploration, followed by two optimisation procedures, as shown in Figure 3.6b. During the design space exploration, all the possible permutations of the geometric design vectors are analysed. The design vector of a geometric variable consists of four values equally distributed between the lower boundary and the upper boundary of the variable. From the resultant configurations of the design space exploration, the best 3,200 individuals are selected and used as the initial population of the subsequent optimisation performed, which is performed over 20 generations. From the first

optimisation, the best 400 configurations are selected and used as the initial population of the subsequent optimisation, which is performed over 200 generations. Last, the best configuration is selected from the resulting Pareto front.

Dividing the optimisation process into three steps permits to create a more efficient method compared to a single-pass optimisation. The first design space exploration ensures that the whole range of different possible design combinations is analysed. The following first optimisation, with a population of 3,200 individuals, narrows down the search over what is expected to be the optimum design region. Last, the third optimisation, with just 400 individuals, permits to quickly fine-tune the optimum design configuration. The optimisations are performed using a mulit-objective genetic-algorithm [105].

The optimisation is intended to identify the geometry that better compromises the following objectives:

- Minimum acquisition cost.
- Minimum perimeter.

The perimeter is defined as the sum of three principal dimensions of each heat exchanger (length, width, height).

The results of each design space exploration and the optimisations are Pareto fronts, where any design within it is an optimal candidate according to the optimisation objectives. Therefore, to select the most suitable configurations for the next it is necessary to impose a criterion. To select the best individuals from each optimisation step, the Selection Parameter (SP) of each resulting configuration is calculated. The configurations with the lowest SP are selected as the initial population of the following optimisation step. In the case of the final optimisation step, only the configuration with the lowest SP is selected. The SP is defined in Eq. 3.16. $F_i(x)$ represents the fitness of each individual, either the cost or the perimeter, and κ_i represents the weighting coefficient. This coefficient allows the designer to place more emphasis on any of the objectives when selecting the heat exchanger. In the current case, their values are set to 0.5, in order to select the configuration that trades equally both objectives.

$$SP(x) = \sqrt{\sum_{i=0}^{n} \kappa_i \frac{F_i(x)}{\max(F_i)}}, \qquad \sum \kappa_i = 1 \tag{3.16}$$

3.8.1 Intercooler and aftercooler

First, the required number of heat exchangers (N_{HX}) is calculated by means of Eq. 3.17 in order to avoid designs with a heat transfer areas outside the valid limits of the ESDU correlations.

$$N_{HX} = \text{ceil}\left(\frac{\dot{Q}/\Delta T_{lm}}{\overline{U}\ A_{\max}}\right) \tag{3.17}$$

where the "ceil" function rounds the number to the next integer, $\dot{Q}$ is the total heat ratio transferred, ΔT_{lm} is the logarithmic mean temperature defined in Eq. 3.18, $A_{\max}$ is the maximum heat transfer area valid for the ESDU cost correlations and $\overline{U}$ is a reference overall heat transfer coefficient, obtained from preliminary studies previously performed.

$$\Delta T_{lm} = \frac{(T_{g,in} - T_{w,out}) - (T_{g,out} - T_{w,in})}{\ln \dfrac{T_{g,in} - T_{w,out}}{T_{g,out} - T_{w,in}}} \tag{3.18}$$

Then, the baseline flow's velocities ($u_g{}'$ and $u_w{}'$) are set to 10 m/s and 0.45 m/s [106, 107] respectively, together with the baseline fin's height ($h_f{}'$), 5 mm, to calculate the baseline number of hot layer ($N_l{}'$), the baseline length of the water passage ($L_{flow_w}{}'$), and the design width of the water passage (L_{p_w}).

$${A_{free_g}}' = \frac{\dot{m}_g}{\overline{\rho}_g u_g{}' N_{HX}} \tag{3.19}$$

$${A_{free_w}}' = \frac{\dot{m}_w}{\overline{\rho}_w u_w{}' N_{HX}} \tag{3.20}$$

${A_{free_g}}'$ is the baseline free flow area of the air-side, ${A_{free_w}}'$ the baseline free flow area of the water-side, $\overline{\rho}_g$ is the average density of the air, and $\overline{\rho}_w$ is the average density of the water.

$$N_l{}' = \sqrt{\frac{A_{free_g}{}'}{2h_f{}'}} \tag{3.21}$$

$$L_{flow_w}{}' = \frac{A_{free_g}{}'}{N_l{}'\ h_f{}'} \tag{3.22}$$

$$L_{p_w} = \frac{A_{free_w}{}'}{(N_l{}' + 1)\ h_f{}'} \tag{3.23}$$

Once the baseline values are estimated, the boundaries for the optimisation are defined as illustrated in Table 3.3. The boundary values of the height of the fins (h_f), the length of the fins (L_f), and the density of fins (N_f) are based on the recommended values in the literature [88, 108].

TABLE 3.3: Boundaries of the intercooler's and aftercooler's design variables [88, 108].

Variable		Lower limit	Upper limit
N_l	[-]	0.8 $N_l{}'$	1.2 $N_l{}'$
L_{flow_w}	[m]	0.8 $L_{flow_w}{}'$	1.2 $L_{flow_w}{}'$
h_f	[mm]	4	10
L_f	[mm]	3	10
N_{f_w}	[1/m]	100	500
N_{f_g}	[1/m]	100	800

3.8.2 Recuperator

The process for calculating the required number of heat exchangers and estimating boundaries of the N_l and the length of the cold flow passage (L_{flow_c}) for the multi-pass configurations, or the width (L_{Nf}) for counter-current configurations, is equivalent to the process followed in the case of the intercooler/aftercooler. The boundaries for the optimisation of the recuperator are presented in Table 3.4, which are based on the recommendations found in the literature [88, 108].

For the optimisation of the recuperator two configurations are investigated: the single pass counter-current and the multi-pass cross-flow. When the optimiser creates a design vector where the number of passes (N_p) is equal to one, the recuperator is designed as a counter-current heat exchanger and the width is the

TABLE 3.4: Boundaries of the recuperator's design variables [88, 108].

Variable		Lower limit	Upper limit
N_p	[-]	1	3
N_l	[-]	0.8 N_l'	1.2 N_l'
L_{flow_c} or L_{Nf}	[m]	0.8 $L_{flow_c}{}'$	1.2 $L_{flow_c}{}'$
h_f	[mm]	4	10
L_f	[mm]	3	10
N_{f_c}	[1/m]	200	800
N_{f_h}	[1/m]	200	800

design variable. If $N_p \geq 2$, the recuperator is designed as a multi-pass cross counterflow heat exchanger and the length of the cold fluid is the design variable.

3.8.3 Economiser

For the optimisation of the economiser design it is not necessary to perform any pre-calculation. The boundaries of the design variables for the optimisation are presented in Table 3.5, which are based on the recommended values in the literature [109] and preliminary analyses. N_{p_d} represents the number of passes of the dry sector, N_r the number of tube's rows per pass, L_{Nf} the length perpendicular to both flows, d_o the tube's outer diameter, d_e the tube's external diameter (including the fins), N_f the density of fins, and p_r the pitch between the rows of tubes.

TABLE 3.5: Boundaries of the economiser's design variables [109].

Variable		Lower limit	Upper limit
N_{p_d}	[-]	10	50
N_r	[-]	1	5
L_t	[m]	2	5
L_{Nf}	[m]	2	5
d_o	[mm]	10	50
d_e/d_o	[mm]	1.4	2.4
N_f	[-]	200	400
p_r/d_e	[-]	1.2	5.2

3.9 Summary

In this chapter, the schematic layout of the selected reheated humid air turbine is presented, together with the architectures chosen for the design of the heat exchangers, the design methodologies of each component, the cost estimation models, and the optimisation process employed in the design of the heat exchangers. The selected reheated humid air turbine consists of a partially humidified dual-shaft gas turbine with a free power turbine, which includes an intercooler, an aftercooler, a recuperator, an economiser, and the saturator tower. Moreover, the water is considered to be circulating in an open loop.

A structured packed bed tower has been selected for the saturator due to its low pressure losses and its high exchange area. A plate-fin architecture has been chosen for the design of the intercooler and the aftercooler because of its compactness and structural strength. The air-side passages are designed with a serrated fin configuration, whereas the water-side is designed using plain fins to reduce the fouling and passage blockage issues. The recuperator architecture also uses a plate-fin configuration, but with serrated fins on the cold and the hot side. However, the economiser is designed using a tube-fin configuration with smooth tubes at the last passages of the heat exchanger to promote the flow of the condensing moisture over the tube's walls. In addition, the models developed for the design of these components, and the gas turbine and the generator have been presented together with the models employed to estimate the acquisition costs.

This chapter explains the component design models required to achieve the objectives of the research.

Chapter 4

Power plant design

The design of the systems integrating the RHAT is influenced by several aspects, which include: the thermodynamic design variables of the cycle, the materials employed for the design of the components, or the designing ambient conditions. Depending on the final application of the power plant it might be worthy to tune the cycle design parameters to better adapt the plant performance to the required duty. The material selected for the construction of the components influences on the deterioration they suffer, especially in the case of the air-water heat exchangers. For some scenarios, it might be more economical to select a more expensive material with a better resistance to corrosion, and vice versa. Moreover, the ambient conditions that the plant will normally face also have a considerable impact on the performance, as well as on the design of the components.

This chapter presents the influence of the design variables on the performance and the design of the power plant at a component level, focusing on the total weight, volume, and cost. A baseline design of the power plant is introduced to prove the feasibility of the components, especially the heat exchangers, and to provide reference values of the total weight, size, and cost. In addition, a design space exploration is conducted to evaluate the exchange rates between the cycle design variables, the design of the components, and the performance of the cycle. The influence of using different materials for the design of the air-water heat exchangers is tested to determine the correlations between the heat exchanger's material choice, and their design and costs. Moreover, the impact of the ambient temperatures on the design point efficiency of the power plant and the design of the components is analysed by means of a parametric analysis. Last, the reheated

humid air turbine power plant is also compared to a reference marine diesel engine and a reference marine gas turbine to contrast the benefits that the studied cycle may offer.

4.1 Thermodynamic simulations

The thermodynamic simulations of the power plant have been performed by Brighenti based on the work presented by Brighenti et al. [110]. The simulation tool is composed of a system of sub-modules integrated into a single platform to interact among themselves. In addition, the platform is integrated into an optimiser in order to obtain the configurations with the highest thermal efficiency

4.1.1 Gas turbine

The performance of the gas turbine and the recuperator is estimated by Turbomatch© [111], a zero-dimensional modular component-based simulation framework where the behaviour of each component is calculated separately using the polytropic process equations and the energy balance equations, together with the defined efficiencies. The software has been validated against experimental and simulated data [112–115]. The blade cooling flows, extracted at the outlet of the high pressure compressor, are calculated using the model proposed by Young and Wilcock [116].

With the objective of simplifying the design point simulation model, the performance modelling assumptions presented in Table 4.1 are considered for all the simulations conducted.

4.1.2 Saturator tower

The performance of the saturator tower is calculated in an independent module, according to the methodology developed by Brighenti et al. [110], which is based on the work presented by Aramayo-Prudencio and Young [68], and Sanchez [10]. The main advantage of the model for design performance simulations is the low number of required design variables. It only requires the thermodynamic conditions of the

TABLE 4.1: Cycle performance modelling assumptions.

Power output	40 MW
Combustor and reheater turbine inlet temperature	1600 K
Compressor polytropic efficiency	0.9
Core turbine polytropic efficiency	0.9
Power turbine polytropic efficiency	0.92
Combustion chamber efficiency	0.999
Combustion chamber pressure loss	5%
Saturator pressure loss	5%
Air-water heat exchangers air-side pressure loss	7.50%
Cold-side recuperator pressure loss	7.50%
Hot-side recuperator pressure loss	5%
Maximum allowed blade metal temperature	1300 K
Film cooling effectiveness	0.4
Internal flow cooling efficiency	0.7

incoming flows and the saturator pinch point temperature difference. Since the model is only based upon first thermodynamic principles, it results to be extremely useful to quickly evaluate a large number of different configurations at design point. The model has been validated against experimental data [66], as proved in the work presented by Brighenti et al. [110].

4.1.3 Heat exchangers

The outlet conditions from the air-water heat exchangers are calculated using the defined effectiveness (ε) of the devices and the energy balance equations. The gas mass flows are imposed by Turbomatch©, whereas the water mass flows are calculated using the designated heat exchanger heat capacity ratio of the dry section ($C^* = C_{\min}/C_{\max}$). It is assumed that $C_w = C_{\max}$ and $C_g = C_{\min}$, where $C = \dot{m}\ c_p$ is defined as the heat capacity of the flow. $\dot{m}$ represents the mass flow, c_p the specific heat capacity, and the subscripts g and w stand for the gas and water respectively.

The models of the heat exchangers must warranty that the water enters the saturator in a liquid face in order to maximise the effectiveness of the mass transfer process. This makes possible to reduce the temperature difference between the water and the air during the mass and heat transfer process, minimising the entropy

generated. Thus, to avoid steaming inside the tower, the following restriction is imposed.

$$T_{w,out} \leq T_{w,sat}@(0.9P_{SAT}) \tag{4.1}$$

$T_{w,out}$ is the water temperature at the outlet of the air-water heat exchangers and $T_{w,sat}@(0.9P_{SAT})$ is the saturation temperature of the water at 0.9 the pressure inside the saturator tower. In case that $T_{w,out}$ exceeds $T_{w,sat}@(0.9P_{SAT})$, the water mass flow is recalculated to satisfy Eq. 4.1 and the value of the heat exchanger heat capacity ratio is overwritten.

4.1.4 Optimiser

To further reduce the number of inputs required by the platform, the performance simulation tool is coupled with a genetic optimisation routine, as shown in the flowchart presented in Figure 4.1, according to Sanchez [10] and Brighenti et al. [110]. The optimiser iterates with C^* of the air-water heat exchangers, the bypass ratio (β), and the relative pressure ratio ($Rel.PR$) with the objective of maximising the thermal efficiency of the plant. Including the optimisation in the design routine permits to reduce the required inputs to the ambient conditions, the OPR, ε of the heat exchangers, and ΔT_{sp}. Once the simulation is finished, the routine provides the optimum value of the thermodynamic variables and the performance parameters of the cycle.

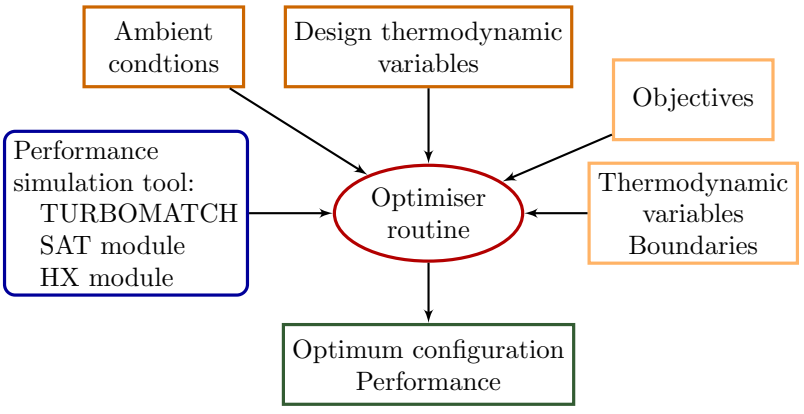

FIGURE 4.1: Flowchart of the cycle's thermodynamic optimisation.

The limits of the optimised variables are presented in Table 4.2, together with their definitions.

TABLE 4.2: Boundaries of the optimised thermodynamic variables

Variable	Definition	Lower limit	Upper limit
β	$\frac{\dot{m}_{g,SAT,in}}{\dot{m}_{g,HPC,out}}$	0	1
$C^*_{IC}, C^*_{AC}, C^*_{EC}$	$\frac{\dot{m}_{g,in}\ c_{p_g}}{\dot{m}_{w,in}\ c_{p_w}}$	0.3	0.95
$Rel.PR$	$\frac{\log\ PR_{LPC}}{\log\ OPR}$	0.25	0.75

4.2 Baseline design

A baseline case is provided to illustrate the detailed layout of the power plant and its main metrics, which include the dimensions, weight, and cost. The reference design ambient conditions are presented in Table 4.3. The cycle design parameters are shown in Table 4.4, where η_{th} represents the thermal efficiency of the cycle, and ω_{CC} the water to air ratio at the combustion chamber (selected as the representative value to indicate the humidity of the gas at the hot section). The water to air ratio is defined as the ratio of mass flow of water vapour to mass flow of dry air ($\omega = \dot{m}_v/\dot{m}_a$).

TABLE 4.3: Baseline ambient conditions.

Pressure	1 atm
$\boldsymbol{T_{air}}$	15°C
$\boldsymbol{T_{water}}$	15°C
Rel. humidity	80%

The results of the thermodynamic optimisation, presented in Table 4.4, show that the C^*_{IC} and C^*_{AC} have an optimum value of 0.95. This permits to maximise the water temperature at the outlet of the heat exchangers in exchange of reducing the water mass flow, which agrees with the work presented by Chiesa et al. [44] and Nyberg and Thern [47]. Nevertheless, a high C^* increases the complexity of the heat exchanger designs, as explained in Chapter 3. Moreover, it enlarges the

TABLE 4.4: Baseline cycle design parameters.

Cycle design variables			**Optimised design variables**		
OPR	[-]	40	C^*_{IC}	[-]	0.95
ΔT_{ps}	[K]	10	C^*_{AC}	[-]	0.95
ε_{IC}	[-]	0.85	C^*_{EC}	[-]	0.73
ε_{AC}	[-]	0.85	β	[-]	0.49
ε_{RC}	[-]	0.85	$Rel.\ PR$	[-]	0.56
ε_{EC}	[-]	0.85			
	$\boldsymbol{\eta_{th}}$			58.31%	
	ω_{CC}			0.18	

required heat transfer area for the same design effectiveness compared to design a lower C^* value [117], as shown in Figure A.8.

The economiser shows a lower C^*, 0.73, than the aftercooler and the intercooler. This is caused by the appearance of a pinch point in the economiser, consequence of the moisture condensation process. Due to the pinch point it is necessary to increase the water mass flow to achieve the imposed effectiveness. Therefore, C^* becomes lower in comparison with the intercooler and the aftercooler. The humidity in the hot section, ω_{CC}=0.18, is similar to the values presented in the experimental test previously conducted [41, 59], which warranties the stable operation of the combustion chambers. In addition, the optimum $Rel.\ PR$, 0.56, is close to the value minimising the compression work, 0.5, in accordance with the literature [44, 47].

The layout of the power plant is shown in Figure 4.2, whereas the detailed design of each component is presented in Appendix B. Table 4.5 presents the main dimensions of the power plant, the total cost, and the total weight, together with their respective breakdowns. The headers of the components and the connection tubes have not been designed in detail, they are just graphical representations to permit the proper illustration of the power plant sketch. Thus, neither the weight nor the cost of these parts is included in the total balance.

The suggested layout permits to obtain a compact configuration, where all the heat exchangers are placed above the gas turbine and the saturator tower is installed next to it. This configuration would allow the construction of a double deck structure, with the gas turbine on the first level and the heat exchangers on the

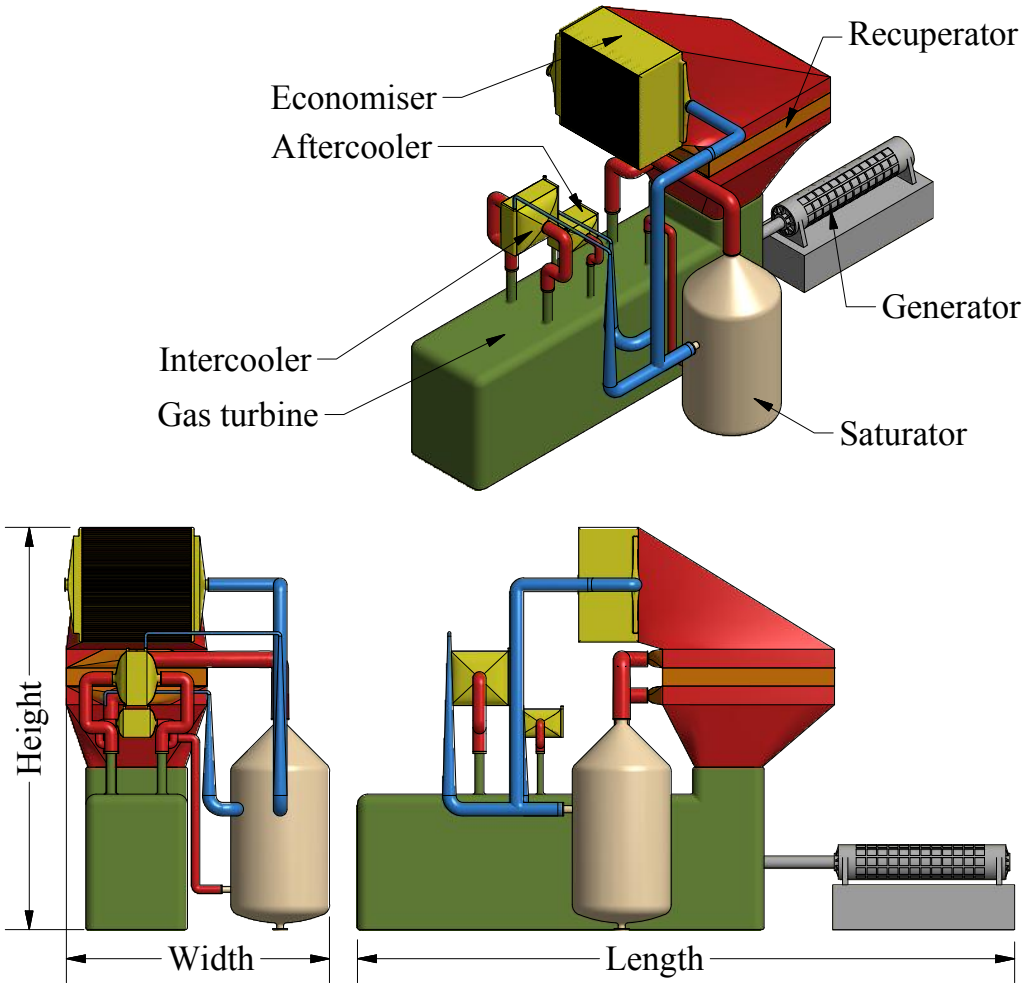

FIGURE 4.2: Representation of the baseline configuration of the reheated humid air turbine.

second. This layout would facilitate the access of the crew to the heat exchange system for maintenance procedures.

TABLE 4.5: Size, weight, and cost of the baseline power plant.

	Length [m]	**Width** [m]	**Height** [m]	**Weight** [t]	**Cost** [k$]
	12.16	4.87	7.45	43.86	13,401
Intercooler				2.7%	2.97%
Aftercooler				1.3%	1.83%
Economiser				7.9%	0.28%
Recuperator				26.4%	11.82%
Saturator				11.4%	0.45%
Gas turbine				20.6%	62.31%
Generator				29.7%	20.34%

The total baseline weight of the components is 43,863 kg, where the heat and mass exchange system represents 49.7% of the total weight. The generator is the heaviest component (29.7% of the total weight), followed by the recuperator, the gas turbine, the saturator, the economiser, the intercooler, and the aftercooler (whose relative contributions to the total weight are 26.4%, 20.6%, 11.4% 7.9%, 2.7%, and 1.3% respectively). The recuperator is the heaviest of all the heat and mass transfer components as it is the device that transfers the largest amount of heat, 27 MW (9.8 MW intercooler, 4.3 MW aftercooler, 18 MW economiser, 19 MW saturator), and presents the lowest U, 125.5 W/K m^2. Therefore, the heat transfer area required is one order of magnitude larger in comparison to the other heat exchangers, which directly affects the weight. Despite the low volume required by the saturator packing for the mass and heat transfer process (50% of the volume required by the recuperator), it is the third heaviest component. The requirement of a thick shell to stand the internal pressure and the space required for the allocation of the inlet and outlet plenum penalises significantly the weight and volume of the component.

The total purchase equipment cost of the baseline configuration is \$13,401,000, which divided by the power output leads to a $SPEC$ of 335.09 \$/kW. These estimates are broadly in accordance with the cost previously calculated presented by Kavanagh and Parks [30] for a humid air turbine of 60 MW, 328 \$/kW. The largest part of the cost is represented by the gas turbine (62.31%) and the generator (20.34%), whereas the whole heat and mass transfer system represent a 17.35% of the total cost. In addition, more than half of the price of the heat exchange and mass transfer system is just represented by recuperator (11.82% of the total cost). The total contribution of the humidification system (intercooler, aftercooler, economiser, and saturator) only constitutes a 5.53% to the total cost of the plant.

According to the optimisation design process explained in Section 3.8, the optimum number of heat exchangers of a certain component can be larger than one. In the case of the intercooler and the aftercooler, the reconfiguration could be easily done by placing both devices one next to other, or one above the other. Nevertheless, in the case of the recuperator, the reconfiguration is more complex since placing one above the other is impossible as they have to work in parallel, and placing one next to the other would increases considerably the required floor area. A solution that permits to solve the issue is to place both recuperator in an inverted V configuration, as depicted in Figure 4.3b. Adopting this configuration, the total

volume occupied by the component does not increase significantly compared to a single heat exchanger configuration, as observed in Figure 4.3.

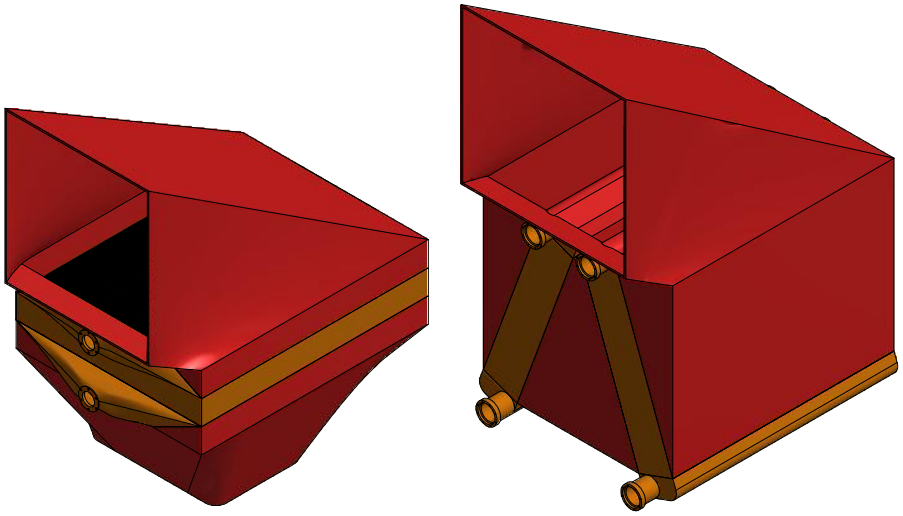

(a) Single recuperator configuration (b) Dual recuperator configuration

FIGURE 4.3: Recuperator's connectors layout.

4.3 Influence of cycle design variables

The correlation between the cycle design parameters, the performance, and the design of the power plant at a component level is assessed via a parametric study. The cycle design parameters include the design effectiveness of the heat exchangers, the overall pressure ratio, and the pinch point temperature difference of the saturator. The baseline cycle configuration (Table 4.4 and Appendix B) is selected as reference to compare the changes produced.

4.3.1 Heat exchangers effectiveness

The value of the heat exchanger's effectiveness is varied from 0.75 to 0.95, as presented in Table 4.6, while keeping constant the OPR and ΔT_{sp}. Table 4.6 also shows the impact on the optimum relative pressure ratio, the bypass ratio, the inlet mass flow, and the humidity of the gas at the combustion chamber.

The effect on the design of the components is shown in Table 4.7, which illustrates the variations of the volume, weight, and cost. The generator is not included

TABLE 4.6: Effect of varying the design effectiveness of the heat exchangers on the cycle's optimised variables. Reference values in Table 4.4. OPR=40 and ΔT_{sp}=10 K.

	Cycle design parameters							
	ε_{IC}		ε_{AC}		ε_{EC}		ε_{RC}	
	0.75	0.95	0.75	0.95	0.75	0.95	0.80	0.90
Δ**Rel. PR**	0.05	-0.03	0.00	0.01	0.00	0.00	0.00	0.01
$\Delta\beta$	0.00	-0.05	-0.10	0.04	-0.18	0.03	0.01	-0.11
$\Delta\dot{m}_{g,in}$	1.0%	-0.1%	1.8%	-1.4%	3.3%	-2.5%	-1.8%	2.2%
$\Delta\omega_{CC}$	0.01	-0.01	-0.01	0.01	-0.02	0.02	0.01	-0.01

because its design only depends on the power, which is kept constant. Only the changes in the design variables that produce a variation larger than a 5% in any of the component's metrics are presented. Although none of the effectiveness variations triggers a change in the gas turbine metrics larger than a 5%, it is interesting to still plot the changes since it is the bulkiest and most expensive component. Therefore, a variation in the design of the gas turbine has a considerably larger repercussion on the final cost and volume of the power plant than any of the rest of the components. A chromatic scale representing the magnitude of the changes is added to enhance the visibility of the correlations between the designs of the components and the effectiveness of the heat exchangers.

Looking at the effect of varying the design effectiveness of the heat exchanger in their own designs, it is observed that the reduction of the effectiveness from 0.85 to 0.75 of any heat exchanger leads to a more compact, lighter, and less expensive design. The economiser is the heat exchanger that undergoes the largest transformation (its cost is reduced a 36.1%, the weight a 52.7%, and the volume a 63.4%), followed by the aftercooler (its cost is reduced a 22.8%, the weight a 53.4%, and the volume a 48.2%), the intercooler (its cost is reduced a 35.7%, the weight a 5.6%, and the volume a 21.8%), and finally the recuperator (its cost is reduced a 20.3%, the weight a 24.9%, and the volume a 14.8%). The decay in the heat transferred, consequence of the drop in the effectiveness, drives the reduction of the heat exchanger's size.

On the other hand, rising the design effectiveness of any heat exchanger produces a bulkier, heavier, and more expensive design. When the design effectiveness is increased from 0.85 to 0.95 the intercooler is the heat exchanger that suffers the largest variations (with a rise in cost of a 257.7%, in weight of a 258.7%, and in

TABLE 4.7: Effect of varying the design effectiveness of the heat exchangers on the design of the components.
OPR=40 and ΔT_{sp}=10 K.

	Cycle design parameters							
	ε_{IC}		ε_{AC}		ε_{EC}		ε_{RC}	
	0.75	0.95	0.75	0.95	0.75	0.95	0.80	0.90
				Intercooler				
Vol.	-21.8%	281.2%			5.1%	-3.2%		
Weight	-5.6%	285.7%			5.1%	-3.2%		
Cost	-35.7%	257.7%			3.1%	-0.9%		
				Aftercooler				
Vol.	-12.8%	-6.3%	-48.2%	143.1%	-10.1%	3.6%	-0.3%	-2.9%
Weight	-8.6%	0.6%	-53.4%	135.2%	3.4%	16.2%	3.0%	6.8%
Cost	-10.3%	-8.8%	-22.8%	95.2%	-14.2%	3.5%	-2.0%	-7.2%
				Economiser				
Vol.					-63.4%	92.7%	-19.2%	-10.4%
Weight					-52.7%	77.0%	-9.0%	24.1%
Cost					-36.1%	58.2%	-1.3%	14.4%
				Recuperator				
Vol.							-14.8%	36.9%
Weight							-24.9%	35.5%
Cost							-20.3%	31.3%
				Saturator				
Vol.			-6.6%	2.6%	-14.2%	4.0%	2.1%	-9.0%
Weight			-6.1%	2.4%	-13.7%	4.2%	2.2%	-8.8%
Cost			-5.2%	2.0%	-11.9%	3.7%	2.0%	-7.7%
				Gas turbine				
Vol.	1.4%	-0.2%	2.7%	-2.2%	5.0%	-3.8%	-2.8%	3.3%
Weight	1.3%	-0.1%	2.4%	-2.0%	4.5%	-3.4%	-2.5%	2.9%
Cost	3.4%	-1.9%	0.4%	-0.1%	0.8%	-0.9%	-0.5%	0.9%

volume of a 281.2%), the aftercooler comes in second places (its cost rises a 95.2%, the weight a 135.2%, and the volume a 143.1%), followed by the economiser (with an increment in cost, weight, and weight of 58.2%, 77% and 92.7% respectively). Last, the recuperator experiences the smallest variation (the cost increases a 31.3%, the weight a 35.5%, and the volume a 36.9%). The substantial change in the intercooler metrics is caused by the necessity of raising the number of the heat exchangers from one to two.

In addition, the alteration of the effectiveness of a heat exchanger has also a knock-on effect on the remaining components of the system (Table 4.7). When ε_{IC} is reduced to 0.75, the aftercooler size, weight, and cost drop a 12.8%, 8.6%,

and 10.3% respectively. The increment in the relative pressure ratio (Table 4.6), derived from the reduction of ε_{IC}, produces a lower gas temperature at the inlet of the aftercooler. Therefore, the heat transferred inside this heat exchanger is reduced. On the other hand, the increment in ε_{IC} also lowers the gas temperature at the inlet of the aftercooler in addition to reducing the optimum bypass ratio (Table 4.6). Thus, the total heat transferred in the aftercooler is lowered, which contributes to an 8.8% reduction in the cost of the aftercooler.

Decreasing the effectiveness of the aftercooler causes a drop in the optimum bypass ratio (Table 4.6). This leads to a 9% reduction of the absolute mass flow passing through the saturator. The lower mass flow yields to a 6.6% reduction in the volume of the saturator, a 6.1% in its weight, and a 5.2% in its cost (Table 4.7). When ε_{AC} rises, the opposite happens.

The variation of the effectiveness of the economiser affects the design of the intercooler, the aftercooler, and the saturator (Table 4.7). When ε_{EC} becomes 0.75 from 0.85, the inlet mass flow rises a 3.3% due to the reduction in the specific power, derived form a 0.02 drop in ω_{CC} (Table 4.6). As consequence of the larger inlet mass flow the intercooler becomes a 5.1% bulkier, 5.1% heavier, and 3.1% more expensive.

The reduction of ε_{EC} also triggers a drop of 0.18 points in the bypass ratio (Table 4.6). The drop of β implies a 14% decrease of the total mass flow passing through the aftercooler and the saturator. Thus, these devices become less voluminous (10.1% the aftercooler and 14% the saturator) and less expensive (14.2% the aftercooler and 11.9% the saturator). Nevertheless, it is observed that the aftercooler presents a 3.4% heavier design. Since the weight is not one of the optimise parameters during the design process, configurations where the weight does not follow the same trend as the volume and the cost may appear.

On the hand, when ε_{EC} increases, the mass flow drops a 2.5% (Table 4.6). Thus, the intercooler becomes smaller and less expensive. Nevertheless, the change in ε_{EC} makes the optimum β to rise 0.03 points (Table 4.6). Therefore, the total mass flow circulating through the aftercooler and saturator grows a 2%, making the aftercooler a 3.5% more expensive. In addition, the increment of ε_{EC} permits to warm a larger amount of water that is then injected in the saturator, which boosts the performance of the device [67]. To achieve this boost in performance,

it is necessary to increase its volume a 4%. This, consequently, produces a rise in the weight, 4.2%, and cost, 3.7%, of the saturator.

Raising the recuperator effectiveness from 0.85 to 0.90 penalises the performance of the humidification system, as it leaves a relatively lower amount of heat available to be recovered in the economiser. Consequently, less water can be warmed, reducing the performance of the saturator [67]. Ultimately, the poorer performance of the saturator leads to a reduction of the optimum bypass ratio of 0.11 points (Table 4.6). Therefore, the mass flow through the aftercooler and saturator drops an 8%. This explains the 7.2% reduction of the cost of the aftercooler and the 7.7% drop of the saturator's cost. However, the price of the economiser rises a 14.4%, result of the larger inlet mass flow (Table 4.6).

On the other hand, when ε_{RC} drops from 0.85 to 0.80, the available heat at the outlet of the recuperator increases, improving the humidification performance (since more water can be heated in the economiser). Therefore, as a consequence of the larger amount of water injected into the saturator, this device becomes 2.1% more voluminous, 2.2% heavier, and 2% more expensive. Nevertheless, the 2% lower inlet mass flow permits to diminish the acquisition cost of the aftercooler by 2% and the economiser by 1.3%.

The size and weight of the gas turbine are directly correlated with the variation of the inlet mass flow due to the nature of its sizing procedure. Thus, the largest variation of the gas turbine weight and volume is produced by the increment of the economiser effectiveness (since it yields to largest variations of the inlet mass flow), which triggers a reduction in the volume of a 3.8% and in the weight of a 3.4%. However, the largest change in its acquisition cost is caused by the variation of ε_{IC}, as it also alters the pressure ratio distribution of the compressors and turbines, increasing their specific cost.

In order to show the cumulative effect of varying the design effectiveness of the heat exchangers, Figure 4.4, Figure 4.5, and Figure 4.6 present the effects of changing all the design effectiveness simultaneously on the thermal efficiency, weight, and cost of the power plant respectively. The x-axis and y-axis of the contour plots represent the aftercooler's and economiser's effectiveness respectively. The contour lines show the estimated cycle thermal efficiency in Figure 4.4. In Figure 4.5 and Figure 4.6 the contours show the percentage variations, compared to the baseline cycle, of the weight and cost respectively. The major x-axis illustrates the variation

of the effectiveness of the intercooler, whereas the major y-axis shows the variation of the effectiveness of the recuperator. Therefore, the baseline cycle is placed in the centre of the central contour plot.

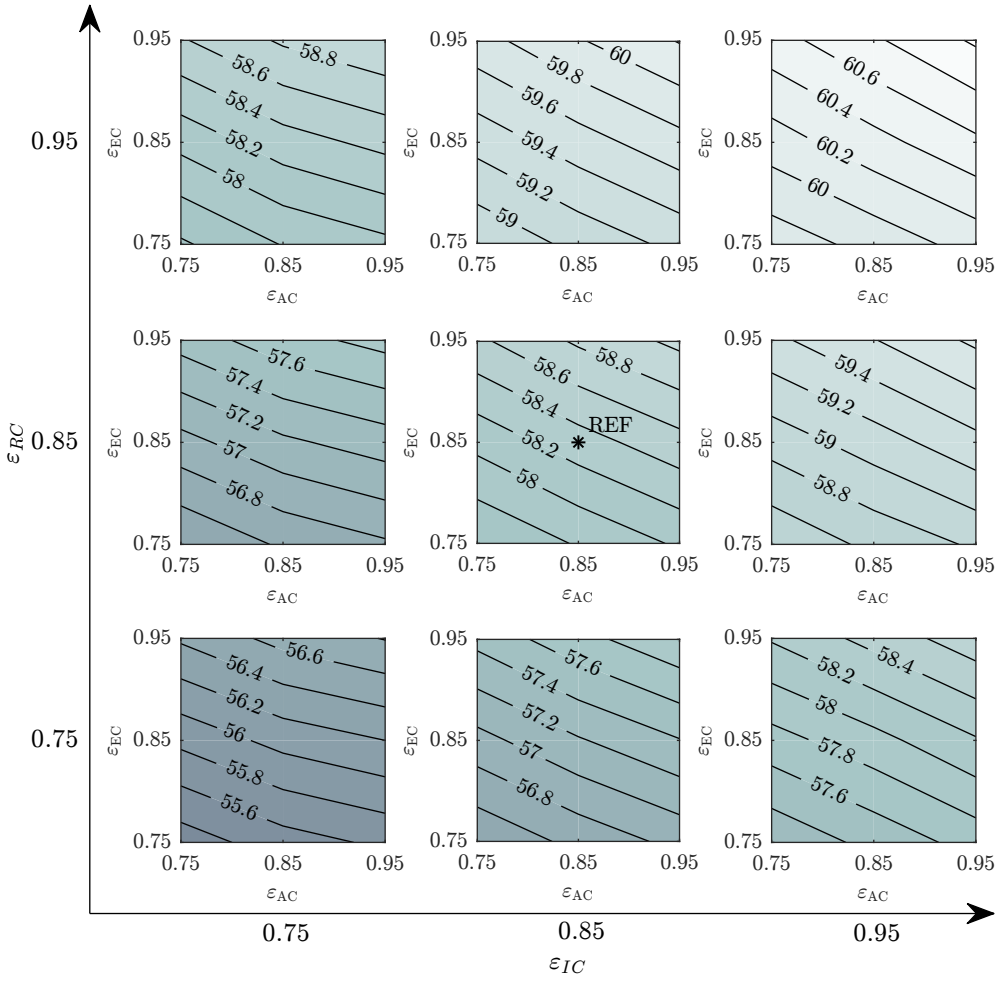

FIGURE 4.4: Thermal efficiency across the design space as a function of the heat exchanger's effectiveness.
OPR=40 and ΔT_{sp}=10 K.

The recuperator's effectiveness drives the largest changes in the thermal efficiency, as shown in Figure 4.4. When the ε_{RC} changes from 0.80 to 0.90, keeping the rest of the effectiveness at their baseline value, the thermal efficiency rises 2.33 pp. Raising the intercooler's effectiveness from 0.75 to 0.95 produces a benefit in the thermal efficiency of 1.94 pp. Whereas the economiser and the aftercooler causes an improvement of 1.1 pp and 0.47 pp, respectively.

When the effectiveness of all heat exchangers is increased simultaneously (top-right point in the tile-plot) the thermal efficiency grows 2.7 pp compared with the reference value. Whereas reducing the design effectiveness of these devices

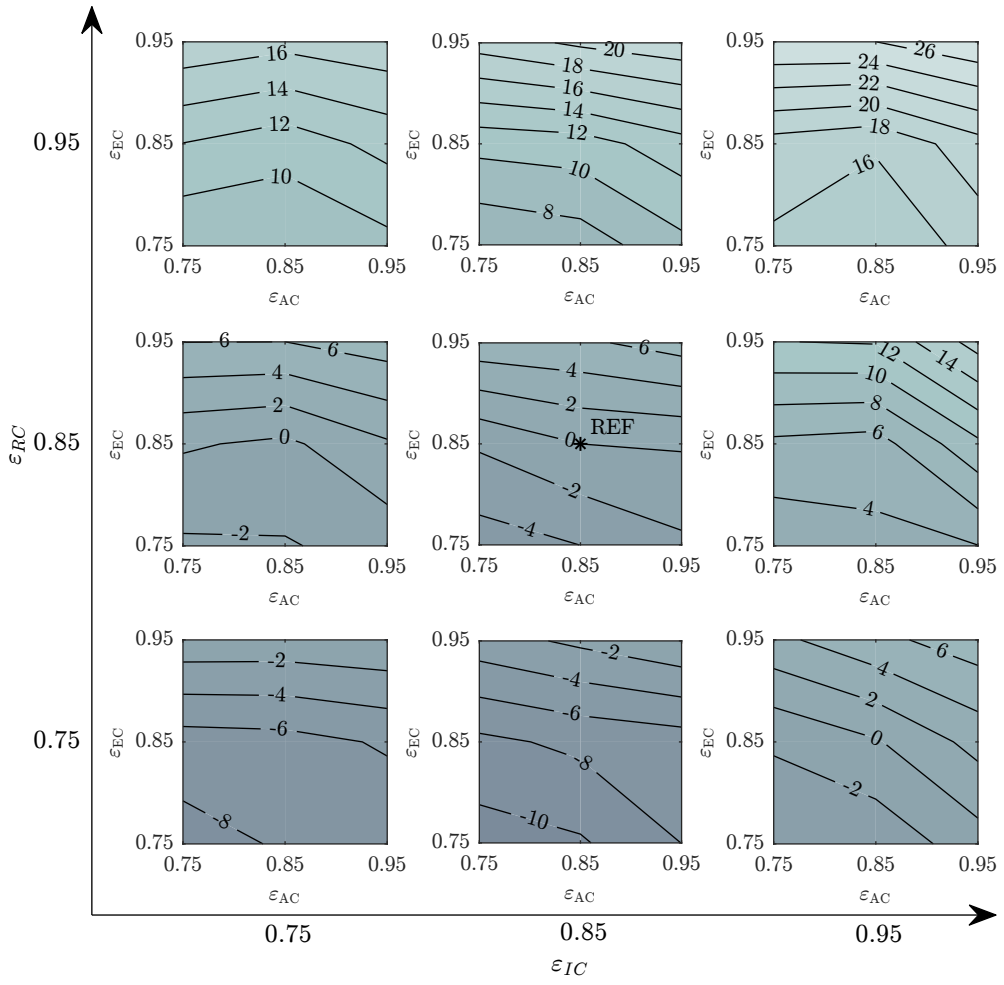

FIGURE 4.5: Percentage variation of the weight of the power plant produced by changing the design effectiveness of the heat exchangers. OPR=40 and ΔT_{sp}=10 K.

simultaneously (bottom-left point in the tile-plot) leads to a reduction of 3 pp in the thermal efficiency. This shows that as the effectiveness of the heat exchanger rises, the benefits obtained by improving their design become lower.

The variation of the recuperator's effectiveness also produces the largest changes on the total weight of the power plant, as illustrated in Figure 4.5. When ε_{RC} drops from 0.85 to 0.80, the total weight diminishes a 7.5%, and when it increases from 0.85 to 0.90, the total weight rises an 11%. The economiser effectiveness produces the second largest impact on the weight. When ε_{EC} falls from 0.85 to 0.75, the total weight is reduced a 4%, and when it increases from 0.85 to 0.95, the total weight rises a 5.6%.

Changing either ε_{IC} or ε_{AC} from 0.85 to 0.75 does not produce any remarkable impact on the total weight of the power plant, as the reduction experienced by

the weight of the heat exchanger is compensated by the increment in the weight of the gas turbine (Table 4.7). However, when ε_{IC} rises from 0.85 to 0.95, the total weight increases a 6%. This change is mainly driven mainly by the increment in the weight of the intercooler. On the other hand, increasing ε_{AC} from 0.85 to 0.95 reduces the total weight of the plant a 0.25% due to the reduction of the weight of the gas turbine (Table 4.7).

The above-mentioned changes are magnified as the design effectiveness of the heat exchangers is increased (Figure 4.5) due to the exponential relationship between the effectiveness and the required heat transfer area, as shown in Figure A.8. The larger the effectiveness, the larger the required increment in the area to keep rising it. Therefore, the collateral changes produced by the alteration of any other design parameters will produce larger changes in the overall metrics.

When the effectiveness of all heat exchangers is increased simultaneously (top-right point in the tile-plot) the total weight of the power plant increases up to a 27.2%. Whereas reducing the design effectiveness of these devices simultaneously (bottom-left point in the tile-plot) leads to a reduction of an 8.3% in the total weight. This proves the mentioned in the above paragraph. Nevertheless, the configuration with the lowest design effectiveness is not the lightest. To obtain the lightest configuration the design effectiveness must be: ε_{IC}=0.85, ε_{AC}=0.75, ε_{EC}=0.75, ε_{RC}=0.80. Further reduction of the intercooler effectiveness leads to a significant increment in the weight of the gas turbine, which outbalances the drop in the weight of the intercooler.

The largest changes in the total acquisition cost of the plant are also produced by the alteration of the effectiveness of the recuperator, as shown in Figure 4.6. Reducing ε_{RC} from 0.85 to 0.80 drops the total price a 2.79%, whereas increasing it from 0.85 to 0.90 rises the cost a 4.18%. When the effectiveness of the intercooler is raised from 0.85 to 0.95, the acquisition cost grows a 3.66%, and a 1.59% in the case of raising the effectiveness of the aftercooler. However, dropping the effectiveness of the intercooler also rises the acquisition price a 0.91%, whereas reducing the aftercooler effectiveness does not have any significant effect. When the effectiveness of this two heat exchangers drops, the increment produced in the cost of the gas turbine overcompensates the reduction in the cost of the heat exchanger.

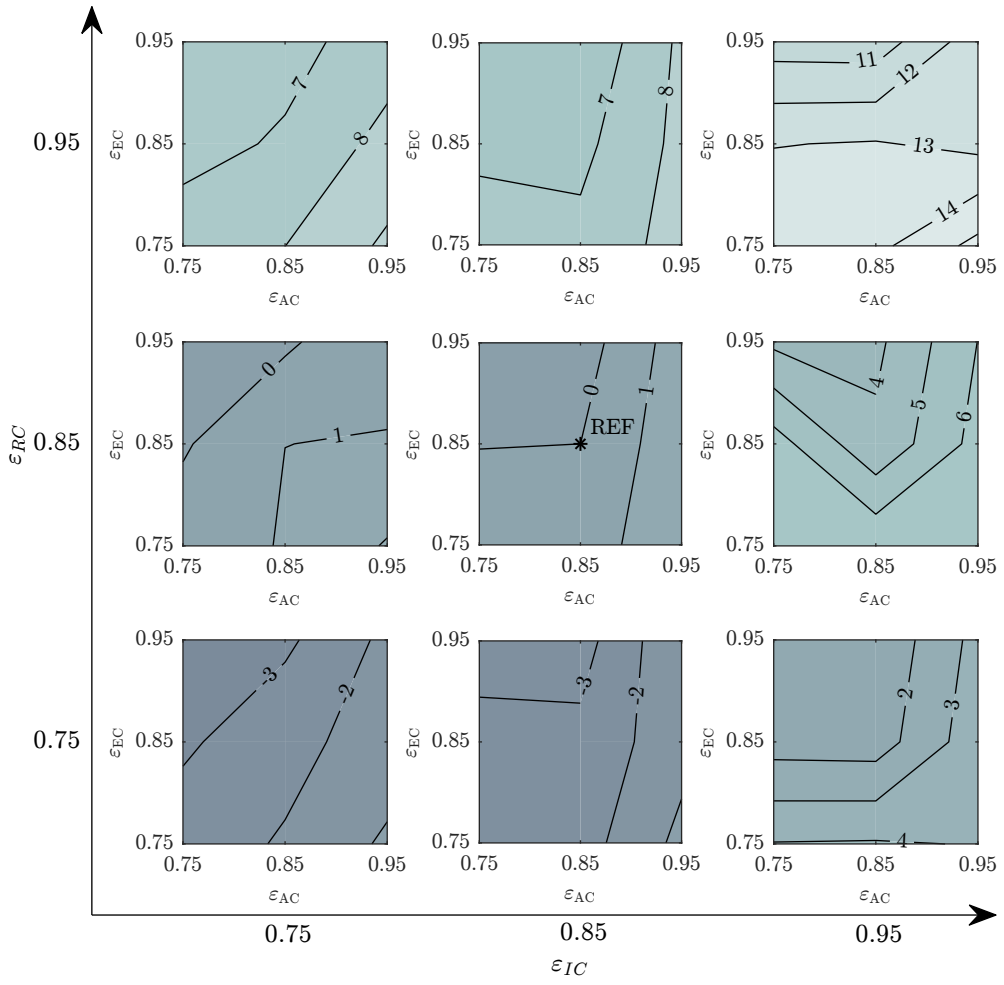

FIGURE 4.6: Percentage variation of the cost of the power plant produced by changing the design effectiveness of the heat exchangers. OPR=40 and ΔT_{sp}=10 K.

Moreover, raising the effectiveness of the economiser from 0.75 to 0.85 produces a 0.43% reduction in the total cost. Further increasing ε_{EC}, from 0.85 to 0.95, reduces the total cost another 0.59%. The drop in the cost of the gas turbine, the intercooler, and the aftercooler overcompensates the increment in the cost of the economiser.

Equivalently to the changes in the weight, the changes in the price are magnified as the design effectiveness of any of the components becomes higher. When the effectiveness of all heat exchangers is increased simultaneously (top-right point in the tile-plot) the total cost of the power plant increases up to a 12.3%. Whereas reducing the design effectiveness of these devices simultaneously (bottom-left point in the tile-plot) leads to a reduction of an 2.67%. In addition, it is worth high-

lighting that the most efficient configuration does not result in the most expensive one, as well as the least efficient configuration is not the cheapest either.

Despite the large changes suffered by the components when varying the effectiveness of the heat exchanger, which grow up to a 258% in the case of the intercooler, the largest variation of the total cost is only a 16.1%. This discrepancy in the other of magnitude of the variations is produced by the large contribution of the gas turbine and the generator to the total cost, around 50%, which barely change their cost when altering the effectiveness of the heat exchangers. Thus, the most efficient configuration is only a 12.3% more expensive than the reference one, but 1.7 pp more efficient. Whereas reducing the effectiveness of the heat exchanger to obtain the cheapest configuration only reduces the price a 3.4% for a 1.9 pp reduction in the thermal efficiency.

Overall, it has been proven that the recuperator is the component whose design effectiveness has the largest impact on the power plant design metrics. It produces the largest changes in the thermal efficiency, the total weight, and the cost. In addition, from an economic point of view, it would be beneficial to have the maximum economiser effectiveness, although it can mean a 9% penalisation in the total weight compared with the baseline case.

4.3.2 Overall pressure ratio

Table 4.8 shows the effect of reducing the overall pressure ratio on the optimised thermodynamic design variables, together with the variation in the inlet mass flow, humidity in the combustion chamber, and thermal efficiency. For this analysis, the effectiveness of the heat exchangers and the saturator pinch point temperature difference are kept constant at their reference values.

When the overall pressure ratio is reduced from 40 to 30, the thermal efficiency drops 0.77 pp and the inlet mass flow rises a 10%. The reductions in the specific work and in the thermal efficiency are enhanced by the poorer air humidification, ω_{CC} drops 0.02 points. The lower temperature of the gas at the inlet of the heat exchangers (the inlet intercooler temperature is reduced by 34 K, the aftercooler by 22 K, and the economiser by 5 K) penalises the amount of warm-water generated and, hence, the humidification level achieved in the saturator [67]. Therefore, the optimum bypass ratio is cut by 0.04 points.

TABLE 4.8: Effect of reducing the overall pressure ratio on the cycle's optimised variables. Reference values in Table 4.4.
ΔT_{sp}=10 K, $\varepsilon_{IC}, \varepsilon_{AC}, \varepsilon_{EC}, \varepsilon_{RC}$=0.85.

$\boldsymbol{OPR}$	30
$\boldsymbol{\Delta Rel.\ PR}$	-0.01
$\boldsymbol{\Delta\beta}$	-0.04
$\boldsymbol{\Delta\dot{m}_{g,in}}$	10%
$\boldsymbol{\Delta\omega_{CC}}$	-0.02
$\boldsymbol{\Delta\eta_{th}}$	-0.77 pp

Figure 4.7 shows the effect of the overall pressure ratio reduction on the design metrics of the power plant and its components. Despite the drop in the specific heat transferred in the intercooler (consequence of the lower inlet temperature), the increment in the mass flow yields to a design 21% bulkier, 13.5% heavier, and 12.7% more expensive, making it the component most sensitive to the change in OPR. The recuperator volume, weight, and cost also increase (20.1%, 18.1%, and 10.5% respectively) consequence of the larger inlet mass flow and the larger residual heat available at the outlet of the turbines. It is crucial to highlight that the reduction in OPR only raises the inlet hot temperature from 770 °C to 807 °C, thus the nickel-based still resists from a temperature point of view. Although the heat transfer area and, therefore, the cost of the economiser increase by an 11.4%, the optimiser is able to find a configuration that reduces the volume and the weight a 13.6% and a 9% respectively.

The total mass flow passing through the aftercooler and the saturator remains unchanged since the increased inlet mass flows is compensated by the reduction in the bypass ratio (Table 4.8). Thus, the heat transferred in the aftercooler is reduced a 2.3%, consequence of the lower inlet temperature. This makes possible to reduce the acquisition cost a 6%. However, in this occasion, the optimiser trades the volume of the device, which increases a 2%, together with the weight, which increases a 7.3%. On the other hand, the volume of the saturator rises a 17.5% due to the lower density of the gas. Nonetheless, the lower pressure permits to reduce the thickness of the vessel walls, which yields to a 10.3% reduction in the weight and 5.2% drop in the cost.

In the case of the gas turbine, the reduction in the pressure ratio leads to a reduction in the specific cost of the components. Nonetheless, the rise in the cost derived from of the higher inlet mass flow overcompensates that fact. Therefore,

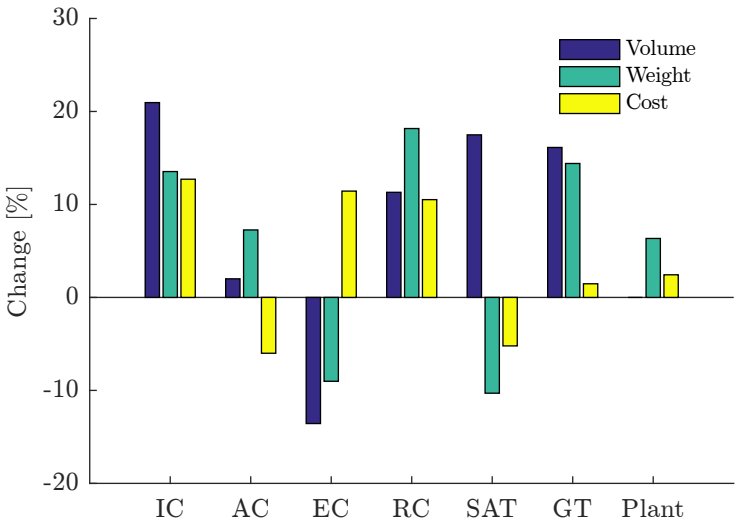

FIGURE 4.7: Effect of reducing the overall pressure ratio, 40→30, on the design of the power plant and its components.
ΔT_{sp}=10 K, $\varepsilon_{IC}, \varepsilon_{AC}, \varepsilon_{EC}, \varepsilon_{RC}$=0.85.

the gas turbine becomes 1.5% more expensive. In addition, the volume and the weight also rise a 16.1% and a 14.4% respectively due to the larger inlet mass flow. It has to be highlighted that the variation of the weight and volume might no be very accurate due to the sizing methods employed for the gas turbine.

Overall, the total weight of the power plant rises a 6.3% and the cost a 2.43%. Therefore, reducing OPR does not offer any advantage as it penalises the weight, the cost, and the thermal efficiency.

4.3.3 Saturator pinch point temperature difference

Table 4.9 presents the effect of increasing and reducing the saturator pinch point temperature difference by 5 K on the optimised cycle thermodynamic design parameters, the inlet mass flow, the humidity, and the thermal efficiency. For this analysis, the overall pressure ratio and the effectiveness of the heat exchangers are kept constant at their reference values.

Increasing or reducing ΔT_{sp} does not produce any remarkable change in the design variables. However, due to the change in the humidification capabilities, the inlet mass flow increases a 1.5% and the thermal efficiency drops 0.34 pp per each 5 K ΔT_{sp} is raised.

TABLE 4.9: Effect of varying saturator pinch point on the cycle's optimised variables. Reference values in Table 4.4.
OPR=40, $\varepsilon_{IC}, \varepsilon_{AC}, \varepsilon_{EC}, \varepsilon_{RC}$=0.85.

$\boldsymbol{\Delta T_{sp}}$	5 K	15 K
$\boldsymbol{\Delta Rel.\ PR}$	0.00	0.01
$\boldsymbol{\Delta \beta}$	0.01	0.00
$\boldsymbol{\Delta \dot{m}_{g,in}}$	-1.5%	1.5%
$\boldsymbol{\Delta \omega_{CC}}$	0.01	-0.01
$\boldsymbol{\Delta \eta_{th}}$	0.34 pp	-0.34 pp

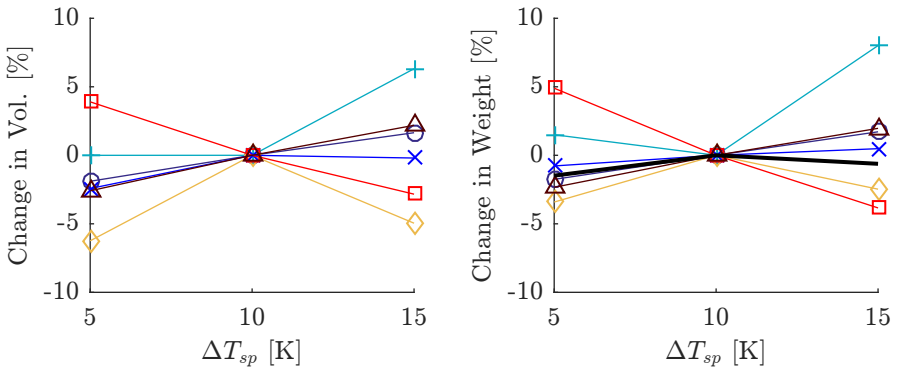

(a) Effect on the volume

(b) Effect on the weight

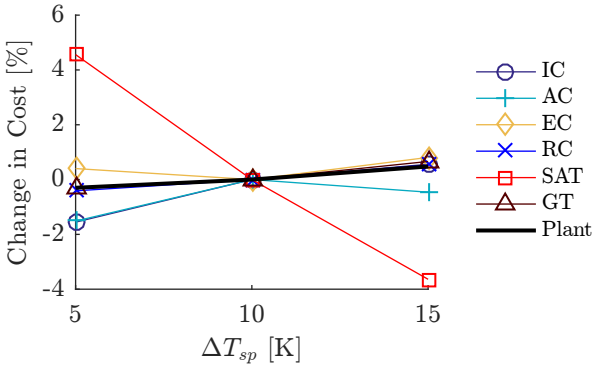

(c) Effect on the cost

FIGURE 4.8: Effect of varying the saturator pinch point on the design of the power plant and its components.
OPR=40, $\varepsilon_{IC}, \varepsilon_{AC}, \varepsilon_{EC}, \varepsilon_{RC}$=0.85.

Figure 4.8 presents the effect of varying the saturator pinch point on the design metrics of the power plant and its components. The variation of ΔT_{sp} does not produce any change in the design metrics of any of the components larger than a 5%, besides the weight and volume of the aftercooler (which are caused by the randomness introduced during the optimisation and selection process). Nonetheless, it is important to highlight the increment in the cost of the gas turbine, 1% for each 5 K, as it drives the rise in cost of the power plant, 0.5% for each 5 K. Hence, it can be concluded that increasing ΔT_{sp} has no benefit as it does not offer any advantage in either the effectiveness, the cost, or the total weight.

4.3.4 Cumulative effect

In order to analyse the cumulative impact of all the design parameters, three cycles have been selected to be compared to the baseline case (named I). The selected cycles include the most efficient configuration (named II), the least expensive configuration (named III), and the lightest configuration (named IV). Table 4.10 presents the metrics of the four selected cycles and Figure 4.9 depicts the layouts.

Table 4.10: Comparison of the design of the power plants.

Cycle		**I**	**II**	**III**	**IV**
$\boldsymbol{OPR}$	[-]	40	40	40	40
$\boldsymbol{\Delta T_{sp}}$	[K]	10	5	5	5
$\boldsymbol{\varepsilon_{IC}}$	[-]	0.85	0.95	0.75	0.85
$\boldsymbol{\varepsilon_{AC}}$	[-]	0.85	0.95	0.75	0.75
$\boldsymbol{\varepsilon_{EC}}$	[-]	0.85	0.95	0.95	0.75
$\boldsymbol{\varepsilon_{RC}}$	[-]	0.85	0.90	0.80	0.80
$\boldsymbol{\eta_{th}}$	[%]	58.31	61.35	58.86	56.75
Length	[m]	12.2	12.0	12.0	12.2
Width	[m]	4.9	5.0	4.9	5.0
Height	[m]	7.5	7.9	7.9	8.0
Weight	[t]	43.9	57.0	43.0	39.2
$\boldsymbol{SPEC}$	[$/kW]	335.0	365.8	322.2	326.7
Rel. HX Cost	[%]	17.4%	25.9%	14.1%	14.8%

It is observed that the thermodynamic design variables of the three configurations agree with the arguments presented in the above sections. The three selected cycles have an OPR of 40 and a ΔT_{sp} of 5 K. The most efficient configuration

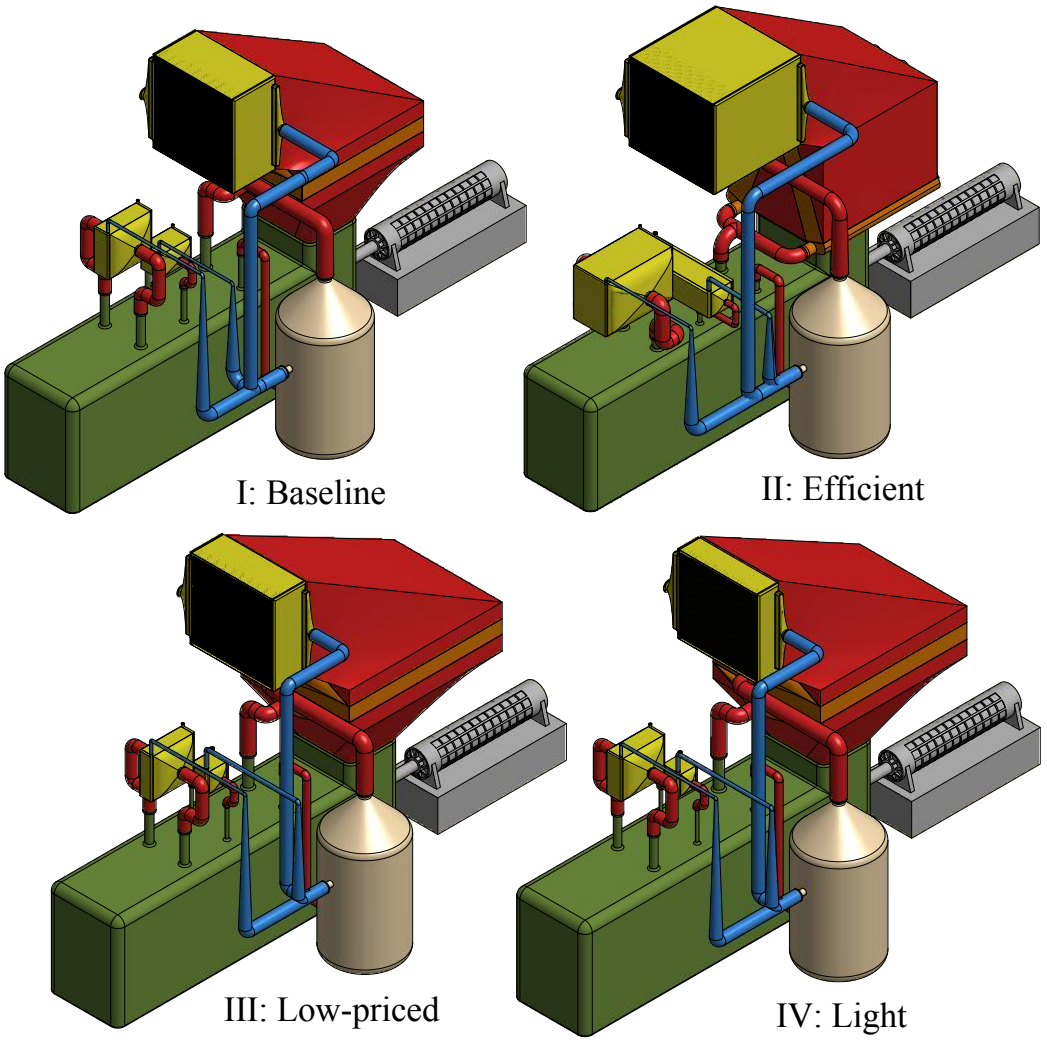

FIGURE 4.9: Power plant layout comparison.
Scale 1:140.

(II), with a thermal efficiency of 61.35%, is achieved when the technology of all four heat exchangers is maximised. For obtaining the least expensive configuration (III), with a $SPEC$ of 322.2 \$/kW, it is necessary to minimise the effectiveness of the intercooler, aftercooler, and recuperator, while maximising the effectiveness of the economiser. Last, the lightest configuration (IV), with a total weight of 39.2 tonnes, is achieved when the design effectiveness of all the heat exchangers is minimised except for the intercooler, whose design effectiveness must be 0.85.

Although the size of the heat exchangers changes significantly between the selected cycles, as observed in Figure 4.9, the overall dimensions of the power plant are barely affected (Table 4.10). It is observed that the main drivers of the overall dimensions are the size of the gas turbine and the saturator tower. However, the

dimensions of these components barely changes when modifying any of the cycle design parameters.

On the other hand, the weight of the plant suffers a considerably larger variation when modifying the cycle design parameters, as the heat and mass transfer components represent between 40% and 60% of the total weight. The most efficient configuration (II) is 29.8% heavier than the baseline configuration (I), and a 45.4% than the lightest configuration (IV).

In terms of cost, the $SPEC$ also suffers noticeable variations when altering the design parameters. The most efficient configuration (II) becomes 9.2% more expensive than the baseline (I), and 13.6% when compared with the cheapest (III). The variations in the cost are mainly produced by the change in the price of the heat exchangers. The acquisition cost of the gas turbine changes less than 1% when comparing the baseline (I), the cheapest (III), and the lightest (IV) configurations, and a up to 2.5% when comparing against the most efficient (II). However, the price of the heat exchanger increases from representing a 17.4% of the total cost for the baseline configuration (I), to represent a 25.9% for the most efficient (II) (Table 4.10). Whereas, for the cheapest (III) and the lightest (IV) the contribution of the heat exchanger to the total cost is reduced to a 14.1% and a 14.8% respectively.

4.4 Influence of the material choice for the heat exchangers

The possibility of using of seawater as a coolant in the air-water heat exchangers for the marine and coastal power generation applications involves the necessity of using materials with high fouling, corrosion, and erosion resistance. Certainly, the use of these materials will have an impact on the design and cost of these components. The impact of using different materials for the design of the air-water heat exchangers is evaluated herein. The designing materials analysed include: 90-10 copper-nickel (good corrosion and excellent fouling resistances [84, 85]) selected as the reference material, stainless steel 316H (cheaper material with lower corrosion and fouling resistance, recomended [84]), and titanium grade 2 (expensive material with excellent corrosion and erosion resistance, good fouling resistance, and low

density [84, 87]). The thermal conductivity and density of the analysed materials are presented in Table 4.11.

TABLE 4.11: Material properties.

Material	$\boldsymbol{k}$ [W/K m]	$\boldsymbol{\rho}$ [kg/m^3]
Stainless steel 316H	14	8,030
90-10 Copper-nickel	40	8,940
Titanium grade 2	22	4,510

The selected cycle design configurations to perform the analysis are presented in Table 4.12. The effectiveness, selected as the parameter to represent the "technology level" of the air-water heat exchangers, is varied in order to study how the variation of the "technology level" affects the impact of using different design materials. The rest of the design variables are kept constant.

TABLE 4.12: Cycle design envelop analysed.

Cycle design parameters		**Scenarios analysed**	
OPR	40	$\varepsilon_{IC}, \varepsilon_{AC}, \varepsilon_{EC}$	0.95
ΔT_{ps}	5 K	$\varepsilon_{IC}, \varepsilon_{AC}, \varepsilon_{EC}$	0.85
ε_{RC}	0.90	$\varepsilon_{IC}, \varepsilon_{AC}, \varepsilon_{EC}$	0.75

Figure 4.10 shows the variation of the weight and volume of the air-water heat exchangers and the power plant for the different scenarios analysed. Shifting the design material from copper-nickel to steel penalises the weight and volume of the intercooler (Figure 4.10a). The weight increases a 31% on average and the volume a 47%, except for the design scenario ε_{IC}=0.85. In that scenario, the weight rises a 59% and the volume a 64%. The lower thermal conductivity of the steel (Table 4.11) leads to an increment of the required heat transfer area to compensate the drop in the overall heat transfer coefficient, which directly impacts the size and weight of the component. The titanium configuration results to be a 59% lighter and have a similar size compared to the copper-nickel design. However, for the design scenario ε_{IC}=0.85, the weight is only reduced a 22% and the volume increases a 43%. The lower density of the titanium (Table 4.11) permits to obtain lighter designs, even for bulkier configurations. The design scenario ε_{IC}=0.85 presents different results than the other two cases due to the 8% lower overall heat transfer value achieved by the titanium and steel configurations. Thus, the impact of having a lower thermal conductivity is emphasized, making necessary to enlarge the increment in the heat transfer area.

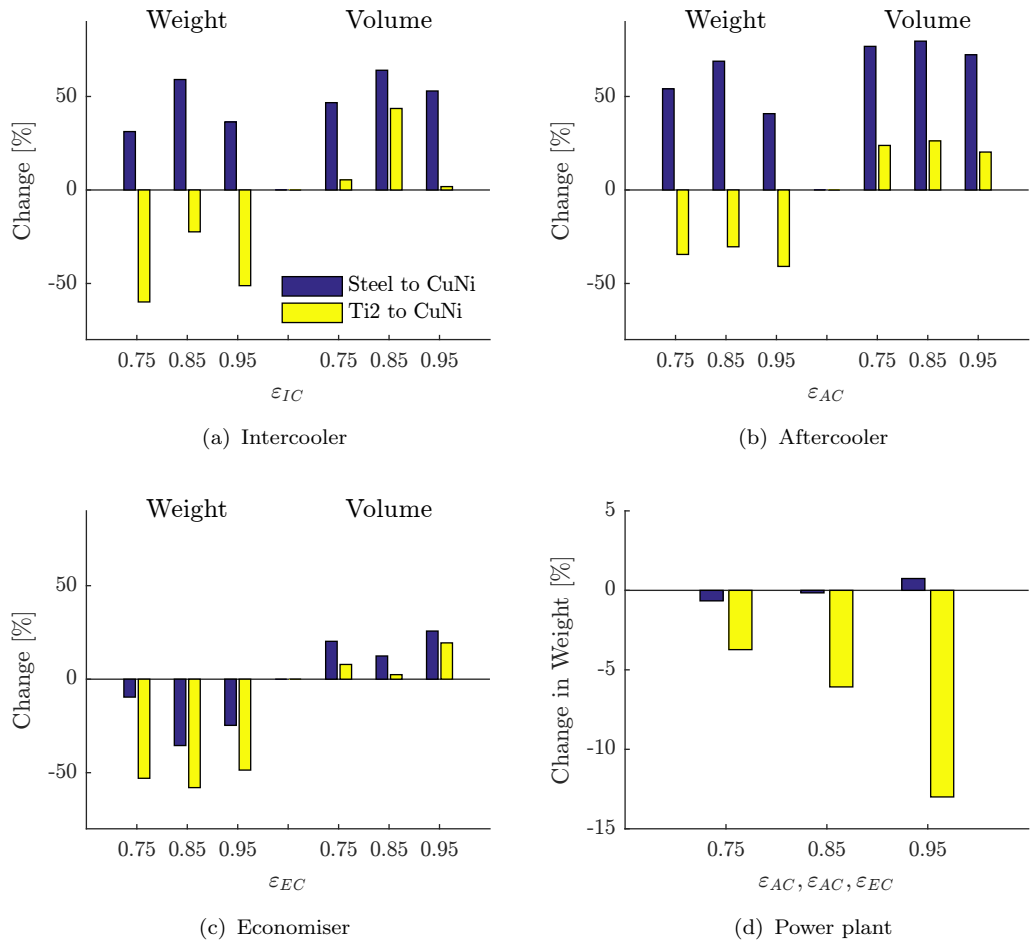

(a) Intercooler

(b) Aftercooler

(c) Economiser

(d) Power plant

FIGURE 4.10: Effect of the designing material of the air-water heat exchangers on the volume and weight of the power plant and its components. OPR=40, ΔT_{sp}=5 K, ε_{RC}=0.90

The aftercooler shows broadly the same trend as the intercooler (Figure 4.10b). When using steel, the device becomes a 55% heavier on average and a 77% bulkier. The lower thermal conductivity of the titanium compared to the copper-nickel also makes necessary to increases the size of the component, resulting in a configuration 24% bulkier in average. However, the required increment in the area is lower due to the higher thermal conductivity of the titanium compared to the steel. The lower density of the titanium compared with the other materials permits to achieve the lightest designs, 35% lighter on average compared to the copper-nickel alloy design.

In the case of the economiser (Figure 4.10c), the lower impact of the material choice on the volume of the device (average rise of 17% for the steel and 7% for the titanium) permits to obtain larger weight reductions when designed in steel or titanium. With the steel, an average reduction of the weight of a 25% is

achieved, whereas with the titanium, the reduction grows up to an average value of 53%. The overall heat transfer coefficient of the economiser is less affected by the conductivity of the material. Therefore, the rise in the required heat transfer area is lower compared to the intercooler and aftercooler cases.

Overall, the use of steel for the design of the air-water heat exchangers does not produce any substantial change in the total weight of the power plant (Figure 4.10d). The increment in the weight derived from the aftercooler and the intercooler is cancelled by the lightening of the economiser. Nevertheless, when using titanium, the total weight is reduced a 3.7% when ε=0.75. This reduction increases up to a 13% when ε=0.95. As the design effectiveness increases, the relative contribution of the heat exchangers to the total weight also does. Hence, the same relative modification of the heat exchanger weight produces a larger impact on the cycle metrics for higher design effectiveness.

Figure 4.11 shows the impact of changing the design material on the acquisition cost of the heat exchangers and on the total cost, for the three design scenarios analysed (Table 4.12). Despite the lower specific cost of the steel compared with the copper-nickel (Table 3.1), the increment in the required material due to the lower thermal conductivity makes the intercooler's steel configuration a 15% more expensive in average than the copper-nickel (Figure 4.11a). In the case of using titanium, the larger specific cost (Table 3.1) added to the extra required heat transfer area makes the configuration a 35% more expensive on average.

The aftercooler (Figure 4.11b) shows a similar trend as that for the intercooler. When using steel, the configuration results to be a 15% more expensive on average and a 30% more expensive when using titanium. In the case of the economiser (Figure 4.11c), the use of steel implies a design a 9% cheaper than the copper-nickel, since the increment in the required area is not large enough to overcompensate the lower specific cost of the steel. Nevertheless, when using titanium the configuration becomes a 30% more expensive on average.

The impact on the cost of the power plant (Figure 4.11d) is similar to the impact on the weight. As the effectiveness of the heat exchanger increases, the impact on the price grows due to the larger contribution of the total cost that the heat exchangers make. In the case of using steel, the cost rises from a 0.1% when ε=0.75, to 2.3% when ε=0.95. In the case of using titanium, the rise of the cost grows from a 1% when ε=0.75, to a 6.4% when ε=0.95.

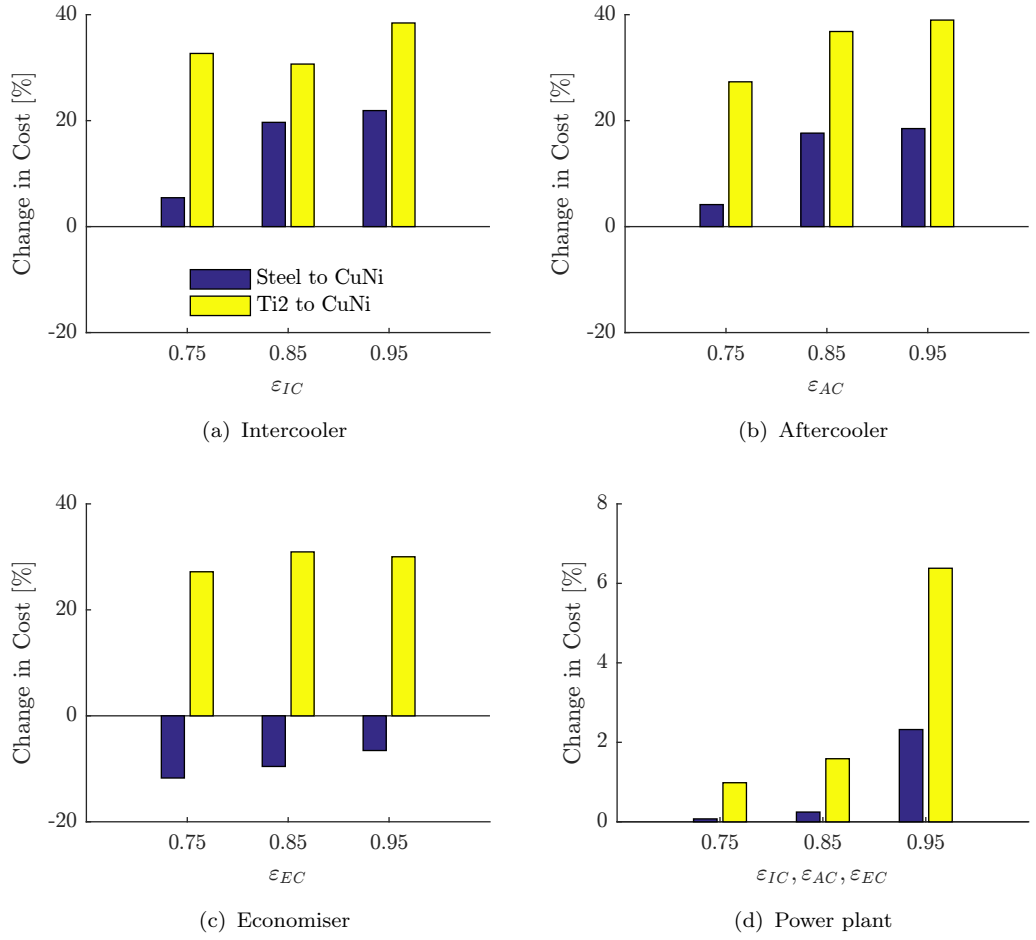

(a) Intercooler

(b) Aftercooler

(c) Economiser

(d) Power plant

FIGURE 4.11: Effect of the designing material of the air-water heat exchangers on the cost of the power plant and its components.
OPR=40, ΔT_{sp}=5 K, ε_{RC}=0.90

Overall, it is observed that the impact in the cycle metrics imposed by the change in the design material of the air-water heat exchangers rises as the design effectiveness of these devices does. The implementation of the steel does not alter the weight, whereas it slightly rises the cost, up to 2.3% when ε=0.95. Due its lower density and higher specific cost, shifting to titanium alloys has a larger impact on the cycle metrics, it can lead up to a 13% reduction in the total weight and a 6.4% rise of the total cost when ε=0.95. Therefore, the use of steel offers no advantage as it increases the total cost of the plant for no benefit in the resistance to fouling or erosion-corrosion. On the other hand, the use titanium improves the erosion-corrosion resistance of the heat exchanger for a rise in the acquisition cost of the plant.

4.5 Influence of the designing ambient conditions

Depending on the allocation of the power plant or the selected marine route of the vessel, the designing ambient conditions might differ considerably, which might alter the performance and design of the power plant. The effects of varying the design ambient and water temperature on the design of the components and the metrics of the power plant are evaluated in this section. The temperatures ranges selected for the analysis are presented in Table 4.13. The selected cycle design configuration for the study is presented in Table 4.14.

Table 4.13: Temperature range analysed.

T_{air}	[°C]	5-35
T_{water}	[°C]	5-35

Table 4.14: Cycle design envelope.

OPR	[-]	40
ΔT_{ps}	[K]	5
ε_{IC}	[-]	0.95
ε_{AC}	[-]	0.95
ε_{RC}	[-]	0.95
ε_{EC}	[-]	0.95

4.5.1 Water temperature

Figure 4.12 shows the changes when altering the designing temperature of the water while keeping the air temperature constant. The variation of the designing water temperature does not affect more than a 1% the specific power and, hence, the inlet mass flow. Thus, all the changes observed in the designs of the components are only a consequence of the temperature variation.

The aftercooler and the intercooler are the components with the highest sensibility to the water temperature. An increment of 10 °C implies an average reduction of 15% in volume and weight, and 20% in cost. The economiser size is also affected by the increment of the water temperature. Nevertheless, the maximum variations achieved are of 12% in volume and weight, and a 14% in the cost. Moreover, the volume of the saturator also reduces a 5.6% for each 10 °C the water temperature

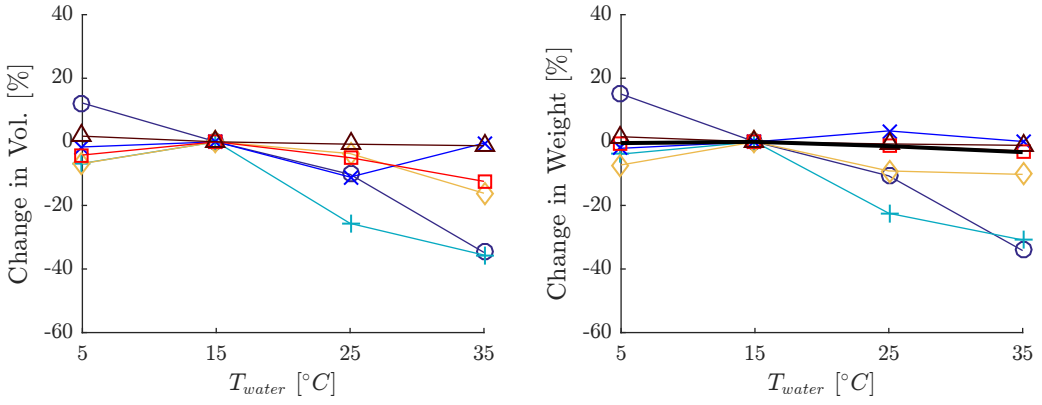

(a) Impact on the volume

(b) Impact on the weight

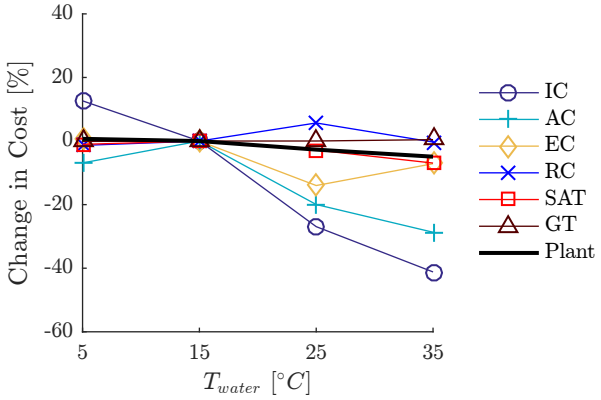

(c) Impact on the cost

FIGURE 4.12: Effect of the designing water temperature on the design of the power plant and its components.
OPR=40, ΔT_{sp}=5 K, ε_{RC}=0.90, $\varepsilon_{IC}, \varepsilon_{AC}, \varepsilon_{EC}$=0.95

rises. The design of the rest of the components does not suffer any significant variation.

Overall, the reduction in the weight and cost of the air-water heat exchangers produces an average reduction in the weight of 1.5% and 3.5% in the cost of the power plant for each 10 °C the water temperature increases. As the water temperature increases, the temperature difference between the hot inlet gasses and the incoming coolant reduces. Thus, the amount of heat that can be extracted from the air drops, reducing the required heat transfer area of the heat exchangers.

4.5.2 Air temperature

Figure 4.13 shows the variations suffered by the design of the components when the designing air temperature is altered while keeping the water temperature constant. The variation of the designing air temperature does not affect the specific power and, hence, the inlet mass flow. Thus, all the changes observed in the designs of the components are only a consequence of the variation of the temperatures.

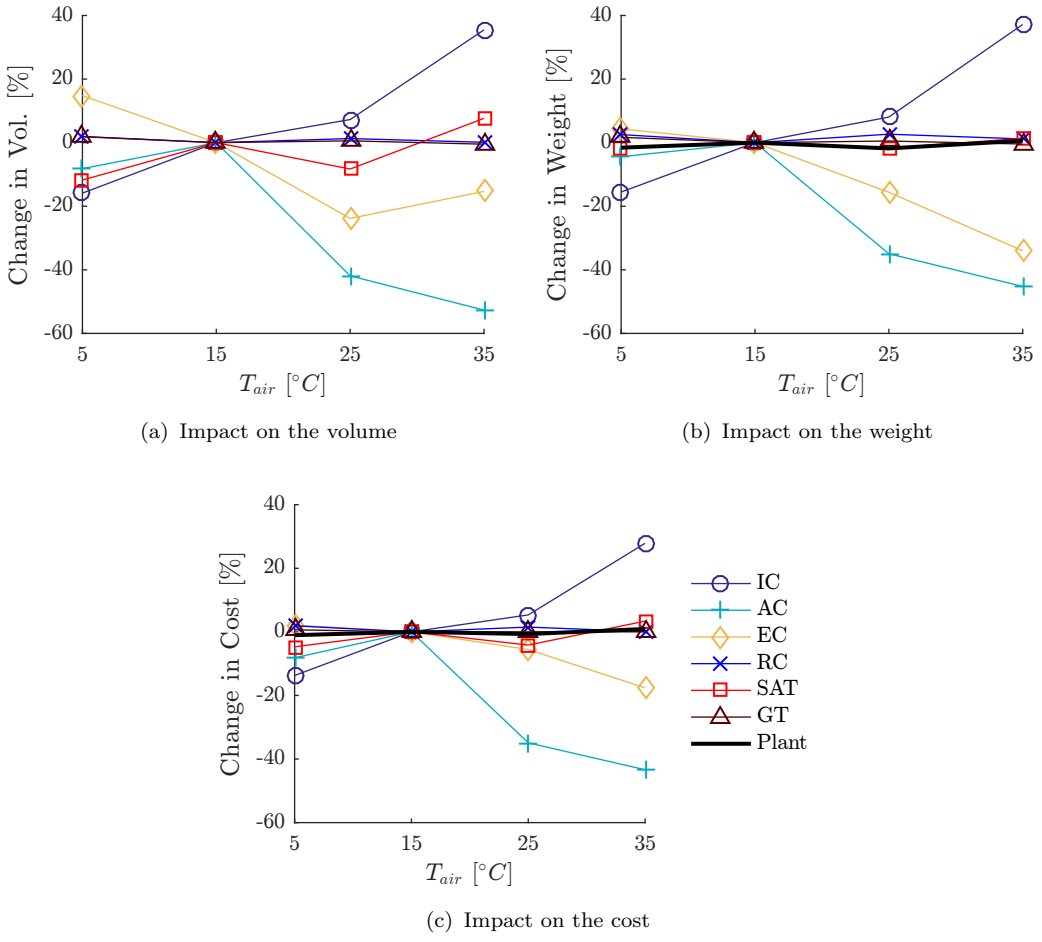

(a) Impact on the volume

(b) Impact on the weight

(c) Impact on the cost

FIGURE 4.13: Effect of the designing air temperature on the design of the power plant and its components.
OPR=40, ΔT_{sp}=5 K, ε_{RC}=0.90, $\varepsilon_{IC}, \varepsilon_{AC}, \varepsilon_{EC}$=0.95

Increasing the air temperature leads to an increment of the size, weight and cost of the intercooler, which is accentuated as the design temperature grows. For the hottest scenario, the volume increases up to a 38%, the weight a 37%, and the cost a 35%. The increment in the ambient temperature is directly seen by the intercooler as an increment in its inlet temperature. Therefore, the temperature

gap between the hot fluid and the coolant increases, leading to a rise in the total heat transferred and, thus, in the required heat transfer area.

In the case of the aftercooler, the rise in the ambient temperature beyond 15 °C produces a reduction in the volume, weight, and cost of the component, which grows up to 52%, 45%, and 43% respectively for an ambietn temperature of 35 °C. The rise in the temperature at the inlet of the aftercooler makes necessary to augment the ratio $\dot{m}_w/\dot{m}_a$ in order not to boil the water in the heat exchanger. The increment in that ratio is translated as a reduction of the designing C^* of the aftercooler from 0.95 to 0.87. This permits to obtain the same effectiveness with a lower heat transfer area [117], as shown in Figure A.8. On the other hand, when the water temperature is reduced below 15 °C the design also becomes a 10% less bulky, 4% less heavy, and 8% less expensive. As the ambient temperature decreases, the gas inlet temperature at the aftercooler also does, reducing the heat transferred within the device. The economiser shows a similar behaviour as the aftercooler. Nevertheless, the impact on the economiser modifications is a 40% lower, on average, in the weight and a 60% lower, on average, in the cost compared with the aftercooler.

Overall, the modification of the designing air temperature does not produce any change in the power plant metrics larger than a 1% since the variations produced by the intercooler are countered by the modifications experienced by the aftercooler and the economiser.

4.5.3 Cumulative effect

Figure 4.14 shows the cumulative impact of varying simultaneously the air and the water designing temperatures on the cycle efficiency, total weight and cost. The counter plots only show the central band, where the temperature of the water and the temperature of the air do not differ more than 10 °C, since it is very improbable to have a designing scenario with larger discrepancies.

The thermal efficiency (Figure 4.14a) is mainly affected by the designing air temperature, whereas the water temperature has a negligible effect. The thermal efficiency decreases 0.12 pp per degree Celsius. The total weight of the power plant (Figure 4.14b) does not show any variations larger than a 2% for any of the temperature combinations analysed. Last, the total cost reduces up to a 4%

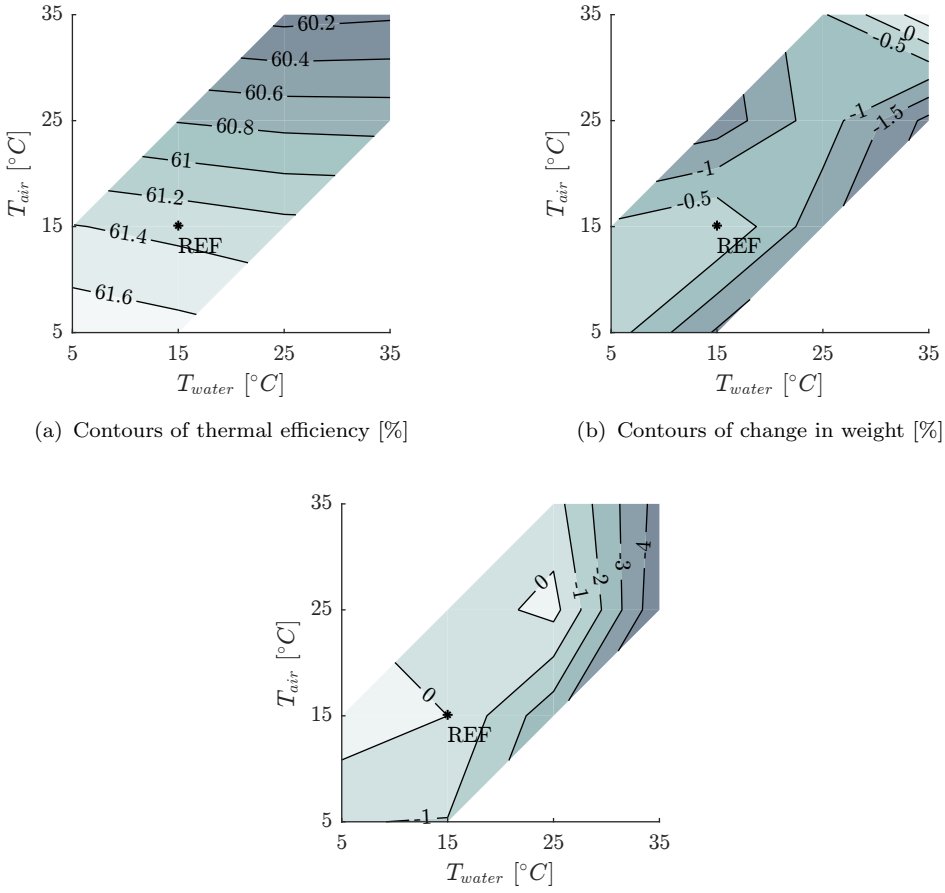

(a) Contours of thermal efficiency [%]

(b) Contours of change in weight [%]

(c) Contours of change in cost [%]

FIGURE 4.14: Effect of the designing ambient conditions on the power plant's efficiency, weight, and cost.
OPR=40, ΔT_{sp}=5 K, ε_{RC}=0.90, $\varepsilon_{IC}, \varepsilon_{AC}, \varepsilon_{EC}$=0.95

for the hottest scenario, effect of the increment in the water temperature (rising the air temperature for a constant water temperature does not have any impact). Nevertheless, moving to colder scenarios does not present any change. Therefore, from an economic point of view, it would be desirable to design the power plant in an environment with a low ambient temperature while having a warm source of water. This scenario would permit to obtain a benefit in the thermal efficiency while achieving a reduced acquisition cost.

4.6 Comparison against reference marine engines

A comparison of the RHAT power plant against a reference modern diesel engine and a reference modern marine gas turbine is presented in Figure 4.15. The

reference diesel engine is represented by the Wärtsilä X92, which can deliver a power output of 40 MW with a 7-cylinder configuration and a thermal efficiency of 50.4% [118]. The engine is 13.1 m long, 8.7 m wide, 15.8 m tall, and has a weight of 1,260 metric tonnes. The reference marine gas turbine selected is the Rolls Royce MT30, which can deliver a power output of 36-40 MW with a thermal efficiency of around 40% [119]. If the packing and the ancillaries are included, which represent an 80% of the total weight, the total weight of the gas turbine is 30 metric tonnes. With the packing the gas turbine is 8.7 m long, 2.7 m wide, and 3.6 m high. The comparison can only be made in terms of design point performance and power plant's dimensions due to the lack of cost data about the marine engines, control equipment costs, installation costs, and the lack of a vessel model to be coupled with the thermodynamic performance model of the RHAT.

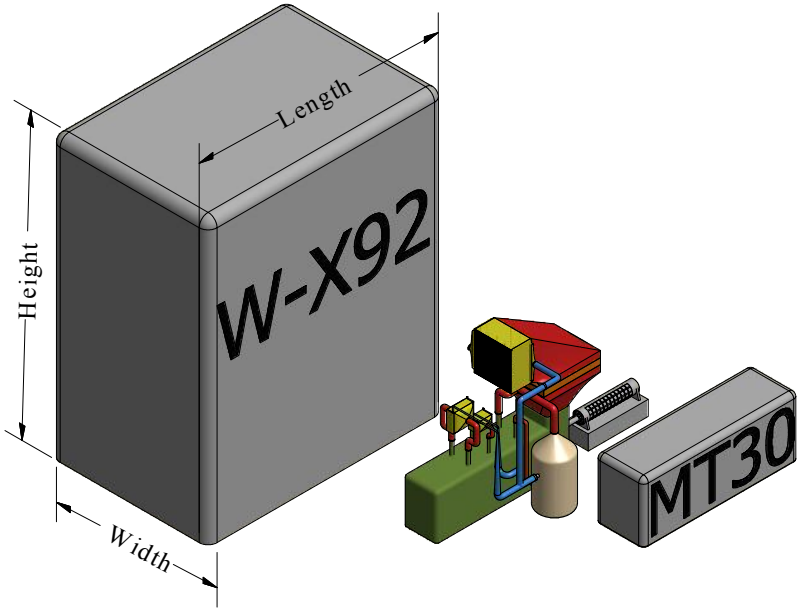

FIGURE 4.15: Comparison of the reheated humid air turbine dimensions against reference diesel (W-X92) engine and marine gas turbine (RR MT30).

Compared to the MT30, the RHAT is capable of achieving a maximum thermal efficiency 21 pp higher (Table 4.10). Nevertheless, the addition of the heat exchanger significantly penalises the size and the weight, becoming twice as wide and tall, and eight times heavier than the MT30 (if assumed that the packing and ancillaries are 80% of the total weight [119] and without including the generator). The penalisation in weight can be reduced if instead of selecting the most efficient cycle, the lightest cycle is selected (Table 4.10). In that case, the RHAT would be five times heavier, but the benefit in efficiency would be reduce to 17 pp. In

addition, the total weight could be further reduced, around a 3%-5% if the heat exchangers were designed using titanium.

When compared to the diesel engine, the RHAT is able to achieve a maximum thermal efficiency 11 pp higher while reducing the weight an 83% and the volume a 75%. Moreover, any of the most interesting configurations (Table 4.10) are capable of exceeding the thermal efficiency of the reference diesel by at least 7 pp and further reduce the weight up to a 90%. In addition, the weight savings can be improved around an extra 1%, if the heat exchangers were designed in titanium, without any deterioration in performance. The thermodynamic benefits might be reduced when designing the engine for high ambient temperatures, as it reduces the thermal efficiency of the RHAT. Nevertheless, the penalties would not be larger than 2 pp (Figure 4.14a), which still leaves a margin of 5 pp in the worst case scenario.

Overall the RHAT has proven to achieve significantly higher efficiency than the reference marine gas turbine and diesel engines. Therefore, from a thermodynamic point of view, and keeping in mind that normally the fuel expenditures are several times larger than the acquisition costs, the RHAT foresees a promising future in the marine market. According to the results, the RHAT could substitute the diesel engines for any application, as it presents a more efficient design, and significantly lighter and more compact. However, for applications where weight is a key restriction and efficiency is not of any concern (as in military destroyers), the simple gas turbine remains as a better option due to the considerable reduction in weight it offers. Nevertheless, to fully demonstrate the potential of the RHAT it would be necessary to couple the engine model with a vessel model and conduct a detailed analysis for a given mission to estimate the performance and the expenditures of the humid engine.

4.7 Summary

In this chapter, the layout and main design metrics of the RHAT power plant are presented, together with the analysis of the components design's sensitivity to the cycle's designing variables, materials, and ambient conditions. Despite the demanding conditions imposed for the design of the heat exchangers (high design effectiveness, large C^* values, extremely different volume flows between the

fluids), it has been proved that feasible designs can be achieved for all the different scenarios analysed.

The recuperator has been found to be the most expensive and heaviest of the heat exchangers, representing an 11.82% of the total cost and a 26.4% of the total weight for the baseline case (Table 4.4). The saturator and the economiser, despite their low acquisition cost (0.45% and 0.28% of the total respectively), make a remarkable contribution to the total weight of the plant, representing the 19.3% of the total weight. The intercooler and the aftercooler compactness permits to achieve light designs, which only represent a 4% of the total weight and a 4.8% of the total cost. Together, all the heat mass transfer devices account for 49.7% of the total weight and 17.35% of the total cost. Therefore, increasing the investment cost less than a 20% permits to enlarge the thermal efficiency more than a 30% compared to a simple gas turbine.

The intercooler's and recuperator's effectiveness are the main drivers of the power plant. An increment of 0.05 points in ε_{RC} leads to a rise in the thermal efficiency of 1.2 pp, 4.18% in the total cost, and 11.08% in the total weight. A ε_{IC} rise of 0.1 points produces a benefit of 0.79 pp in the thermal efficiency while enlarging the cost and the weight a 5.9% and a 6% respectively. On the other hand, reducing OPR or increasing ΔT_{sp} do not imply any benefit. Both actions produce an increment in the total price and weight of the plant, while reducing the thermal efficiency. It is worthy to highlight that the raising the effectiveness of the economiser produces an increment in the thermal efficiency, as well as a reduction in the total cost.

The most efficient configuration (Table 4.10) has a thermal efficiency 61.35%, and a $SPEC$ of 365.9 \$/kW. Nevertheless, the acquisition cost can be reduced a 11.9% by lowering the design effectiveness of the intercooler, aftercooler, and recuperator, though it would penalise the thermal efficiency 2.5 pp. Moreover, the total weight can be reduced a 31.2%, compared to the most efficient configuration, by cutting the effectiveness of all the heat exchanger and, consequently, penalising the efficiency 4.6 pp. The three configurations present extremely similar overall plant dimensions (height, length, width). The reason being that the volume of the plant mainly depends on the arrangement of the heat exchangers around the gas turbine and the size of the gas turbine, rather in the heat exchanger's size. Nonetheless, it has to be mentioned that the variations of the weight and cost are

mainly caused by the changes in the design of the heat exchangers, as the weight or cost of the gas turbine does not vary more than a 3%.

Among the materials studied for the design of the air-water heat exchangers, the stainless steel is found to be the worst option. It offers no weight or cost reduction compared to the copper-nickel alloys, while showing the poorest resistance properties. Using of titanium instead of copper-nickel alloys, which has better erosion-corrosion resistance than the copper-nickel but poorer fouling resistance, can imply a reduction in the total weight up to a 13% for the most efficient configuration, while increasing the price a 6.4%. The changes produced in the cost and the weight are reduced as the design effectiveness of the heat exchangers decreases.

The study of the influence of the ambient conditions has proven that the thermal efficiency of the cycle is mainly affected by the air temperature. The efficiency increases 0.12 pp per degree Celsius the design air temperature is increases. On the other hand, the water temperature shows no significant effect on the thermal efficiency. However, increasing the design water temperature leads to less expensive designs designs when the designing temperatures are above 25 °C.

Last, compared to a reference marine gas turbine, as it can be the MT30, the RHAT offers a thermal efficiency 16-21 pp higher, whereas it becomes five to eight times heavier and twice as bulky. However, compared to a reference marine diesel engine, as it can be the Wärtsilä X92, the RHAT offers at least a 7 pp benefit in thermal efficiency, which can grow up to 11 pp when maximising the effectiveness of the heat exchangers. In addition, the RHAT offers a reduction in weight around 80%-90% and 75% in volume occupied. Therefore, from a thermodynamic and design point of view, and having in mind that normally the fuel expenditures are several times larger than the acquisition costs, the RHAT foresees a promising future. It is able to offer a better performance than the diesel engines, occupying a lower volume and being considerably lighter. On the other hand, in applications where weight is a main priority and efficiency is not of any concern, the simple gas turbine still stands as a better option due to its lower weight. However, to fully demonstrate the potential of the RHAT, the engine model would need to be coupled with a vessel model and perform an route analysis to obtain the performance and expenditures.

This chapter has covered the objective of determining the correlations between the technology level of the components, and the design of them and the power

plant. The effects of employing different design materials for the heat exchangers have also been evaluated. In addition, the sensitivity of the components and the power plant to the designing ambient conditions has been identified. Last, the performance and design of the reheated humid air turbine has been compared against the achieved by current reference marine prime movers.

Chapter 5

Economic analysis for power generation

The RHAT has demonstrated to be capable of achieving a thermal efficiency exceeding the barrier of the 60%. Nowadays, very few gas turbine based power plants are able to exceed that barrier. The only ones capable are heavy-duty combined cycle power plants, as the new H-Class created by General Electric [23]. Nevertheless, there is no option available in the mid-power market, below 100 MW, capable of achieving such high efficiency. Therefore, the RHAT seems to present a large potential for power generation applications in the mid-power range from a thermodynamic point of view. However, to confirm such potential it is required to perform an economic analysis.

This chapter presents an economic analysis of the RHAT for power generation applications. A parametric design space exploration is performed to evaluate the impact of the cycle design variables on the economic metrics. The effect of the thermal efficiency degradation along the life of the power plant is also included in the study. An uncertainty analysis indicates the impact of the main cost driver's fluctuations on the cost of the electricity. Finally, the economic performance of the investigated cycle is benchmarked against the performance achieved by high efficiency humid and combined cycle systems previously presented.

5.1 Economic analysis

The economic analysis of the system relies on the total cost of investment and the thermodynamic performance of the cycle to estimate the annual expenses, which are then employed to derive the cost of the electricity. The economic model is mainly based on the work published by Bejan et al.[120].

The Total Cost of Investment (TCI) is composed by the sum of the Fixed Capital Investment (FCI) and the other outlays (Table 5.1). The FCI represents the capital required to acquire the land, purchase all the necessary equipment, and install it for the proper operation of the power plant. The other outlays represents the capital required to acquire the licenses and start operating the power plant.

Likewise, the FCI is the sum of the Direct Costs (DCo) and the Indirect Costs (ICo). The DCo is the total capital necessary to purchase all the equipment and goods involved in the fabrication, erection, and installation of the facilities. The ICo are required to pay for all the human work necessary for the construction of the facilities.

The installation cost covers the cost of unloading, handling, foundations, supports, and all other expenses related to the construction of the plant and the necessary connections. The piping cost covers the labour and material cost required for creating all the required pipe connections. The instruments and control systems costs cover the required money to pay for all the instrumentation required to guaranty a safe operation and management of the plant. The land cost covers the price of the required terrain to build the plant. The civil, structural, and architectural work costs includes the total cost for building all the roads, buildings, fencing, etc. The service facilities costs covers the cost required to operate all the necessary subsystems.

The cost of engineering and supervision includes the required money to pay for the detailed plant design, engineering supervision, scale models, administration, consultant fees, etc. The construction costs covers the cost of the required hand-work to built the plant. The contingency cost includes the money for covering unpredicted events related to the weather, work stoppages, price changes, etc.

The startup cost includes the labour, material, equipment, and overhead expenses to be used during the startup time. The working capital represents the expected expenses of the power plant operation before the first payment is received. The

licensing, and research and development cost includes the capital required to acquire the necessary licenses and to pay for the research and development directly related to the system.

In absence of any detailed data about the infrastructure required, the TCI is estimated from the PEC assuming that the price of the rest of the facilities and required elements can be calculated as a percentage of the PEC, the DCo, or the FCI, as suggested by Bejan et al. [120]. The assumed values of these costs are based on the work published by Barberis et al. [121] and are represented in Table 5.1. The calculation of the PEC is explained in detail in Chapter 3.

TABLE 5.1: Economic assumptions for the estimation of the total cost of investment [121].

Total Cost of Investment	Fixed Capital Investment	Direct Costs	Purchase equipment cost	
			Installation	20% of PEC
			Piping	10% of PEC
			Instruments and control systems	6% of PEC
			Electric equipment and materials	10% of PEC
			Land	5% of PEC
			Civil, structural, and architectural work	15% of PEC
			Service facilities	30% of PEC
		Indirect Costs	Engineering and supervision	25% of PEC
			Construction	15% of DCo
			Contingency	8% of above
	Other Outlays		Startup	8% of FCI
			Working capital	15% of FCI
			Licensing, and research and development	7% of FCI

The economic analysis is based on the payment of the cost of the annual expenses (Ξ_{AE_i}) derived from building and operating the power plant. The annual expenses are estimated using the model proposed by Bejan et al. [120], which accounts for the payment of the initial investment (Ξ_{ini}), the interest generated by the required loan (cost of financing, Ξ_{fin}), the taxes (Ξ_{tax}), the cost of fuel (Ξ_{fuel}),

and the Operation and Maintenance costs (Ξ_{OM}), as shown in Eq. 5.1. The model is explained in detail in Appendix C.

$$\Xi_{AE_i} = \Xi_{ini_i} + \Xi_{fin_i} + \Xi_{tax_i} + \Xi_{fuel_i} + \Xi_{OM_i} \tag{5.1}$$

The assumed values for the economic analysis are presented in Table 5.2. The financing loan is distributed in three parts (debt, common equity, and preferred stock) with different interest rates. The price of the natural gas is taken as an average of the monthly prices of 2015. The analysis is conducted in current-dollars [120] since the effects of the inflation are taken into account. It has to be considered that a current-dollar analysis overestimates the expenses compared to today's value of the money. The alternative, performing the analysis in constant dollars without considering the inflation would have underestimated the costs and the cash flows, which is undesired.

TABLE 5.2: Assumptions for the economic analysis [31, 120–122].

Assumed starting year of the project	January 2015
Time until commissioning starts	1 year
Assumed plant commissioning time	2 years
Plant book life	20 years
Plant life for tax purposes	10 years
Income tax rate	30%
Other taxes and insurances	2% of FI[1]
Real inflation	2.5%
Real inflation for the fuel	3.0%
Fraction funded by common equity	35%
Fraction funded by preferred stock	15%
Fraction funded by debt	50%
Interest rate of the common equity	6.5%
Interest rate of the preferred stock	6.0%
Interest rate of the debt	5.5%
Fuel price (LNG)	0.25 $/kg
OM variable	2% of FCI
OM fixed	0.83 $/MWh of fuel
Availability	85%

The Cost of Electricity (COE) is calculated using Eq. 5.2. τ represents the total amount of hours that the power plant is operating per year, and $\dot{W}$ the power

[1]The Fixed Investment (FI) is calculated as the Fixed Capital Investment minus the cost of the land

output. τ is calculated as the total numbers of hours in a year multiplied by the availability.

$$COE_i = \frac{\Xi_{AE_i}}{\tau \, \dot{W}} \tag{5.2}$$

The COE represents the total cost of generating a kilowatt hour and reflects the minimum sale price to recover the annual expenses. The COE varies during the book life of the power plant following the annual cost variation. As such, the average COE ($\overline{COE}$) for the book life is used as an economic index, calculated from Eq. 5.3, to represent the total average cost of generating one kWh accounting for the annual expenses along the whole book life (n).

$$\overline{COE} = \frac{\sum_{i=1}^{n} \Xi_{AE_i}}{n \, \tau \, \dot{W}} \tag{5.3}$$

5.2 Effect of the cycle design variables

Table 5.3 represents the cycle design envelope analysed. The objective of this study is to evaluate the effect of each design variable on the economic performance of the plant and identify the most economic configuration for the assumed scenario (Table 5.2).

Table 5.3: Envelope of the cycle design variables.

$\boldsymbol{OPR}$	[-]	30,40
$\boldsymbol{\Delta T_{sp}}$	[K]	5,10,15
$\boldsymbol{\varepsilon_{IC}}$	[-]	0.75,0.85,0.95
$\boldsymbol{\varepsilon_{AC}}$	[-]	0.75,0.85,0.95
$\boldsymbol{\varepsilon_{EC}}$	[-]	0.75,0.85,0.95
$\boldsymbol{\varepsilon_{RC}}$	[-]	0.80,0.85,0.90

The impact of the cycle design variables on the thermal efficiency, the $SPEC$, and the $\overline{COE}$ is shown in Figure 5.1. For this study the configuration presented in Table 5.4 has been used as reference to calculate the relative changes. The value of the design variables is varied across its specified design range in order to identify its relative contribution to the overall economic metrics of the system. The reference ambient conditions are presented in Table 4.3.

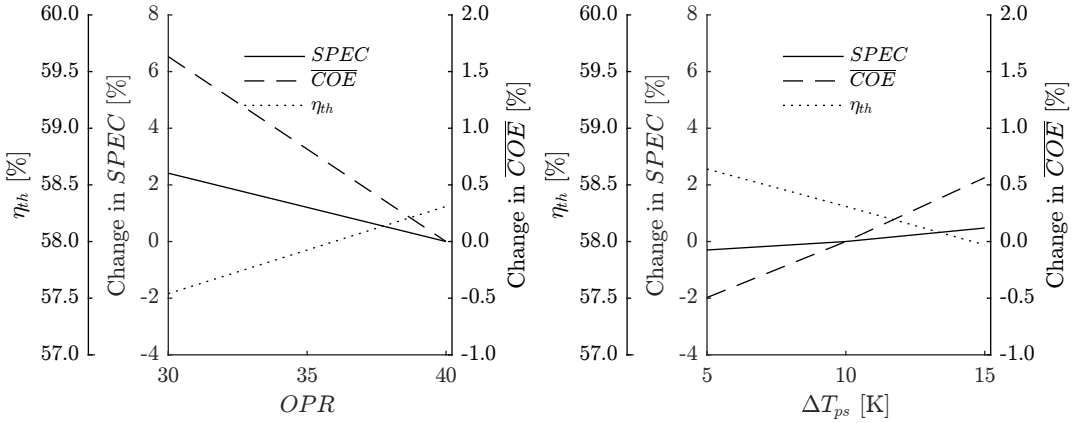

(a) Effect of the overall pressure ratio

(b) Effect of the saturator pinch point

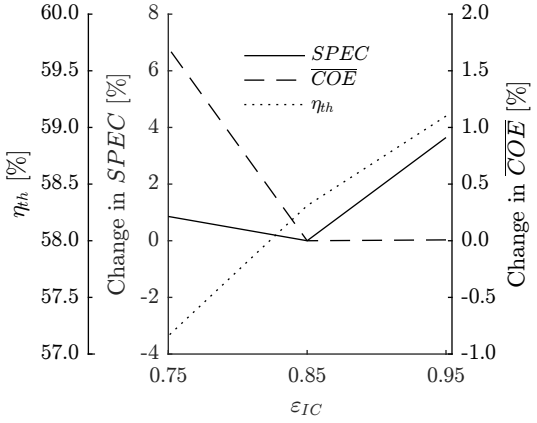

(c) Effect of the intercooler effectiveness

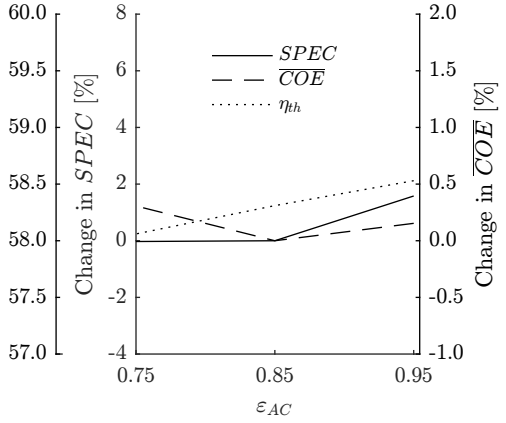

(d) Effect of the aftercooler effectiveness

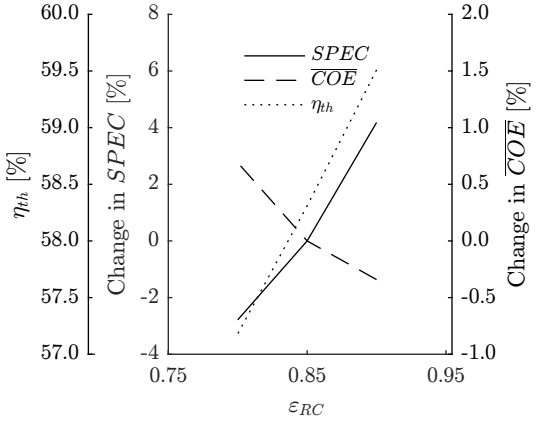

(e) Effect of the recuperator effectiveness

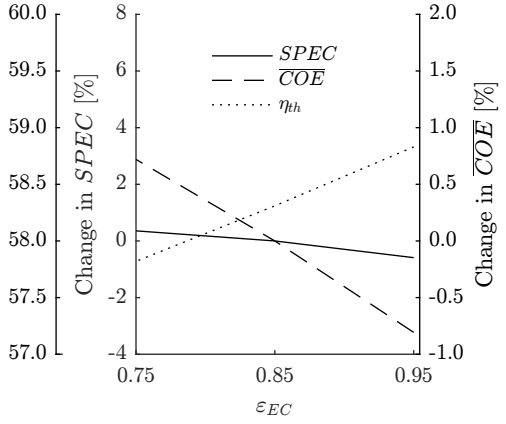

(f) Effect of the economiser effectiveness

FIGURE 5.1: Effect of the cycle design variables on the thermo-economic metrics.

Table 5.4: Reference cycle of the economic design space exploration.

$\boldsymbol{OPR}$	[-]	40
$\boldsymbol{\Delta T_{sp}}$	[K]	10
$\boldsymbol{\varepsilon_{IC}}$	[-]	0.85
$\boldsymbol{\varepsilon_{AC}}$	[-]	0.85
$\boldsymbol{\varepsilon_{RC}}$	[-]	0.85
$\boldsymbol{\varepsilon_{EC}}$	[-]	0.85
$\boldsymbol{\eta_{th}}$	[%]	58.31
$\boldsymbol{SPEC}$	[$/kW]	335.03
$\boldsymbol{\overline{COE}}$	[c$/kWh]	6.85

Reducing the OPR from 40 to 30 cuts the thermal efficiency 0.77 pp, as shown in Figure 5.1a. In addition of worsening the thermodynamic performance of the cycle, the drop of the OPR involves a 2.4% increment in the $SPEC$. As the OPR drops, the components become bulkier to accommodate the larger mass flow. Therefore, the drop in the thermal efficiency together with the increment of the $SPEC$ yield to a rise in the $\overline{COE}$ of a 1.63%.

When the pinch point of the saturator is changed, the variation of the cost of the electricity is primarily driven by the modification of the thermal efficiency, since the $SPEC$ is barely altered (Figure 5.1b). For an increment of 5 K, the thermal efficiency drops 0.35 pp and the $SPEC$ rises a 0.3%, which leads to a 0.5% increase of the $\overline{COE}$. The lower humidification capabilities produced by the rise of the pinch point temperature permit to reinject a lower amount of low-quality heat into the system. This finally increases the heat dumped into the atmosphere, reducing the thermal efficiency.

Figure 5.1c shows that the reduction of the intercooler's effectiveness from 0.85 to 0.75 increases the average cost of electricity by 1.6%. The effectiveness reduction has a small influence on the $SPEC$, which only increases a 0.9%. However, a notable penalty on the thermal efficiency is imposed, which drops by approximately 1 pp. Poor air humidification and the higher required compression work promoted by the less effective intercooling reduces the specific power of the plant causing an increase in size. Therefore, the lower acquisition cost of the less effective intercooler is compensated by the higher price of the rest of the units which slightly increases the $SPEC$. On the other hand, an intercooler's effectiveness of 0.95 drives the system to more efficient but also higher $SPEC$ configurations which effectively cancel each other out leaving the average cost of electricity almost unaffected.

The aftercooler unit shows broadly a similar behaviour as the intercooler (Figure 5.1d). However, the changes in $SPEC$ and thermal efficiency triggered by the increase in effectiveness are found to have a secondary effect on the predicted $\overline{COE}$. The average cost of the electricity only rises a 0.3% when the effectiveness drops from 0.85 to 0.75, and a 0.15% when the effectiveness rises from 0.85 to 0.95.

A 5 pp reduction in the recuperator's effectiveness (0.8 from 0.85, Figure 5.1e) entails a 0.7% increase in the predicted $\overline{COE}$ due to the associated penalties in thermal efficiency (-1.12 pp), which are not compensated by the 2.8% $SPEC$ reduction. The reason behind the thermal efficiency deterioration is the reduced capacity of the system to exploit the waste heat that raises the humidity for the cycle. For a 5 pp increase in the recuperator's effectiveness (0.9 from 0.85), the thermal efficiency gain (+1.18 pp) out-competes the 4% increase in $SPEC$ yielding to 0.4% reduction in the $\overline{COE}$.

The increment of the economiser's effectiveness is found to drive the cost of the electricity towards lower values (Figure 5.1f). Changing the effectiveness from 0.75 to 0.95 makes the cost drop from a +0.8% to a -0.7% compared to the reference value. This change is mainly driven by the rise in the thermal efficiency (1 pp), since the $SPEC$ barely decreases a 0.8% in total. Making the economiser more effective permits to increase the low-quality heat recovered and consequently evaporate a larger amount of water within in the saturator. The boost in the specific power reduces the size off all the components, which cost reduction cannot be overcompensated by the more expensive economiser.

The analysis shows that the OPR, the saturator, the recuperator, and the economiser primarily drive the cost metrics of the power plant, while the intercooler has a big impact only for low effectiveness values. From this design space exploration the cost optimum configuration can be identified which features an overall pressure ratio of 40, a saturator pinch point of 5 K, an intercooler's and aftercooler's effectiveness of 0.85, an economiser's effectiveness 0.95, and a recuperator's effectiveness 0.90, as presented in Table 5.5. The identified values of design variables that produce the cost optimum configuration balance the capacity of the cycle to recuperate heat directly against its capacity to exploit unrecuperated waste heat to raise humidity. Overall, increasing the value of the design variables has a positive effect on the thermal efficiency and the $\overline{COE}$. This makes the cycle very appealing from an emissions point of view since the most economic configuration is among the one with lowest emissions.

TABLE 5.5: Configuration of the cycle design variables for minimum cost of electricity.

$\boldsymbol{OPR}$	[-]	40
$\boldsymbol{\Delta T_{sp}}$	[K]	5
$\boldsymbol{\varepsilon_{IC}}$	[-]	0.85
$\boldsymbol{\varepsilon_{AC}}$	[-]	0.85
$\boldsymbol{\varepsilon_{RC}}$	[-]	0.90
$\boldsymbol{\varepsilon_{EC}}$	[-]	0.95
$\boldsymbol{\eta_{th}}$	[%]	60.33
$\boldsymbol{SPEC}$	[$/kW]	345.33
$\boldsymbol{\overline{COE}}$	[c$/kWh]	6.74

5.3 Effect of cycle performance degradation

The performance of the power plants degrades over their lifetime due to the deterioration of the components. The main causes of this deterioration are fouling and erosion of the heat exchangers (which reduces their effectiveness and increases the pressure losses), and fouling, erosion and corrosion of the turbomachinery (which reduces the pressure ratio, increases the pressure losses, and reduces the mass flow).

To analyse the impact of the degradation on the economic metrics of the cycle, the clean performance of the cycle configuration represented in Table 5.5 is compared against two scenarios with different degradation levels. The degradation is imposed as a penalty on the thermal efficiency by means of multiplying the design value by a coefficient. It is assumed that the degradation increases linearly from 0% at the year 1, up to the maximum imposed value at the end of the book life. It is also assumed that the power plant is operated to always provide the design power output (40 MW). Based on the results obtained in Chapter 6, two different scenarios have been simulated: no degradation, 5% and 10% thermal efficiency reduction at the end of the book life. The objective is to observe the variation of the COE across a range of different degradation levels in order to predict future scenarios (where the actual degradation rates are known).

The outcomes of this comparison are shown in Figure 5.2. The solid line represents the metrics of the clean power plant, whereas the dashed line represents the metrics of the two degraded cases simulated. The evolution of the thermal efficiency for

the different scenarios is shown in Figure 5.2a, whereas the evolution of the COE is depicted in Figure 5.2b.

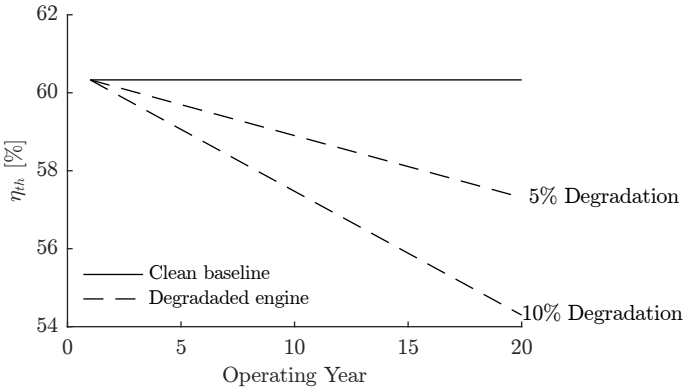

(a) Degradation of the thermal efficiency

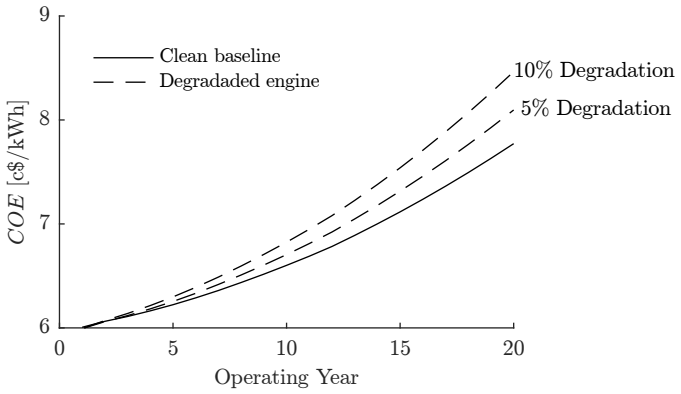

(b) Effect on the cost of electricity

FIGURE 5.2: Effect of the progressive performance degradation of the power plant on the cost of the electricity.

As shown in Figure 5.2b, the COE increases annually as a consequence of the inflation in the price of the fuel. However, the increment in the case of the degraded power plants is more significant due to the necessity of burning a larger amount of fuel to continue achieving a power output of 40 MW. The difference between the COE of the clean power plant and the COE of the degraded power plants increases each year a 0.21% for the 5% degradation scenario, and a 0.42% for the 10% degradation scenarios respectively.

If the loss in efficiency is taken into consideration from the beginning, it is possible to foresee the gradual increment in the COE and impose a constant $\overline{COE}$ which would take into account the loss in thermal efficiency. The average cost would be higher than the yearly cost at the beginning of the book life. However, in the final

period, the average cost becomes considerably cheaper than the yearly cost. The values are represented in Table 5.6. It is observed that the $\overline{COE}$ linearly rises a 2.1% for each 5% of thermal efficiency degradation.

TABLE 5.6: Impact of the engine degradation on the average cost of the electricity.

Scenario	$\overline{\boldsymbol{COE}}$ [c$/kWh]	**Change** [%]
Clean baseline	6.74	0.0
5% degradation	6.88	+2.1
10% degradation	7.02	+4.2

It is concluded that the degradation of the thermal efficiency of the power plant can lead to a significant increment of the COE, which can grow up to 4.3% and 9.1% at the last year of the book life for 5% and 10% degradation respectively. However, if the penalisation is foreseen to happen at the beginning and a $\overline{COE}$ is fixed, the penalisation is constant along the whole life of the power plant, and considerably lower than the one obtained at the last years if a varying COE.

5.4 Uncertainty analysis

The total annual expenses of the power plant operation depends on four key parameters: (i) fuel costs, (ii) purchase equipment costs (PEC), (iii) interest rates over the loan period to pay off the initial investment, and (iv) Operation and Maintenance (OM) costs. The nature of these cost elements is associated with an implicit uncertainty. Fuel prices may undergo severe fluctuations over time following global financial trends. Purchase cost estimates rely on correlations derived statistically from public domain data with an implicit standard deviation. The assumed interest rates may change significantly depending on the risk of the economic project, which is declared by the investor and heavily influenced by the current financial conditions. Finally, the OM costs can vary across a wide range depending on the technology level of the equipment installed, the location of the power plant, operation mode, ambient conditions as well as other unforeseen circumstances which need to be accounted for as contingency.

According to the above considerations, an imposed variation, across a range between -20% to +20%, is applied to each of the four parameters over the lifetime of

the plant. This study aims to assess the sensitivity of the average cost of electricity on these cost drivers. The selected uncertainty range is based on the expected error ranges derived from the calculation methods shown by Traverso et al. [103] and Bejan et al. [120], which justifies that such a range is representative for the type of cost studies presented herein. The cycle configuration shown in Table 5.5 is used as reference to show the variations of the $\overline{COE}$. The reference values of interest rates, baseline fuel cost, and the OM costs are the presented in Table 5.2, whereas the baseline PEC ($13,813,200) is derived from the $SPEC$ shown in Table 5.5.

Figure 5.3 shows the impact of the four parameters analysed on the $\overline{COE}$. The fuel cost is found to have the strongest influence on the $\overline{COE}$, showing a change of 0.70% for each percentage point variation of the cost of the fuel. The PEC uncertainty causes small changes on the $\overline{COE}$, of the order of 0.28% for each PEC percentage point variation. Variations in the OM costs or the interest rates of the debts have minor importance, producing changes of only 0.08% per percent variation. Looking at the breakdown of the total expenses of the baseline case, the fuel costs represent the 69% of them, the costs based on the PEC the 18%, and the OM and interest rates based costs 8% and 5% respectively. Thus, it is concluded that the larger the contribution to the total expenses of these costs, the higher the impact on the $\overline{COE}$. The analysis reveals a linear correlation between any of the four cost drivers and the $\overline{COE}$. Therefore, such a study enables calculating the impact of larger fluctuations of any of the four cost drivers by extrapolation using the data presented herein as reference.

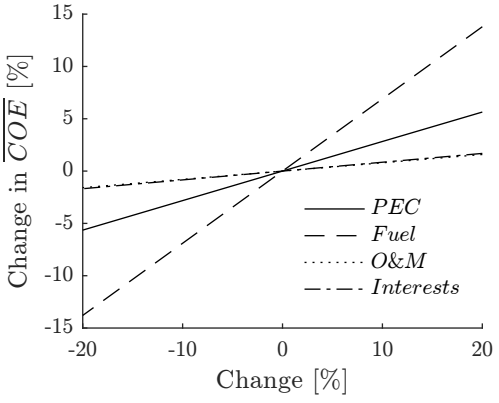

FIGURE 5.3: Cost of the electricity sensitivities in the cost drivers for the most cost efficient configuration.

The tile-plot shown in Figure 5.4 identifies the exchange rates rates between all cost drivers across the design space and the $\overline{COE}$. On each sub-plot, the x-

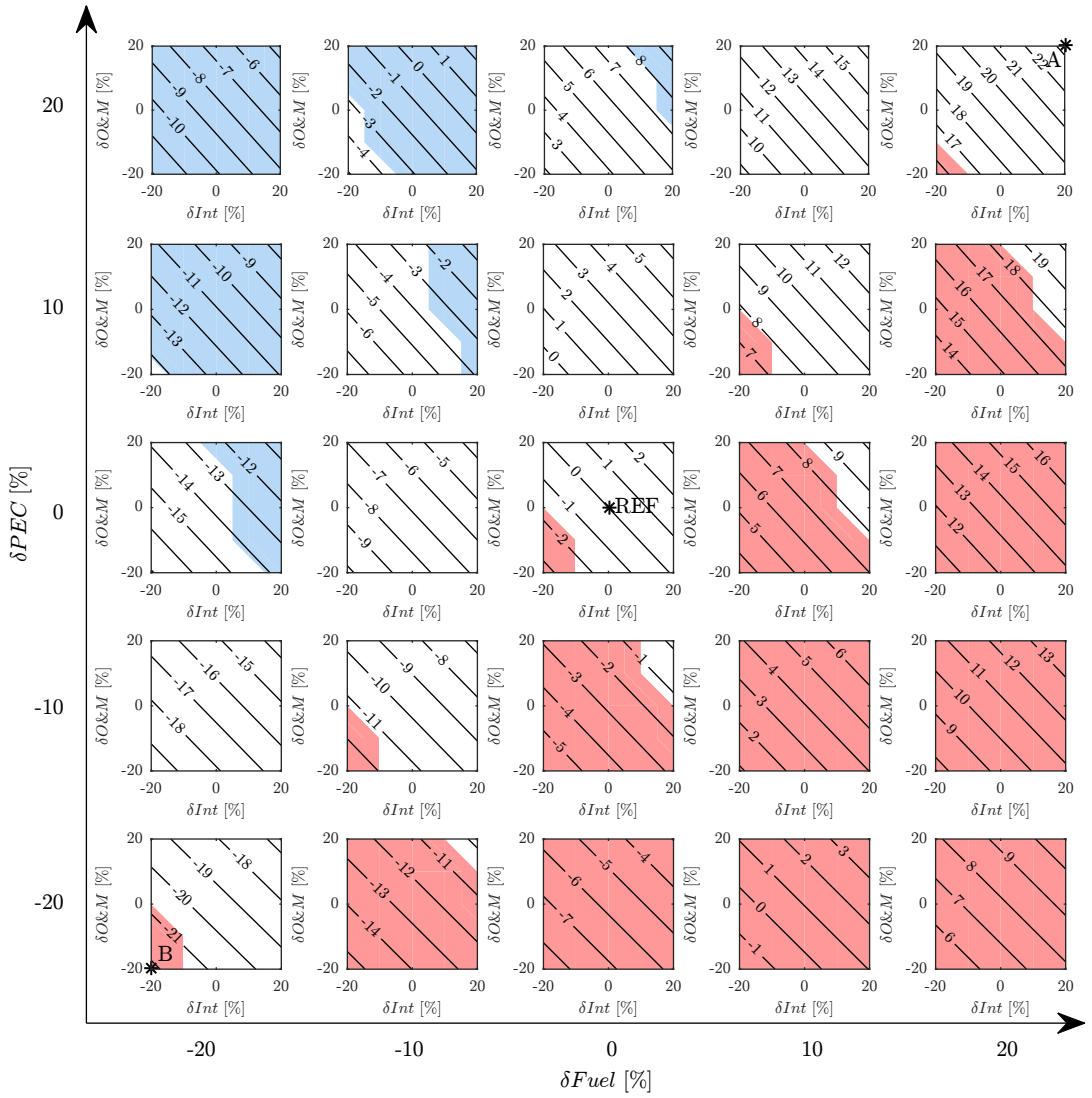

FIGURE 5.4: Percentage variation of the average cost of the electricity for the full sensitivity analysis.
Cost optimum configuration in blue region ε_{IC}=0.85, ε_{RC}=0.85,.
Cost optimum configuration in blank region ε_{IC}=0.85, ε_{RC}=0.90.
Cost optimum configuration in red region ε_{IC}=0.95, ε_{RC}=0.90.
Rest of design variables as in Table 5.5.

axis represents the percentage variation of the interest rates, and the y-axis the percentage variation of the OM costs from the reference values (Table 5.2). Fuel cost variation from nominal values is shown in the major x-axis, while uncertainty in PEC is shown in the major y-axis. The contour lines represent the percentage $\overline{COE}$ departure from the reference value (Table 5.5).

The most pessimistic scenario, whereby the variation of the four parameters is +20% with regards to their reference values, is represented by Point A in Figure 5.4. In that case, $\overline{COE}$ is estimated to be around 23% higher with respect to the baseline case (point REF in Figure 5.4). The most optimistic scenario, where the variation for the four parameters is -20% in relation to their baseline values, is represented by point B (bottom left corner in Figure 5.4). This scenario shows a $\overline{COE}$ reduced by 22% compared to the baseline case (point REF in Figure 5.4). In addition, as the PEC decreases, the dependency of the $\overline{COE}$ on the change in interest rates and in the OM cost variations diminishes. The reason being that these two parameters show a strong dependence on the purchasing costs.

Figure 5.4 also identifies the dependency of the optimum cycle design parameters on the variation of the four costs drivers analysed herein. There are three distinct optimum configurations for the range studied. On each one of these regions, the effectiveness of the intercooler and the recuperator are traded depending on the imposed variations. Within the blank part, the baseline configuration (Table 5.5, ε_{IC}=0.85, ε_{RC}=0.90) is identified as the most economic configuration. Within the blue zone, the configuration minimising the $\overline{COE}$ features a recuperator effectiveness of 0.85 instead of 0.90 (ε_{IC}=0.85, ε_{RC}=0.85). Last, in the red region, a "high technology" level system seems to be the most economic option, with an intercooler effectiveness of 0.95 instead of 0.85 (ε_{IC}=0.95, ε_{RC}=0.90).

The frontier between the different optimum design regions is set by the percentage contribution of the fuel cost to the total expenses, as it is demonstrated in Figure 5.5. The figure depicts the percentage contribution of the fuel costs to the total expenses. The border between the red region (high "technology level") and the blank region is set for a fuel's relative cost of around 70%, and the border between the blank and the blue region (low "technology level") for a fuel's relative cost of around 65%. Therefore, as the fuel's relative cost decreases, it becomes more economic to trade the "technology level" (therefore, the thermal efficiency), in exchange for a less expensive power plant.

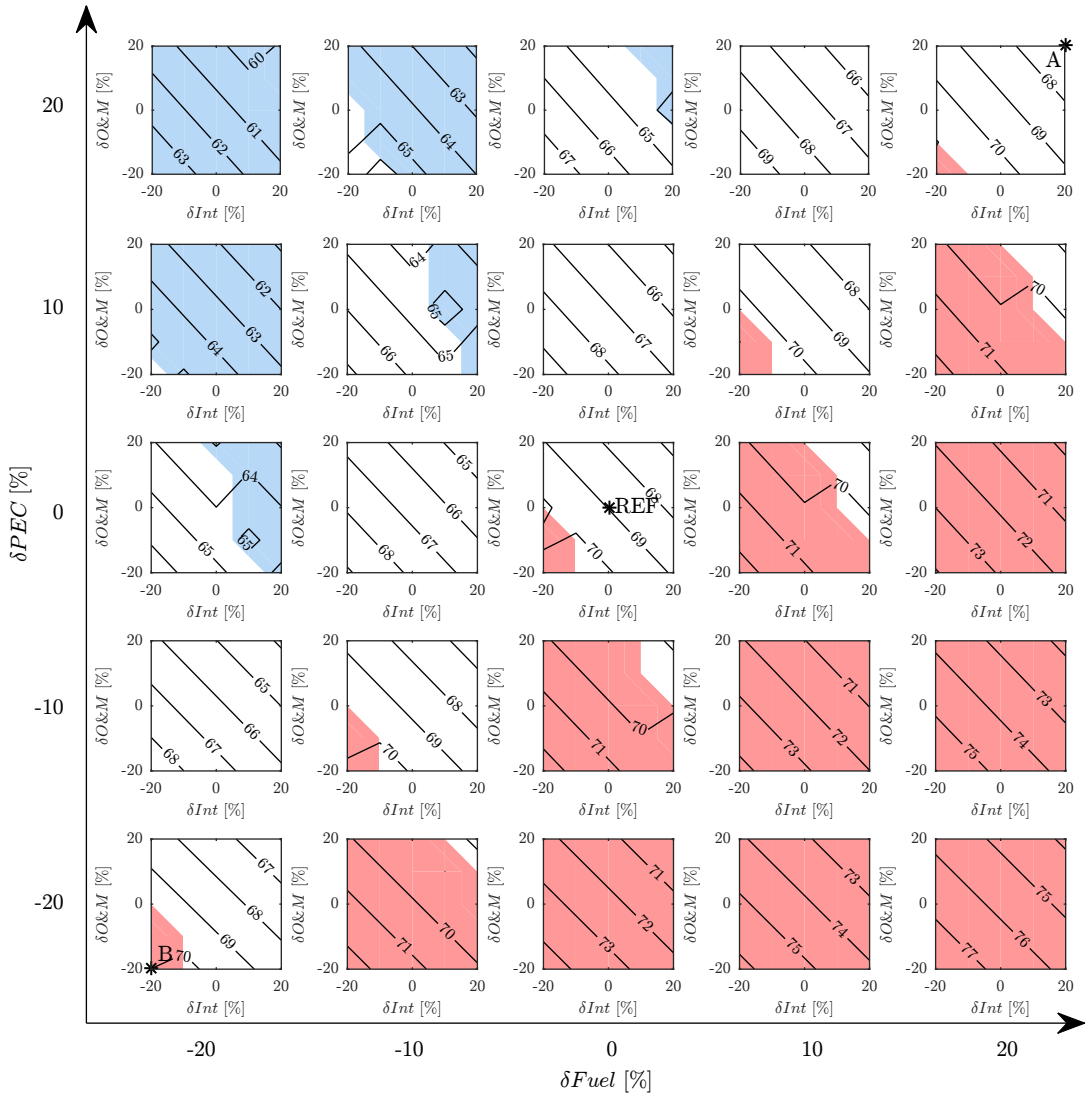

FIGURE 5.5: Percentage contribution of the fuel cost to the total expenses for the full sensitivity analysis.
Cost optimum configuration in blue region ε_{IC}=0.85, ε_{RC}=0.85,.
Cost optimum configuration in blank region ε_{IC}=0.85, ε_{RC}=0.90.
Cost optimum configuration in red region ε_{IC}=0.95, ε_{RC}=0.90.
Rest of design variables as in Table 5.5.

5.5 Comparison against other advanced cycles

Although the RHAT cycle has demonstrated to present a promising thermo-economic performance, it is necessary to analyse the metrics in a reference frame to fully prove its capacity. In Table 5.7 the RHAT configuration shown in Table 5.5 is compared against the cost metrics of humid cycles previously reported by Kavanagh and Parks [30], and Traverso and Massardo [31]. A CCGT cycle [30] is also included for reference. The cost metrics of the current RHAT system are recalculated under the assumptions of previous studies (Kavanagh et al. [30], Traverso and Massardo [31]). These models are presented in Appendix C.

TABLE 5.7: Comparison of optimum reheated humid air turbine (Table 5.5) economic performance against previously reported advanced cycles.

Cycle	η_{th} [%]		$SPEC$ [$/kW]		$\overline{COE}$ [c$/kWh]	
	Ref.	RHAT	Ref.	RHAT	Ref.	RHAT
Steam injected cycle [30]	49.36	+22.2%	323	-14.9%	6.85	-26.4%
Gas-steam combined cycle [30]	53.00	+13.8%	720	-61.8%	6.85	-28.0%
Humid air turbine [30]	52.26	+15.4%	300	-8.3%	6.48	-22.2%
TOP Humid air turbine [30]	54.12	+11.5%	187	+47%	6.00	-16.0%
Humid air turbine [31]	51.74	+16.6%	n/a	n/a	4.21	-5.5%
Humid air water injected turbine [31]	50.04	+20.6%	n/a	n/a	4.07	-2.2%

Table 5.7 shows that the RHAT system features a 62% lower predicted cost of investment than an equivalent CCGT. As a result, the average cost of electricity ($\overline{COE}$) is reduced by 28%, also due to the RHAT's 14% higher thermal efficiency. Comparing against previous humid cycles, it is observed that the RHAT cycle features a 15% and roughly 8.5% lower $SPEC$ than STIG and simpler HAT cycles respectively (Kavanagh and Parks [30]). The lower $SPEC$ is a consequence of the higher specific power achieved by the RHAT (130% compared with the STIG and 38% compared with the HAT), as it reaches higher humidification ratios. As such, despite the second combustion chamber and the requirement for advanced materials, the reduction in the size of all the components (consequence of the higher specific power) enables a cost reduction that out-competes the above-mentioned

drawbacks. Nevertheless, the reduction is not sufficiently large to achieve a lower $SPEC$ than the TOP HAT [30], which does not require the intercooler, the aftercooler, neither the humidifier.

From Table 5.7 is also observed that the RHAT cycle outcompetes the other candidates in terms of thermal efficiency due to its increased capacity to exploit waste heat and introduce humidity into the cycle, as well as reduce the eergy losses in the combustion chamber. Finally, the enhanced thermal efficiency and the low purchasing costs of the RHAT system yield to a notably lower estimated average cost of electricity against the competitor systems with the $\overline{COE}$ reductions ranging from -28% against the CCGT plant [30] to roughly -2% against the humid air water injected system shown in [31].

5.6 Summary

In this chapter, a thermo-economic analysis of a reheated humid air turbine system is conducted across the whole design envelope and the most economic configuration is compared against previously developed advanced gas turbine based power plants. Lifecycle cost analysis showed that the average cost of electricity is primarily driven by the overall pressure ratio, the humidifier pinch point, and the effectiveness of the recuperator and economiser. These four design parameters have the common characteristic of reducing the cost of the electricity as their "technology level" increases. In addition, the most economic configuration with an OPR of 40, a ΔT_{sp} of 5 K, a ε_{IC} and ε_{AC} of 0.85, a ε_{RC} of 0.90, and a ε_{EC} of 0.95 presents a $\overline{COE}$ of 6.74 c$/kWh. Moreover, degradation of the power plant thermal efficiency can yield to a 4.2% penalisation in the $\overline{COE}$ if a 10% efficiency degradation at end of the book life is imposed.

The uncertainty study showed that possible variations in fuel costs and the uncertainty of the purchased equipment cost are the main parameters driving the fluctuations in the average cost of the electricity. The cost of the electricity increases by 0.70% per percentage point of fuel price increase, and by 0.28% per percentage point rise in purchase equipment cost. In addition, it is has been illustrated the dependency of the optimum cycle design parameters on the variation of the four costs drivers. The frontier between the optimum design is set by the percentage contribution of the fuel cost to the total expenses. Beyond a 70% it is necessary

to increase ε_{IC} to obtain the most economic configuration, whereas below a 65% it is required to reduce ε_{RC} to obtain the most economic configuration.

Last, comparisons against previously reported studies on combined and humid cycles show that the reheated humid air turbine features 61.8% lower purchasing costs than a typical CCGT and 8.3% less expensive than a HAT. Moreover, due to its high efficiency (60.31%, approximately 14% higher than a reference combined cycle and 10%-20% more efficient than other versions of the humid air turbine), the estimated average costs of electricity are 28% lower than these of CCGT system and 2%-22% than these of the of humid cycles. Therefore, the RHAT not only shows a better thermo-economic performance than CCGTs, but also stands as the best option among the humid cycles.

This chapter has covered the objective of evaluating the economic performance of the cycle across its design envelope. In addition, the reheated humid air turbine has also been compared against previously developed advanced gas turbine based power plants.

Chapter 6

Component's degradation

Considering an open loop for the water systems makes the air-water heat exchangers prone to suffer degradation problems since the use of untreated water is known to produce issues such as fouling, especially for marine applications [84, 123–125]. Therefore, a reduction of the heat exchange capabilities of these devices is expected to happen.

This chapter analyses the impact of the component's degradation on the performance of the cycle. A methodology to simulate the degraded performance of the heat exchangers has been developed and presented herein. The effects of the degradation of the air-water heat exchangers are analysed for three design scenarios of different "technology levels". Moreover, the studies are complemented with addition of the turbomachinery degradation. In addition, the economic and performance effects of designing the air-water heat exchangers with a preset fouling to prevent the degradation penalties is also analysed. Exergy analysis is used to identify the components triggering the performance variations.

6.1 Performance modelling

The off-design performance of the RHAT is simulated using a platform comprising modules that estimate the thermal behaviour of each component of the RHAT system. The performance of the gas turbine and the recuperator is simulated by Turbomatch©, whereas the performance of the intercooler, aftercooler,

economiser, and saturator is calculated by separate subroutines. The flowchart of the model is depicted in Figure 6.1.

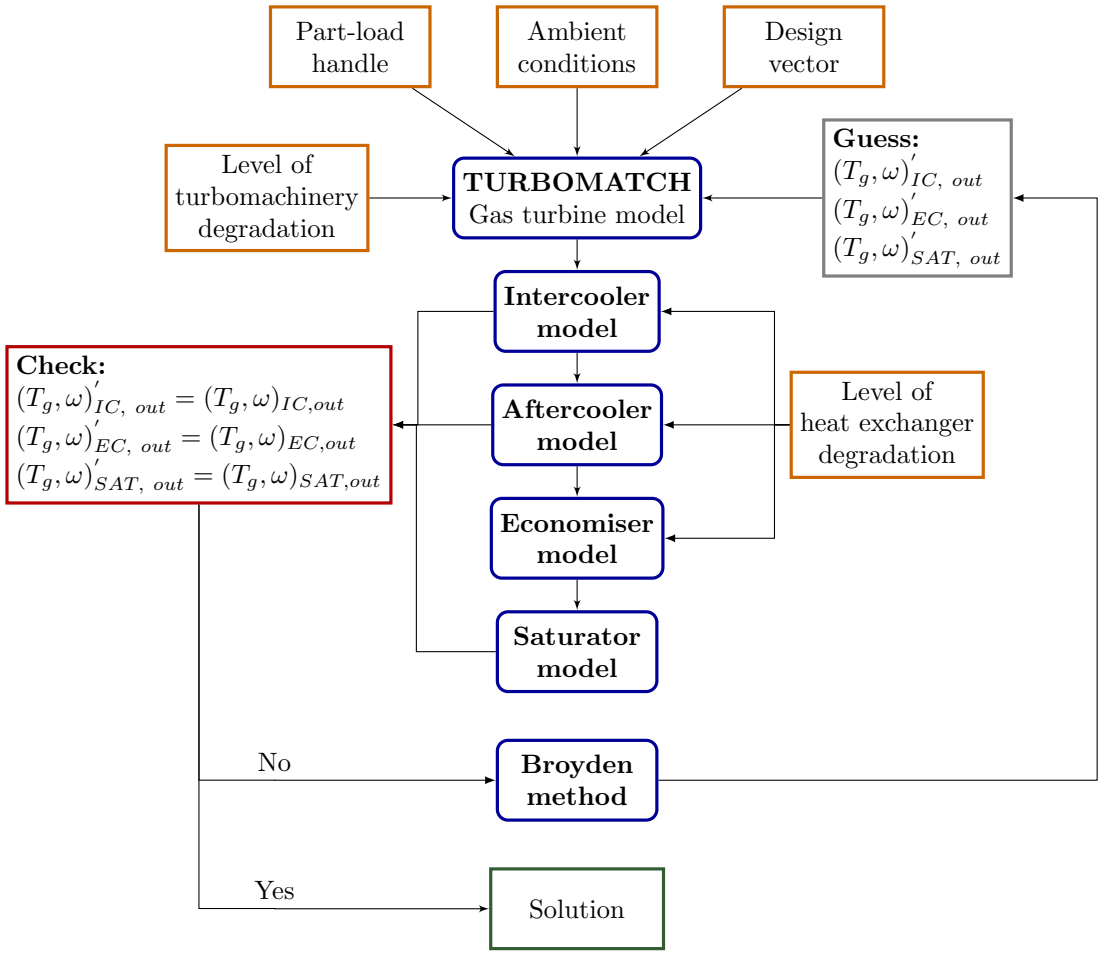

FIGURE 6.1: Flowchart of the reheated humid air turbine cycle off-design simulation methodology.

The required inputs are the design variables of the cycle, the design fouling values of the heat exchangers (in case the heat exchangers consider a preset fouling resistance), and the off-design handles. The off-design handles include the TIT, the ambient conditions, the imposed fouling resistance to be added to the air-water heat exchangers, and the degradtion level of the turbomachinery. To initialise the iterative procedure the temperature and humidity are guessed at the outlet of the intercooler, the economiser, and the saturator are guessed, making possible to run Turbomatch© the first time. The outcomes of Turbomatch© simulation are employed to calculate the performance of the air-water heat exchangers and the saturator. Then, the temperature and the humidity obtained from the calculations are compared against the guessed values. If the discrepancy is larger than the threshold, the guessed values are recalculated using a Broyden method [126]

until convergence is reached. The model assumes that all the components are adiabatic, no mechanical losses, the power turbine is operated at constant rotational speed assuming it is directly connected with the generator, the bypass ratio is kept constant, and the ratio $\dot{m}_g/\dot{m}_w$ of the air-water heat exchangers is kept constant unless $T_{w,out} > T_{sat}$ (in such case, $\dot{m}_w$ would be increased).

6.1.1 Heat exchangers

The degradation of the heat exchangers is simulated by means of the fouling resistance term ($R_{f,tot}$) as defined in Eq. 6.1. $R_{f,tot}$ acts as a resistance that reduces the design overall heat transfer coefficient.

$$\frac{1}{(UA)_f} = \frac{1}{(UA)_{clean}} + R_{f,tot} \tag{6.1}$$

where $(UA)_{clean}$ represents the product of the overall heat transfer coefficient at clean conditions and the heat transfer area, and $(UA)_f$ represents the same product at degraded conditions.

Fouling affects differently each side of the heat exchanegr depending on the fluid [127]. Hence, $R_{f,tot}$ is calculated as the weighted average of the fouling resistance of the air-side and the water-side, where the heat transfer areas (A_{HX}) of each side are employed as the weighting coefficients, as shown in Eq. 6.2 [127].

$$\frac{R_{f,tot}}{A_{HX,tot}} = \frac{R_{f,w}}{A_{HX,w}} + \frac{R_{f,a}}{A_{HX,a}} \tag{6.2}$$

where $R_{f,w}$ and $R_{f,a}$ are the fouling resistance of the water-side and the fouling resistance of the air-side respectively.

When the mass flows on any of both sides of the heat exchanger changes, the velocity of the fluid varies, modifying of the overall heat transfer coefficient. Assuming that the properties of the fluids do not change significantly compared with the design conditions, it is possible to state that the Prandtl and the thermal conductivity stay constant. This permits to calculate the new overall heat transfer by means of the Dittus-Boelter heat transfer correlation, which only uses the variation of the mass flows, as shown in Eq. 6.3. The reference conditions are specified for the performance at design point.

$$UA = (UA)_{Ref} \left(\frac{\dot{m}_w^{0.8} \ \dot{m}_g^{0.8}}{\dot{m}_{w,Ref}^{0.8} \ \dot{m}_{g,Ref}^{0.8}} \right) \left(\frac{\dot{m}_{w,Ref}^{0.8} + \dot{m}_{g,Ref}^{0.8}}{\dot{m}_w^{0.8} + \dot{m}_g^{0.8}} \right) \tag{6.3}$$

Combining Eq. 6.1 and Eq. 6.3 into Eq. 6.4 permits to calculate the off-design performance of the degraded heat exchangers. It is necessary to highlight that the term $R_{f,tot,DP}$ has been added to include the possibility of employing heat exchangers designs that consider a preset fouling resistance.

$$UA = \frac{1}{1/(UA)_{Ref} + (R_{f,tot} - R_{f,tot,DP})} \left(\frac{\dot{m}_w^{0.8} \ \dot{m}_g^{0.8}}{\dot{m}_{w,Ref}^{0.8} \ \dot{m}_{g,Ref}^{0.8}} \right) \left(\frac{\dot{m}_{w,Ref}^{0.8} + \dot{m}_{g,Ref}^{0.8}}{\dot{m}_w^{0.8} + \dot{m}_g^{0.8}} \right) \tag{6.4}$$

Once the UA is known, ε is calculated using the $\varepsilon - NTU$ method proposed by Kays and London [90] by means of Eq. 6.5, in the assumption that the air-water heat exchangers present a counter-flow configuration.

$$\varepsilon = \frac{1 - \exp[-NTU(1 - C^*)]}{1 - C^* \ \exp[-NTU(1 - C^*)]} \tag{6.5}$$

$NTU = UA/C_{\min}$ is the number of transfer units, and $C^* = C_{\min}/C_{\max}$ is the heat capacity ratio of the heat exchanger. The new value of the effectiveness permits to calculate the outlet temperatures of both streams ($\varepsilon = \dot{Q}/\dot{Q}_{\max}$).

The pressure losses (ΔP) of the air-side is estimated using a modified version of the correlation suggested by Walsh and Fletcher [97].

$$\frac{\Delta P}{P_{in}} = \kappa \left(\frac{\dot{m}_{in} \ \sqrt{T_{in}}}{P_{in}} \right)^2 \Delta P_f \tag{6.6}$$

κ is a coefficient, whose value is calculated using the design point, $\dot{m}_{in}$, T_{in} and P_{in} are the inlet mass flow, temperature and pressure respectively, and ΔP_f is a coefficient to include the penalisation due to fouling ($\Delta P_f \geq 1$).

The pressure losses of the water-side are calculated using Eq. 6.7. L_{flow} represents the length of the flow passage and ρ the density. The estimation of the friction factor (f) the mass flux ($\dot{G}$) and the hydraulic diameter at clean conditions ($D_{h|clean}$) are specified in Section A.2. The degraded hydraulic diameter (D_h) is estimated

considering the thickness of the fouling film (t_{film}) and the hydraulic diameter at clean conditions using Eq. 6.8.

$$\Delta P = \frac{4\ f\ L_{flow}\ \dot{G}^2}{2\ \rho\ D_h} \tag{6.7}$$

$$D_h = D_{h|clean} - 2t_{film} \tag{6.8}$$

The thickness of the film is estimated with the thermal conductivity of the film (k_{film}) and $R_{f,w}$, as presented in Eq. 6.9 [128]. Because the biofilm mass is mainly water (90%-99%), k_{film} can be considered equal to that of the water [128].

$$t_{film} = R_{f,w}\ k_{film} \tag{6.9}$$

6.1.2 Saturator

The off-design performance of the saturator is estimated using the model presented in Appendix A.1, based on the work presented by Aramayo-Prudencio and Young [69]. If the geometry of the tower is known and the inlet thermodynamic conditions of the gas and water are declared, the model is able to calculate the outlet conditions of both streams. For estimating the performance of the tower, the models divides the saturator in sections of constant height and solves the energy and mass balance equations in each section.

6.1.3 Gas turbine

The off-design performance of the gas turbine and the recuperator is calculated using Turbomatch©. The characteristics of the different components of the turbomachinery are defined by maps. Therefore, the off-design values depend on the new equilibrium operating point. Firstly it performs an initial simulation to scale the maps of the different components to match the design point specifications such as pressure ratios, efficiency, mass flows, etc. The new steady state performance is calculated by means of an iterative procedure based on the defined maps of the

different components. The guesses and checks of the model are well described by Pellegrini et al. [115].

6.2 Exergy analysis model

Exergy analysis has been previously used to conduct performance studies of advanced cycles for aero-engines or land-based applications as well as humid air turbines [54, 55, 129, 130] at design point and part-load operating conditions [131, 132]. The key outcome of an exergy analysis is the identification of the inefficiency sources within a complex system that penalise its overall thermal performance. For this study, an exergy analysis is conducted to further quantify the effect of the heat exchanger degradation on the cycle performance.

The key assumptions made include steady flow, adiabatic components, no changes in kinetic or potential exergy and ideal mixture of gases. A reference temperature of 288.15 K is assumed while reference partial pressures are evaluated at 1 atm and relative humidity of 80%. With these assumptions, the exergy destruction in a component is calculated by the balance defined in Eq. 6.10.

$$\dot{E}x_{heat} - \dot{E}x_{work} + \dot{E}x_{mass,in} - \dot{E}x_{mass,out} = \dot{E}x_{dest} \tag{6.10}$$

$$\begin{aligned} \dot{E}x_{heat} &= \sum \left(1 - \frac{T_{Ref}}{T_k}\right) \dot{Q}_k \\ \dot{E}x_{work} &= \dot{W} \\ \dot{E}x_{mass,in} &= \sum \left(\dot{m}\ \psi\right)_{in} \\ \dot{E}x_{mass,out} &= \sum \left(\dot{m}\ \psi\right)_{out} \end{aligned} \tag{6.11}$$

$\dot{E}x_{heat}$ represents the exergy transferred by the heat $\dot{Q}_k$ from a source at temperature T_k. $\dot{E}x_{work}$ is the exergy transferred by work $\dot{W}$ delivered by the system. $\dot{E}x_{mass}$ stands for the exergy transferred by the mass $\dot{m}$, where ψ is the specific flow exergy defined as in Eq. 6.12 for the gas and as in Eq. 6.13 for the water. Last, $\dot{E}x_{dest}$ is the exergy destroyed within the component.

$$\psi_g = [(h - h_{Ref}) - T_{Ref}(s - s_{Ref})]_a + \omega\,[(h - h_{Ref}) - T_{Ref}(s - s_{Ref})]_w \quad (6.12)$$

$$\psi_w = [(h - h_{Ref}) - T_{Ref}(s - s_{Ref})]_w \quad (6.13)$$

h is the specific enthalpy, s the specific entropy, ω the water to air ratio, the subscript Ref indicates properties at the reference conditions, the subscript g refers to the gas or humid air, the subscript a refers to the dry gas, and the subscript w refers to the water. When calculating the flow exergy, the properties are evaluated at their partial pressures.

The destroyed exergy within each component and the outlet exergy rejected to the atmosphere are normalised using the exergy of the incoming fuel, as in Eq. 6.14.

$$\widehat{\dot{E}x_{dest,x}} = \frac{\dot{E}x_{dest,x}}{\dot{E}x_{in,fuel}} \quad (6.14)$$

With the previous assumptions, the exergy balance of the cycle can be calculated using the following equations for each component.

Compressors

$$\dot{E}x_{dest,comp} = \dot{W}_{comp} + (\dot{m}_g\ \psi_g)_{in} - (\dot{m}_g\ \psi_g)_{out} \quad (6.15)$$

Combustion chambers

$$\dot{E}x_{dest,CC} = (\dot{m}_{fuel}\ \psi_{fuel})_{in} + (\dot{m}_g\ \psi_g)_{in} - (\dot{m}_g\ \psi_g)_{out} \quad (6.16)$$

The exergy of the fuel is composed of the physical exergy and the chemical exergy (Eq. 6.17). Nevertheless, the physical exergy of the fuel can be neglected when compared to the chemical. LHV represents the low heating value, H the hydrogen atomic fraction, C the carbon atomic fraction. For this study, the chemical composition of the marine diesel is assumed to be a standard diesel $C_{12}H_{23}$ [133], and the natural gas CH_4.

$$\psi_{fuel} = LHV(1.033 + 0.0169\ H/C - 0.0698\ 1/C) \tag{6.17}$$

Turbines

$$\dot{E}x_{dest,turb} = -\dot{W}_{turb} + (\dot{m}_g\ \psi_g)_{in} - (\dot{m}_g\ \psi_g)_{out} \tag{6.18}$$

Air-air heat exchanger

$$\dot{E}x_{dest,AAHX} = (\dot{m}_g\ \psi_g)_{h,in} + (\dot{m}_g\ \psi_g)_{c,in} - (\dot{m}_g\ \psi_g)_{h,out} - (\dot{m}_g\ \psi_g)_{c,out} \tag{6.19}$$

Air-water heat exchangers

$$\dot{E}x_{dest,AWHX} = (\dot{m}_g\ \psi_g)_{in} + (\dot{m}_w\ \psi_w)_{in} - (\dot{m}_g\ \psi_g)_{out} - (\dot{m}_w\ \psi_w)_{out} - (\dot{m}_{cond}\ \psi_w)_{out} \tag{6.20}$$

The term $(\dot{m}_{cond}\ \psi_w)_{out}$ is added in order to include exergy of the possible water condensed from the moist in the air during the cooling process.

Saturator

$$\dot{E}x_{dest,SAT} = (\dot{m}_g\ \psi_g)_{in} + (\dot{m}_w\ \psi_w)_{in} - (\dot{m}_g\ \psi_g)_{out} - (\dot{m}_w\ \psi_w)_{out} \tag{6.21}$$

Exhaust

The exergy rejected into the atmosphere, defined as the sum of the exergy of the gas flow going out the economiser and the water flow going out of the saturator, as shown in Eq. 6.22.

$$\dot{E}x_{dest,OUT} = (\dot{m}_g\ \psi_g)_{EC,out} + (\dot{m}_w\ \psi_w)_{SAT,out} \tag{6.22}$$

6.3 Cases analysed

The effectiveness, selected as the parameter to represent the "technology level", of the air-water heat exchangers is varied in order to study how the performance degradation penalties are affected by the "technology level" of these components. The rest of the design parameters of the cycle are kept constant. The design scenarios herein analysed are presented in Table 6.1. The effectiveness of the three air-water heat exchangers is varied simultaneously, leading to three scenarios: high effectiveness design scenario (0.95), average effectiveness design scenario (0.85), and low effectiveness design scenario (0.75).

TABLE 6.1: Design envelop analysed.

Fixed cycle design parameters		**Scenarios analysed**	
OPR	40	$\varepsilon_{IC}, \varepsilon_{AC}, \varepsilon_{EC}$	0.95
ΔT_{sp}	5 K	$\varepsilon_{IC}, \varepsilon_{AC}, \varepsilon_{EC}$	0.85
ε_{RC}	0.90	$\varepsilon_{IC}, \varepsilon_{AC}, \varepsilon_{EC}$	0.75

For the first study, *degraded performance*, no fouling is considered during the design process of the heat exchangers. The performance of the air-water heat exchanger is parametrically degraded by increasing the fouling resistance on the airside and waterside side respectively, and the pressure drop coefficient. The level of deterioration is characterised defined by the Degradation Coefficient (DC), defined in Eq. 6.23. The fouling resistance of both sides and the pressure drop penalty coefficient are normalised against reference values [106, 134–136], showed in Table 6.2. In the absence of any experimental data of marine fouling in plate-fin heat exchangers, the water-side fouling resistances are taking from the standards of the tubular exchanger manufacturers association [134], which might overestimate the penalties.

The different terms in Eq. 6.23 imply that the normalised air-side fouling, water-side fouling, and the pressure drop penalty coefficient are varied simultaneously. They all have the same value imposed by DC. The imposed DC ranges from 0 to 2, which drives the cycle at off-design while keeping a constant turbine inlet temperature of 1600 K in both combustors.

$$DC \equiv \frac{R_{f,a}}{(R_{f,a})_{Ref}} = \frac{R_{f,w}}{(R_{f,w})_{Ref}} = \frac{\Delta P_f}{(\Delta P_f)_{Ref}} = [0-2] \tag{6.23}$$

TABLE 6.2: Reference fouling values.

Intercooler Aftercooler	R_f, [m^2 K/W]	ΔP_f
Water	0.000 200 [134]	Calculated based on the thickness of the film.
Air	0.000 176 [106]	32% [135]
Economiser	R_f, [m^2 K/W]	ΔP_f
Water	0.000 200 [134]	Calculated based on the thickness of the film.
Air	0.000 176 [106]	20% [136]

In addition, the effect of the turbomachinery degradation is added on top of the degradation of the three air-water heat exchangers to observe the total penalisation on the performance produced by a full deterioration of the cycle's components. Two types of degradation are analysed herein: component fouling, and component erosion [137–139]. Component fouling translates into the degradation of the flow capacity and the efficiency caused by adherence of contaminants to the gas turbine surfaces. Component erosion is defined as the wearing away of airfoils and seals surfaces by hard particles in the has path. Erosion yields to degradation of the efficiency and degradation of the compressor inlet mass flow, whereas the flow capacity of the turbine increases. The scenarios analysed are presented in Table 6.3 [140]. The studies are performed for the average effectiveness cycle design (Table 6.1).

TABLE 6.3: Levels analysed of turbomachinery degradation.

		Fouling		**Erosion**	
		2.50%	**5.0%**	**2.50%**	**5.0%**
Compressors	Flow capacity	-2.50%	-5.0%	-2.50%	-5.0%
	Efficiency	-1.25%	-2.5%	-1.25%	-2.5%
Turbines	Flow capacity	-2.50%	-5.0%	2.50%	5.0%
	Efficiency	-1.25%	-2.5%	-1.25%	-2.5%

For the second study, *degraded design*, the heat exchangers are designed with a preset fouling resistance on each side, anticipating the future fouling. This way, it is assumed that the heat exchanger is going to suffer from fouling degradation, and permits to ensures that the design performance will be achieved when the degradation grows up to the imposed design values.

Preset a fouling resistance on the design of the heat exchangers has two effects. On one hand, the required heat transfer area would be larger than if no degradation

was considered. This makes possible to compensate the reduction in the overall heat transfer coefficient produced by the future degradation. Therefore, the size and the acquisition cost of the device would increase. On the other hand, the *clean performance* of the device would be higher than the design one. The *clean performance* is defined as the operating conditions when fouling has not yet grown in any of the heat exchangers ($R_{f,a} = R_{f,w} = \Delta P_f = 0$). Since no degradation has yet happened and the area would be oversized, the amount of heat exchanged would be larger than the value calculated at design point.

To analyse both effects, the preset fouling resistance on the air-side and the water-side ($R_{f,a,DP}$ and $R_{f,w,DP}$), and the preset pressure drop penalty coefficient ($\Delta P_{f,DP}$) are parametrically increased. The level of preset deterioration is characterised by the Design Point Degradation Coefficient (DC_{DP}), defined in Eq. 6.24. The imposed DC_{DP} ranges from 0 to 2, which varies the acquisition cost of the heat exchangers and drives the cycle at off-design when no R_f is considered. The temperature of the combustors is kept constant at 1600 K .

$$DC_{DP} \equiv \frac{R_{f,a,DP}}{(R_{f,a})_{Ref}} = \frac{R_{f,w,DP}}{(R_{f,w})_{Ref}} = \frac{\Delta P_{f,DP}}{(\Delta P_f)_{Ref}} = [0-2] \tag{6.24}$$

6.3.1 Exergy analysis of baseline designs

The exergy analysis of the three baseline configurations analysed (Table 6.1) is presented in Figure 6.2. The figure shows the relative exergy destroyed by each component and the exergy rejected to the atmosphere. The main combustion chamber destroys the largest portion of the exergy inserted in the cycle (18-20%), followed by the reheater (7-10%). The large exergy destruction is a consequence of the high irreversibility of the combustion process at constant pressure. The outlet exergy (5%) represents the third larger source of exergy destruction. The rest of the components do not overcome the 5% individually.

As the design effectiveness increases from 0.75 to 0.95, the $\widehat{\dot{E}x_{dest}}$ by the intercooler drops from a 2.5% to a 1%. In the case of the economiser the $\widehat{\dot{E}x_{dest}}$ drops from a 4% to a 1.6%, the rest of the component do not show a variation larger than 0.5%, except the combustion chambers. In the case of the combustion chambers, the reduction produced in the main combustion chamber is compensated by the increment produced in the reheater and, therefore, the balance is zero. Thus, the

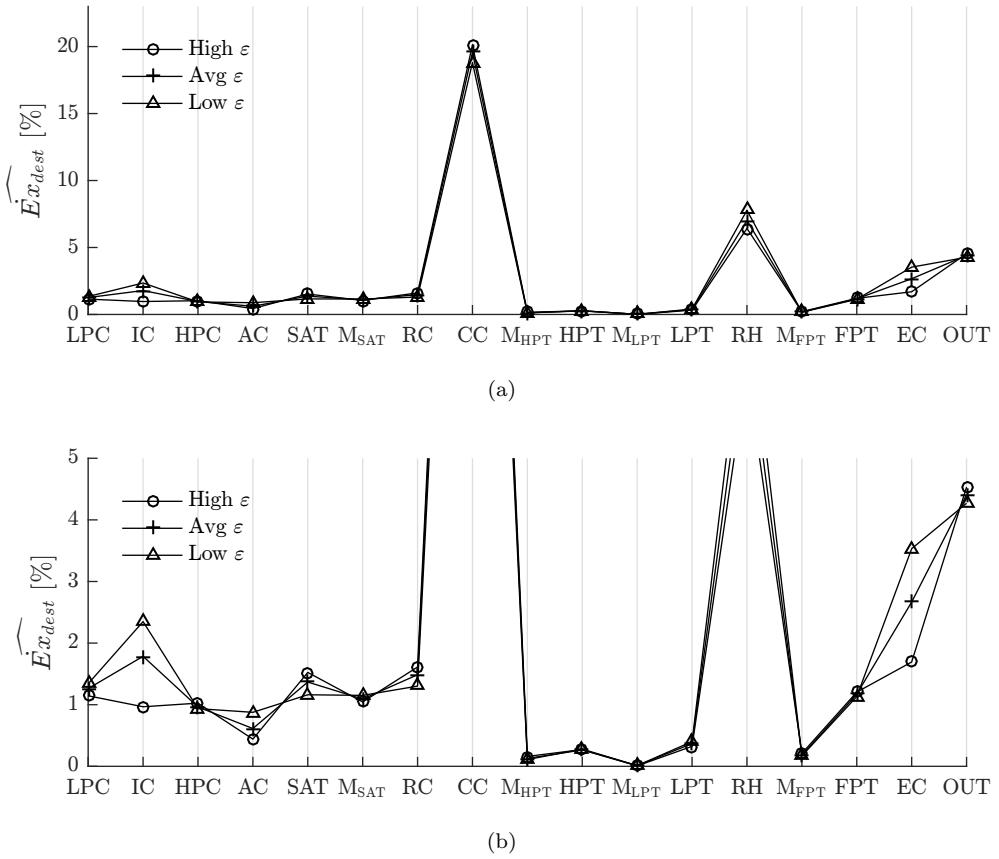

FIGURE 6.2: Relative exergy destroyed by the components for different design scenarios.

reduction of the exergy destroyed in the intercooler and economiser is the main cause of the rise the thermal efficiency, which changes from 57.8%, to 59.7%, and finally to 61.4% as the design effectiveness increases from 0.75, to 0.85, and to 0.95 respectively.

6.4 Degraded performance

6.4.1 Heat exchanger degradation

The effect of the degradation of the air-water heat exchangers on the thermal efficiency of the cycle for the different cycles analysed (Table 6.1) is presented in Figure 6.3. The degradation of the intercooler imposes the largest penalties on the thermal efficiency (Figure 6.3a). For the average ε scenario when a $DC_{IC} = 1$ is imposed the thermal efficiency drops 0.70 pp. If the degradation grows up to

$DC_{IC} = 2$, the drop linearly increases up to 1.78 pp. Nevertheless, the degradation of the economiser has a less detrimental effect (Figure 6.3b). For the average ε scenario the drop in the thermal efficiency for a $DC_{EC} = 1$ is only of 0.2 pp. Whereas, the degradation of the aftercooler imposes no appreciable penalties on the thermal efficiency for any of the three scenarios analysed (Figure 6.3c). When the three heat exchangers are degraded simultaneously (Figure 6.3d) the change in the thermal efficiency is the result of linearly adding the penalisations imposed by each heat exchanger. For the average ε scenario and a $DC_{Sim} = 1$ (simultaneous degradation of the three heat exchangers) the thermal efficiency drops 0.90 pp, and 2.18 pp for a $DC_{Sim} = 2$.

As the baseline design effectiveness of the intercooler increases, the reduction rate of the thermal efficiency becomes less severe. When the design effectiveness is raised from 0.75 to 0.85 (Figure 6.3a), the degradation of the thermal efficiency decreases around a 40%, If the design effectiveness is further raised, from 0.85 to

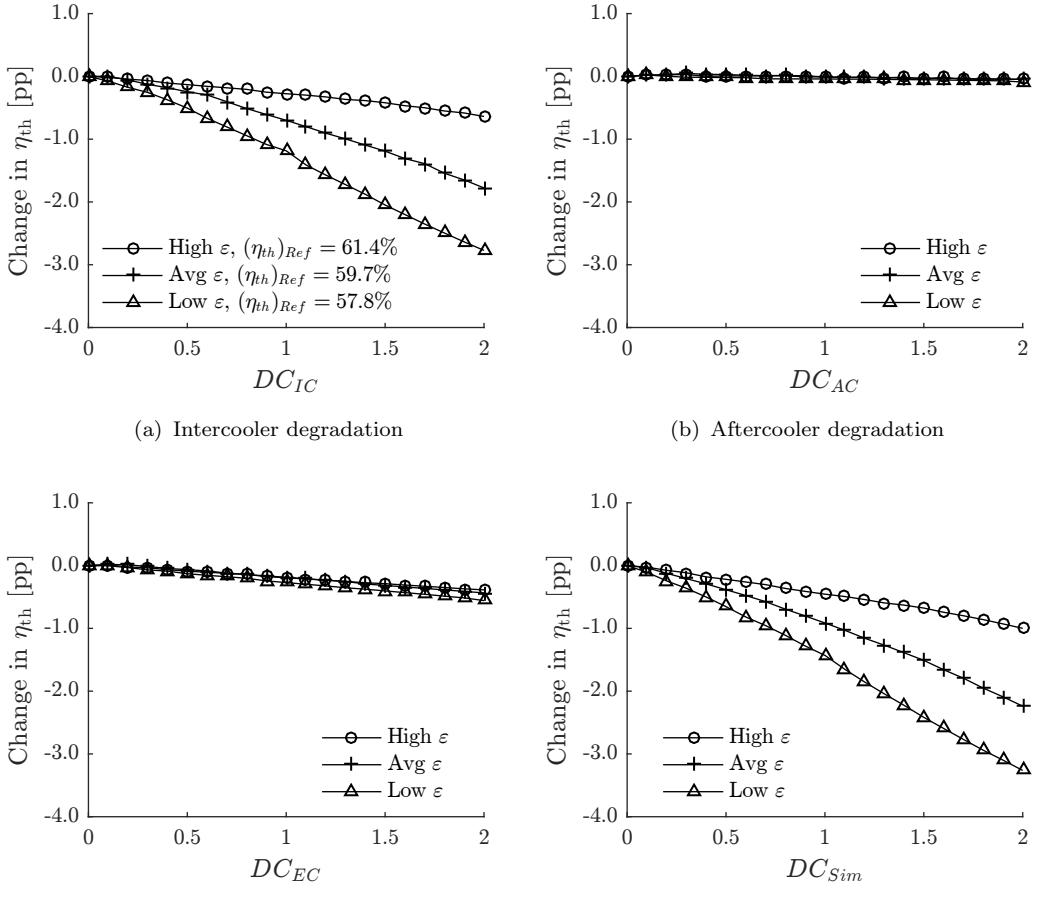

(a) Intercooler degradation

(b) Aftercooler degradation

(c) Economiser degradation

(d) Simultaneous heat exchanger degradation

FIGURE 6.3: Effect of the heat exchanger degradation on the thermal efficiency.

0.95, the efficiency degradation drops another 60%. A similar effect is observed when the three heat exchangers are degraded simultaneously (Figure 6.3d). However, heat exchanger baseline effectiveness are found to have no impact on the degradation rate as far as the aftercooler and the economiser are concerned.

5

Figure 6.4 shows the power output penalties across the analysed range of hat exchanger degradation coefficients. As anticipated, the degradation of the intercooler (Figure 6.4a) drives the most notable penalties in power output. For the average heat exchanger effectiveness design scenario, $DC_{IC} = 1$ yields to a 13.9% reduction in power output in relation to the clean configuration, while a 28.3% reduction was found for $DC_{IC} = 2$. The degradation level of the aftercooler or the economiser are found to have weaker impact. For the average heat exchanger effectiveness design scenario, a $DC_{AC} = 1$ only causes a 1.3% penalty to the plant's

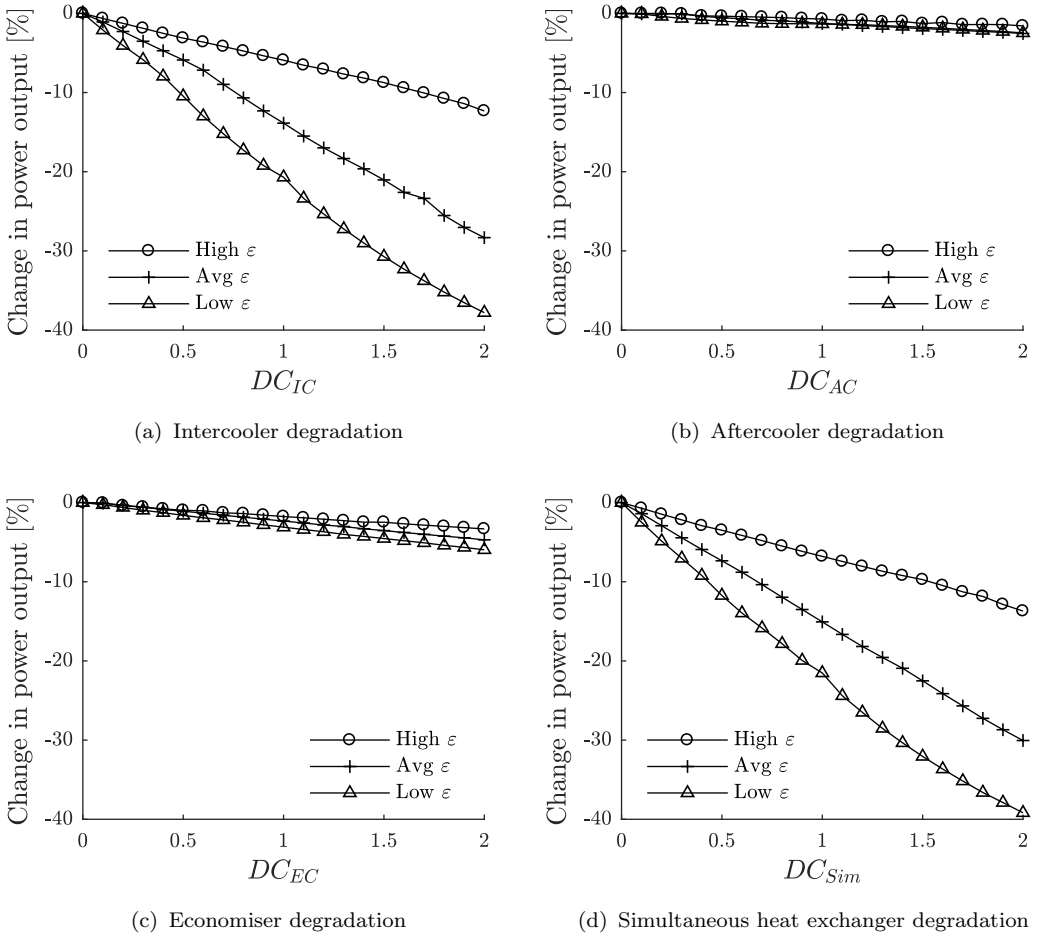

(a) Intercooler degradation

(b) Aftercooler degradation

(c) Economiser degradation

(d) Simultaneous heat exchanger degradation

FIGURE 6.4: Effect of the heat exchanger degradation on the power output.

power output (Figure 6.4b) while $DC_{EC} = 1$ causes a 2.3% (Figure 6.4c). When the degradation occurs in the three heat exchangers simultaneously the overall power output penalty is about 15% for a $DC_{Sim} = 1$, and a 30% for a $DC_{Sim} = 2$. Similarly to the efficiency variations, the highest rate of change is found to occur for the low heat exchanger effectiveness design scenario. As the design effectiveness rises, the effect of degradation on the reduction rate of the system's power output is less pronounced.

In order to explain the reasons behind the different behaviours depending on the design effectiveness of the heat exchangers, it is necessary to study how the performance of these devices changes when they are deteriorated. Figure 6.5 represents the change in the operating point of the air-water heat exchangers as the DC increases. On this figure the degradation gradually increases from $DC = 0$ (points with the larger marker) up to $DC = 2$ (other extreme of the lines).

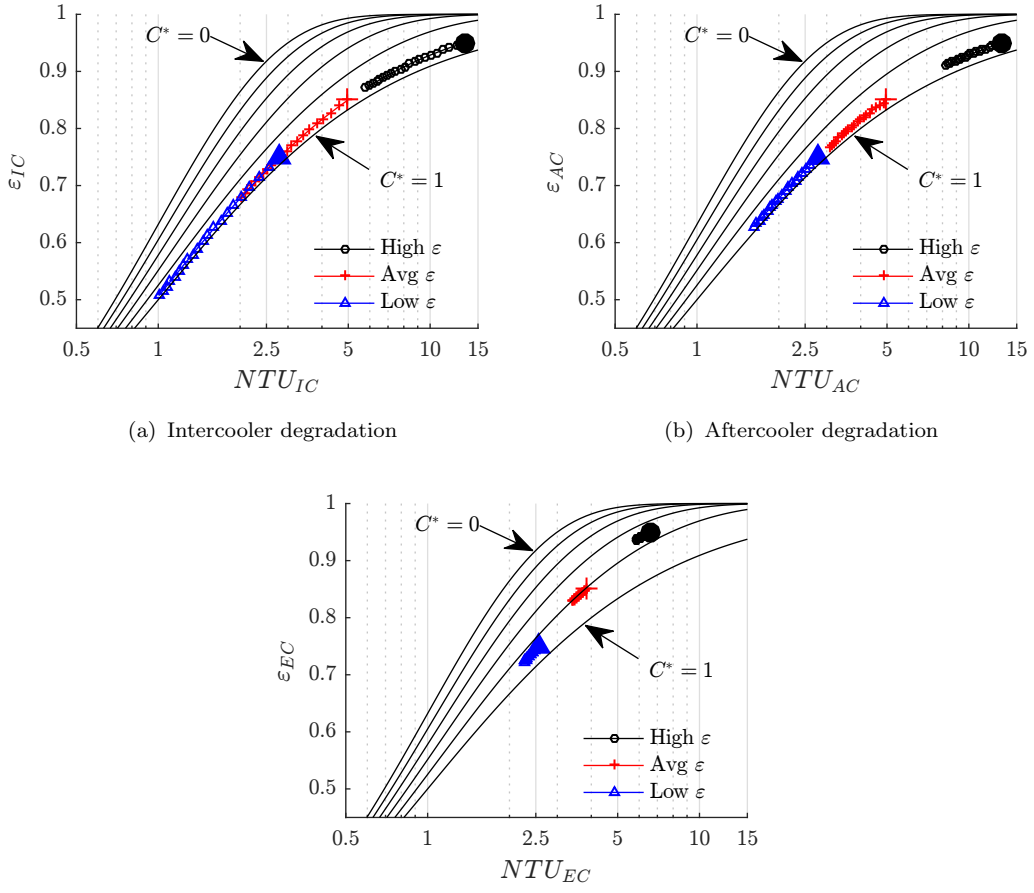

(a) Intercooler degradation

(b) Aftercooler degradation

(c) Economiser degradation

FIGURE 6.5: Effect of the heat exchanger degradation on the heat exchanger's performance.
$DC = 0$, represented by the larger marker. DC ranges from 0-2.

The high ε design scenario suffers the largest reduction in the NTU. When DC rises from 0 up to 2, the NTU of the intercooler drops by 7.5, 3.0, and 1.8 units for the high, average, and low ε scenarios respectively. However, the largest variations in the effectiveness happen for the low effectiveness design scenarios. The intercooler effectiveness drops by 0.08, 0.17, and 0.24 units for the high, average, and low ε scenarios respectively. The trends are similar for the aftercooler and economiser cases.

For the higher design effectiveness scenarios, the required UA_{Ref} is obviously larger. That is why the modification of $R_{f,tot}$ on Eq. 6.4 has a larger impact on the UA, and consequently on the NTU. Nevertheless, due to the characteristics of the map (Figure 6.5) the repercussion in the effectiveness is reversed, and the impact on the effectiveness ends up being larger for the low technology scenarios. This, explains why the lower technology of the air-water heat exchangers, the larger the effect on the performance of the cycle.

Figure 6.6 shows the relative exergy destruction changes across a range of degradation rates for the average effectiveness design scenario (Table 6.1). The change in the exergy destroyed is calculated as in Eq. 6.25. The lines connect the change in $\widehat{\dot{E}x_{dest}}$ points, of the different components, that are calculated for the same level of degradation (DC). The colour of the line represents the assumed level of degradation. Therefore, the exergy analysis tool can be used to recognise the components whose design, or operation should consider the effects derived from the degradation of the heat exchangers in order to minimise the penalties in the performance of the power plant. Moreover, it also allows simplifying the thermodynamic analysis by just focusing on the components that suffer the largest variations in the exergy they destroy.

$$\text{Change in } \widehat{\dot{E}x_{dest}} = \widehat{\dot{E}x_{dest,deg}} - \widehat{\dot{E}x_{dest,DP}} \tag{6.25}$$

The exergy analysis shows that the degradation of the intercooler (Figure 6.6a) triggers a change in the exergy destroyed by several components, which include the LPC, the saturator, the recuperator, the combustion chamber, the reheater, and the intercooler itself. For a DC_{IC}=1, the exergy destroyed by the LPC increases 0.12 pp, by the intercooler 0.43 pp, and by the reheater 0.15 pp, whereas the exergy destroyed by the saturator reduces 0.2 pp, by the recuperator 0.15 pp, and by the combustion chamber 0.26 pp. This means that the entropy generated within in

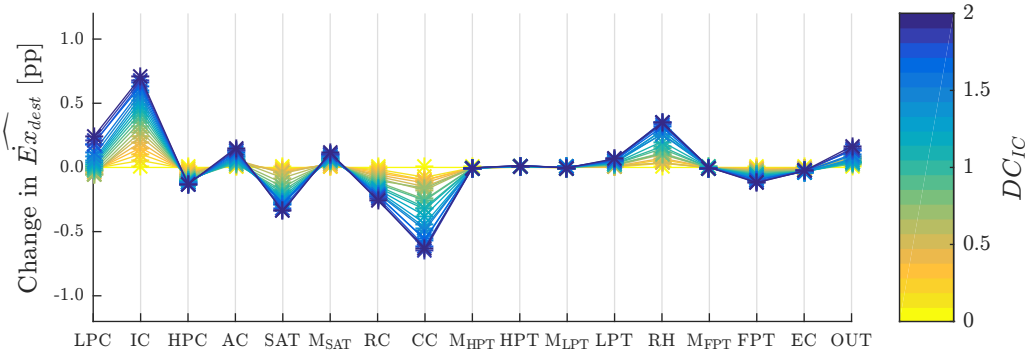

(a) Intercooler degradation

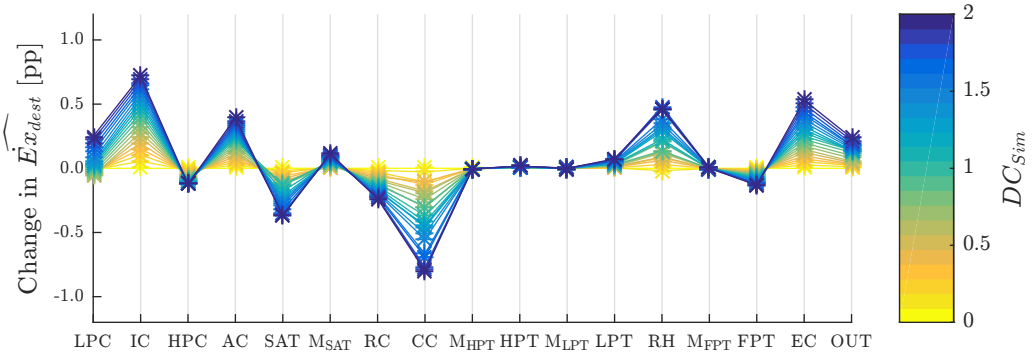

(b) Simultaneous heat exchanger degradation

FIGURE 6.6: Effect of heat exchanger degradation on the component's exergy destruction. Average effectiveness design scenario.

the LPC, intercooler, and reheated grows, making the thermodynamic processes more irreversible, i.e. less efficient. The opposite happens inside the saturator, the recuperator, and the combustion chamber. Hence, the thermal efficiency penalty observed across the range of intercooler degradation levels is mainly the result of a trade-off between the benefits in the performance produced by the saturator, recuperator, and main combustion chamber, and the deterioration caused by the LPC, the intercooler, and the reheater.

Similar analyses have proven that the deterioration of the aftercooler or the economiser does not produce any remarkable changes in the exergy destroyed by the rest of the components. This explains the similarity between Figure 6.6a and Figure 6.6b, where all air-water heat exchangers are degraded simultaneously. Figure 6.6b looks like Figure 6.6a with the only difference that the exergy destroyed by the aftercooler and the economiser also rises as DC_{Sim} increases, consequence of the degradation of these devices. Therefore, assuming that a change in the exergy destroyed is directly related to a change in the performance of the component, it is

proved that the deterioration of the intercooler causes a cascade effect altering the performance of several components of the power plant, whereas the degradation of the aftercooler and economiser only affect their own performance.

The exergy analysis has permitted to reveal that the LPC and the reheater also play a primary role in the thermal efficiency reduction derived from the degradation of the intercooler. However, if the design and operation of these components was revaluated, the rise in their exergy destruction (Figure 6.6) could be prevented. In the case of the LPC, the installation of variable geometry and variable inlet guide vanes would permit to adjust the stators angle of attack to reduce the flow separation and, therefore, decrease the rise in exergy destruction. In the case of the reheater there is little to do from a design point, as the exergy destroyed in the chamber is mainly related with the temperature rise. However, increasing the outlet temperature in the main combustion chamber would rise the inlet temperature at the reheater, which would reduce the exergy destruction in the reheater. Nevertheless, this option would reduce the life of the core turbines and increase the exergy destruction in the main combustor chamber. Other possibility would be reducing the outlet temperature of the reheater, although it would also penalise the power output. In order to obtain the most efficient solution a deeper analysis is required.

To better understand the change in the behaviour of the system when the heat exchangers are degraded, the compressors maps are analysed. Figure 6.7 shows the changes in the compressor operating points across a range of intercooling degradation levels for the average effectiveness design scenario as baseline. In the case of the HPC (Figure 6.7b), the non-dimensional mass flow and the pressure ratio are reduced simultaneously. Therefore, the surge margin is not affected. Nevertheless, in the case of the LPC (Figure 6.7a), the reduction in the non-dimensional mass flow is more notable compared to the reduction in the pressure ratio. This produces a considerable loss of the surge margin as the intercooler degrades that could lead to an unstable operation of the plant, or even avoid a safe operation. In addition, the operating point moves to lower efficiency regions, which explains the increment in the exergy destroyed by the component (Figure 6.6).

The reduced inlet mass flow (Figure 6.7a) is beneficial for the performance of the recuperator. Since $C_{\min}$ decreases faster than the UA, producing a benefit in the NTU and consequently in the effectiveness. This justifies the reduction in

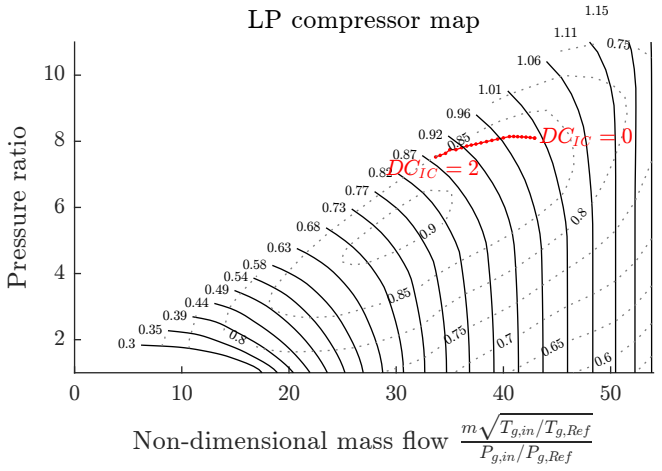

(a) LPC map

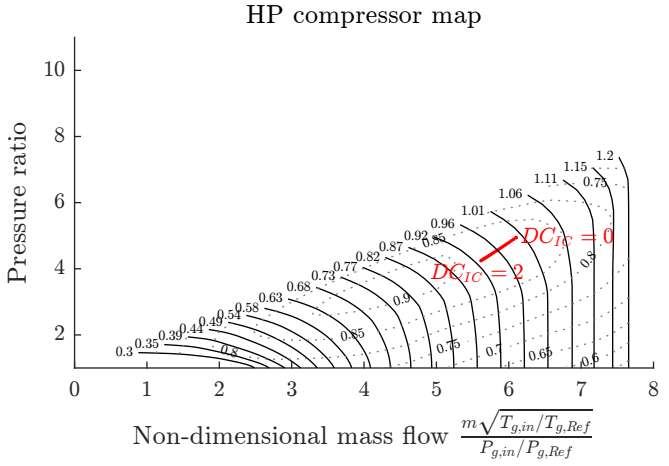

(b) HPC map

FIGURE 6.7: Effect of the intercooler degradation on the compressor's operating point. Average effectiveness design scenario.

the exergy destroyed in the recuperator identified in Figure 6.6, hence its performance improves in comparison to the baseline configuration with no degradation in the intercooler. At the inlet of the combustion chamber, the gas temperature increases due to the better performance of the recuperator, reducing the required temperature rise. This leads to a reduction in the relative exergy destroyed in the combustion chamber. In the reheater, the temperature jump is kept constant since the FPT is chocked and the outlet is kept at 1600 K. However, the relative reduction in the exergy entering the cycles (lower temperature jump in the main combustion chamber) produces the increment of the relative exergy destroyed in the reheater. In the saturator, the reduction of the temperature of the inlet water, together with the increment in the ratio of $\dot{m}_{w,in}/\dot{m}_{g,in}$, diminishes the tempera-

ture leap between the water and the gas, making heat and mass transfer process more efficient from an exergy point of view. Nevertheless, the amount of water leaving the saturator rises, increasing the exergy dumped into the atmosphere.

The degradation of the aftercooler or the economiser does not imply any remarkable changes in the operation point of any of the compressors. The degradation of these components does not alter significantly the work delivered by the turbines or the required compression work. Therefore, the operation point of the compressors stays fairly stable. This justifies the lack of knock-on effect when these components are degraded, as opposed to the intercooler degradation.

To explain the nature of the variation of the power output when the heat exchangers are deteriorated, it is necessary to explore the changes experienced by the thermodynamic variables of the cycle. Figure 6.8 shows the variation of the inlet mass flow, the specific power, and the water to air ratio at the combustion chamber when the different heat exchangers are degraded for the average effectiveness design scenario.

Comparing Figure 6.4 and Figure 6.8 demonstrates that the reduction of the power output is directly ligated with the reduction of the inlet mass flow and the specific power, as the parameters follow the same trends when the different heat exchangers are degraded. The specific power deterioration is primarily driven by the reduction in the humidity (Figure 6.4c), which reduces the work imbalance between the compressor and the turbines. In addition, the deterioration of the intercooler's performance increases the HPC inlet temperature, which rises the required compression work. Therefore, the degradation of the intercooler is expected to produce a larger penalisation in the specific power, as shown in Figure 6.4b. Both events, the reduction in humidity and the rise in the compression work, lead to the movement of the operating point of the compressor towards lower power settings.

As previously explained, as the design ε of the heat exchangers reduces the consequences of the degradation are magnified. This impacts the performance of the compressors as well. The magnification of these changes leads to a more severe reduction of the surge margin in the case of the LPC. Figure 6.9 shows how the operation point of the LPC changes when the intercooler is degraded for the low ε design scenario. Compared with the average ε design scenario (Figure 6.7a) it is observed that the reduction of the surge margin becomes more severe for the

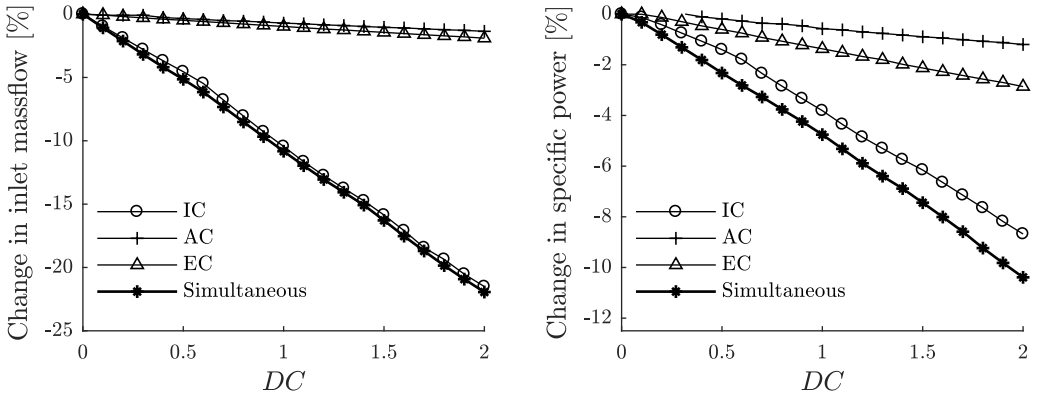

(a) Impact on the inlet mass flow

(b) Impact on the specific power

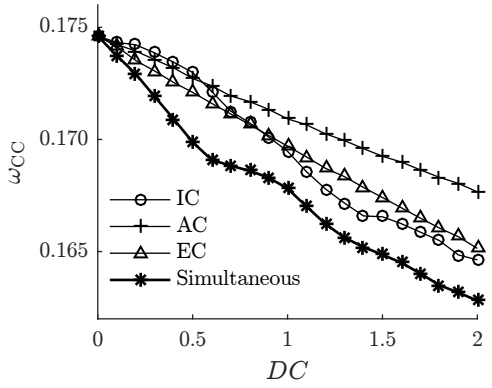

(c) Impact on ω_{CC}

FIGURE 6.8: Effect of the heat exchanger degradation on the inlet mass flow, specific power, and humidity. Average effectiveness design scenario.

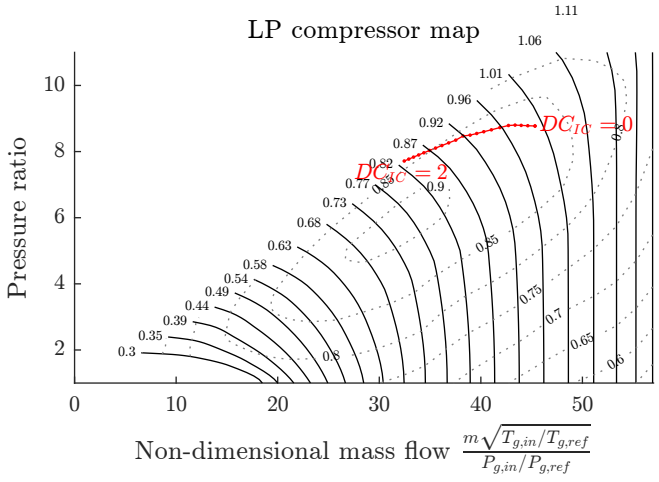

FIGURE 6.9: Effect of the intercooler degradation on the low pressure compressor's operating point. Low effectiveness design scenario.

largest DC_{IC} values. This will difficult, or even impede, the operability of the plant. Thus, the reduction of the design ε not only increases the penalties derived from the degradation of the heat exchangers but also reduces the operability of the power plant when the intercooler is among the components degraded. Therefore, the reduction of the surge margin of the LPC further supports the idea of considering variable geometry and variable inlet guide vanes in its design.

6.4.2 Turbomachinery degradation

Turbomachinery fouling

Figure 6.10 shows the change in the thermal efficiency and power output produced by the simultaneous degradation of the heat exchangers for the three turbomachinery fouling scenarios analysed, while keeping a 0.85 of design effectiveness in the air-water heat exchangers. The fouling deterioration of the turbomachinery produces a drop in the thermal efficiency of 0.36 pp for a deterioration of 2.5%, and 0.91 pp for a deterioration of 5% and DC_{Sim}=0, Figure 6.10a. The effect of the turbomachinery deterioration is intensified as the degradation of the heat exchangers grows. For a DC_{Sim}=1, the reduction in the thermal efficiency escalates to 0.60 pp and 1.48 pp, for 2.5% and 5% fouling respectively, compared with the clean turbomachinery case. When DC_{Sim}=2, the deterioration increases up to 0.9 pp and 1.79 pp, for 2.5% and 5% fouling respectively, compared with the clean turbomachinery case. Therefore, the total penalisation in the efficiency is 1.5 pp and 2.38 pp for 2.5% and 5% turbomachinery fouling respectively and DC_{Sim}=1, and 3.07 pp and 3.97 pp for DC_{Sim}=2.

The effect of the turbomachinery fouling is also felt in the power output, as shown in Figure 6.10b. Nevertheless, the degradation fouling of the turbomachinery only shifts down the line of the heat exchanger degradation, without altering the slope. For a deterioration of 2.5% the power output drops 9 pp compared with the non-fouled turbomachinery scenario. In the case of 5% fouling, the drop grows up to 19 pp.

The power reduction is a consequence of the larger reduction in the inlet mass flow and the specific power, compared to the clean turbomachinery case. The inlet mass flow reduction increases 6.9 pp and 14.5 pp, for 2.5% and 5% fouling respectively, and the specific power 1.9 pp and 4.3 pp respectively. These values are

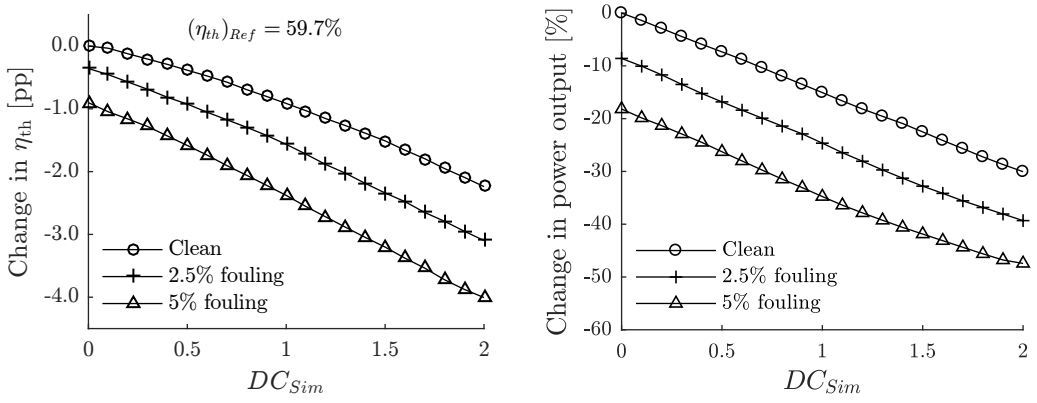

(a) Impact on the thermal efficiency

(b) Impact on the power output

FIGURE 6.10: Effect of turbomachinery fouling and heat exchanger degradation on the thermal efficiency and power. Average effectiveness design scenario.

constant along the whole range of DC_{Sim} analysed. The inlet mass flow is reduced as a consequence of the deterioration of the flow capacity of the compressors and turbines, whereas the specific power drops as a result of the increased compressor work and lowered turbine work delivered resulting from the loss in their efficiencies.

Figure 6.11 displays the change in the exergy destroyed by each component as DC_{Sim} grows for the different turbomachinery fouling levels studied. Comparing Figure 6.11a, with Figure 6.11b and Figure 6.11c it is observed that the fouling of the turbomachinery yields to a rise in the exergy destroyed by the compressors, turbines, saturator and the outlet exergy increase with the fouling degradation, whereas the exergy destroyed by the combustion chamber experiences a reduction.

For DC_{Sim}=0, the 2.5% fouling yields to an increment in the change in exergy destroyed by the LPC of 0.052 pp, the HPC 0.063 pp, the saturator 0.051 pp, the HPT 0.068 pp, the FPT 0.247 pp, and the outlet exergy 0.063 pp, whereas the exergy destruction in the combustion chamber drops 0.161 pp. Finally, the total exergy destroyed increases 0.43 pp, leading to the 0.36 pp reduction in the thermal efficiency. Therefore, the exergy analysis shows that the deterioration of the compressors and turbines also degrades the efficiency of the saturator and rises the exergy released to the atmosphere. It is also observed that the FPT is the component with the largest sensitivity to the turbomachinery fouling, followed by the combustion chamber.

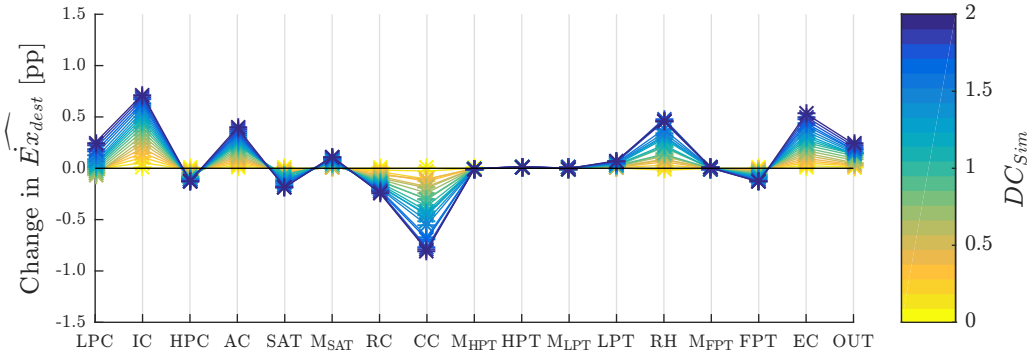

(a) Clean turbomachinery

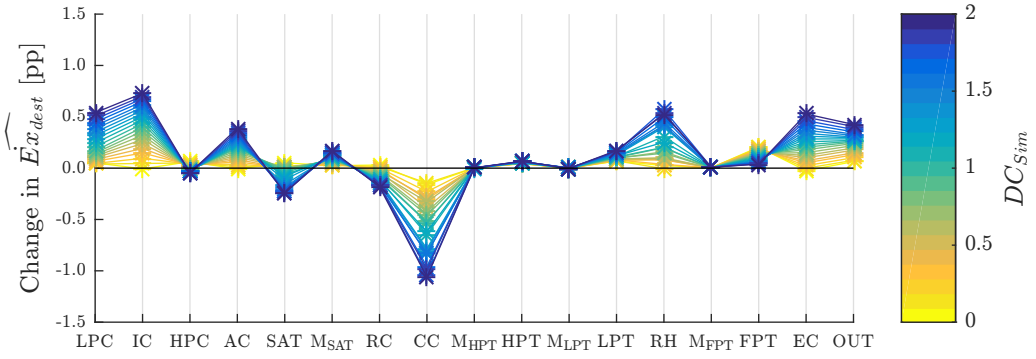

(b) 2.5% of fouling

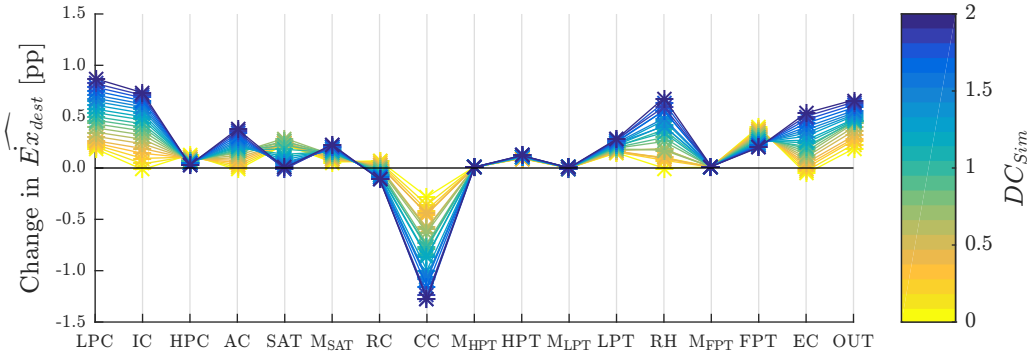

(c) 5% of fouling

FIGURE 6.11: Effect of the turbomachinery fouling and heat exchanger degradation on the component's exergy destruction. Average effectiveness design scenario.

Turbomachinery erosion

Figure 6.12 shows the change in the thermal efficiency and power output produced by the simultaneous degradation of the heat exchangers for the three turbomachinery erosion scenarios analysed. The erosion of the turbomachinery leads to a drop in the thermal efficiency of 0.6 pp for a deterioration of 2.5% and DC_{sim}=0, and 1.37 pp for a deterioration of 5%. As in the fouling case, the effect of the turbomachinery erosion is intensified for larger heat exchanger deterioration. The efficiency reduction increases up to 0.78 pp and 1.60 pp compared with the non-deteriorated turbomachinery case, for 2.5% and 5% erosion respectively, when DC_{Sim}=1. When DC_{Sim}=2, the efficiency deterioration rises up to 0.87 pp and 1.80 pp, for 2.5% and 5% erosion respectively, compared to the clean turbomachinery. The total penalisation in the efficiency is 1.68 pp and 2.5 pp for 2.5% and 5% turbomachinery fouling respectively and DC_{Sim}=1, and 3.05 pp and 3.99 pp for DC_{Sim}=2. Therefore the erosion of the turbomachinery has a larger impact on thermal efficiency for low DC_{Sim} than the fouling (Figure 6.10a), but this difference is levelled as the DC_{Sim} grows.

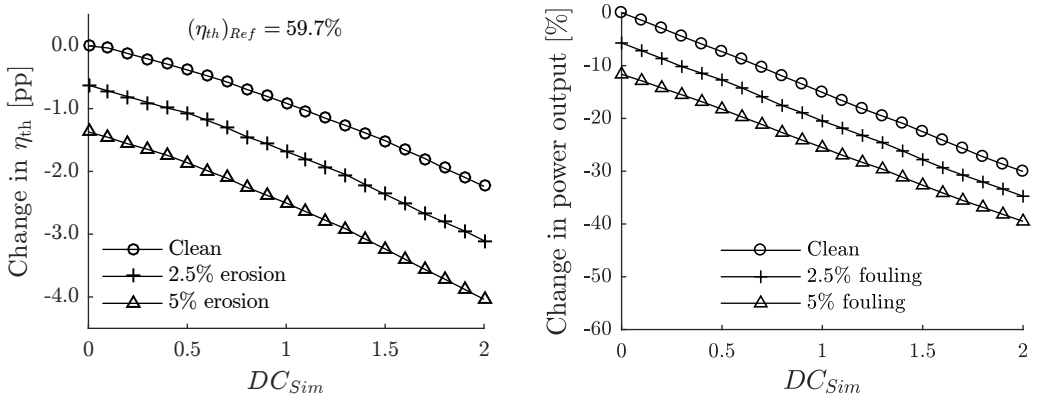

(a) Impact on the thermal efficiency

(b) Impact on the power output

FIGURE 6.12: Effect of the turbomachinery erosion and heat exchanger degradation on the thermal efficiency and power. Average effectiveness design scenario.

The erosion of the turbomachinery also contributes towards a reduction of the power output, as depicted in Figure 6.12b. For an erosion of 2.5%, the power output is reduced 6 pp compared with the non-eroded configuration, and 12 pp for an erosion of 5%. As in the previous case, this difference is kept constant for all the range of DC_{Sim} studied. Hence, although the erosion causes a larger

penalisation in the thermal efficiency than the turbomachinery fowling, it imposes lower penalisations on the power output of the cycle (Figure 6.10).

The exergy analysis shows results very similar results to the ones obtained for the fouling case, showing that the compressors, turbines, and saturator increment in their outlet exergy are the main causes of the drop in the thermal efficiency. However, the exergy destroyed by this components is intensified compared with the turbomachinery fouling case. For a DC_{Sim}=0 and erosion of 2.5% the change in the exergy destroyed by the LPC rises up to 0.10 pp, HPC 0.11 pp, saturator 0.09 pp, LPT 0.05 pp, FPT 0.15 pp and outlet exergy 0.14 pp, whereas the change in the exergy destroyed in the combustion chamber is -0.17 pp. Thus the change in the total exergy destroyed grows up to 0.63 pp, which is 0.20 pp larger than the increment produced by the turbomachinery fouling.

6.5 Degraded design

The effect of presetting a fouling resistance in the design of the air-water heat exchanger to prevent the performance deterioration is presented in this section. The analysis contemplates the three design scenarios presented in Table 6.1. The first part of the study shows the economic impact caused by the modification of the air-water heat exchanger's designs, whereas the second part focuses on the impact on the *clean performance* of the cycle.

6.5.1 Economic impact

Figure 6.13 shows how the acquisition cost of the air-water heat exchangers changes as the prescribed fouling resistance rises. The reference specific costs of the devices are presented in Table 6.4. As DC_{DP} increases, the acquisition cost of the three heat exchangers rises linearly, being the economiser the component suffering the largest penalties.

The intercooler's cost increases a 26% per DC_{DP} point for the three design scenarios (Figure 6.13a). However, a sudden increment of 27 pp is observed when the DC_{DP} passes from 0.1 to 0.2 for the high effectiveness design scenario. The sudden rise reflects the necessity of increasing the number of required heat exchangers

TABLE 6.4: Cost of the air-water heat exchangers for *clean design* conditions.

	Cost for *clean design* [$/kW]		
	IC	AC	EC
High ε	27.5	13.6	1.7
Avg ε	10.0	6.1	1.0
Low ε	6.5	4.6	0.6

from one to two in order not to overcome the maximum design heat transfer area, as explained in Section A.2.

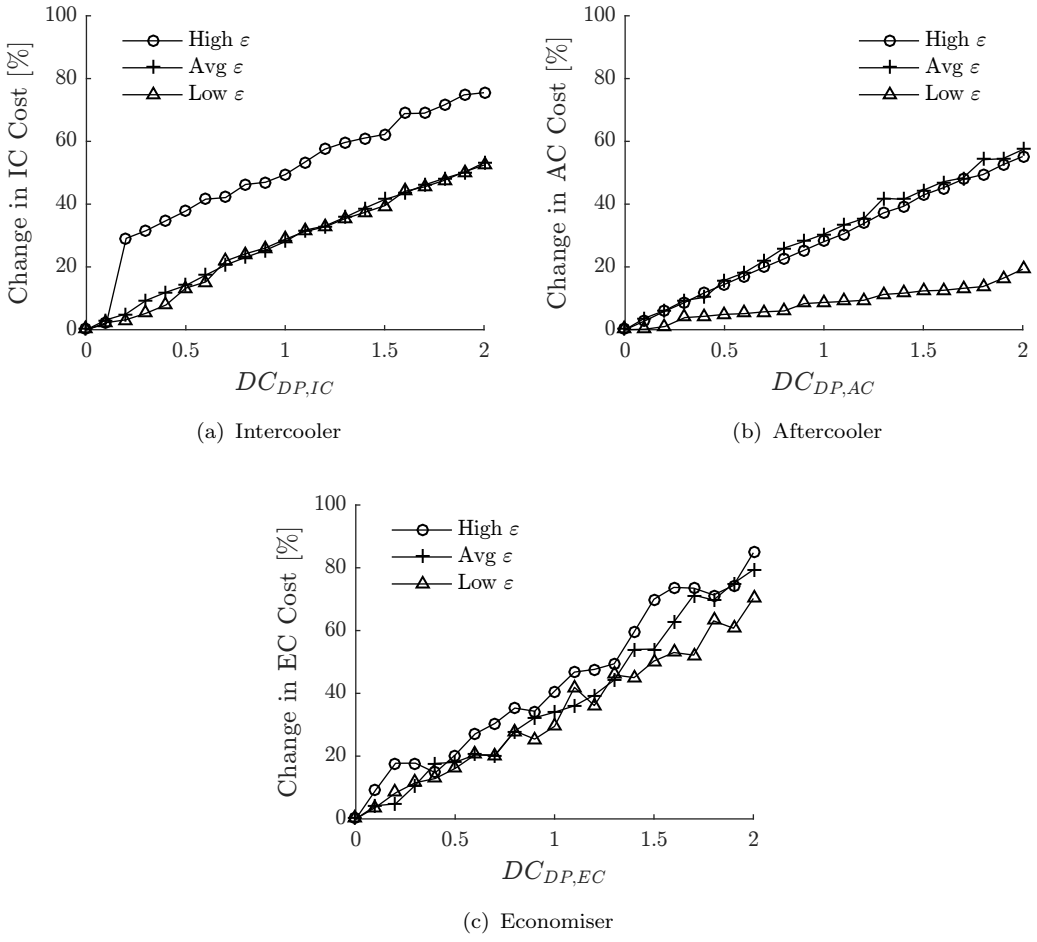

(a) Intercooler

(b) Aftercooler

(c) Economiser

FIGURE 6.13: Effect of the heat exchanger's preset fouling on their acquisition cost.

The cost of the aftercooler rises a 28% per DC_{DP} point for the high and average ε design scenarios (Figure 6.13b). Nevertheless, for the low ε design scenario the cost only grows an 8% per DC_{DP} point. The discrepancy in the slopes is due to the different cost per area the aftercooler presents for each design scenario. For the

low ε design scenario, the design falls into a region where increasing the required area leads to a considerable reduction in the cost per area. Thus, on one hand, the cost increases as DC_{DP} rises due to the necessity of a larger area. On the other hand, that increment is smoothed by the reduction in the cost per area [75]. However, for the other two design scenarios, this later reduction is considerably lower.

The cost of the economiser rises a 36% in average per each DC_{DP} point for the three design scenarios (Figure 6.13c). The cost of the economiser shows a steeper slope compared with the intercooler and the aftercooler since its cost per area is fixed, whereas in the case of the plate-fin heat exchangers the cost per area reduces as the design area increases. In addition, it can be noticed that the trend is slightly bumpy. This behaviour is a consequence of the introduction of the optimiser in the design process. The genetic algorithm implies a random component in the design process, creating small change in the design parameters that can lead to small differences in the final design.

The effect of preset a fouling resistance on the acquisition cost of the plant is presented in Figure 6.14. The reference $SPEC$ of the each design scenarios is presented in Table 6.5. As the DC_{DP} rises, the cost grows linearly, except for the sudden jump introduced by the intercooler's modification.

TABLE 6.5: Specific purchase equipment for *clean design* conditions.

	***SPEC* for *clean design* conditions** [$/kW]
High ε	365.9
Avg ε	348.0
Low ε	351.4

Although the economiser is the component experiencing the largest change in its acquisition cost (Figure 6.13c), it causes a negligible effect on the total cost (Figure 6.14c). The modification of the aftercooler's design also has a discrete contribution to the $SPEC$ (Figure 6.14b), being the intercooler the component creating the largest changes (Figure 6.14a).

Similarly to the degradation study, changing the design effectiveness of the heat exchangers alters the effects produced. As the design effectiveness increases, the impact on the acquisition price is magnified due to the larger contribution of the

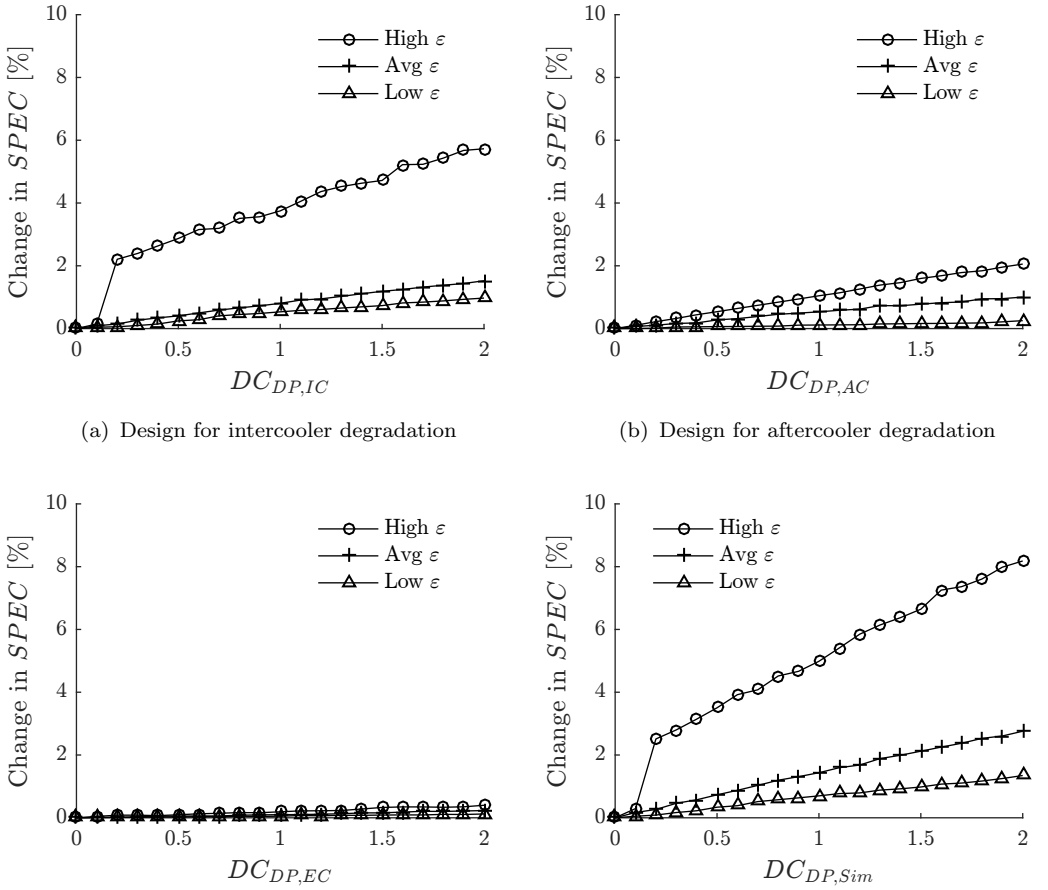

(a) Design for intercooler degradation

(b) Design for aftercooler degradation

(c) Design for economiser degradation

(d) Design for sim. heat exchanger degradation

FIGURE 6.14: Effect of the heat exchanger's preset fouling on the power plant's cost.

cost of the heat exchangers to the total cost increases. For a $DC_{DP,Sim}$=1 (the design of all the heat exchangers is modified simultaneously) the $SPEC$ increases 0.6% for the low ε design scenario, 1.4% for the average ε design scenario, and a 4.7% for the high ε design scenario (Figure 6.14d).

In addition, the impact on the $SPEC$ has a reverse order compared with the impact in the performance caused by the heat exchangers degradation. The high ε design scenario presents the largest variation on the $SPEC$ while it is the design scenario with lowest performance deterioration. This makes the modification of the heat exchanger's design more attractive as the design effectiveness drops. Modifying the design of the three heat exchanger for the low ε design scenario increases the cost less than 1% (Figure 6.14) and can avoid a penalisation of 3.4 pp (Figure 6.3) in thermal efficiency and 39% (Figure 6.4) in power output. However, for the average ε design scenario the extra investment can grow up to a 2% (Fig-

ure 6.14) and the penalisation drops to 2.2 pp in thermal efficiency (Figure 6.3) and 30% in power (Figure 6.4). Last, for the high ε design scenario the extra investment can grow up to an 8% (Figure 6.14) and the penalisation drops to 1.1 pp in thermal efficiency (Figure 6.3) and a 12% in power (Figure 6.4).

6.5.2 Thermodynamic impact

The effect of considering the *degraded design* of the air-water heat exchangers on the thermal efficiency of the cycle operating at *clean conditions* for the different design scenarios (Table 6.1) is presented in Figure 6.15. The variation of the design of the economiser yields to the largest benefit in thermal efficiency at *clean performance* (Figure 6.15c). For the average ε design scenario and a $DC_{DP,EC}$=1 the benefit is 0.22 pp. If the design degradation grows up to $DC_{DP,EC}$=2 the benefit rises up to 0.37 pp. Nevertheless, the benefits in the *clean performance* efficiency derived from the *degraded design* of the intercooler are less notable (Figure 6.15a). For the average ε design scenario are of the efficiency only grows 0.14 pp for a $DC_{DP,IC}$=2. On the other hand, the modification of the design of the aftercooler does not cause any appreciable benefits in the efficiency at *clean performance* (Figure 6.15b). When the designs of the three heat exchangers are modified simultaneously a synergy effect takes place. The benefit in the thermal efficiency is larger than just adding the separate contribution of each heat exchanger. For a $DC_{DP,Sim}$=1 the thermal efficiency at *clean performance* rises 0.42 pp, and 0.62 pp for a $DC_{DP,Sim}$=2.

As the design effectiveness of the heat exchangers becomes higher, the effect on the thermal efficiency at *clean performance* becomes shorter. The impact is around 50% lower when comparing the high to the average ε design scenario, and a 45% lower when comparing the average to the low ε design scenario.

The modification of the heat exchanger's designs not only benefits the thermal efficiency at *clean performance*, these modifications also enhance the power output. Figure 6.16 illustrates the evolution of the power output at *clean performance* as the preset fouling resistance increases. Again, the modification of the design of the economiser produces the largest benefits. The power output grows a 3.2% when $DC_{DP,EC}$ = 1, and up to a 4.8% when $DC_{DP,EC}$=2 (Figure 6.16c). The modification of the design of the intercooler or the aftercooler does not produce any remarkable benefit on the power output, except for the low ε design scenario.

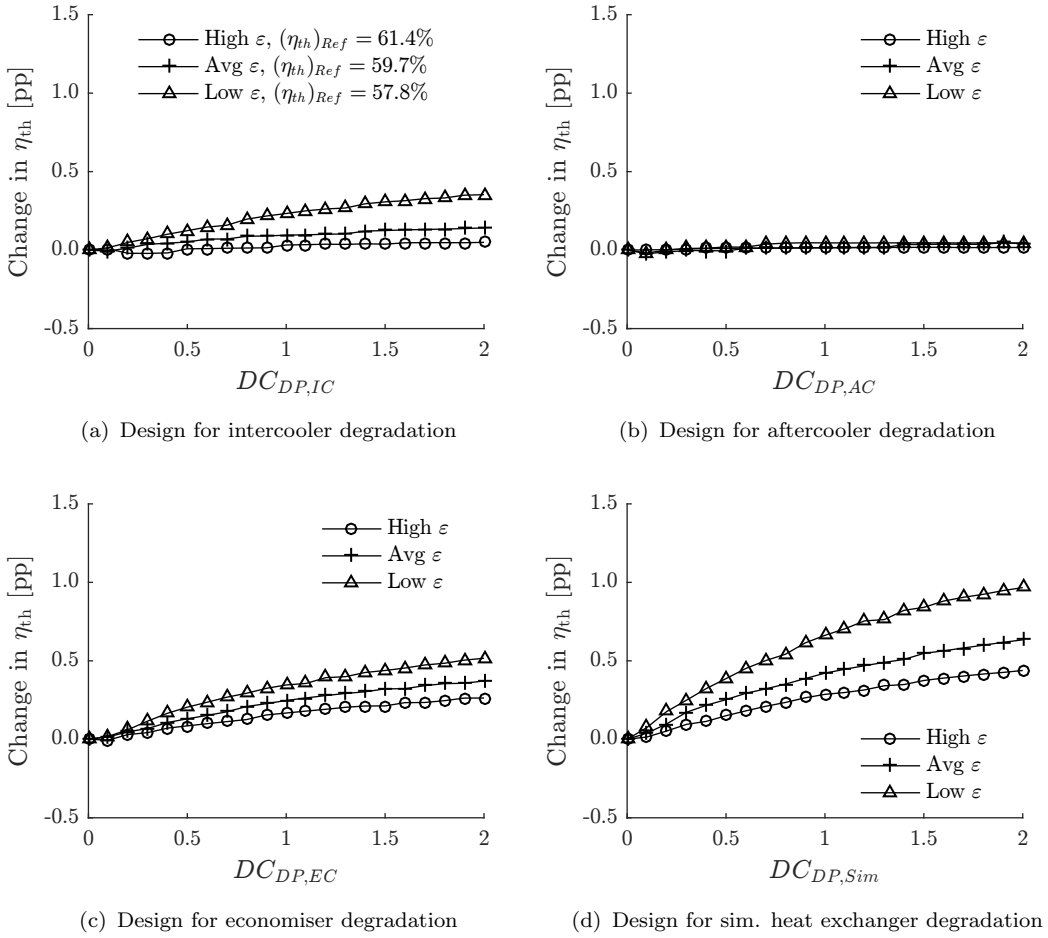

(a) Design for intercooler degradation

(b) Design for aftercooler degradation

(c) Design for economiser degradation

(d) Design for sim. heat exchanger degradation

FIGURE 6.15: Effect of the heat exchanger's preset fouling on the thermal efficiency at *clean performance*.

In that case, for a $DC_{DP,IC}$=1 the *clean performance* power output is improved a 5.2%, and an 8.3% for $DC_{DP,IC}$=2 (Figure 6.16a).

If the design of the heat exchangers is modified simultaneously, the power output rises a 7.2% and a 10.2% for $DC_{DP,Sim}$=1 and $DC_{DP,Sim}$=2 respectively, for the average ε design scenario. Similarly to the case of the efficiency, the impact on the power output is less severe as the design effectiveness of the heat exchangers increases.

Analysing how the performance of the heat exchangers at *clean performance* varies when modifying their designs permits to understand the nature of the different behaviour observed depending on the design effectiveness of the heat exchangers. Figure 6.17 represents, for the three design scenarios (Table 6.1), how the operating point of the heat exchangers at *clean performance* varies as the prescribed fouling

resistance grows. The considered degradation is gradually increased from DC_{DP}=0 (point with larger marker) up to 2 (other extreme of the lines).

The largest variations of the *NTU* always occur for the high ε design scenario. In the case of the intercooler when $DC_{DP,IC}$ rises from 0 to 2 the *NTU* at *clean performance* grows 17, 3, and 2 units for the high, average, and low ε design scenarios respectively (Figure 6.17a). Similar trends are observed when observing the impact on the performance of the aftercooler or the economiser. Nevertheless, due to the shape of the maps, the largest changes in the effectiveness occur in the low *NTU* region, hence, for the low ε design scenario. This explains why the effects of changing the design for the low ε design scenario are always larger when compared with the other design scenarios.

To easily identify which components are the main influencers in the variation of the thermal efficiency of the cycle at *clean performance*, an exergy analysis is

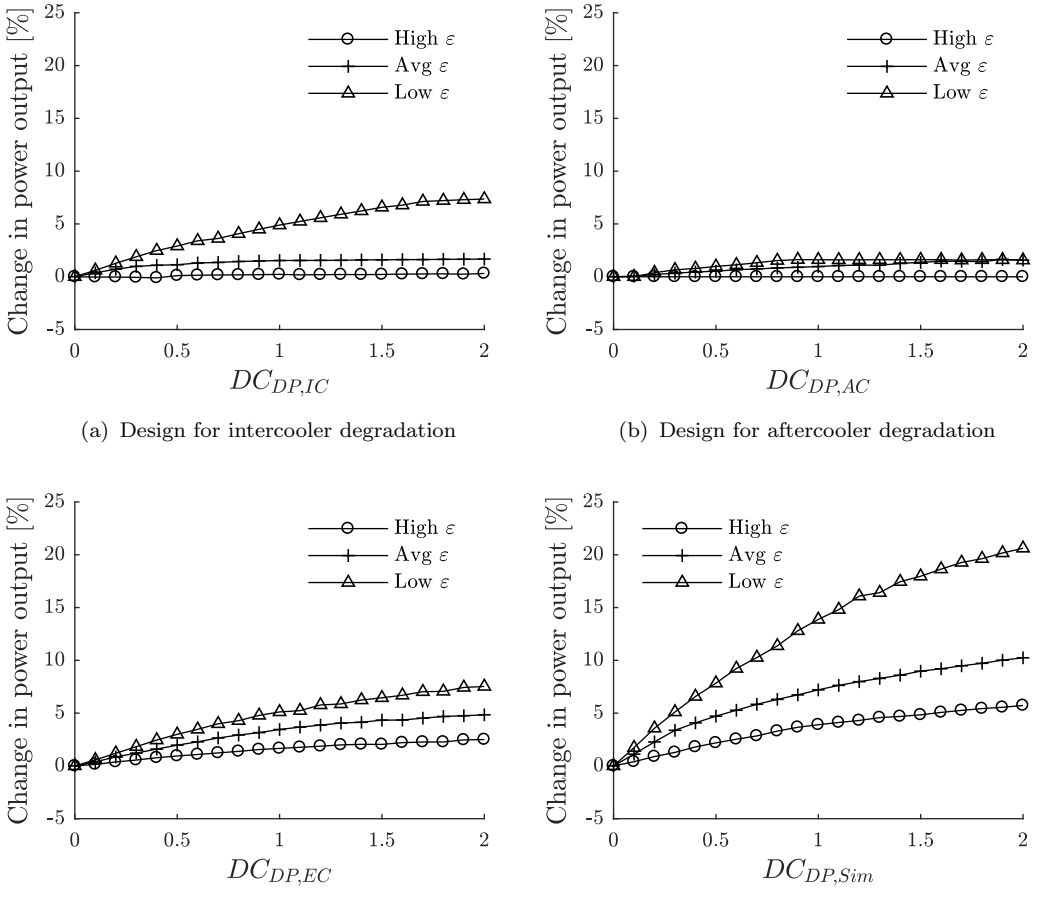

(a) Design for intercooler degradation

(b) Design for aftercooler degradation

(c) Design for economiser degradation

(d) Design for sim. heat exchanger degradation

FIGURE 6.16: Effect of the heat exchanger's preset fouling on the power output at *clean performance*.

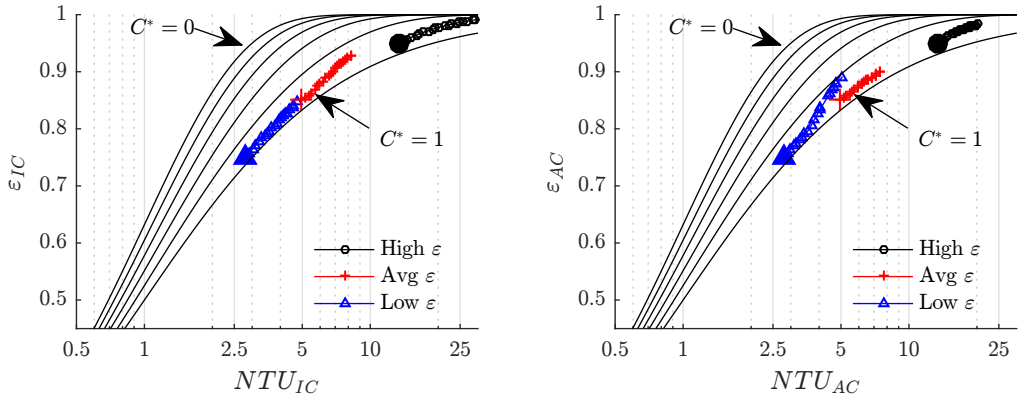

(a) Design for intercooler degradation

(b) Design for aftercooler degradation

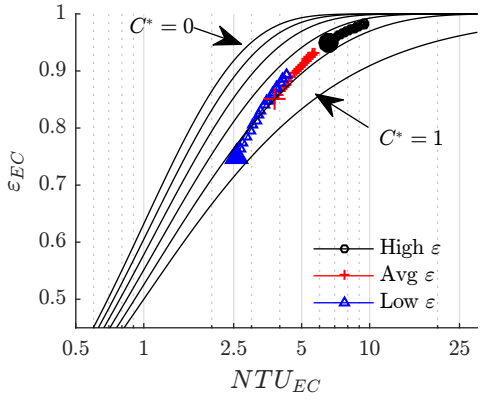

(c) Design for economiser degradation

FIGURE 6.17: Effect of the heat exchanger's preset fouling on the heat exchanger's *clean performance*.
$D_{DP} = 0$, represented by the larger marker. DC_{DP} ranges from 0-2.

performed. Figure 6.18 presents how the exergy destroyed in each component and the exergy rejected into the atmosphere varies when increasing DC_{DP} for the average effectiveness design scenario.

The exergy analysis shows that the modification of the intercooler's design (Figure 6.18a) only triggers a change in the exergy destroyed by the saturator and the economiser, apart from the intercooler itself. For a $DC_{DP,IC}$=1 the reduction in the exergy destroyed by the intercooler (0.26 pp), is compensated by the increment in the exergy destroyed by the saturator (0.27 pp). Thus, the rise in the performance is obtained due to the benefit in the economiser efficiency (0.11 pp reduction in $\widehat{\dot{E}x_{dest}}$) and the drop in the exergy rejected (0.11 pp).

Presetting a fouling resistance in the economiser (Figure 6.18b) yields to a considerable reduction in the exergy destroyed by the economiser (0.47 pp for a

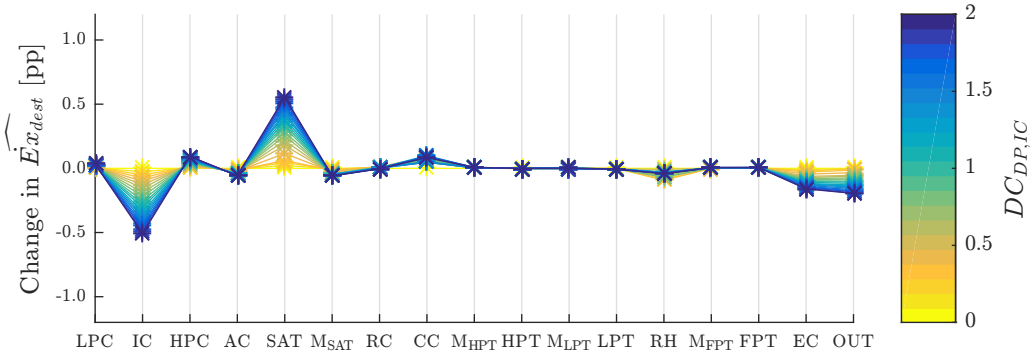

(a) Design for intercooler degradation

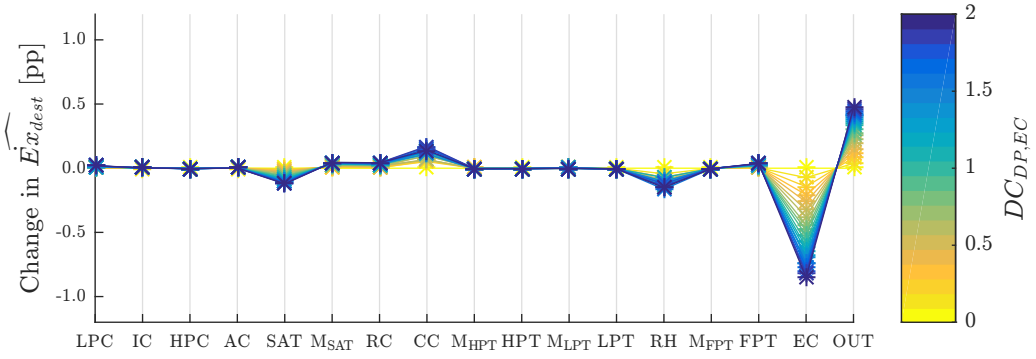

(b) Design for economiser degradation

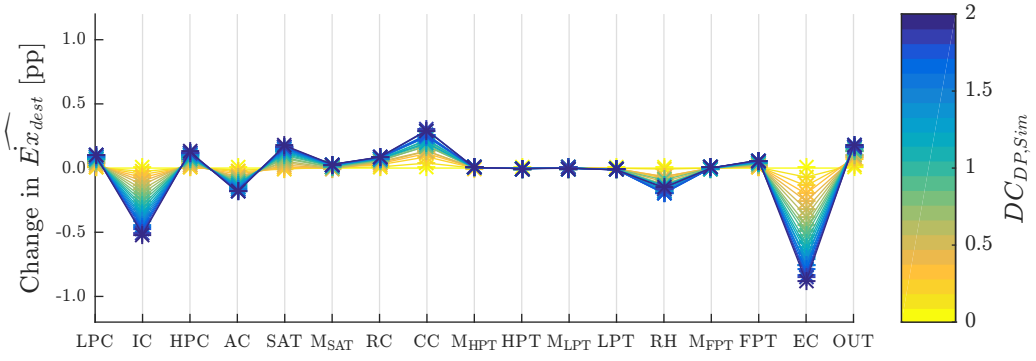

(c) Design for simultaneous heat exchanger degradation

FIGURE 6.18: Effect of the heat exchanger's preset fouling on the component's exergy destruction at *clean performance*. Average effectiveness design scenario.

$DC_{DP,EC}$=1). However, the exergy rejected to the atmosphere increases (0.24 pp), compensating the performance benefit produced by the economiser.

The exergy analysis performed for the modification of the aftercooler's design does not show any remarkable change in the exergy destroyed by any component, not even the aftercooler. This explains the lack of impact in the *clean perofrmance* of the cycle and the similarity between Figure 6.18c, and Figure 6.18a and Figure 6.18b. Figure 6.18c looks like the addition of Figure 6.18a and Figure 6.18b, with the only difference that the increment in the saturator exergy destruction is almost cancelled. This, explains the synergy effect obtained when modifying the design of the three heat exchangers simultaneously.

Further analyses on the operation of the compressors showed that no remarkable changes in their operating points at *clean performance* occurred when the prescribed fouling resistance is increased. This explains why the changes in the mass flow are not larger than 3%, except when the design of the three heat exchangers is altered simultaneously, as depicted in Figure 6.19a.

Examining Figure 6.16 and Figure 6.19a it is observed that the boost in the power output is mainly linked with the rise in the inlet mass flow. However, although the modification of the intercooler's design involves a larger increment of the inlet mass flow at *clean performance* (2.2% for a $DC_{DP,IC} = 1$) compared to the modification of the economiser (1.4% for a $DC_{DP,EC} = 1$), the effect in the power output is reversed (Figure 6.16). For a $DC_{DP,EC} = 1$ the power output rises a 3.5%, whereas for a $DC_{DP,IC} = 1$ it rises a 1.5%.

The origin of this contradictory behaviour lies in the different evolution of the specific power (Figure 6.19b). While the modification of the economiser's design enlarges the specific power at *clean performance*, the modification of the intercooler's design degrades it. This justifies the reason why the modification of the intercooler, despite it involves a larger increment of the inlet mass flow, achieves a lower boost of the power output compared with the modification of the economiser. In addition, it is observed that the variation in the specific power is linked with the modification of the humidity level (Figure 6.19b and Figure 6.19c), except when the design of the three heat exchangers is altered simultaneously. In that case, the boost in specific power comes from the reduction in the compressor work caused by the better intercooling.

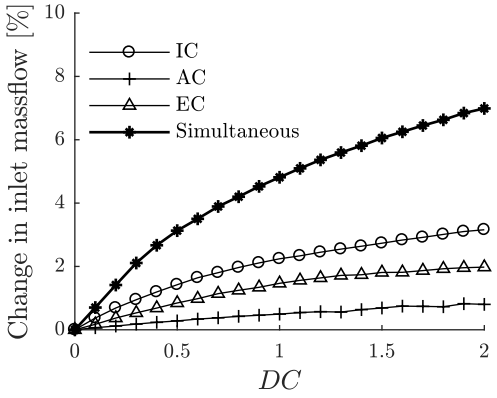

(a) Impact on the inlet mass flow

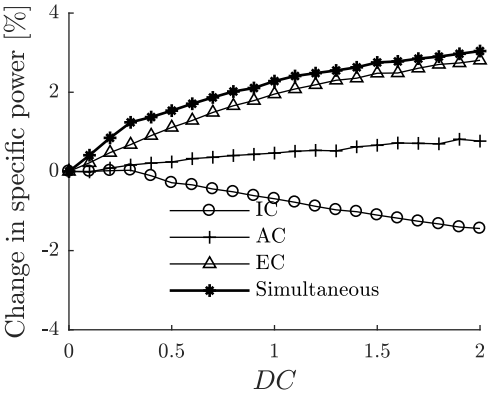

(b) Impact on the specific power

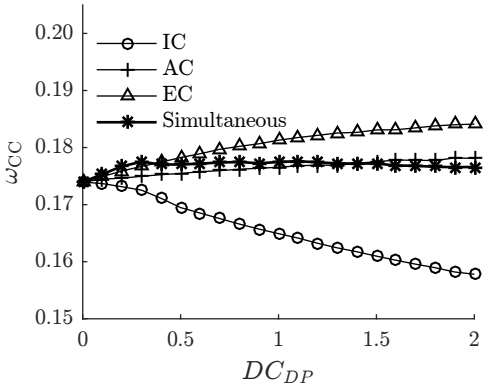

(c) Impact on ω_{CC}

FIGURE 6.19: Effect of the heat exchanger's preset fouling on the plant inlet mass flow, power, and humidity at *clean performance*. Average effectiveness design scenario.

The thermodynamic results further support the outcomes obtained from the economic analysis. Imposing a prescribed fouling resistance during the design of the heat exchangers not only avoids the future possible degradation, but also benefits the *clean performance* of the power plant. In addition, the benefits are larger as the design effectiveness reduces. This further supports the argument about obtaining larger economic and performance benefits for lower design effectiveness.

6.6 Summary

In this chapter, the effects of the air-water heat exchanges degradation on the cycle performance are analysed. The study is completed by the addition of the effects produced by the fouling and the erosion of the turbomachinery. Moreover, the

effect of designing the air-water heat exchangers with a preset fouling resistance to prevent the performance degradation is analysed from an economic and *clean performance* point of view.

The performance of the reheated humid air turbine is significantly affected by the degradation of the air-water heat exchangers. The degradation of the intercooler imposes the largest penalties on the thermal efficiency and power output of the cycle, which decrease 0.7 pp and a 13.9% respectively for the average "technology level" of the heat exchangers and standard degradation levels. The degradation of the economiser only produces a drop of just 0.2 pp in the thermal efficiency and a 2.3% in the power output for the same degradation level. On the other hand, the deterioration of the aftercooler has no remarkable influence on the performance of the power plant. When the three heat exchangers are degraded simultaneously the thermal efficiency drops 0.9 pp and the power output a 15.1%. Nevertheless, these penalties contract as the design effectiveness of the heat exchangers increases. Raising the design effectiveness from 0.75 to 0.85 reduces the thermal efficiency and power output drop around a 40%, and about a 60% when the design effectiveness increases from 0.85 to 0.95.

The exergy analysis has been proved as a useful tool to identify the sources causing the change in the performance when the heat exchangers are degraded. It has been demonstrated that the degradation of the intercooler triggers a change in the performance of several components, which include the LPC, the saturator, the recuperator, the main combustion chamber and the reheater, apart from the intercooler itself. On the other hand, the exergy analysis also revealed that the degradation of the economiser or the aftercooler does not affect the performance of the rest of the components.

In addition, by exploring the compressor's maps it has been discovered that the degradation of the intercooler can lead to stability issues in the LPC for the largest DC. Therefore, considering the installations of variable inlet guide vanes and variable geometry in the low pressure compressor during the design process is highly recommended. Thus, it would be possible to reduce the flow instabilities and the strong deterioration of its performance caused by the degradation of the intercooler.

If the fouling of the turbomachinery is also considered, together with the degradation of the heat exchangers, the deterioration of the thermal efficiency can increase

up to 2.38 pp for a 5% of fouling. The power output is reduced due to the turbomachinery fouling 19 pp more than in the clean turbomachinery case, which can lead to a total reduction of 34.1%. The erosion of the turbomachinery produces a similar effect on the thermal efficiency, while the impact on the power output is lower. If a 5% of erosion is considered, in addition to the heat exchanger deterioration, the power output drops a 27.1%. Therefore, although the heat exchangers produces a significant impact on the performance of the cycle, the deterioration of the turbomachinery implies larger penalties.

The degraded design study showed that the intercooler is the main driver of the $SPEC$ variations. If all the three heat exchangers were redesign simultaneously, presetting an standard fouling resistance, the $SPEC$ would increase a 4.7% for the high, a 1.4% for the average, and a 0.6% for the low effectiveness design scenarios. Since the extra investment required is fairly low, it might be economically beneficial to design the heat exchangers with a preset fouling resistance. This might be specially interesting for the low effectiveness design scenario, which would require the lowest extra investment and avoid the largest penalties. As the design effectiveness is increased, the possible economic benefit is reduced since the required extra investment is larger and the penalties avoided are lower.

The economic profitability is further supported by the rise in the *clean performance* of the plant derived from the degraded design of the air-water heat exchangers. The redesign of the three heat exchangers rises the *clean performance* efficiency 0.42 pp and 7.2% the power output for the average effectiveness design scenario. These changes are enlarged as the design effectiveness is reduced, which reinforces the economic profitability of redesigning low effectiveness heat exchangers.

This chapter has covered the objective of evaluating the performance degradation produced by the deterioration of the components. In addition, the economic and performance impacts of redesigning the components to reduce the degradation issues have also been assessed.

Chapter 7

Conclusions & future work

7.1 Conclusions

The work described in this thesis is intended to evaluate the potential of the reheated humid air turbine cycle for its use in power generation and marine propulsion applications. With such purpose, the conducted research aims to assess thermodynamic and economic viability of the cycle in the mentioned applications.

A design space exploration has been performed to evaluate the correlations between the cycle thermodynamic design parameters and the size, cost, weight, and performance of the power plant. The design parameters included the overall pressure ratio, the "technology level" of the saturator, and the effectiveness of the heat exchangers. The exploration has permitted to prove the feasibility of the heat exchangers and the saturator tower across the analysed range. In addition, it pointed the recuperator's and the intercooler's effectiveness as the thermodynamic design parameters with the largest influence in the overall design of the plant. An increment of 0.05 points in the recuperator's effectiveness yields to a benefit of 1.2 pp in the thermal efficiency while increasing the cost and the weight a 4.18% and an 11.08% respectively. On the other hand, a raise of 0.1 points in the intercooler's effectiveness raises the thermal efficiency 0.79 pp and increases the cost and the weight a 5.9% and a 6% respectively. The design space exploration has also permitted to identify that configurations with lower pressure ratios or saturator technologies do not offer any economic advantage, weight saving, or benefit in the thermal efficiency.

The design space exploration has also revealed that the most efficient configuration is capable of achieving a design thermal efficiency of 61.35% with a specific purchase equipment cost of 365.9 $/kW and a total weight of 57 metric tonnes. The dimensions of this power plant are 12.2 m long, 4.9 m wide, and 7.5 m high. However, the acquisition cost can decrease up to a 11.9%, in exchange of a 2.5 pp loss in efficiency, if the effectiveness of the intercooler, aftercooler, and recuperator are reduced. It is also possible to drop the weight up to a 31.2%, in exchange of a 4.6 pp loss in efficiency, if the effectiveness of the four heat exchangers are reduced. Moreover, the analysis concluded that the overall size of the plant is barely affected by the thermodynamic design variables. Instead, it is merely determined by the size of the gas turbine and the arrangement of the heat exchangers.

Depending on the allocation of the power plant or the typical route of the vessel, the ambient conditions might differ considerably, which obviously has an impact on the design of the engine and its performance. Thus, the effect of the ambient temperatures has been also evaluated. The thermal efficiency is found to have a significant dependency on the designing ambient temperature, as it drops 0.12 pp per degree Celsius increased, with no remarkable effect on the physical metrics. Oppositely, the water temperature only influences the total cost of the plant, if the designing temperature is above 25 °C, while showing no significant effect on the thermal efficiency.

The idea of using seawater as the coolant for the air-water heat exchangers carries the drawback of using materials with high fouling, corrosion, and erosion resistance. Three materials with different resistance levels have been analysed to study how they affect the acquisition cost. The 90-10 copper-nickel, used as reference material, is presented as the most economical alternative among the different materials choices for the air-water heat exchangers. A better erosion-corrosion resistance can be achieved, in exchange of a lower fouling resistance, by the use titanium grade 2. The use of titanium rises the acquisition cost from a 1% for the lowest design effectiveness, up to a 6.4% for the highest design effectiveness. It has to be mentioned that the use of titanium can reduce the overall weight of the plant from a 2% for the lowest design effectiveness, up to a 13% for the highest design effectiveness. However, the use of stainless steel offers no advantage, it increases the acquisition cost while offering a lower fouling and corrosion resistances.

In absence of a performance vessel model, the reheated humid air turbine could only be compared in terms of design point thermal efficiency and power plant's

dimensions. Compared to a reference diesel engine, the reheated humid air turbine presents an 80%-90% reduction in the total weight and 75% in the volume occupied, while achieving a thermal efficiency 7-11 pp above the diesel's efficiency value. In addition, when compared to a reference marine gas turbine the benefit in thermal efficiency grows up to 17-21 pp, although the weight and the volume are heavily penalised, becoming five to eight times heavier and two times bulkier. Therefore, from a thermodynamic point of view and having in mind that normally the fuel expenditures are several times larger than the acquisition costs, the reheated humid air turbine foresees a promising future. This engine could replace the diesel as prime mover for any application, as it is lighter, more compact, and considerably more efficient. However, for applications where the weight is a prime concern and a low fuel consumption is not a requirement, the simple gas turbine still stands as a better option. Nevertheless, to fully demonstrate the potential of the reheated humid air turbine it would be necessary to couple the engine model with a vessel model and perform a route analysis to obtain the performance and expenditures of the humid engine.

To prove the potential of the reheated humid air turbine in the energy generation market, a thermo-economic analysis has been performed. This analysis reveals that the most economic configuration is able of producing power at an average cost of the electricity of 6.74 c$/kWh. Compared to previously reported combined cycles, the reheated humid air turbine offers a 61.8% reduction in the specific purchase equipment cost and a cost of electricity 28% lower. On the hand, compared to previously reported humid cycles, the reheated version offers an 8.3% lower acquisition cost than a humid air turbine. Furthermore, thanks to its high efficiency, 10%-20% more efficient than other humid cycles, the reheated humid air turbine is able to offer a 2%-22% lower cost of the electricity. Therefore, the reheated humid air turbine not only proves to offer a better performance than combined cycles, but also stands as the most economic option among the humid cycles.

In addition, it is interesting to notice that the most economic configuration is not the most efficient. Instead, it trades the effectiveness of the intercooler and the aftercooler to reduce the acquisition cost to 345.33 $/kWh while keeping a thermal efficiency of 60.33%. Moreover, the economic analysis highlighted the large dependency of the cost of the electricity on the price of the fuel. A 10% increment in the price of the fuel yields to a 7% rise in the cost of the electricity.

Despite using materials with high resistance, the use of seawater as coolant always leads to degradation of the heat exchanger's performance due to fouling and corrosion. Consequently, a study to correlate the degradation of these components with the loss in performance has been conducted. For the analysis, the performance of the heat exchangers has been deteriorated by increasing the fouling resistance according to reference levels. As reported by the degradation studies, the performance of the reheated humid air turbine is found to be significantly affected by the degradation of the intercooler. When the intercooler is degraded up to the reference value, the power output is reduced a 13.9% and the thermal efficiency 0.7 pp for the average effectiveness design scenario. On the other hand, the degradation of the economiser has an impact four times lower on the thermal efficiency and six times lower on the power output, whereas the degradation of the aftercooler does not produce any significant penalty.

In the case that three heat exchangers are degraded simultaneously, the thermal efficiency drops 0.9 pp and the power output a 15.1% or the average effectiveness design scenario. However, these penalties contract as the design effectiveness of the heat exchangers increases. When the design effectiveness rises from 0.75 to 0.85 the penalties drop about a 40%, and around a 50% when the effectiveness increases from 0.85 to 0.95.

The exergy analysis revealed that the deterioration of the intercooler has a knock-on effect on the performance of the low pressure compressor and the reheater mainly, reducing their performance. However, the degradation of the aftercooler or the economiser does not produce any alteration in the efficiency of the rest of the components. Furthermore, the fouling of the intercooler can lead to serious reductions in the compressor surge margin, especially for the lowest effectiveness design scenarios. Therefore, the installation of variable inlet guide vanes and variable geometry in the low pressure compressor is highly recommended in order to reduce the flow instabilities and the strong deterioration of its performance caused by the intercooler's degradation.

If the deterioration of the turbomachinery is also considered while degrading the three heat exchangers simultaneously, the total penalty in the thermal efficiency grows up to 2.38 pp, instead of 0.9 pp, and the drop in the power output rises up to a 34.1% for turbomachinery fouling and up to a 27.1% for turbomachinery erosion. Thus, despite the large influence of the heat exchangers degradation on

the cycle performance, the deterioration of the turbomachinery implies even larger penalties.

Nevertheless, the penalisations derived from the heat exchangers degradation can be avoided if a preset fouling resistance is included during the design process. The fouled design would imply a 4.7% rise in the acquisition of the plant for the highest effectiveness design scenario, although the rise decreases up to a 0.6% for the lowest effectiveness design scenario. Since the extra investment is not excessively high, it might be economically worthy to design the heat exchangers with a prescribed fouling. This action is of special interest for the low effectiveness design scenarios, which would require the lowest extra investment and prevent larger penalties. However, as the design effectiveness rises, the possible economic benefit is reduced as the increment in the investment grows and the prevent loss in performance becomes lower. The possible economic profitability is further supported by the improvements in the *clean performance* obtained from the redesign of the heat exchangers, which grow as the design effectiveness is reduced. This further reinforces the possible economic for the low effectiveness designs. However, to fully prove the economic advantages, an economic analysis considering degradation derived effects should be conducted.

Overall, the conducted research has shown the promising thermodynamic performance of the reheated humid air turbine across the design space analysed while showing competitive acquisition costs. These figures have allowed to further prove the potential of the cycle to be employed for marine and energy generation applications. Nevertheless, the oprators of the power plant should pay special attention to the maintenance of the heat exchangers and the turbomachinery as the performance considerably drops when these components are degraded. In conclusion, this thesis constitutes a step forward in understanding the design and degraded performance of a new complex cycle across its design space, and appreciates the potential of such system for applications where high efficiency in addition to low overall plant volume and weight are of importance.

7.2 Future work

Despite all the research conducted so far on humid air turbines, the major disadvantage they have over their competitors is their lower Technology Readiness

Level (TRL). The main competitors of the reheated humid air turbine are power plants that have dominated the markets for more than half a century and that have ratified extensively their high operability and efficiency values. For this reason, it is necessary to demonstrate a clear benefit in performance and ensure a high operability to fully prove the benefits of the reheated humid air turbine. With that purpose and in order to close the technology gap with their competitors, it is necessary to perform further research and work towards the demonstration of the humid air turbine's capabilities. Several tasks are identified as possible guidelines to perform subsequent research activities.

The following step would be to design in detail the turbomachinery components of the cycle. The mass flow imbalance between the cold and the hot sections of the gas turbine hampers the adaptation of already existing aero-derivative or industrial power plants without compromising the performance of the cycle. The detailed design will permit to improve the accuracy of the dimensions and facilitate the integration of the different systems of the cycle.

Moreover, due the high pressure ratio, in addition to the presence of the intercooler and low mass flow required by the cycle, there exists a possibility of having design problems with the last stages of the high pressure compressor. At that section of the compressor the air is expected to have a considerably high density, occupying a very low volume. This could difficult the design of the last stages. Therefore, the detailed design of the turbomachinery would permit to identify the main design challenges and open the window to the study of possible solutions.

One of the main challenges that the reheated humid air turbine would have to face is the degradation of the heat exchangers due to the use of seawater. Despite there is available information on the public domain about the degradation of the turbomachinery components to create time-dependent models, little information exists on the degradation of the air-water heat exchangers. Therefore, it would be extremely convenient to develop a testbed for the evaluation of the time-dependent deterioration suffered by the air-water heat exchangers. This way, it would be possible to estimate how the performance of the cycle will degrade in time and increase the information about the required maintenance. In addition, these tests would permit to investigate about the most effective cleaning techniques from an economic and a feasibility point of view. Anyway, despite the use of the most effective cleaning techniques, the best solution to avoid the issues related with fouling is to use a good filtration system. Therefore, the detailed design of the

power plant should include the design of the heat exchanger's filters, as they are expected to be a key element to prevent the fouling issues.

Another major challenge will be the design of the control system of the reheated humid air turbine to handle the deign and off-design performance of the plant. Having several heat exchangers and two combustion chamber chambers increases considerably the logistics required by the control system of the cycle compared to a simple cycle. Hence, it is necessary to conduct a study about the equipment that would be necessary to keep a steady and safe operation of the power plant.

Moreover, the control system will be crucial for handling the part-load performance of the power plant. Due to the integration of new systems never employed before in the design of gas turbines, the optimum procedure to drive the power plant in off-design is still unknown. Possible methods to drive the power plant into off-design performance include the variation of the combustion temperature in both chambers simultaneously or independently, modification of the water flow through the heat exchangers, bypass of the heat exchangers, variation of the amount of air bypassing the aftercooler and saturator, and use of variable geometry to change the main gas flow. In addition, it has always to be guaranteed that the temperature does not exceed the boiling temperature inside any of the heat exchangers. As observed, there exists a vast number of different possible procedures to the drive the power plant into part-load, specially if combination of the above methods is also considered. Consequently, an investigation including all the possible methods to reduce or increase the power output of the cycle should be analysed in order to identify the most efficient one depending on the requirements.

Additional research on the load conditions required for the different applications of the reheated humid air turbine, together with the detailed design of the components of the cycle and the developed off-design thermodynamic models, would enable the possibility to perform a lifing analysis. Lifing analyses would permit to predict the expected life of the different components and elaborate overhaul schedules, as well as expand the knowledge of the required maintenance and the derived costs.

Combining the lifing and degradation information produced with the loads required, depending on the application, would permit to conduct a more detailed economic analysis with a higher fidelity. On one hand, a simulation of the engine performance integrated within a vessel is required to fully prove the potential of the

cycle for marine applications. Conducting this analysis would require to develop a vessel performance model to estimate the required power depending on the sailing conditions. Then, that model would have to be integrated with the off-design performance model of the cycle. Once both models were coupled, the performance of the new propelled vessel would have to be simulated along a baseline route and compared with the one achieved by the current propulsion alternatives.

On the other hand, the thermo-economic analysis of the cycle for its use in the power generation could be further improved if the variation of the required loads along the day, and the defined overhauls and maintenance works would be included. In addition, the variation of the ambient temperatures along the day and the seasons could also be implemented to improve the veracity of the results.

These economic analyses could be completed with a full optimisation with the objective to minimise the expenditures, or reduce emissions, or even perform a multi-objective optimisation unifying both objectives. Nevertheless, for performing such optimisation it will be necessary to develop fast prediction methods to substitute the current design models, which are significantly time-consuming. That could be done by the implementation of neural-networks or responses surfaces, which have been proven to work very well when coupled with optimisers.

Nevertheless, all the theoretical work would have to be validated via a test plan to fully ratify the promising performance of the reheated humid air turbine. Therefore, a test campaign should be created to first validate the efficiency numbers prognosticated by the theoretical work. Then, the experiments would also have to corroborate the part load operability of the cycle and test the control systems. Moreover, and most importantly, the test should also validate the integrity of the recuperator as it one of the most delicates components in the cycle. The recuperator has to stand extreme temperature, deal with large temperature and pressure gradients, and resist the expansion and retraction suffered during the start and stop of the power plant. Therefore, it is vital to check the integrity of this component as it the one recovering the largest part of the heat.

Overall, the following steps should face the design challenges of the different components and the control system. Once with the geometry defined, the best procedures to operate the plant in off-design should be identified. This information would then permit to conduct more detailed economic analyses for power and marine applications. However, for the marine applications it has to be considered

that the integration of the engine-vessel simulation platform its vital to prove the viability of the project. Last, all the theoretical work should then be verified via an experimental campaign.

Appendix A

Design model of the components and validation

This appendix introduces the description and validation of the different models employed for designing the saturator tower and the heat exchangers.

A.1 Saturator

The model of the saturator has been developed to estimate its size and weight. The model consists in a new approach that combines the work developed by Coulson and Richardson [65], and Aramayo-Prudencio and Young [69].

The following assumptions are made to simplify the sizing model:

- No variation of the flow properties in the radial direction.
- Steady conditions.
- Adiabatic component.
- Constant pressure along the tower.
- Negligible variations of the kinetic and potential energy.
- The air at the interface with the liquid water is saturated.
- Water assumed to be fresh water.

The list of input variables includes:

- The temperature, pressure, mass flow, and humidity of the gas at the bottom and at the top of the tower.
- The temperature, pressure, and mass flow of the water at the bottom and at the top of the tower.

The list of outputs provided includes:

- The diameter of the packing.
- The height of the packing.
- The main dimensions of the tower.
- The weight of the tower.

First, the diameter of the packing is calculated using the thermodynamic data and the tower packing specifications. Then, the height of the packing is calculated through an iterative process. This process starts with an initial guess of the height of the packing that permits to estimate the performance of the tower. In the next step, the estimated outlet conditions of the water and the gas are compared with the design thermodynamic data. Last, if the difference is larger than the declared threshold, the height of the packing is guessed again and the iterative process is repeated until converges of the outlet thermodynamic conditions is reached. The flowchart of the model is presented in Figure A.1.

As reported by Dalili [64] the pressure losses per length unit selected are 300 Pa/m, and the maximum velocity is 60% of the flooding velocity in order to ensure a stable operation and avoid water over-flood. The packing's dimensions (Figure A.2) are B=25 mm, H=7.9 mm, and S=14.8 mm, which are based on the values presented by Lindquist et al. [66]. The selected void fraction (ϵ) is 0.95 and the surface area per volume (A_c) is 250 m^2/m^3 based on the reference values of structured packing beds presented by Dalili [64].

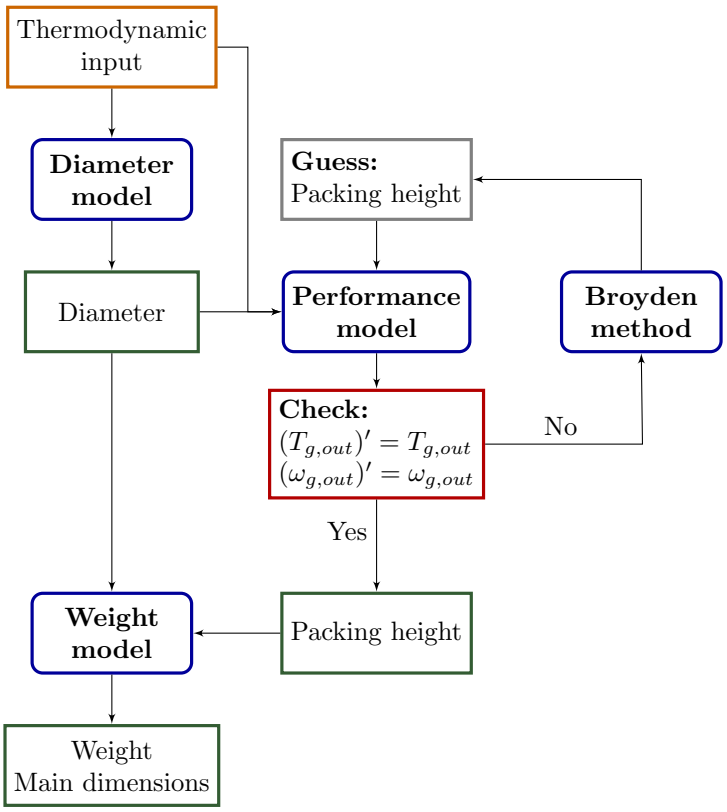

FIGURE A.1: Flowchart of the saturator's sizing model.

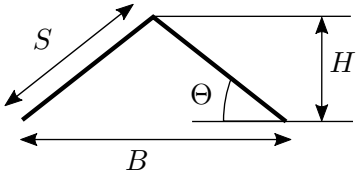

FIGURE A.2: Geometry of the saturator's packing [66].

A.1.1 Diameter calculation

The diameter of the packing is estimated using the correlations developed by Coulson and Richardson [65], which are presented in Figure A.3. $\dot{G}$ represents the mass flux, F the packing factor which has a constant value of 50 [64], μ the dynamic viscosity, ρ the density, g the gravitational constant, the subscript g the gas properties and w the liquid water properties. $\mu_{w,Ref}$ and $\rho_{w,Ref}$ are evaluated at 298.15 K and 1 atm.

The $\dot{G}_g \sqrt{\rho_g}/\dot{G}_w \sqrt{\rho_w}$ parameter, representing the x coordinate in Figure A.3, is calculated at the top and bottom of the tower. Then, for the x obtained at the top and at the bottom of the tower, the y coordinate at 60% of the flood value and the y coordinate for 300 Pa/m pressure loss are calculated. From the two y values

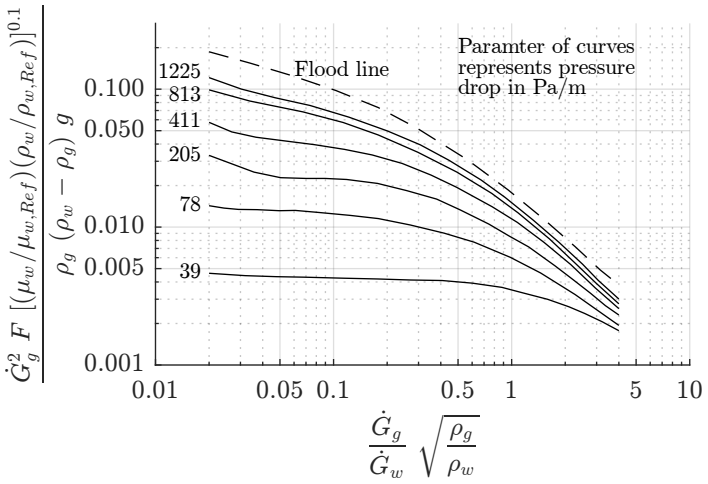

FIGURE A.3: Pressure drop correlation for structured packing bed towers [65].

obtained for each x coordinate, the minimum is selected to calculate the diameter from $\dot{G}_g$. Once the diameter is calculated at the top and the bottom stations, the largest value is selected to design the tower.

A.1.2 Height calculation

The height of the packing (H_p) is calculated by means of an iterative process based on the work developed by Aramayo-Prudencio and Young [69]. H_p is initially guessed, which permits to estimate the performance of the tower. Next, the estimated temperature and humidity of the gas at the top of the tower, and temperature and mass flow of the water at the bottom of the tower are compared against the design values. In case that the estiamted values and the design parameters differ, H_p is recalculated via a Boryden method [126] until the calculated conditions at the outlet of both flows match the known thermodynamic design conditions (Figure A.1).

For estimating the performance of the saturator, the packing is divided into sections of 25 mm of height (dz) illustrated in Figure A.4. In each section, the steady-flow energy equation (Eq. A.1) is solved to obtain the interface temperature (T_f). To solve this equation, it is assumed that the heat transfer is driven by temperature gradients and the heat transfer coefficient, and the mass transfer process is driven by density gradients and the mass transfer coefficient. This allows the derivation of Eq. A.2, Eq. A.3, and Eq. A.4.

$$d\dot{Q}_{w\to f} + d\dot{Q}_{g\to f} = h_{fg}@(T_f)\ d\dot{m}_v \tag{A.1}$$

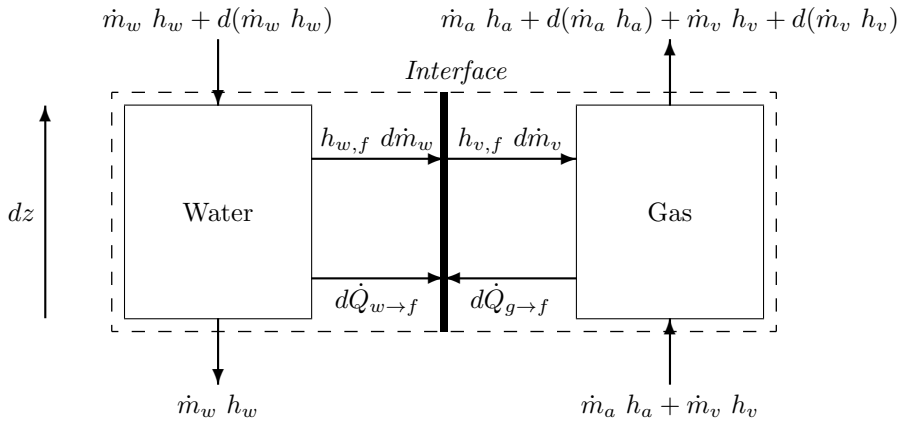

FIGURE A.4: Heat and mass transfer in a differential element of the saturator.

where $h_{fg}@(T_f)$ is the specific enthalpy of evaporation evaluated at the interface temperature. The heat transferred from the water to the interface ($d\dot{Q}_{w\to f}$) is calculated accordingly to Eq. A.2, where α_w represents the heat transfer coefficient between the water and the interface, T_w the bulk water temperature, A_{cross} is the cross sectional area of the tower, and A_c the contact area between the water and air per volume unit.

$$d\dot{Q}_{w\to f} = \alpha_w\ (T_w - T_f)\ A_c\ A_{cross}\ dz \tag{A.2}$$

The heat transferred from the gas to the interface ($d\dot{Q}_{g\to f}$) is calculated according to Eq. A.3, where α_g represents the heat transfer coefficient between the gas and the interface and T_g the bulk gas temperature.

$$d\dot{Q}_{g\to f} = \alpha_g\ (T_g - T_f)\ A_c\ A_{cross}\ dz \tag{A.3}$$

The water mass flow evaporated in each section (dm_v) is calculated by means of Eq. A.4, where λ_g^* represents the mass transfer coefficient between the humid air and the interface, $\rho_{v,f}$ the vapour mass concentration per volume at the interface, and ρ_v the vapour mass concentration per volume at the bulk gas.

$$d\dot{m}_v = \lambda_g^*\ (\rho_{v,f} - \rho_v)\ A_c\ A_{cross}\ dz \tag{A.4}$$

After dividing the tower in sections of constant height, the gas water temperature, and the air humidity are intitally guessed at each section and node. Then, Eq. A.1 is solved at each node by means of an iterative process. Once the interface temperature has been calculated, a pseudo-transient model proposed by Aramayo-Prudencio and Young [69] (Eq. A.5 and Eq. A.6) is used to update the initially guessed temperature distributions, where $\bar{T}$ is the average temperature of the section. This process is repeated until convergence between $\bar{T}^n$ and $\bar{T}^{n+1}$ is reached, where $\bar{T}^n$ represent the average section temperature for the n iteration and c_p is the specific heat capacity. The relaxation factor RX_w and RX_g have been tuned to improve the convergence of the model, their values are 2.4 10^{-4} and 4.8 10^{-4} respectively. The flowchart of the performance model employed to compute H_p is presented in Figure A.5.

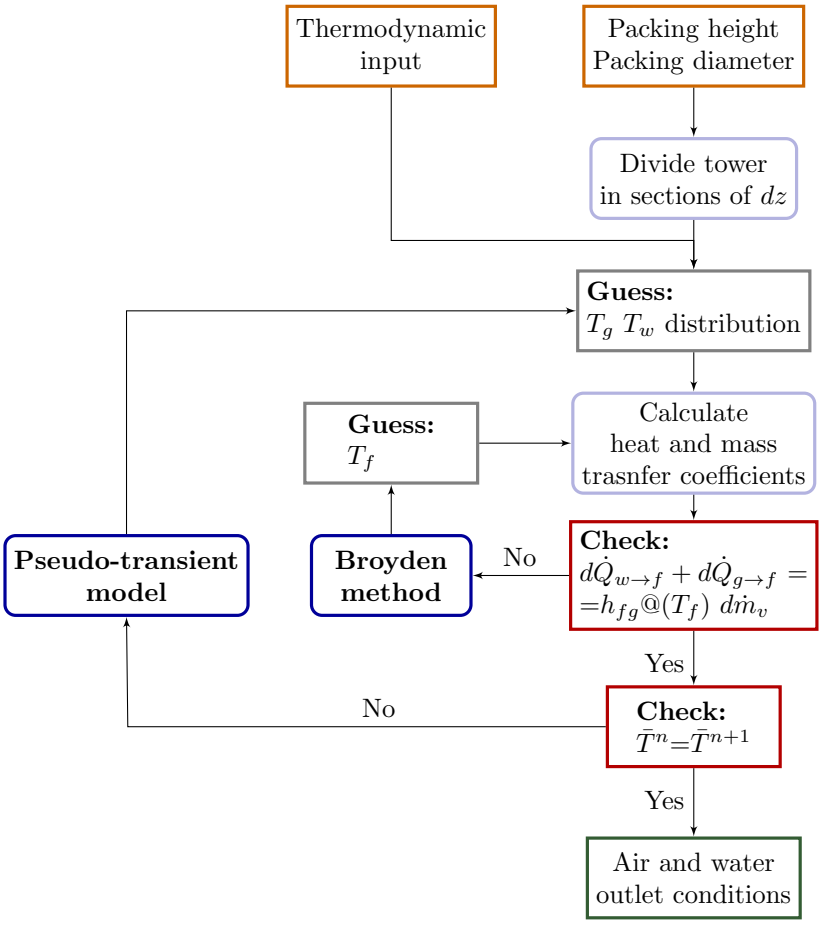

FIGURE A.5: Flowchart of the saturator off-design performance model.

$$\bar{T}_w^{n+1} = \bar{T}_w^n + \left(\frac{RX_w}{\dot{m}_a\ c_{p_w}}\right)\Big[\bar{\dot{m}}_w\ \Delta h_w^n - \\ - \bar{\alpha}_w\left(\bar{T}_w - \bar{T}_f\right) A_c\ A_{cross}\ \Delta z + \left(\bar{h}_w^n - \bar{h}_{w,f}^n\right)\Delta\dot{m}_v^n\Big] \tag{A.5}$$

$$\bar{T}_g^{n+1} = \bar{T}_g^n + \left(\frac{RX_g}{\dot{m}_a\ c_{p_a}}\right)\Big[-\bar{\dot{m}}_a\ \Delta h_a^n - \bar{m}_v\ \Delta h_v^n - \\ - \bar{\alpha}_g\left(\bar{T}_g - \bar{T}_f\right) A_c\ A_{cross}\ \Delta z + \left(\bar{h}_{v,f}^n - \bar{h}_v^n\right)\Delta m_v^n\Big] \tag{A.6}$$

The heat and the mass transfer coefficients are calculated by means of the following semi-empirical correlations.

Water heat transfer coefficient

The heat transfer coefficient between the water and the interface is calculated using Eq. A.7, suggested by Lindquist et al. [66].

$$\alpha_w = \frac{k_w}{t_w} \tag{A.7}$$

where k_w is the thermal conductivity of the water, and t_w is the thickness of the water film estimated by

$$t_w = \left(\frac{3\ \mu_w\ \Gamma}{\rho_w^2\ g}\right)^{0.333} \tag{A.8}$$

where Γ is the mass flow per unit of length obtained with Eq. A.9.

$$\Gamma = \frac{\dot{m}_w}{A_{cross}\ Per} \tag{A.9}$$

A_{cross} is the cross-flow area of the packing, and Per is the perimeter defined as

$$Per = \frac{4\ S}{B\ H} \tag{A.10}$$

Mass transfer coefficient

The mass transfer coefficient between the gas and the interface is estimated using Eq. A.11. The correlation was first employed by Bravo et al. [141, 142] for triangular flow channels.

$$\lambda_g = \frac{Sh\ D_{wg}}{d_{eq}} \tag{A.11}$$

where Sh is the Sherwood number calculated as in Eq. A.13, D_{wg} is the diffusion coefficient between the water and the gas defined in Eq. A.18, and d_{eq} is the equivalent diameter determined as

$$d_{eq} = B\ H\ \left(\frac{1}{B + 2\ S} + \frac{1}{2\ S}\right) \tag{A.12}$$

The Sherwood number represents the ratio of the convective mass transfer to the rate of diffusive mass transport, and in this occasion is calculated as

$$Sh = 0.00338\ Re^{0.8}\ Sc^{0.333} \tag{A.13}$$

where Re is the Reynolds number, and Sc is the Schmidt number. The Schmidt number is defined as

$$Sc = \frac{\mu_g}{\rho_g\ D_{wg}} \tag{A.14}$$

The Reynolds number is calculated as

$$Re = \frac{\rho_g\,(u_{g,eff} + u_{w,eff})\,d_{eq}}{\mu_g} \tag{A.15}$$

where $u_{g,eff}$, and $u_{w,eff}$ are effective velocities of the gas and water respectively. The effective velocity of the gas is determined by

$$u_{g,eff} = \frac{\dot{m}_g}{\rho_g\ A_{cross}\ \epsilon\ \sin\Theta} \tag{A.16}$$

where $\Theta = \arcsin(H/S)$ is the angle of inclination of the triangular channels in the packing.

The effective velocity of the water is defined as

$$u_{w,eff} = \frac{3\ \Gamma}{2\ \rho_w} \left(\frac{\rho_w^2\ g}{3\mu_w\ \Gamma} \right)^{0.333} \tag{A.17}$$

Finally, the diffusion coefficient between the water and the gas is estimated using the Fuller-Schettler-Giddings definition.

$$D_{wg} = \frac{10^{-7}\ T_g^{1.75}\ \left(\frac{1}{M_g} + \frac{1}{M_w} \right)^{0.5}}{P\ \left(v_g^{1/3} + v_w^{1/3} \right)^2} \tag{A.18}$$

where M_g and M_w are the molecular weights of the gas and water respectively, P is the absolute total pressure in atm, and v_g and v_w are the diffusion volumes of the gas and water respectively. The values for the diffusion volumes were taken from the work presente by Gesellschaft [143], $v_g = 19.7$ and $v_w = 13.1$.

Mass transfer coefficient corrections

In order to take into account the non-negligible distortion effects in the concentration, velocity, and temperature profiles produced by the high mass transfer rates, it is necessary to correct the mass transfer coefficient using the Ackerman's correction factor, as suggested by Parente et al. [72].

$$\lambda_g^* = \frac{\Phi_M}{e^{\Phi_M} - 1}\ \lambda_g \tag{A.19}$$

where λ_g^* is the corrected mass transfer coefficient and Φ_M is the Ackerman's correction factor defined as

$$\Phi_M = \frac{d\dot{m}_v / A_{cross}}{M_w} \Big/ \frac{\lambda_g\ \rho_g}{M_g} \tag{A.20}$$

Gas heat transfer coefficient

To calculate the heat transfer coefficient of the gas, it is necessary to employ the Chilton-Colburn analogy, which relates the heat transfer coefficient with the mass transfer coefficient.

$$\alpha_g = \rho_g \ \lambda_g^* \ c_{p_g} \ \left(\frac{Pr}{Sc}\right)^{-2/3} \tag{A.21}$$

where Pr is the Prandtl number defined as in Eq. A.22 and k_g represents the thermal conductivity of the gas.

$$Pr = \frac{c_{p_g} \ \mu_g}{k_g} \tag{A.22}$$

A.1.3 Weight calculation

Once the packing is sized, the rest of the dimensions of the tower can be derived, as shown in Figure A.6. The thickness of the vessel is calculated using the ASME Boiler and Pressure Vessel Code [144]. The outlet cone is approached as a conical head, the packing section as a cylindrical vessel, and the bottom part as a torispherical head. Then, the weight of the vessel is calculated based on the volume of the material required and the density of the material. The weight of the packing is derived from the volume it occupies and the void fraction. The procedure does not account for the weight of the droplet eliminator or the water distribution system as they are assumed to be negligible in comparison to the total weight.

A.1.4 Validation

The sizing model has been validated against the experimental data reported by Lindquist et al. [66]. Table A.1 shows the validation of the sizing model where discrepancies no larger than 0.5% were observed in the outlet conditions of the gas. Nevertheless, the water exit temperature was over-predicted by 1.6%. This is attributed to the perfect fluid assumption and the assumption of considering the gas a mixture of ideal gases. It must be mentioned that the validation height of the packing in Lund University considers the actual height of the packing plus

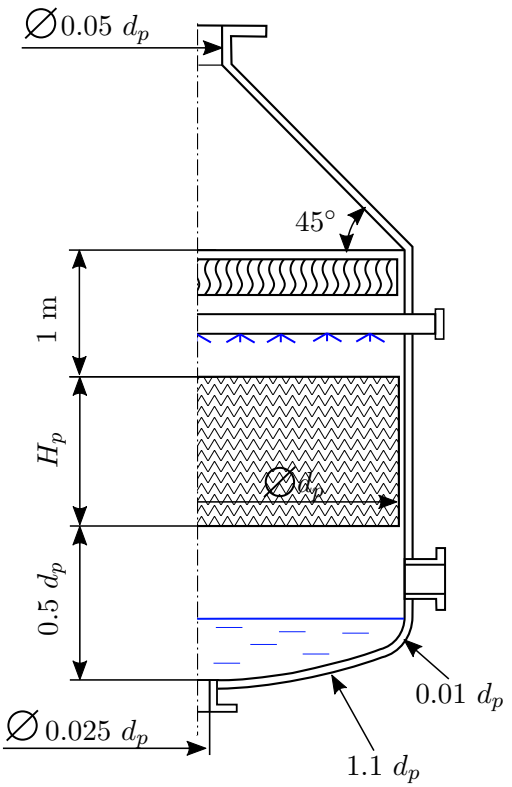

FIGURE A.6: Dimensions of the saturator tower.

the equivalent height of the droplets zone before and after the packing-bed, which also contributes to the heat and mass transfer. Therefore, when using this method the calculated height of the packing is expected to be overestimated by 100 mm, approximately, since it also includes the droplets zone.

TABLE A.1: Validation of the tower's packing height model against experimental data from [66].

Inlet/Input conditions			Outlet conditions				
	Units	Data		Units	Data	Model	Discrepancy
$m_{g,1}$	(kg/s)	2.17	$m_{g,2}$	(kg/s)	2.55	2.57	0.7%
$T_{g,1}$	(K)	346.75	$T_{g,2}$	(K)	389.15	389.97	0.2%
p_1	(bar)	7.88	ω_2	(-)	0.18	—	—
$m_{g,2}$	(kg/s)	3.48	$m_{w,1}$	(kg/s)	3.10	3.11	0.4%
$T_{w,2}$	(K)	419.35	$T_{w,1}$	(K)	352.85	358.67	1.6%
H_p	(m)	0.57					

A.2 Plate-fin heat exchangers

The model of the plate-fin heat exchangers has been developed to estimate the size and weight of the intercooler, aftercooler, and recuperator. The calculation procedure is based on the effectiveness-Number of Transfer Units ($\varepsilon - NTU$) method presented by Kays and London [90]. The model considers different geometry arrangements (multi-pass cross counterflow, single-pass counter-current), different working fluids (air and water), and different internal configurations (serrated-fins and plain-fins).

The following assumptions are made to simplify the model:

- Steady conditions.
- Adiabatic component.
- The thermodynamic properties of the fluids are calculated at the average temperature of the fluid.
- Constant pressure along the component.
- Water assumed to be fresh water.

First, using the thermodynamic data and the geometry arrangement, the effectiveness (ε) and the heat capacity ratio (C^*) of the heat exchanger are calculated. Then, these values are employed to obtain the Number of Transfer Units (NTU) and the consequent thermodynamic size (UA). Next, by means of an iterative procedure the full geometry that matches the calculated UA, for the given thermodynamic conditions, is obtained. Once the geometry is calculated, it is possible to finally estimate the weight of the component. The flowchart of the model is presented in Figure A.7.

A.2.1 Recuperator. Single-pass counter-flow configuration

The inputs variables for the model are:

- The temperature, pressure, mass flow, and humidity of the hot gas at the inlet and the outlet.

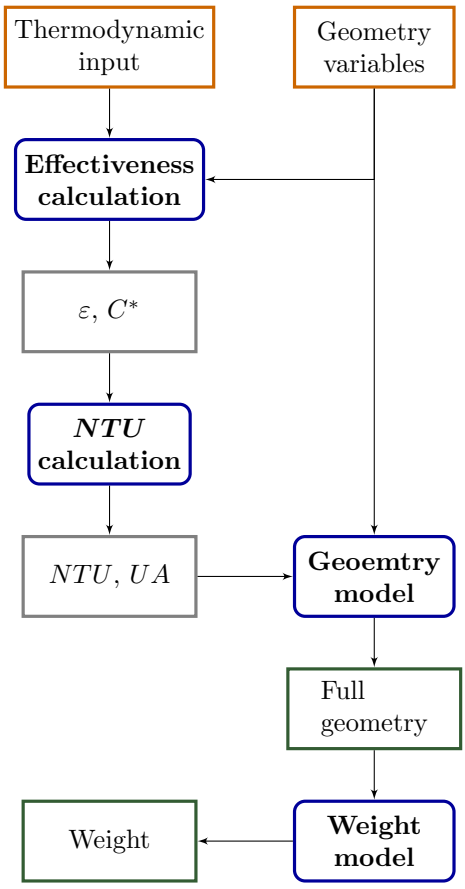

FIGURE A.7: Flowchart of the heat exchangers sizing model.

- The temperature, pressure, mass flow, and humidity of the cold gas at the inlet and the outlet.
- The number of hot layers per pass (N_l). The number of layers of the cold pass is always equal to $N_l + 1$.
- The height of the fins (h_f) of the cold and hot side.
- The length of the fins (L_f).
- The density of fins (N_f) of the cold and hot side.
- The minimum thickness of the fins (t_f).
- The width of the heat exchanger (L_{Nf}).
- The material of the heat exchanger.
- The preset fouling of (R_f) of the cold and hot side.

The outputs obtained are:

- The pressure losses on both sides.
- The total height.
- The length of the flow passage.
- The weight of the component.

First, ε and C^* of the heat exchanger are calculated as:

$$\varepsilon = \frac{\max\left[(T_{c,out} - T_{c,in}), (T_{h,in} - T_{h,in})\right]}{T_{h,in} - T_{c,in}} \tag{A.23}$$

$$C^* = \frac{\min(\dot{m}_c \ c_{p_c}, \dot{m}_h \ c_{p_h})}{\max(\dot{m}_c \ c_{p_c}, \dot{m}_h \ c_{p_h})} \tag{A.24}$$

where the subscript c stands for cold side and h for hot side. Once ε and C^* are obtained, the NTU is derived from the correlations presented in Figure A.8, developed by ESDU [91] for counter-current configurations. Next, the UA is calculated as in Eq. A.25.

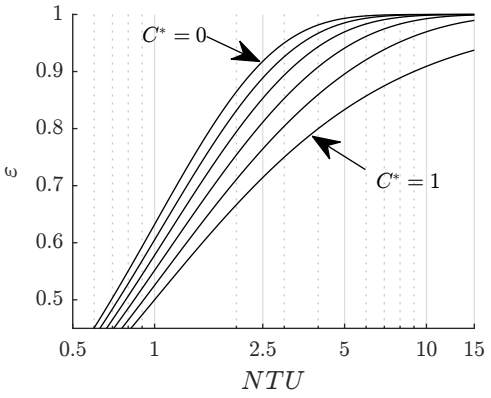

FIGURE A.8: Correlation between the effectiveness and the number of transfer units for a counter-current heat exchanger.

$$UA = \frac{NTU}{\min(\dot{m}_c \ c_{p_c}, \dot{m}_h \ c_{p_h})} \tag{A.25}$$

The inverse of UA is defined as the total resistance of the heat exchanger. It is composed by the sum of the resistances of the different media involved (hot and cold fluid, and the heat exchange walls), as presented in Eq. A.26.

$$\frac{1}{UA} = \left(\frac{1}{\alpha\ \eta_o\ A_{HX}} + \frac{R_f}{A_{HX}}\right)_c + R_{wl} + \left(\frac{1}{\alpha\ \eta_o\ A_{HX}} + \frac{R_f}{A_{HX}}\right)_h \tag{A.26}$$

where α is the heat transfer coefficient, η_o is the overall efficiency of the extended surfaces, R_f is the fouling resistance, and A_{HX} is the heat transfer area. R_{wl} is the resistance of the wall to the heat transfer process, which is defined in Eq. A.27.

$$R_{wl} = \frac{t_{wl}}{k_{wl}\ A_{wl}} \tag{A.27}$$

where t_{wl} is the thickness of the wall, k_{wl} is the thermal conductivity of the wall, and A_{wl} is the surface area of the wall.

To obtain the full geometry of the heat exchanger, an iterative process is employed to converge the actual value of the length of the flow passage (L_{flow}). This process is carried as follows:

1. Guess the initial value of L_{flow}.
2. Calculate the heat transfer areas.
3. Calculate the heat transfer coefficients of the hot and cold sides.
4. Calculate the overall effectiveness of the extended surfaces of the hot and cold sides.
5. Calculate the right term of the Eq. A.26.
6. Calculate the error between the target UA and the $(UA)_{calc}$. If convergence is reached, the problem is solved. Otherwise, L_{flow} is recalculated and the iterative process is repeated from step 2.

Once the final dimensions of the heat exchanger are obtained, the pressure losses are calculated for both sides, as well as the weight of the component.

A.2.2 Recuperator. Multi-pass cross counterflow configuration

The inputs variables for the model are:

- The temperature, pressure, mass flow, humidity of the hot gas at the inlet and the outlet.
- The temperature, pressure, mass flow, and humidity of the cold gas at the inlet and the outlet.
- The number of passes (N_p).
- The number of hot layers per pass (N_l). The number of layers of the cold pass is always equal to $N_l + 1$.
- The height of the fins (h_f) of the cold and hot side.
- The length of the fins (L_f).
- The density of fins (N_f) of the cold and hot side.
- The minimum thickness of the fins (t_f).
- The length of the cold flow passage (L_{flow_c}).
- The material of the heat exchanger.
- The preset fouling of (R_f) of the cold and hot side.

The outputs obtained are:

- The pressure losses on both sides.
- The total height.
- The length of the hot flow passage.
- The weight of the component.

First, ε and C^* are calculated based on the design thermodynamic conditions by means of Eq. A.23 and Eq. A.24. Then, the effectiveness of each pass (ε_{pass}) is calculated with the following equation [90].

$$\varepsilon_{pass} = \begin{cases} \dfrac{\varepsilon}{N_p\ (1-\varepsilon)+\varepsilon}, & \text{if } C^* = 0 \\ \dfrac{[(1-C^*\ \varepsilon)/(1-\varepsilon)]^{1/N_p}-1}{[(1-C^*\ \varepsilon)/(1-\varepsilon)]^{1/N_p}-C^*}, & \text{otherwise} \end{cases} \tag{A.28}$$

Once ε_{pass} is obtained, the NTU of one pass (NTU_{pass}) is derived from the correlations presented in Figure A.9, developed by ESDU [91]. This makes possible to calculate the UA of a pass (UA_{pass}) using Eq. A.25, where NTU_{pass} substitutes NTU. The internal arrangement is solved for only one pass. Then, the passes are packed one upon the other and the total A_{HX}, the total NTU, and the total UA are calculated by addition of the values obtained.

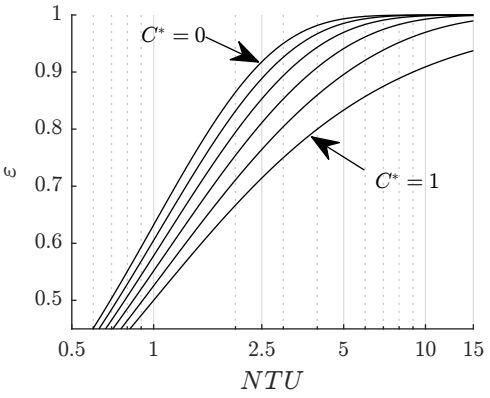

FIGURE A.9: Correlation between the effectiveness and the number of transfer units for a cross-flow heat exchanger.

To estimate the full geometry of the pass, an iterative process is employed to converge the actual value of the length of the hot flow passage (L_{flow_h}). This process is carried as follows:

1. Guess the initial value of L_{flow_h}.
2. Calculate the heat transfer areas.
3. Calculate the heat transfer coefficients of the hot and cold sides.

4. Calculate the overall effectiveness of the extended surfaces of the hot and cold sides.

5. Calculate the right term of the Eq. A.26.

6. Calculate the error between the target UA and the $(UA)_{calc}$. If convergences is reached, the problem is solved. Otherwise, L_{flow_h} is recalculated and the iterative process is repeated from step 2.

Once the final dimensions of the heat exchanger are obtained, the pressure losses are calculated for both sides, as well as the weight of the component.

A.2.3 Intercooler and aftercooler

The inputs variables for the model are:

- The temperature, pressure, mass flow, and humidity of the air at the inlet and the outlet.
- The temperature, pressure, and mass flow of the water at the inlet and the outlet.
- The number of hot layers per pass (N_l). The number of layers of the cold pass is always equal to $N_l + 1$.
- The height of the fins (h_f) of the air and water-side.
- The length of the fins (L_f).
- The density of fins (N_f) of the air and water-side.
- The minimum thickness of the fins (t_f).
- The length of the water passage (L_{flow_w}).
- The width of the water passage (L_p).
- The material of the heat exchanger.
- The preset fouling of (R_f) of the gas and water side.

The outputs obtained are:

- The pressure losses on both sides.
- The total height.
- The number of passes and the total length of the air channel.
- The weight of the component.

Since the designs of the intercooler and the aftercooler always present more than five passages, it is possible to assume that they have a counter-current configuration for calculating the required UA [117]. Thus the process to obtain the design UA value is the same as the one followed for the counter-flow recuperator.

To obtain the full geometry of the heat exchanger, an iterative process is employed to converge the actual value of the number of passes. This process is carried as follows:

1. Guess the initial value of N_p.
2. Calculate the heat transfer areas.
3. Calculate the heat transfer coefficients of the air-side and water-side.
4. Calculate the overall efficiency of the extended surfaces of the air-side and water-side.
5. Calculate the right term of the Eq. A.26.
6. Calculate the error between the target UA and the $(UA)_{calc}$. If convergence is reached, the problem is solved. Otherwise, N_p is recalculated and the iterative process is repeated from step 2.

Once the final dimensions of the heat exchanger are obtained, the pressure losses are calculated for both sides, as well as the weight of the component weight.

A.2.4 Areas and coefficients calculation

The procedure to calculate the heat transfer areas and the heat transfer coefficients is analogous for the three configurations since they present the same internal architectures.

Heat transfer area

The heat transfer area is calculated as the sum of the area of the fins (A_f), the area of the walls (A_{wl}), and the area of the header plates (A_{header}). The process is analogous for either the cold or the hot side as long as the fluid is gas. However, when calculating A_f for the water-side Eq. A.29 must be employed, and when calculating A_f for the air-side Eq. A.30 must be employed.

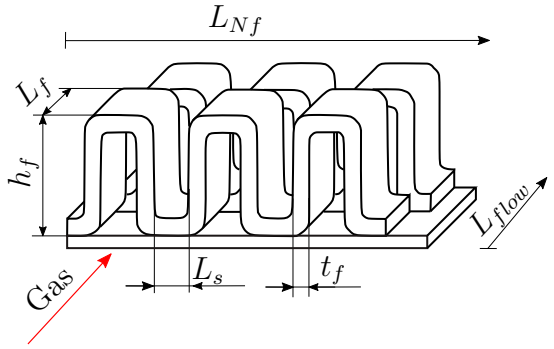

(a) Serrated configuration, air-side

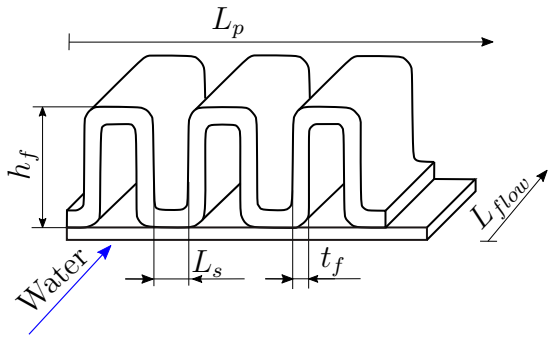

(b) Plain configuration, water-side

FIGURE A.10: Plate-fin geometry.

$$A_{f_w} = 2\ h_f^*\ N_f\ L_p\ L_{flow}\ N_l\ N_p \tag{A.29}$$

$$A_{f_a} = 2\ h_f^*\ N_f\ L_{Nf}\ L_{flow}\ N_l + \\ + \frac{\left[h_f^*\ t_f + t_f\ \ (0.5/N_f - t_f)\right]\ 2\ N_f\ L_{flow}\ L_{Nf}\ N_l}{L_f} \tag{A.30}$$

where $h_f^* = h_f - t_f$ is the height of the flow passage. L_{Nf} is the total width of the passage. It has to be added that in the case of the intercooler and aftercooler

designs the length of the air passage is equal to the width of the water passage times the number of passes ($L_{flow_a} = N_p\ L_p$).

$$A_{wl} = (L_{Nf} - t_f\ N_f\ L_{Nf})\ \ 2\ N_l\ L_{flow} \tag{A.31}$$

$$A_{header} = 2\ h_f^*\ N_l\ L_{flow} \tag{A.32}$$

Once the three areas have been calculated, the total heat transfer area is simply calculated as the sum of the three areas.

$$A_{HX} = A_f + A_{wl} + A_{header} \tag{A.33}$$

Air-side heat transfer coefficient and pressure losses

The heat transfer coefficient and the friction factor of the air-side are calculated according to the method published by Yang and Li [92]. Before calculating the coefficients, the free-flow area (A_{free}) is calculated as:

$$A_{free} = h_f^*\ L_s\ N_f\ L_{Nf}\ N_l \tag{A.34}$$

where $L_s = 1/N_f - t_f$ is the fin spacing. Next the mass flux is obtained using Eq. A.35 and the hydraulic diameter (D_h) by means of Eq. A.36.

$$\dot{G} = \frac{\dot{m}}{A_{free}} \tag{A.35}$$

$$D_h = \frac{4\ L_s\ h_f^*\ L_f}{2\ (L_s\ L_f + h_f\ L_f + t_f\ h_f) - t_f\ L_s} \tag{A.36}$$

Once the $\dot{G}$ and D_h are known, the Reynolds number is estimated using the following equation.

$$Re = \frac{\dot{G}\ D_h}{\mu} \tag{A.37}$$

The heat transfer coefficient is calculated using the Chilton-Colburn factor (j) which is obtained from Eq. A.38.

$$j = 2.34812 \left(\frac{L_f}{De}\right)^{0.19411} \Omega^{0.00656}\ a^{-0.35987}\ c^{0.10391}\ de^{-0.45337}\ Re_j^* \tag{A.38}$$

where $De = 2h_f\ L_s/h_f + s$, $a = t_f/h_f$, $c = t_f/L_s$, $de = t_f/L_f$ are geometric parameters, and Ω is the combined non-dimensional parameter calculated as in Eq. A.39. The Re_j^*, obtained by means of Eq. A.40, is a cubic polynomial that describes the log-linear correlation between j and the Reynolds number.

$$\Omega = \left(\frac{1}{a} + \frac{1}{2\ c} - 2\right)^{2\ c\ (1-a)+c\ (1-2\ a)} + \frac{4\ c\ (1-a) + a\ (1-2\ c)}{4\ (a + c - 2\ a\ c)} \tag{A.39}$$

$$\begin{aligned} R_j^* = \exp\Bigg[& -1.01546\ \ln(Re) + 0.05633\ (\ln(Re))^2 - \\ & - 0.00064 \left(\frac{h_f}{De}\right)^{0.49317} c^{-0.16019}\ (\ln(Re))^3 \Bigg] \end{aligned} \tag{A.40}$$

Once j is calculated, the heat transfer coefficient is obtained applying the Chilton-Colburn analogy:

$$\alpha = j\ c_p\ \dot{G}\ Pr^{2/3} \tag{A.41}$$

The friction factor (f) for calculating the pressure losses is obtained by means of Eq. A.42 and Eq. A.43.

$$\begin{aligned} f = 2300.24 \left(\frac{L_f}{De}\right)^{-1.42491} & \Omega^{0.26188} \left(\frac{1}{1-2\ a}\right)^{2.04570} \\ & \left(\frac{1}{1-2\ c}\right)^{2.16338} de^{-0.93414}\ Re_f^* \end{aligned} \tag{A.42}$$

$$R_f^* = \exp\Bigg[-4.52412\ \ln(Re) + 0.49785\ (\ln(Re))^2 - \\ -0.0158 \left(\frac{h_f}{De}\right)^{0.00222}\ c^{-0.08664}\ (\ln(Re))^3 \Bigg] \tag{A.43}$$

Last, the pressure drop ΔP is obtained using the following expression, which only considers the pressure losses due to friction along the passages.

$$\Delta P = \frac{4\ f\ L_{flow}\ \dot{G}^2}{2\ \rho\ D_h} \tag{A.44}$$

Water-side heat transfer coefficient and pressure losses for water

The geometry employed on the water-side passages, plain fins, can be approximated as circular tubes with an equivalent hydraulic diameter, as shown in Eq. A.45.

$$D_h = \frac{4\ L_s\ h_f^*}{2\ (L_s + h_f^*)} \tag{A.45}$$

Then, the Reynolds number is calculated using Eq. A.37, where $\dot{G}$ is obtained by means of Eq. A.35. The free flow are for the water-side is obtained using Eq. A.46.

$$A_{free} = h_f^*\ L_s\ N_f\ L_p\ (N_l + 1) \tag{A.46}$$

Prior the estimation of the coefficients, the flow is classified according to its Reynolds number as a turbulent or laminar fluid. It is assumed to be turbulent when Re >4,000, otherwise it is assumed to be laminar [93]. The coefficients are calculated following the procedures presented in the ESDU data items [93, 94].

$$f = \begin{cases} \dfrac{1}{4(1.82\ \log_{10}(Re) - 1.64)^2}, & \text{if } Re > 4000 \\ \\ \dfrac{16}{Re}, & \text{otherwise} \end{cases} \tag{A.47}$$

$$Nu = \begin{cases} \dfrac{f/2\ (Re)\ Pr}{1.07 + 1.27\ \sqrt{f/2}\ (Pr^{2/3} - 1)}, & \text{if } Re > 4000 \\ \\ \left(84.11 + (2.117\ Gz^{1/3} - 0.6)^3\right)^{1/3}, & \text{otherwise} \end{cases} \tag{A.48}$$

were Gz is the Graetz number calculated as in Eq. A.49 and Re is obtained as in Eq. A.37.

$$Gz = \frac{\pi\ Re\ Pr\ D_h}{4\ L_{flow}} \tag{A.49}$$

Finally, the heat transfer coefficient is obtained from the Nusselt number definition, Eq. A.50, and the pressure losses using Eq. A.44.

$$\alpha = \frac{Nu\ k}{2\ D_h} \tag{A.50}$$

Overall effectiveness of the extended surfaces

Despite the high thermal conductivity of the metals, the temperature of the fins can be non-uniform. Thus, it is necessary to employ a correction factor to take this fact into consideration. The overall effectiveness of the extended surfaces (η_o) is calculated accordingly to the method explained in the ESDU Data Items [88].

$$\eta_o = 1 - \frac{A_f}{A_{HX}}\ (1 - \eta_f) \tag{A.51}$$

The fin efficiency (η_f) is obtained from Eq. A.53, where m^* is a coefficient calculated with Eq. A.52.

$$m^* = h_f\ \sqrt{\frac{\alpha}{2\ t_f\ k_w}} \tag{A.52}$$

$$\eta_f = \frac{\tanh(m^*)}{m^*} \tag{A.53}$$

A.2.5 Weight calculation

Once the dimensions of the fins have been defined (N_f and h_f), and before calculating any of the areas or coefficients, the thickness of the fins, the endwalls, and the plates are determined using the ASME Boiler Pressure Vessel Code [144]. The geometry between two plates is approximated as a rectangular vessel with multiple stay plates, represented by the fins. The thickness is calculated for the hot and the cold sides, and the maximum one is selected. If any of the calculated thickness is not larger than the minimum thickness of the fins, the value of the minimum thickness of the fins is selected. Once the volume of the required material is calculated, the total weight is obtained based on the density of the material. The procedure does not account for the weight of the headers as they are not designed.

A.2.6 Validation

The sizing model has been validated against data obtained from a model developed by Traverso and Massardo [145]. Table A.2 shows the validation results, where the largest discrepancy is of 5.29% on the L_{flow}. The different correlations employed to obtain the heat transfer coefficients are the cause of the discrepancies between both results.

A.3 Economiser

The model of the economiser has been developed to estimate its size and the weight. The calculation procedure of the dry part, where no condensation takes place, is based on the $\varepsilon - NTU$ method presented by Kays and London [90], whereas the wet part, where the moisture condensates over the tube, is calculated based on the model presented by Gesellschaft [96].

The following assumptions are made to simplify the calculations:

- Steady conditions.
- Adiabatic component.

TABLE A.2: Validation of the plate-fin heat exchanger model against data from [145].

Input data					
Thermodynamics			Geometry		
	Units	Data		Units	Data
$T_{c,in}$	(K)	467.15	N_l	(-)	44.00
$T_{c,out}$	(K)	852.56	h_{f_c}	(mm)	1.91
$T_{h,in}$	(K)	910.15	h_{f_h}	(mm)	5.08
$T_{h,out}$	(K)	533.15	N_{f_c}	(1/m)	950.00
P_c	(bar)	4.00	N_{f_h}	(1/m)	980.00
P_h	(bar)	1.05	t_f	(mm)	0.10
$\dot{m}_c$	(kg/s)	0.49	L_{Nf}	(m)	0.31
$\dot{m}_h$	(kg/s)	0.49			

Output data							
Thermodynamics			Geometry				
	Units	Data		Units	Data	Model	Discrepancy
			L_{flow}	(m)	0.21	0.23	5.29%
ΔP_c	(%)	1.00				1.12	0.12
ΔP_h	(%)	4.00				3.72	−0.28

- The thermodynamic properties of the fluids are calculated at the average temperature of the fluid.
- Constant pressure along the component.
- Water assumed to be fresh water.

The list of input variables for the model is:

- The temperature, pressure, mass flow, and humidity of the air at the inlet, the outlet, and pinch point.
- The temperature, pressure, and mass flow of the water at the inlet, the outlet, and pinch point.
- The number of passes of the dry section. ($N_{p_{dry}}$).
- The outer diameter of the tube (d_o).
- The height of the fins (h_f).
- The density of fins (N_f).

- The thickness of the fins (t_f).
- The minimum thickness of the tubes (t_t).
- The number of tube rows per pass (N_r).
- The pitch between the rows of tubes (p_r).
- The length of the tubes (L_t).
- The length perpendicular to both fluids (L_{Nf}).
- The material of the tubes and fins.
- The preset fouling of (R_f) of the gas and water side.

The outputs obtained are:

- The pressure losses of both sides.
- The total height of the component.
- The total length of the component.
- The weight of the component.
- The pitch between the tubes of the same row.

A.3.1 Dry part

The design of the dry part always includes more than five tube passes, thus when calculating the NTU, the heat exchanger can be approximated as a counter-flow device [117]. The process followed to obtain the required value of UA equivalent to the process used for the counter-current recuperator, Section A.2.1.

To obtain the full geometry of the dry part of the heat exchanger, an iterative process is employed to converge on the velocity of the water (u_w) and the velocity of the gas (u_g). The iterative process is carried as follows:

1. Guess the initial value of the flow velocities u_w and u_g.
2. Calculate the mass flux of the air-side based on $\dot{m}_g$ and ρ_g.

3. Calculate the required air-side frontal area (A_{fro_g})
4. Calculate the total number of tubes (N_t) required based on the inner diameter of the tubes (d_i), N_r, and u_w.
5. Calculate the pitch between the tubes of the same rows (p_t) based on N_t, N_r, and L_{Nf}.
6. Calculate the frontal area ($A_{fro_{g,Calc}}$) of the gas side based on L_{Nf}, L_{tube}, N_t, and N_r.
7. Calculate the inner and outer heat transfer areas.
8. Calculate the heat transfer coefficients of the air-side and water-side.
9. Calculate the overall efficiency of the extended surfaces.
10. Calculate the right term of the Eq. A.26.
11. Calculate the error between the target UA and the $(UA)_{calc}$, and the required A_{fro_g} and the $A_{fro_{g,Calc}}$. If convergence is reached, the problem is solved. Otherwise, u_w and u_g are recalculated and the iterative process is repeated from step 2.

Once the problem has converged the pressure losses of both sides are estimated, as well as the weight of the component.

A.3.2 Wet part

In case that the air is humid enough, and cooled down below the dew temperature, condensation appears over tubes at the rear part of the heat exchanger. The wet part is designed as a prolongation of the heat exchanger, where the number of passes ($N_{p_{wet}}$) is calculated based on the area required to condense the specified amount of moisture. Since the architecture of dry and the wet parts need to be identical, the constraints for calculating the wet part are the same length, width, diameter, and pitch of the tubes and the same pitch of the rows as in the dry part. The process followed to estimate the required area is explained in full detail by Gesellsachaft [96].

A.3.3 Areas and coefficients calculation

Prior to calculating the areas and the coefficients, it is necessary to specify that the tube bundle is arranged in triangular configurations, as shown in Figure A.11a.

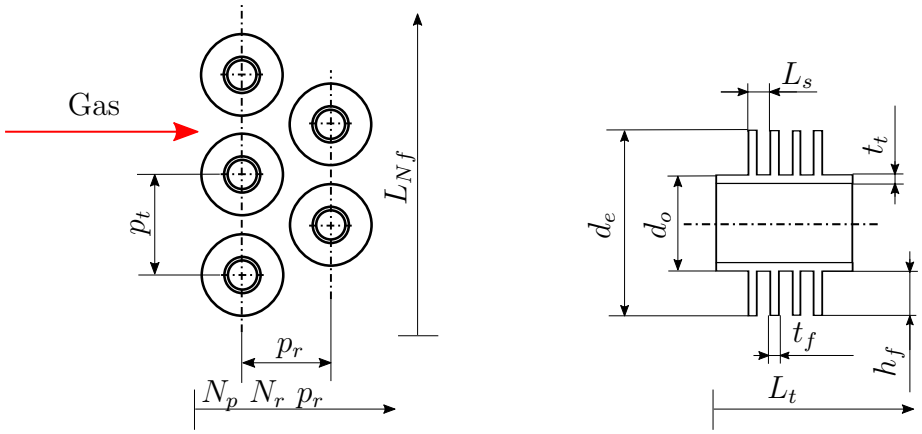

(a) Tube bundle dimensions (b) Finned-tube dimensions

FIGURE A.11: Geometry of the economiser's tube bundle.

Required air-side frontal area

The mass flux of the gas is obtained by means of Eq. A.54.

$$\dot{G}_g = \rho_g \; u_g \tag{A.54}$$

Then, the required frontal area of the humid air is obtained as follows.

$$A_{fro_g} = \frac{\dot{m}_g}{\dot{G}_g} \tag{A.55}$$

Outer heat transfer area

Before calculating the air-side heat transfer area, it is necessary to estimate N_t, which is calculated based on A_{free_w} and d_i, as shown in Eq. A.58.

$$A_{free_w} = \frac{\dot{m}_w}{\rho_w \; u_w} \tag{A.56}$$

$$d_i = d_o - 2\ t_t \tag{A.57}$$

$$N_t = \frac{A_{free_w}}{0.25\ \pi\ d_i^2} \tag{A.58}$$

Once the N_t is known, it is possible to derive the air-side heat transfer area as the area of the fins, plus the outer tube area (A_t).

$$A_f = \pi\ N_f\ \left[2\ \left((d_e^2 - d_o^2)\ 0.25\right) + d_e\ t_f\right]\ L_t\ N_t\ N_p \tag{A.59}$$

where d_e is the external diameter of the tube of the fin calculated as $d_e = d_o + 2h_f$.

$$A_t = \pi\ d_o\ (1 - N_f\ t_f)\ L_t\ N_t\ N_p \tag{A.60}$$

Finally, the air-side heat transfer area is just the sum of the two areas.

$$A_{HX_g} = A_f + A_t \tag{A.61}$$

Inner heat transfer area

The water-side heat transfer area is obtained by means of Eq. A.62.

$$A_{HX_w} = \pi\ d_i\ L_t\ N_t\ N_p \tag{A.62}$$

Dry air-side heat transfer coefficient and pressure loss

The heat transfer coefficient and friction factor are estimated following the procedure presented by ESDU [109]. First, the free flow area and the frontal area are calculated using Eq. A.63 and Eq. A.64 respectively, where the pitch between the tubes of the same row is defined as $p_t = L_{Nf}\ N_r/N_t$.

$$A_{free_g} = \begin{cases} (p_t - d_o - 2\ N_f\ t_f\ h_f)\ \dfrac{N_t}{N_r}\ L_t, & \text{if } \dfrac{p_r}{d_o} > \sqrt{\dfrac{2\ p_t}{d_o} + 1} \\ \left(\sqrt{4\ p_r^2 + p_t^2} - 2\ d_o - 4\ N_f\ t_f h_f\right) \dfrac{N_t}{N_r}\ L_t, & \text{otherwise} \end{cases} \tag{A.63}$$

$$A_{fro_{g,Calc}} = \frac{N_t}{N_r}\ p_t\ L_t \tag{A.64}$$

Next, the Reynolds number is calculated.

$$Re_g = \frac{\dot{G}_g\ d_o}{\mu_g} \tag{A.65}$$

Once with the Reynolds number, it is straightforward to obtain the Nusselt number by means of Eq. A.65, and the air-side heat transfer coefficient using Eq. A.67.

$$Nu_g = 0.242\ Re_g^{0.658}\ Pr_g^{1/3}\ \left(\frac{L_s}{h_f}\right)^{0.297}\ \left(\frac{p_t}{p_r}\right)^{-0.091} \tag{A.66}$$

$$\alpha_g = \frac{Nu_g\ k_g}{2\ d_o} \tag{A.67}$$

The pressure losses are calculated accordingly to Eq. A.69. This equation considers the pressure losses produced by the friction with the tubes and the fins, and the losses produced by the acceleration of the gas due to the change in temperature.

$$K = 4.567\ Re^{-0.242}\ \left(\frac{A_{HX_g}}{A_t}\right)^{0.504}\ \left(\frac{p_t}{d_o}\right)^{-0.376}\ \left(\frac{p_r}{d_o}\right)^{-0.546} \tag{A.68}$$

$$\Delta P_g = \frac{\dot{G}_g^2}{2\ \bar{\rho}_g}\left[\left(1 + \left(\frac{A_{free_g}}{A_{fro_g}}\right)^2\right)\ \bar{\rho}_g\ \left(\frac{1}{\rho_{g,out}} - \frac{1}{\rho_{g,in}}\right) + N_p\ N_r\ K\right] \tag{A.69}$$

where $\bar{\rho}_g$ is the average density of the gas.

Overall effectiveness of the extended surfaces

It is necessary to add the correction factor, known as the overall effectiveness of the extended surfaces, to consider the non-uniform temperature of the extended surfaces. This effectiveness is calculated as suggested in the ESDU data items [109].

First the coefficients m^* and ϕ are obtained by means of Eq. A.70 and A.71.

$$m^* = \left(\frac{2\ \alpha_g}{k_{wl}\ t_f} \right)^{0.5} \tag{A.70}$$

$$\phi = 0.5\ d_o\ \left(\frac{d_e}{d_o} + 1 \right)\ \left[1 + 0.35\ \log\left(\frac{d_e}{d_o} \right) \right] \tag{A.71}$$

Then, the efficiency of the fins can be calculated as follows:

$$\eta_f = \frac{\tanh(m^*\ \phi)}{m\ \phi} \tag{A.72}$$

Last, the overall effectiveness of the extended surfaces is estimated using Eq. A.73, where F_f is a correction factor to consider the non-uniform heat transfer defined in Eq. A.74.

$$\eta_o = 1 - \frac{A_f}{A_{HX}}\ (1 - F_f\ \eta_f) \tag{A.73}$$

$$F_f = 0.97 - 0.056\ m^*\ h_f \tag{A.74}$$

Wet air-side heat transfer coefficient and pressure loss

The correlations employed to estimate the heat transfer coefficient and the pressure losses are explained in full detail by Gesellschaft [96].

Water-side heat transfer coefficient and pressure loss

The heat transfer coefficient and the pressure losses are calculated in the same fashion as they are calculated for the water-side of the plate-fin heat exchangers, see Section A.2.4, with the difference that the hydraulic diameter is equal to the tube's inner diameter.

A.3.4 Weight calculation

Once L_f, L_{Nf}, and h_f have been defined, and before calculating any of the areas or coefficients, the thickness of the tubes, and the thickness of the walls is determined using the ASME Boiler Pressure Vessel Code [144]. The geometry of the tubes is approximated as a cylindrical vessel and the heat exchanger as a rectangular vessel. The thickness of the walls, as well as the thickness of the tubes, are oversized as the walls are reinforced by the presence of the tubes (working as columns) and the tubes are reinforced by the presence of the fins (working as jackets). If any of the calculated thickness is not larger than the minimum thickness of the tube, the value of the minimum thickness of the tube is selected. Once the volume of the required material is calculated, the total weight is obtained based on the density of the material. The procedure does not account for the weight of the headers as they are not designed.

A.3.5 Validation

The model has been validated against the theoretical data presented by Ganapathy [146]. Table A.3 shows that the largest error, 5.7%, is produced on the calculation of the L_t. This is produced due to the underestimation of the heat transfer coefficient, which leads to the requirement of a higher heat transfer area.

TABLE A.3: Validation of the tube-fin heat exchanger model against data from [146].

Input data					
Thermodynamics			Geometry		
	Units	Data		Units	Data
$T_{w,in}$	(K)	533.71	d_o	(mm)	51.00
$T_{w,out}$	(K)	676.48	d_i	(mm)	44.10
$T_{g,in}$	(K)	838.71	h_f	(mm)	12.70
$T_{g,out}$	(K)	757.59	t_f	(mm)	1.90
P_w	(bar)	44.82	N_f	(1/m)	78.74
P_g	(bar)	1.00	N_p	(-)	6.00
$\dot{m}$	(kg/s)	6.30	N_r	(-)	1.00
$\dot{m}$	(kg/s)	28.35	N_t	(-)	18.00

Output data							
Thermodynamics			Geometry				
	Units	Data		Units	Data	Model	Discrepancy
			p_t	(m)	0.10	0.11	4.49%
			L_t	(m)	3.04	3.21	5.70%
U	(W/m^2 K)	71.43				68.06	−3.80%
ΔP_g	(Pa)	253.82				254.69	−0.24%

Appendix B

Design of the reheated humid air turbine components

This appendix presents the detailed geometry of the systems integrating the reheated humid air turbine. The objective of this appendix is to describe the architectures obtained for each of the different components in the cycle. The geometries illustrated correspond to the reference cycle used in the design space exploration of Chapter 4, whose thermodynamic design variables are in Table 4.4. The description of the components of a single cycle is enough to illustrate the geometry of each component since several designs performed have proven that the optimum internal arrangement does not change significantly when altering the design variables of the cycle.

B.1 Intercooler and aftercooler

The dimensions of the intercooler are presented in Table B.1. Figure B.1 depicts the layout of the component obtained from the optimisation process, together with the arrangement of the internal architecture. The gas path is represented by the solid line and the water path by the dashed line. The design solution permits to obtain a compact configuration with a heat exchange density of 23.1 MW/m^3.

The dimensions of the optimum configuration of the aftercooler are presented in Table B.2. The design solution permits to achieve a compact architecture with a heat exchange density of 21.4 MW/m^3. In comparison with the intercooler,

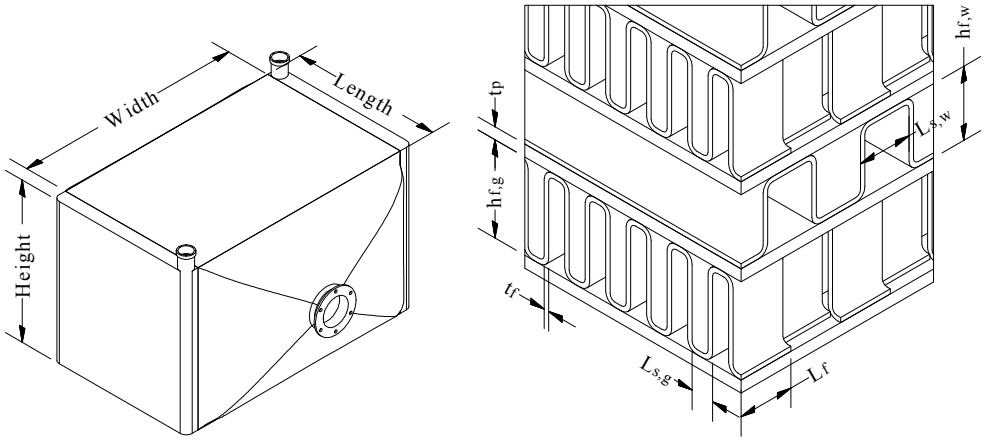

(a) Main dimensions

(b) Internal arrangement

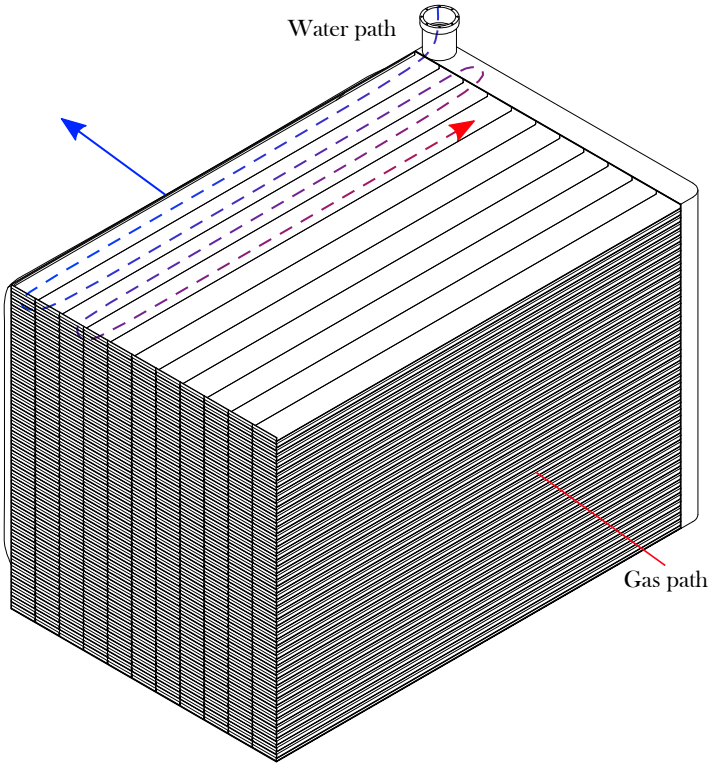

(c) Flow arrangement

FIGURE B.1: Intercooler's and aftercooler's geometry.

TABLE B.1: Baseline intercooler detailed design.

Length [m]	**Width** [m]	**Height** [m]	**Volume** [m^3]	**Weight** [t]	**Cost** [k$]	$\boldsymbol{A_{HX}}$ [m^2]
0.38	1.07	0.98	0.40	1.17	397.5	487.9
$\boldsymbol{h_{f,w}}$ [mm]	$\boldsymbol{h_{f,g}}$ [mm]	$\boldsymbol{L_f}$ [mm]	$\boldsymbol{L_{s,w}}$ [mm]	$\boldsymbol{L_{s,g}}$ [mm]	$\boldsymbol{t_f}$ [mm]	$\boldsymbol{t_p}$ [mm]
4.0	4.0	3.3	2.2	1.8	0.3	0.6

although the temperature jump is almost the same since they present similar gas inlet temperatures, it occupies a volume 50% lower than the intercooler as it only sees half of the flow (bypass ratio 0.49). Nevertheless, it is observed that the internal arrangement of both devices is very similar.

TABLE B.2: Baseline aftercooler detailed design.

Length [m]	**Width** [m]	**Height** [m]	**Volume** [m^3]	**Weight** [t]	**Cost** [k$]	$\boldsymbol{A_{HX}}$ [m^2]
0.76	0.50	0.52	0.20	0.58	245.5	254.0
$\boldsymbol{h_{f,w}}$ [mm]	$\boldsymbol{h_{f,g}}$ [mm]	$\boldsymbol{L_f}$ [mm]	$\boldsymbol{L_{s,w}}$ [mm]	$\boldsymbol{L_{s,g}}$ [mm]	$\boldsymbol{t_f}$ [mm]	$\boldsymbol{t_p}$ [mm]
4.0	5.3	3.1	3.0	1.3	0.3	0.7

Hence, it is proven that despite the large difference in the volume flows between the two fluids the optimiser is able to find a compact and economic architecture, where all the design parameters are within the recommended values in the literature.

B.2 Economiser

The dimensions of the economiser are presented in Table B.3. The external layout, the dimensions of the tubes, and the tube bundle arrangement are shown in Figure B.2, where the dashed lines represent the water path and the solid lines the gas path. The heat exchange density of the economiser, 3.77 MW/m^3, is around an 84% lower than the achieved in the intercooler and the economiser. The main reason for this discrepancy is the substantially lower surface area per unit volume that the tube-fin configuration has compared to the plate-fin. Nevertheless, this

bulky configuration permits to reduce considerably the acquisition cost compared with the other two air-water heat exchangers, being an 87% cheaper than the aftercooler.

TABLE B.3: Baseline economiser detailed design.

Length [m]	**Width** [m]	**Height** [m]	**Volume** [m^3]	**Weight** [t]	**Cost** [k$]	A_{HX} [m^2]	
1.11	2.02	2.12	4.72	3.46	37.8	541.5	
$N_{p,cond}$ [-]	N_r [-]	d_o [mm]	h_f [mm]	L_s [mm]	p_t [mm]	p_r [mm]	t_t [mm]
1	1	10.2	2.1	4.8	30.7	18.7	0.4

B.3 Saturator

The main dimensions of the saturator tower are presented in Table B.4 and the layout showing the internal disposal is displayed in Figure B.3. Despite the large height of the tower, 3.61 m, the packing only accounts for a 24%. The rest of the volume is occupied by the water distribution and droplet eliminator, and the inlet and outlet plenums. In terms of weight, the packing only represents the 10% of the total weight. The rest of the weight is represented by the vessel, which requires a thickness of 4 mm in order to stand the stress generated by the internal pressure, which is 3.4 MPa.

TABLE B.4: Baseline saturator detailed design.

Height [m]	d_p [m]	H_p [m]	**Volume** [m^3]	**Weight** [t]	**Cost** [k$]
3.61	1.79	0.86	9.08	4.99	60.3

B.4 Recuperator

Table B.5 presents the dimensions of the optimum recuperator architecture for the baseline case. The optimum configuration of the recuperator for the baseline cycle

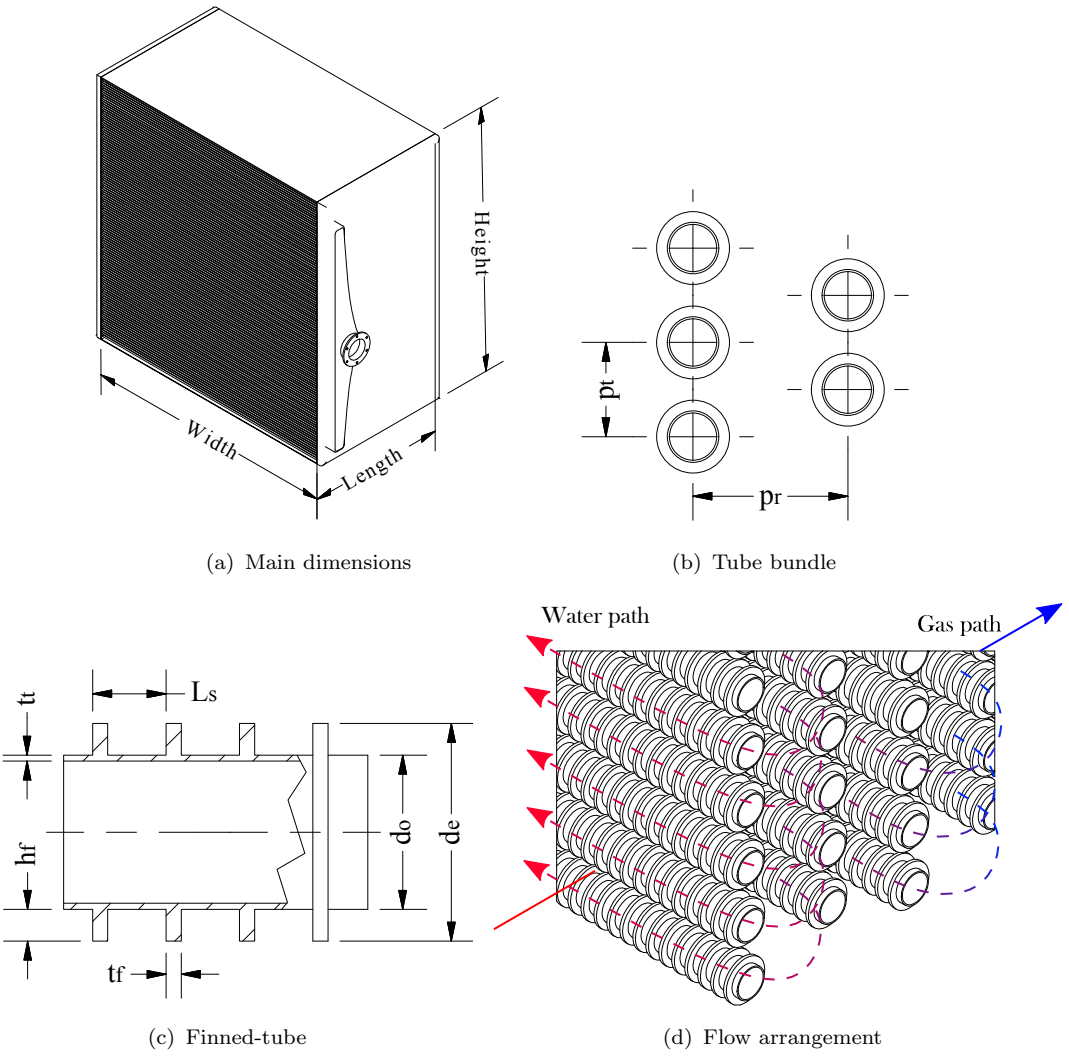

(a) Main dimensions (b) Tube bundle

(c) Finned-tube (d) Flow arrangement

FIGURE B.2: Economiser's geometry.

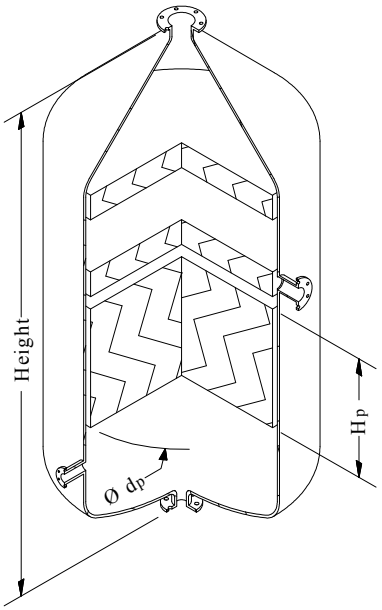

FIGURE B.3: Saturator's geometry.

results to be a single-pass counter-flow configuration, as depicted in Figure B.4. The solid line represents the path of the hot gas, whereas the dashed lines indicate the track of the cold gas.

TABLE B.5: Baseline recuperator detailed design.

N_{HX} [-]	Length [m]	Width [m]	Height [m]	Volume [m^3]	Weight [t]	Cost [k$]	A_{HX} [m^2]
1	0.41	3.07	3.66	4.56	11.6	1,584.4	3,771.4
N_p [-]	$h_{f,c}$ [mm]	$h_{f,h}$ [mm]	L_f [mm]	$L_{s,c}$ [mm]	$L_{s,h}$ [mm]	t_f [mm]	t_p [mm]
1	4.1	8.6	3.3	3.2	2.8	0.5	0.5

The main characteristic the recuperator is its large frontal area compared to its length. With this configuration, it is possible to not overcome the maximum pressure losses of the hot side. Since the relative pressure losses on the hot side per unit length are considerably high due to the low density of the gas and the low pressure, the design must present a large frontal area in order not to overcome the imposed maximum pressure loses. However, the relative pressure losses on the cold side are smaller due to the higher density and pressure of the flow, allowing larger flow velocities. This is the reason why the height of the fins on the cold side is 47% the height on the hot side.

Although the type of heat exchanger is the same as the employed for the design of the intercooler and aftercooler, the heat exchange density achieved in the recuperator is fairly lower, 5.87 MW/m^3. The reason is that the air-air heat transfer coefficient is around four times smaller compared with the air-water configurations.

Although the optimum configuration for the baseline recuperator is single-pass counter-flow, for larger design effectiveness or larger mass flows the optimum configuration might be multi-pass cross-flow. For such case, the architecture would be as presented in Figure B.5.

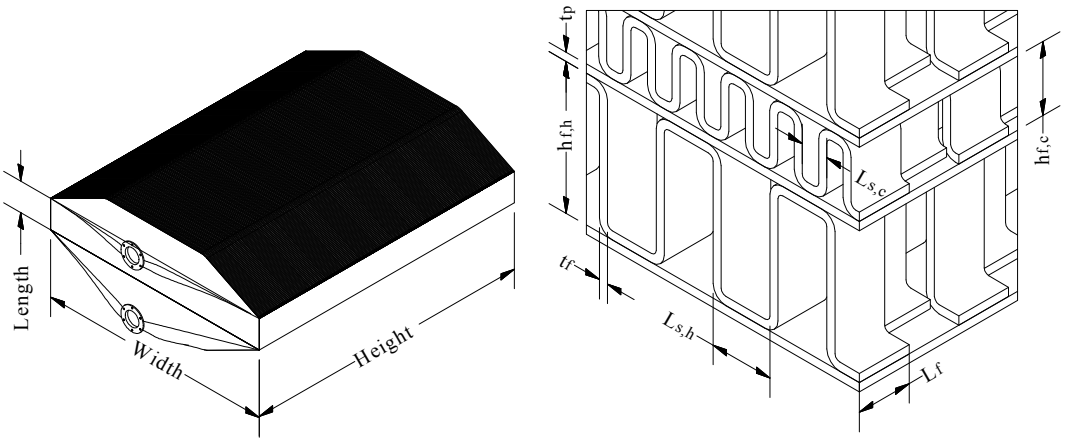

(a) Main dimensions

(b) Internal arrangement

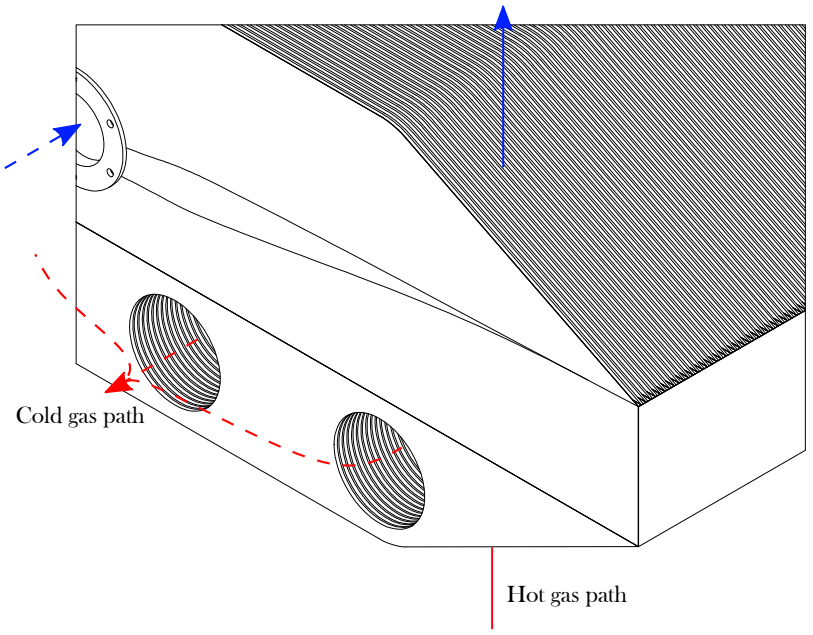

(c) Flow arrangement

FIGURE B.4: Recuperator's geometry. Counter-flow configuration.

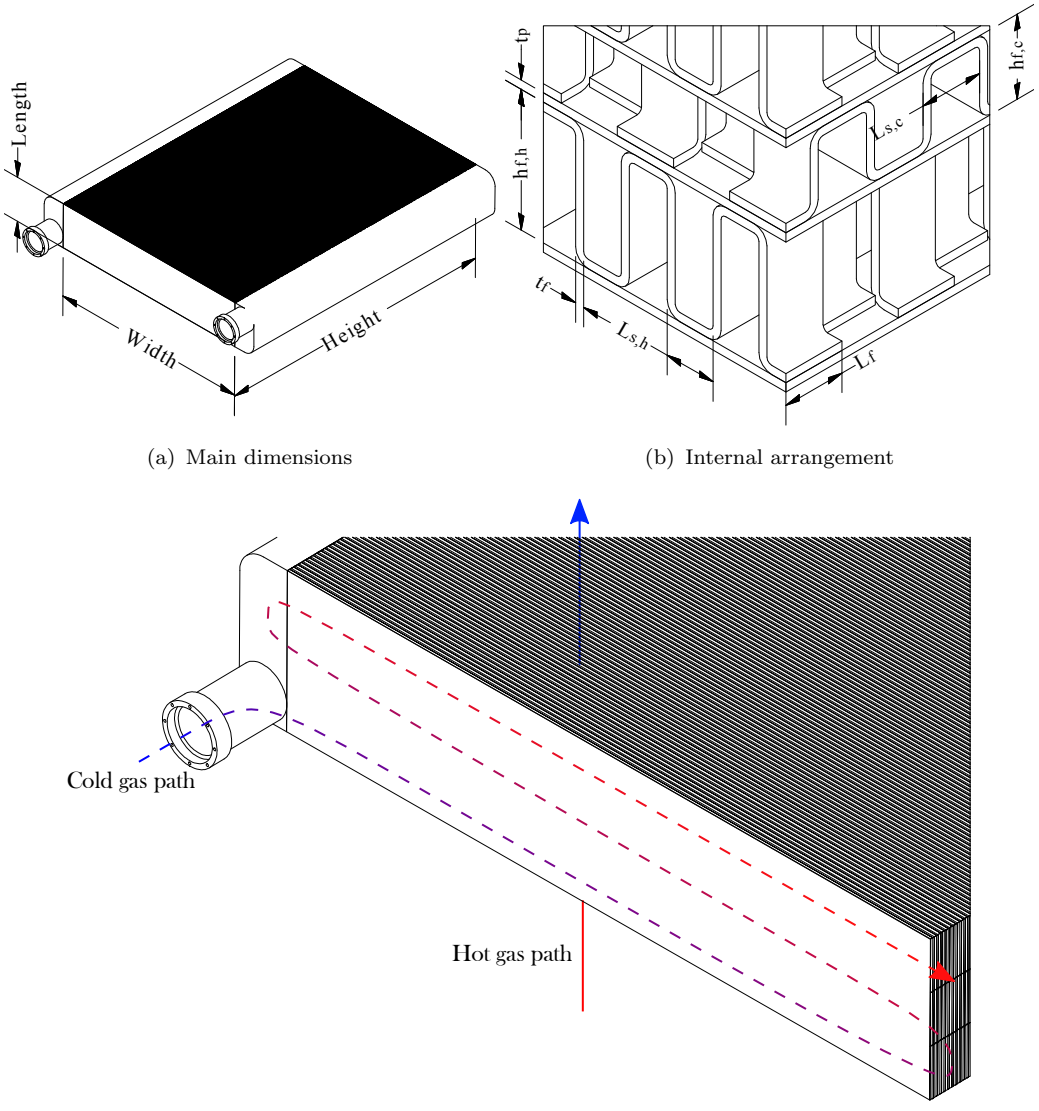

(a) Main dimensions

(b) Internal arrangement

(c) Flow arrangement

FIGURE B.5: Recuperator's geometry. Cross-flow configuration.

B.5 Gas turbine

The main metrics of the baseline gas turbine are presented in Table B.6. Figure B.6 shows the layout of the gas turbine. The vertical tubes leaving the top of the packing represent the ducts connecting the gas turbines with the multiple heat exchangers and the saturator. The step allocated at the rear part of the packing serves as the connecting duct between the gas turbine outlet and the recuperator.

TABLE B.6: Baseline gas turbine detailed design.

Length [m]	**Width** [m]	**Height** [m]	**Volume** [m^3]	**Weight** [t]	**Cost** [k$]
7.53	1.88	2.51	35.54	9.04	8,350.5

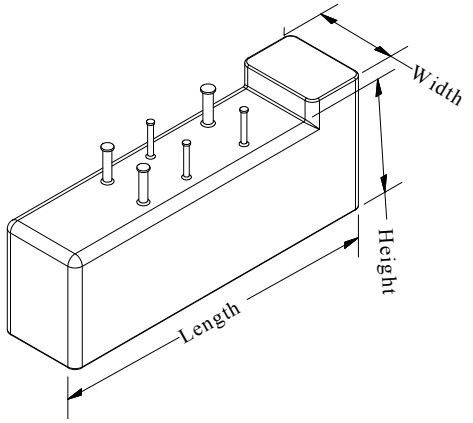

FIGURE B.6: Gas turbine's geometry.

B.6 Generator

The main dimensions, weight, and cost of the permanent magnet generator are presented in Table B.7, whereas Figure B.7 depicts its layout. The generator is placed on top a support in order to alienate its rotation axis with the shaft of the gas turbine. Therefore, the height of the support depends on the dimensions of the gas turbine.

TABLE B.7: Baseline generator detailed design.

Length [m]	**Width** [m]	**Diameter** [m]	**Weight** [t]	**Cost** [k$]
3.37	1.30	0.64	13.0	2,725.0

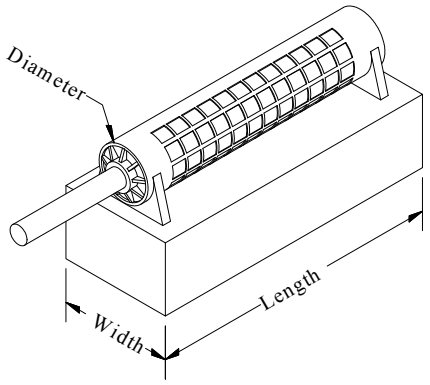

FIGURE B.7: Generator's geometry.

Appendix C

Economic models

This appendix introduces the different economic models employed for the analyses conducted in Chapter 5. Due to the complexity of the methodology developed by Bejan et al. [120], the explanation of the model is complemented with a working example.

C.1 Bejan et al. Model

The model employed for the economic analysis in Chapter 5 is based on the work presented by Bejan et al. [120]. To initialise the analysis, it is required to first establish the starting date of the project, the designing time (n_{des}), the construction time (n_{con}), the system life for tax purposes (n_{tax}), and the book life (n). Once the time scale has been defined, it is possible to calculate the total net investment and finally the cost of the annual expenses.

C.1.1 Total net investment calculation

The Total Net Investment (TNI) represents the total amount of money required to build and start operating the power plant. The TNI is calculated as the Total Net Outlay (TNO) minus the investment tax credit (which is assumed to be 0 for this study).

For the estimation of the TNO is necessary to know when the payments are going to take place and how they are going to be split. It is a common practice to divide

the Fixed Investment (FI), which includes the FCI minus the cost of the land, in two payments. The first part is paid when the construction begins and the second when the construction period has finished. In this study it is assumed that the first payment represents the 40% of the FI (fc_{1st}=0.4), and the second payment the rest (fc_{2nd}=0.6).

The analysis accounts for the inflation. Thus, the prices must be updated according to:

$$\Xi_j = \Xi_{Ref}(1 + r_i)^j \tag{C.1}$$

where Ξ_j represents the price at year j, Ξ_{Ref} the reference price, and r_i the general inflation rate.

Keeping in mind the above-explained considerations, the TNO is calculated as:

Cost of land	Paid at construction start	$j = n_{des}$
First part of the FI (FI fc_{1st})	Paid at construction start	$j = n_{des}$
Second part of the FI (FI fc_{2nd})	Paid at construction end	$j = n_{des} + n_{con}$
Startup costs	Paid at construction end	$j = n_{des} + n_{con}$
Working capital	Paid at construction end	$j = n_{des} + n_{con}$
License, research and development	Paid at project start	$j = 0$
Total net outlay		

Then the Total Non Depreciable of Investment ($TNDI$) is calculated as:

Cost of land
Working capital
Total nondepreciable investment

The Total Depreciable Investment (TDI) is calculated as:

Total net outlay
- Total nondepreciable capital
Total depreciable investment

Since the investment tax credit has been assumed to be 0, the TNI is equal to the TNO.

C.1.2 Cost of annual expenses

The cost of the annual expenses (Ξ_{AE}), also called the Total Revenue Requirement (TRR) by Bejan et al. [120], represents the revenue that must be collected per year to compensate the system operation expenses incurred during the year and be able to guaranty a sound activity.

The TRR is equal to the sum of the Total Capital Recovery (TCR), the minimum Return of the Common Equity (RCE), the minimum Return of the Preferred Stock (RPS), the minimum Return of the Debt (RD), the Income Taxes (ITX), the Other Taxes and Insurance ($OTXI$), the Fuel Cost (FC), and the Operation and Maintenance Cost (OMC), as presented in Eq. C.2.

$$\overbrace{TRR_j}^{\Xi_{AE}} = \overbrace{TCR_j}^{\Xi_{ini}} + \overbrace{RCE_j + RPS_j + RD_j}^{\Xi_{fin}} + \overbrace{ITX_j + OTXI_j}^{\Xi_{tax}} + \overbrace{FC_j}^{\Xi_{fuel}} + \overbrace{OMC_j}^{\Xi_{OM}} \tag{C.2}$$

The TCR represents the initial investment (Ξ_{ini}) in Eq. 5.1, RCE, RPS, and RD the different parts of the cost of financing (Ξ_{fin}), ITX and $OTXI$ the taxes (Ξ_{tax}), FC the cost of the fuel (Ξ_{fuel}), and OMC the Operation and Maintenance costs (Ξ_{OM}).

Total capital recovery

The TCR accounts for the yearly payment required to recover the net investment. To calculate its value it is necessary to previously estimate the annual Book Depreciation (BD) and the Deferred Income Taxes ($DITX$).

The BD is estimated from the book life and the TDI using a straight-line method:

$$BD_j = \frac{TDI}{n} \tag{C.3}$$

The $DITX$ are based on the difference between the annual Tax Depreciation (TXD) and the BD, as shown in Eq. C.4. However, it is required to first obtain the TXD as in Eq. C.5.

$$DITX_j = (TXD_j - BD_j)\,\chi, \qquad j = 1, ..., n_{tax} + 1 \tag{C.4}$$

$$TXD_j = TDI\ fc_{MACRS,j}, \qquad j = 1, ..., n_{tax} + 1 \tag{C.5}$$

where χ represents the income tax rate and the values for fc_{MACRS} are taken from Bejan et al. [120]. The $DITX$ for the year $n_{tax} + 2$ onwards are calculated from:

$$DITX_j = \frac{\sum_{k=1}^{n_{tax}+1} DITX_k}{n - (n_{tax} + 1)}, \qquad j = n_{tax} + 2, ..., n \tag{C.6}$$

Finally, the TCR is calculated as the sum of the $DITX$ and the BD.

$$TCR_j = BD_j + DITX_j, \qquad j = 1, ..., n \tag{C.7}$$

Return of the loan Interests

The RCE, RPS, and RD represent the payments of the interests generated by the required loan, which is divided in three: common equity, preferred stock, and debt. For calculating the payment of the interests, it is necessary to first establish the Balance at the Beginning of each Year (BBY) for each type of loan. The TNI is distributed at the beginning of the first year of the book life among the three financing fraction according to the corresponding coefficients (fc_{ce},fc_{ps},fc_d).

$$BBY_{1,x} = TNI\ fc_x, \qquad x = ce, ps, d \tag{C.8}$$

where the subindexes ce,ps,d stand for common equity, preferred stock, and debt.

It is assumed that the $DITX$ are distributed among the three type of financing according to the corresponding fraction. The obtained value is the adjustment (ADJ) of each type of financing.

$$ADJ_{j,x} = DITX_j\ fc_x, \qquad j = 1, ..., n, \quad x = ce, ps, d \tag{C.9}$$

Once the ADJ has been calculated for each type of financing, the labelled Book Depreciation (BD) is calculated using a straight-line depreciation.

$$BD_{j,x} = \frac{BBY_{1,x} - \sum_{k=1}^{n} ADJ_{k,x}}{n}, \qquad j = 1, ..., n, \quad x = ce, ps, d \tag{C.10}$$

Finally, the BBY is calculated according to:

$$BBY_{j,x} = BBY_{j-1} - (BD_{j,x} + ADJ_{j,x}), \qquad j = 2, ..., n, \quad x = ce, ps, d \tag{C.11}$$

For each type of investment, the return of investment is based on the remaining loan to be paid, which is equal to the BBY, calculated as in Eq. C.12.

$$RCE_j = BBY_{ce,j}\ i_{ce}, \qquad j = 1, ..., n \tag{C.12a}$$
$$RPS_j = BBY_{ps,j}\ i_{ps}, \qquad j = 1, ..., n \tag{C.12b}$$
$$RD_j = BBY_{d,j}\ i_d, \qquad j = 1, ..., n \tag{C.12c}$$

where i_x represents the annual rate of return for each type of investment.

Taxes

The ITX and the $OTXI$ are calculated as:

$$ITX_j = \frac{\chi}{1-\chi}(RCE_j + RPS_j) - DITX_j \tag{C.13}$$

$$OTXI_j = FI\ fc_{OTXI} \tag{C.14}$$

The $OTXI$ is calculates based on the Fixed Investment and fc_{OTXI} represents the percentage part.

Fuel cost

The FC is estimated based on the power output, the thermal efficiency, and the availability of the plant.

$$FC_j = \left(\kappa_f \frac{\dot{W}}{\eta_{th}\ LHV}\ \tau \right) (1 + r_f)^{n_{des}+n_{con}+j-1} \tag{C.15}$$

where κ_f represents the cost per kilogram of fuel, τ the operating hours per year, calculated as the hours in a year multiplied by the availability, and r_f the real inflation rate for the fuel.

Operation and maintenance cost

The OMC is calculated assuming a fixed part that depends on the FCI, and a variable part that depends on the fuel consumption [32].

$$OMC_j = \left(0.02\ FCI + 0.83\ \frac{\dot{W}}{\eta_{th}}\ \tau \right) (1 + r_i)^{n_{des}+n_{con}+j-1} \tag{C.16}$$

C.1.3 Example

An example to estimate the TRR and the consequent COE is presented herein. The cycle design parameters and main thermo-economic metrics of the configuration selected for the example are presented in Table C.1. The FCI ($36,241,000) is calculated based on the percentage ratios introduced in Table 5.1.

The TNO is calculated as:

Cost of land	$687,000	$j = 1$
First part of the FI ($FI\ fc_{1st}$)	$14,584,000	$j = 1$
Second part of the FI ($FI\ fc_{2nd}$)	$22,983,000	$j = 3$
Startup costs	$1,951,000	$j = 3$
Working capital	$5,854,000	$j = 3$
License, research and development	$2,537,000	$j = 0$
Total net outlay	**$48,596,000**	

TABLE C.1: Reference cycle for the example.

$\boldsymbol{OPR}$	[-]	40
$\boldsymbol{\Delta T_{sp}}$	[K]	10
$\boldsymbol{\varepsilon_{IC}}$	[-]	0.85
$\boldsymbol{\varepsilon_{AC}}$	[-]	0.85
$\boldsymbol{\varepsilon_{RC}}$	[-]	0.85
$\boldsymbol{\varepsilon_{EC}}$	[-]	0.85
$\boldsymbol{\eta_{th}}$	[%]	58.31
$\boldsymbol{SPEC}$	[$/kW]	335.03
$\boldsymbol{\overline{COE}}$	[c$/kW h]	6.85

Then the $TNDI$ is calculated as:

Cost of land	$687,000
Working capital	$5,854,000
Total nondepreciable investment	**$6,541,000**

The TDI is obtained as:

Total net outlay	$48,596,000
- Total nondepreciable capital	(-) $6,541,000
Total depreciable investment	**$42,055,000**

Since the investment tax credit has been assumed to be 0, the TNI is equal to the TNO.

The yearly TCR is presented in Table C.2. The yearly BBY of the three loans is presented in Table C.3. Last, the yearly TRR and the yearly COE are presented in Table C.4.

Table C.2: Example of detailed calculation of the total capital recovery. The costs are in k$.

Year	Annual book depreciation	Deferred income taxes	TCR
1	2,103	0	2,103
2	2,103	568	2,671
3	2,103	448	2,551
4	2,103	341	2,443
5	2,103	244	2,346
6	2,103	155	2,258
7	2,103	114	2,216
8	2,103	114	2,216
9	2,103	115	2,218
10	2,103	114	2,216
11	2,103	115	2,218
12	2,103	-258	1,844
13	2,103	-258	1,844
14	2,103	-258	1,844
15	2,103	-258	1,844
16	2,103	-258	1,844
17	2,103	-258	1,844
18	2,103	-258	1,844
19	2,103	-258	1,844
20	2,103	-258	1,844
Subtotal	42,055	0	42,055

Table C.3: Example of detailed calculation of thebalance at the beginning of the year of the loans.
The costs are in k$.

Year	Common equity			Preferred stock			Debt		
	Balance beginning year	Book depreciation	Adjustment	Balance beginning year	Book depreciation	Adjustment	Balance beginning year	Book depreciation	Adjustment
1	17,009	850	0	7,289	364	0	24,298	1,215	0
2	16,158	850	199	6,925	364	85	23,083	1,215	284
3	15,109	850	157	6,475	364	67	21,584	1,215	224
4	14,102	850	119	6,044	364	51	20,146	1,215	170
5	13,132	850	85	5,628	364	37	18,760	1,215	122
6	12,197	850	54	5,227	364	23	17,424	1,215	78
7	11,292	850	40	4,839	364	17	16,131	1,215	57
8	10,402	850	40	4,458	364	17	14,860	1,215	57
9	9,512	850	40	4,076	364	17	13,588	1,215	57
10	8,621	850	40	3,695	364	17	12,316	1,215	57
11	7,731	850	40	3,313	364	17	11,044	1,215	57
12	6,840	850	-90	2,931	364	-39	9,772	1,215	-129
13	6,080	850	-90	2,606	364	-39	8,686	1,215	-129
14	5,320	850	-90	2,280	364	-39	7,600	1,215	-129
15	4,560	850	-90	1,954	364	-39	6,514	1,215	-129
16	3,800	850	-90	1,629	364	-39	5,429	1,215	-129
17	3,040	850	-90	1,303	364	-39	4,343	1,215	-129
18	2,280	850	-90	977	364	-39	3,257	1,215	-129
19	1,520	850	-90	651	364	-39	2,171	1,215	-129
20	760	850	-90	326	364	-39	1,086	1,215	-129
21	0	0	0	0	0	0	0	0	0

TABLE C.4: Example of detailed calculation of the annual expenses and cost of the electricity. The costs are in k$. The cost of the electricity is in c$/kWh

Year	*TCR*	*RCE*	*RPS*	*RD*	*ITX*	*OTXI*	*FC*	*OMC*	*TRR*	*COE*
1	2,103	935	437	1,336	588	751	10,659	1,237	18,047	6.06
2	2,671	889	415	1,270	-9	751	10,978	1,268	18,233	6.12
3	2,551	831	389	1,187	75	751	11,308	1,300	18,391	6.17
4	2,443	776	363	1,108	147	751	11,647	1,332	18,567	6.23
5	2,346	722	338	1,032	211	751	11,996	1,366	18,762	6.30
6	2,258	671	314	958	267	751	12,356	1,400	18,975	6.37
7	2,216	621	290	887	277	751	12,727	1,435	19,205	6.45
8	2,216	572	267	817	246	751	13,109	1,471	19,450	6.53
9	2,218	523	245	747	214	751	13,502	1,507	19,707	6.62
10	2,216	474	222	677	185	751	13,907	1,545	19,977	6.71
11	2,218	425	199	607	153	751	14,324	1,584	20,261	6.80
12	1,844	376	176	537	495	751	14,754	1,623	20,557	6.90
13	1,844	334	156	478	469	751	15,196	1,664	20,893	7.01
14	1,844	293	137	418	442	751	15,652	1,705	21,243	7.13
15	1,844	251	117	358	416	751	16,122	1,748	21,608	7.25
16	1,844	209	98	299	390	751	16,606	1,792	21,988	7.38
17	1,844	167	78	239	364	751	17,104	1,836	22,384	7.52
18	1,844	125	59	179	337	751	17,617	1,882	22,795	7.65
19	1,844	84	39	119	311	751	18,145	1,929	23,224	7.80
20	1,844	42	20	60	285	751	18,690	1,978	23,669	7.95

C.2 Traverso and Massardo model

The model employed to compare the COE of the RHAT against the results presented by Traverso and Massardo [31] uses the same methodology as the Bejan et al. [120] model presented in the previous section. The only differences in the assumed economic scenario are presented in Table C.5.

TABLE C.5: Assumptions of the economic model presented by Tavrerso and Massardo.

Assumed starting year of the project	January 2000
Fuel price (LNG)	0.19 \$/kg
OM variable	0
OM fixed	4% PEC
Availability	91.3%

C.3 Kavangh and Park model

The model employed to compare the COE of the RHAT against the results presented by Kavanagh and Parks [30] uses a simpler approach. The TCI is calculated by multiplying the PEC by the Capital Recovery Factor (CRF). This operation results in the distribution of the PEC into yearly payment over a life of n years, considering an annual rate of return i. Last, the COE is obtained as the sum of the cost rate of the TCI, the fuel, the CO_2, and the OM.

$$CRF = \frac{(1+i)^n \; i}{(1+i)^n - 1} \tag{C.17}$$

$$\dot{\Xi}_{TCI} = \frac{PEC \; CRF}{\tau} \tag{C.18}$$

$$\dot{\Xi}_f = \dot{m}_f \; \kappa_f \tag{C.19}$$

$$\dot{\Xi}_{CO_2} = \dot{m}_{CO_2} \; \kappa_{CO_2} \tag{C.20}$$

$$COE = \frac{\dot{\Xi}_{TCI} + \dot{\Xi}_f + \dot{\Xi}_{CO_2} + \dot{\Xi}_{OM}}{\dot{W}} \tag{C.21}$$

The assumptions made for the model are presented in Table C.6.

Table C.6: Assumptions of the economic model presented by Kavanagh and Parks.

Assumed starting year of the project	January 2009
Plant economic life	20 years
Interest rate	7%
Fuel price (methane)	0.30 $/kg
Carbon price	0.01 $/kg
OM price	$0
Operation hours	7500 h/year

References

[1] J. Fuglestvedt, T. Berntsen, V. Eyring, I. Isaksen, D. S. Lee, and R. Sausen, 2009. "Shipping Emissions: From Cooling to Warming of Climates — and Reducing Impacts on Health." *Environmental Science and Technology*, 43(24); pp. 9057–9062. doi:10.1021/es901944r.

[2] Royal Academy of Engineering, 2013. "Future Ship Powering Options: Exploring Alternative Methods of Ship Propulsion." Tech. rep., Royal Academy of Engineering. URL https://www.raeng.org.uk/publications/reports/future-ship-powering-options

[3] UNCTAD, 2015. "Developments in International Seaborne Trade." *United Nations Publication*.

[4] M. Christiansen, K. Fagerholt, B. Nygreen, and D. Ronen, 2007. "Maritime Transportation." In "Handbooks in Operations Research and Management Science, Vol 14," chap. 4, pp. 189–284. Elsevier. doi:10.1016/S0927-0507(06)14004-9.

[5] J. J. Corbett and P. Fischbeck, 1997. "Emissions from Ships." *Science*, 278(5339); pp. 823–824. doi:0.1126/science.278.5339.823.

[6] K. Capaldo, J. J. Corbett, P. Kasibhatla, P. Fischbeck, and S. N. Pandis, 1999. "Effects of Ship Emissions on Sulphur Cycling and Radiative Climate Forcing Over the Ocean." *Nature*, 400(6746); pp. 743–746. doi:10.1038/23438.

[7] International Maritime Organization, 2008. "MARPOL Annex VI and NTC 2008 with Guidelines for Implementation." URL http://www.imo.org/es/Publications/Documents/SupplementsandCDs/English/QB664E{_}092015.pdf{#}page=20{&}zoom=auto,-67,480

[8] E. D. Boer and M. Hoen, 2015. "Scrubbers – An Economic and Ecological Assessment." Tech. rep., CE Delft, Delft, Netherlands. URL https://www.nabu.de/downloads/150312-Scrubbers.pdf

[9] J. P. Hansen, J. Kaltoft, F. Bak, J. Gørtz, M. Pedersen, and C. Underwood, 2014. "Reduction of SO_2, NO_x and Particulate Matter from Ships with Diesel Engines." Tech. rep. URL http://www.alfalaval.com/microsites/puresox/documents/978-87-93026-57-5.pdf

[10] L. Sanchez, 2014. *Advanced Gas-Turbine-Based Power Plants for Marine Commercial Applications*. Phd thesis, Cranfield University, Cranfield, UK.

[11] T. J. McCoy, 2002. "Trends in Ship Electric Propulsion." In "Power Engineering Society Summer Meeting IEEE," vol. 1, pp. 343–346. IEEE, Chicago, IL, USA. doi:10.1109/PESS.2002.1043247.

[12] J. S. Thongam, M. Tarbouchi, A. F. Okou, D. Bouchard, and R. Beguenane, 2013. "All-Electric Ships: A Review of the Present State of the Art." In "Eighth International Conference and Exhibition on Ecological Vehicles and Renewable Energies," doi:10.1109/EVER.2013.6521626.

[13] M. Frank, P. Van Haßelt, P. Kummeth, P. Massek, W. Nick, H. Rothfischer, H. Schmidt, B. Wacker, H. W. Neumüller, G. Nerowski, J. Frauenhofer, R. Hartig, and W. Rzadki, 2006. "High-Temperature Superconducting Rotating Machines for Ship Applications." *IEEE Transactions on Applied Superconductivity*, 16(2); pp. 1465–1468. doi:10.1109/TASC.2005.864263.

[14] B. Gamble, G. Snitchler, and T. Macdonald, 2011. "Full Power Test of a 36.5 MW HTS Propulsion Motor." *IEEE Transactions on Applied Superconductivity*, 21(3); pp. 1083–1088. doi:10.1109/TASC.2010.2093854.

[15] W. Nick, M. Frank, P. Kummeth, J. J. Rabbers, M. Wilke, and K. Schleicher, 2010. "Development and Construction of an HTS Rotor for Ship Propulsion Application." *Journal of Physics: Conference Series*, 234(3). doi:10.1088/1742-6596/234/3/032040.

[16] W. Nick, J. Grundmann, and J. Frauenhofer, 2012. "Test Results from Siemens Low-Speed, High-Torque HTS Machine and Description of Further Steps Towards Commercialisation of HTS Machines." *Physica C: Superconductivity and its Applications*, 482; pp. 105–110. doi:10.1016/j.physc.2012.04.019.

[17] T. Nakamura, 2011. "Progress of HTS Rotating Machine Development in Japan." *Superconductivity and Cryogenics*, 13(2).

[18] International Energy Agency, 2017. "World Energy Outlook 2017." Tech. rep. doi:10.1016/0301-4215(73)90024-4. URL http://www.iea.org/bookshop/750-World{_}Energy{_}Outlook{_}2017

[19] International Energy Agency, 2017. "Energy Efficiency 2017." Tech. rep. doi:10.1787/9789264284234-en. URL http://www.oecd-ilibrary.org/energy/energy-efficiency-2017{_}9789264284234-en

[20] Deloitte, 2015. "The Future of the Global Power Sector: Preparing for Emerging Opportunities and Threats." Tech. rep., Deloitte Global Services Limited, London, UK. URL https://www2.deloitte.com/content/dam/Deloitte/global/Documents/Energy-and-Resources/gx-power-future-global-power-sector-report.pdf

[21] British Petrol, 2017. "BP Energy Outlook 2017." Tech. rep. URL https://www.bp.com/content/dam/bp/pdf/energy-economics/energy-outlook-2017/bp-energy-outlook-2017.pdf

[22] R. K. Bhargava, 2006. "Global Energy Market: Past, Present and Future." In "Proceedings of ASME Turbo Expo," Paper No. GT2006-91322, pp. 577–588. ASME, Barcelona, Spain. doi:10.1115/GT2006-91322.

[23] General Electric, 2015. "9HA fact sheet - GE Power." *GE Power & water*, (GEA31744); pp. 9–10.

[24] R. Bhargava, M. Bianchi, A. De Pascale, G. Negri di Montenegro, and A. Peretto, 2007. "Gas Turbine Based Power Cycles — A State-of-the-Art Review." In "Proceedings of International Conference on Power Engineering," pp. 309–319. Hangzhou, China. doi:10.1007/978-3-540-76694-0_56.

[25] D. E. Brandt, 1988. "The Design and Development of an Advanced Heavy-Duty Gas Turbine." *Journal of Engineering for Gas Turbines and Power*, 110(2); pp. 243–250. doi:10.1115/1.3240113.

[26] L. Balling, H. Termuehlen, and R. Baumgartner, 2002. "40 Years of Combined Cycle Power Plants." In "International Joint Power Generation Conference," Paper No. IJPGC2002-26111, pp. 537–548. ASME, Scottsdale, Arizona, USA. doi:10.1115/IJPGC2002-26111.

[27] D. L. Chase, 2000. "Combined-Cycle Development Evolution and Future." Tech. rep. URL https://physics.oregonstate.edu/{~}hetheriw/energy/topics/doc/elec/natgas/cc/combinedcycledevelopmentevolutionandfutureGER4206.pdf

[28] A. D. Rao, 1989. "Process for Producing Power." US Patent 4,829,763.

[29] A. Rao, 2014. "Evaporative Gas Turbine (EvGT)/Humid Air Turbine (HAT) Cycles." In "Handbook of Clean Energy Systems," John Wiley & Sons, Ltd, Chichester, UK. doi:10.1002/9781118991978.hces141.

[30] R. M. Kavanagh and G. Parks, 2009. "A Systematic Comparison and Multi-Objective Optimization of Humid Power Cycles — Part II: Economics." *Journal of Engineering for Gas Turbines and Power*, 131. doi:10.1115/1.3026562.

[31] A. Traverso and A. F. Massardo, 2002. "Thermoeconomic Analysis of Mixed GasSteam Cycles." *Applied Thermal Engineering*, 22(1). doi:10.1016/S1359-4311(01)00064-3.

[32] M. Jonsson and J. Yan, 2003. "Economic Assessment of Evaporative Gas Turbine Cycles With Optimized Part Flow Humidification Systems." In "Proceedings of ASME Turbo Expo," Paper No. GT2003-38009. ASME, Atlanta, Georgia, USA. doi:10.1115/GT2003-38009.

[33] A. D. Rao, V. J. Francuz, J. C. Shen, and E. W. West, 1991. "A Comparison of Humid Air Turbine (HAT) Cycle and Combined-cycle Power Plants." Tech. rep., Palo Alto, CA, USA.

[34] A. Cohn, 1993. "Power Plant Cycles Featuring Air Humidification." *Electric Power Research Institute Journal*, 18(7); pp. 43–47.

[35] W. L. R. Gallo, 1997. "A Comparisson Between the HAT Cycle and Other Gas-Turbine Based Cycles: Efficiency, Specific Power and Water Consumption." *Energy Conversion and Management*, 38(15); pp. 1595–1604. doi:10.1016/S0196-8904(96)00220-8.

[36] S. Higuchi, S. Hatamiya, N. Seiki, and S. Marushima, 2003. "A Study of Performance on Advanced Humid Air Turbine Systems." In "Proceedings of the International Gas Turbine Congress," IGTC2003 TS-090. Tokyo, Japan.

[37] S. Hatamiya, H. Araki, and S. Higuchi, 2004. "An Evaluation of Advanced Humid Air Turbine System With Water Recovery." In "Proceedings of ASME Turbo Expo," Paper No. GT2004-54031, pp. 585–591. ASME, Viena, Austria. doi:10.1115/GT2004-54031.

[38] R. M. Kavanagh and G. Parks, 2009. "A Systematic Comparison and Multi-Objective Optimization of Humid Power Cycles — Part I: Thermodynamics." *Journal of Engineering for Gas Turbines and Power*, 131. doi:10.1115/1.3026562.

[39] T. Kim, C. Song, S. Ro, and S. Kauh, 2000. "Influence of Ambient Condition on Thermodynamic Performance of the Humid Air Turbine Cycle." *Energy*, 25(4); pp. 313–324. doi:10.1016/S0360-5442(99)00074-2.

[40] T. Takahashi, Y. Nakao, and E. Koda, 2007. "Analysis and Evaluation about Advanced Humid Air Turbine System." In "Challenges of Power Engineering and Environment," pp. 341–344. Springer Berlin Heidelberg, Berlin, Germany. doi:10.1007/978-3-540-76694-0_61.

[41] T. Lindquist, 2002. *Evaluation, Experience and Potential of Gas Turbine Based Cycles with Humidification.* Phd thesis, Lund Institute of Technology, Lund, Sweden.

[42] S. Higuchi, T. Koganezawa, Y. Horiuchi, H. Araki, T. Shibata, and S. Marushima, 2008. "Test Results From the Advanced Humid Air Turbine System Pilot Plant: Part 1 Overall Performance." In "Proceedings of ASME Turbo Expo," Paper No. GT2008-51072, pp. 691–700. ASME, Berlin, Germany. doi:10.1115/GT2008-51072.

[43] H. Nakamura, T. Takahasshi, N. Narazki, K. Yamamoto, and N. Sayama, 1985. "Regenerative Gas Turbine Cycle." US Patent 4,573,023.

[44] P. Chiesa, G. Lozza, E. Macchi, and S. Consonni, 1995. "An Assessment of the Thermodynamic Performance of Mixed Gas-Steam Cycles Part B — Water-Injected and HAT Cycles." *Journal of Engineering for Gas Turbines and Power*, 117(3); pp. 499–508. doi:10.1115/1.2814122.

[45] A. Lazzaretto and F. Segato, 2001. "Thermodynamic Optimization of the HAT Cycle Plant Structure. Part I: Structure of the Heat Exchanger Network." *Journal of Engineering for Gas Turbines and Power*, 123(January 2001). doi:10.1115/1.1339000.

[46] A. Lazzaretto and F. Segato, 2001. "Thermodynamic Optimization of the HAT Cycle Plant Structure. Part II: Structure of the Heat Exchanger Network." *Journal of Engineering for Gas Turbines and Power*, 123(January 2001). doi:10.1115/1.1339000.

[47] B. Nyberg and M. Thern, 2012. "Thermodynamic Studies of a HAT Cycle and its Components." *Applied Energy*, 89(1); pp. 315–321. doi:10.1016/j.apenergy.2011.07.036.

[48] B. Wang, S. Zhang, and Y. Xiao, 2007. "Steady State Off-Design Performance of Humid Air Turbine Cycle." In "Proceedings of ASME Turbo Expo," Paper No. GT2007-27350, pp. 139–149. ASME, Montreal, Canada. doi:10.1115/GT2007-27350.

[49] M. Nakhamkin, E. Swensen, J. M. Wilson, G. Gaul, and M. Polsky, 1996. "The Cascaded Humidified Advanced Turbine (CHAT)." *Journal of Engineering for Gas Turbines and Power*, 118(3); pp. 565–571. doi:10.1115/1.2816685.

[50] M. Nakhamkin, E. C. Swensen, J. R. Scheibel, and A. Cohn, 1998. "CHAT Technology: An Alternative Approach to Achieve Advanced Turbine Systems Efficiencies With Present Combustion Turbine Technology." In "ASME International Gas Turbine and Aeroengine Congress and Exhibition," Paper No. 98-GT-43. ASME, Stockholm, Sweden. doi:10.1115/98-GT-143.

[51] M. O. J. Westermark, 2002. "Method and Device for Generation of Mechanical Work and, if Desired, Heat in an Evaporative Gas Turbine Process." International patent application No. PCT/ SE96/00936.

[52] N. D. Agren and M. O. J. Westermark, 2003. "Design Study of Part-Flow Evaporative Gas Turbine Cycles: Performance and Equipment Sizing. Part I: Aeroderivative Core." *Journal of Engineering for Gas Turbines and Power*, 125; pp. 201–215. doi:10.1115/1.1476924.

[53] N. D. Agren and M. O. J. Westermark, 2003. "Design Study of Part-Flow Evaporative Gas Turbine Cycles: Performance and Equipment Sizing. Part II: Industrial Core." *Journal of Engineering for Gas Turbines and Power*, 125; pp. 216–227. doi:10.1115/1.1476925.

[54] M. Jonsson and J. Yan, 2002. "Exergy Analysis of Part Flow Evaporative Gas Turbine Cycles: Part 1 Introduction and Method." In "Proceedings

of ASME Turbo Expo," Paper No. GT2002-30125, pp. 457–464. ASME, Amsterdam, Netherlands. doi:10.1115/GT2002-30125.

[55] M. Jonsson and J. Yan, 2002. "Exergy Analysis of Part Flow Evaporative Gas Turbine Cycles: Part 2 Results and Discussion." In "Proceedings of ASME Turbo Expo," Paper No. GT2002-30126, pp. 465–473. ASME, Amsterdam, Netherlands. doi:10.1115/GT2002-30126.

[56] M. Rosen, 2000. *Evaporative Cycles - in Theory and in Practise*. Phd thesis, Lund Institute of Technology, Lund, Sweden.

[57] M. Thern, T. Lindquist, and T. Torisson, 2003. "Theoretical and Experimental Evaluation of a Plate Heat Exchanger Aftercooler in an Evaporative Gas Turbine Cycle." In "Proceedings of ASME Turbo Expo," Paper No. GT2003-38099, pp. 103–111. ASME, Atlanta, Georgia, USA. doi:10.1115/GT2003-38099.

[58] H. Kuroki, S. Hatamiya, T. Shibata, T. Koganezawa, N. Kizuka, and S. Marushima, 2008. "Development of Elemental Technologies for Advanced Humid Air Turbine System." *Journal of Engineering for Gas Turbines and Power*, 130(031701). doi:10.1115/1.2833490.

[59] T. Koganezawa, K. Miura, T. Saito, K. Abe, and H. Inoue, 2007. "Full Scale Testing of a Cluster Nozzle Burner for the Advanced Humid Air Turbine." In "Proceedings of ASME Turbo Expo," Paper No. GT2007-27737, pp. 569–576. ASME, Montreal, Canada. doi:10.1115/GT2007-27737.

[60] H. Araki, S. Higuchi, T. Koganezawa, S. Marushima, S. Hatamiya, and M. Tsukamoto, 2008. "Test Results From the Advanced Humid Air Turbine System Pilot Plant: Part 2 Humidification, Water Recovery and Water Quality." In "Proceedings of ASME Turbo Expo," Paper No. GT2008-5189, pp. 701–712. ASME, Berlin, Germany. doi:10.1115/GT2008-51089.

[61] M. Yagi, H. Araki, H. Tagawa, T. Koganezawa, C. Myoren, and T. Takeda, 2013. "Progress of the 40 MW-Class Advanced Humid Air Turbine Tests." *Journal of Engineering for Gas Turbines and Power*, 135(11). doi:10.1115/1.4025037.

[62] T. Takeda, H. Araki, Y. Iwai, T. Morisaki, and K. Sato, 2014. "Test Results of 40MW-Class Advanced Humid Air Turbine and Exhaust Gas Water

Recovery System." In "Proceedings of ASME Turbo Expo," Paper No. GT2014-27281. ASME, Dusseldorf, Germany. doi:10.1115/GT2014-27281.

[63] F. Dalili and M. Westermark, 1998. "Design of Tubular Humidifiers for Evaporative Gas Turbine Cycles." In "ASME International Gas Turbine and Aeroengine Congress and Exhibition," Paper No. 98-GT'203. ASME, Stockholm, Sweden.

[64] F. Dalili, 2003. *Humidification in Evaporative Power Cycles*. Phd thesis, Royal Institute of Technology, Stockholm, Sweden.

[65] J. M. Coulson, J. F. Richardson, J. H. Harker, and J. R. Backhurst, 2002. *Chemical Engineering: Particle Technology and Separation Process*, vol. 2. Butterworth-Heinemann, Oxford, UK., 5th ed.

[66] T. Lindquist, M. Thern, and T. Torisson, 2002. "Experimental and Theoretical Results of a Humidification Tower in an Evaporative Gas Turbine Cycle Pilot Plant." In "Proceedings of ASME Turbo Expo," Paper No. GT2002-30127, pp. 475–484. ASME, Amsterdam, Netherlands. doi: 10.1115/GT2002-30127.

[67] A. A. Pedemonte, A. Traverso, and A. F. Massardo, 2008. "Experimental Analysis of Pressurised Humidification Tower for Humid Air Gas Turbine Cycles. Part A: Experimental Campaign." *Applied Thermal Engineering*, 28; pp. 1711–1725. doi:10.1016/j.applthermaleng.2007.10.030.

[68] A. Aramayo-Prudencio and J. B. Young, 2003. "The Analysis and Design of Saturators for Power Generation Cycles: Part 1 - Thermodynamics." In "Proceedings of ASME Turbo Expo," Paper No. GT2003 - 38945, pp. 411–421. ASME, Atlanta, Georgia, USA. doi:10.1115/GT2003-38945.

[69] A. Aramayo-Prudencio and J. B. Young, 2003. "The Analysis and Design of Saturators for Power Generation Cycles : Part 2 - Heat and Mass Transfer." In "Proceedings of ASME Turbo Expo," Paper No. GT2003 - 38946, pp. 423–432. ASME, Atlanta, Georgia, USA. doi:10.1115/GT2003-38946.

[70] R. Cevasco, J. Parente, A. Traverso, and a. F. Massardo, 2004. "Off-Design and Transient Analysis of Saturators for Humid Air Turbine Cycles." In "Proceedings of ASME Turbo Expo," Paper No. GT2004-53315, pp. 263–271. ASME, Viena, Austria. doi:10.1115/GT2004-53315.

[71] R. Enick, S. Klara, and J. Marano, 1995. "A Robust Algorithm for High-Pressure Gas Humidification." *Computers & Chemical Engineering*, 19(10); pp. 1051–1061. doi:10.1016/0098-1354(94)00103-U.

[72] J. O. Parente, A. Traverso, and A. F. Massardo, 2003. "Saturator Analysis for an Evaporative Gas Turbine Cycle." *Applied Thermal Engineering*, 23(10); pp. 1275–1293. doi:10.1016/S1359-4311(03)00060-7.

[73] H. Araki, S. Higuchi, S. Marushima, and S. Hatamiya, 2006. "Design Study of a Humidification Tower for the Advanced Humid Air Turbine System." *Journal of Engineering for Gas Turbines and Power*, 128(3). doi:10.1115/1.2132384.

[74] A. J. Crisalli and M. L. Parker, 1993. "Overview of the WR-21 Intercooled Recuperated Gas Turbine Engine System: A Modern Engine for a Modern Fleet." In "ASME International Gas Turbine and Aeroengine Congress and Exhibition," Paper No. 93-GT-231. ASME, Cincinnati, Ohio, USA. doi:10.1115/93-GT-231.

[75] ESDU, 1994. "Selection and Costing of Heat Exchangers." *ESDU Data Items*, (Data Item No. 92013).

[76] C. F. McDonald, 2003. "Recuperator Considerations for Future Higher Efficiency Microturbines." *Applied Thermal Engineering*, 23(12); pp. 1463–1487. doi:10.1016/S1359-4311(03)00083-8.

[77] P. J. Maziasz and R. W. Swindeman, 2003. "Selecting and Developing Advanced Alloys for Creep-Resistance for Microturbine Recuperator Applications." *Journal of Engineering for Gas Turbines and Power*, 125(1); pp. 310–315. doi:10.1115/1.1499729.

[78] D. Aquaro and M. Pieve, 2007. "High Temperature Heat Exchangers for Power Plants: Performance of Advanced Metallic Recuperators." *Applied Thermal Engineering*, 27; pp. 389–400. doi:10.1016/j.applthermaleng.2006.07.030.

[79] J. K. Min, J. H. Jeong, M. Y. Ha, and K. S. Kim, 2009. "High Temperature Heat Exchanger Studies for Applications to Gas Turbines." *Heat and Mass Transfer*, 46(2); pp. 175–186. doi:10.1007/s00231-009-0560-3.

[80] R. C. Sanders and G. C. Louie, 1999. "Development of the WR-21 Gas Turbine Recuperator." In "International Gas Turbine and Aeroengine Congress and Exhibition," Paper No. 99-GT-314. ASME, Indianapolis, Indiana, USA. doi:10.1115/99-GT-314.

[81] D. Teraji, 2005. "Mercury 50 Field Evaluation and Product Introduction." In "16th Symposium on Industrial Application of Gas Turbines," Banff, Alberta, Canada.

[82] G. Xiao, T. Yang, H. Liu, D. Ni, M. L. Ferrari, M. Li, Z. Luo, K. Cen, and M. Ni, 2017. "Recuperators for Micro Gas Turbines: A Review." *Applied Energy*, 197; pp. 83–99. doi:10.1016/j.apenergy.2017.03.095.

[83] S. J. Pugh, G. F. Hewitt, and H. Müller-Steinhagen, 2005. "Fouling During the Use of Seawater as Coolantthe Development of a User Guide." *Heat Transfer Engineering*, 26(1); pp. 35–43. doi:10.1080/01457630590890148.

[84] ESDU, 2003. "Fouling in Cooling Systems Using Seawater." *ESDU Data Items*, (Data Item No. 03004).

[85] C. A. Powel and H. T. Michels, 2000. "Copper-Nickel Alloys for Seawater Corrosion Resistance and Antifouling - A State of the Art Review." In "Corrosion 2000," NACE.

[86] M. S. Parvizi, A. Aladjem, and J. E. Castle, 1988. "Behaviour of 9010 Cupronickel in Sea Water." *International Materials Reviews*, 33(1); pp. 169–200. doi:10.1179/imr.1988.33.1.169.

[87] I. Gorynin, 1999. "Titanium Alloys for Marine Application." *Materials Science and Engineering*, 263(2); pp. 112–116. doi:10.1016/S0921-5093(98)01180-0.

[88] ESDU, 2003. "Selection and Costing of Heat Exchangers: Plate-Fin Type." *ESDU Data Items*, (Data Item No. 97006).

[89] P. V. Tous de Felipe, 2017. *Advanced Gas Turbine-Based Power Plants for Commercial Marine Applications. Heat Exchanger Design and Operation.* Msc thesis, Cranfield University, Cranfield, UK.

[90] W. M. Kays and A. L. London, 1984. *Compact Heat Exchangers.* Krieger Pub. Co, New York, USA, 3rd ed.

[91] ESDU, 1998. "Design and Performance Evaluation of Heat Exchangers: The Effectiveness - NTU Method Part 3." *ESDU Data Items*, (Data Item No. 98005).

[92] Y. Yang and Y. Li, 2014. "General Prediction of the Thermal Hydraulic Performance for Plate-Fin Heat Exchanger with Offset Strip Fins." *International Journal of Heat and Mass Transfer*, 78; pp. 860–870. doi: 10.1016/j.ijheatmasstransfer.2014.07.060.

[93] ESDU, 1993. "Forced Convection Heat Transfer in Straight tubes. Part 1: Turbulent Flow." *ESDU Data Items*, (Data Item No. 92003).

[94] ESDU, 2001. "Forced Convection Heat Transfer in Straight Tubes. Part 2: Laminar and Transitional Flow." *ESDU Data Items*, (Data Item No. 93018).

[95] ESDU, 1988. "Low-Fin Staggered Tube Banks: Heat Transfer and Pressure Loss for Turbulent Single-Phase Corssflow." *ESDU Data Items*, (Data Item No. 84016).

[96] V. Gesellschaft, 2010. "Film Condensation of Binary Mixtures with and without Inert Gas." In "VDI Heat Atlas," chap. J2. Springer Science & Business Media, Berlin, Germany, 2nd ed. doi:10.1007/978-3-540-77877-6.

[97] P. P. Walsh and P. Fletcher, 2004. *Gas Turbine Performance*. Blackwell Science Ltd, Oxford, UK., 2nd ed. doi:10.1002/9780470774533.

[98] S. Z. Vijlee, A. Ouroua, L. N. Domaschk, J. H. Beno, and A. Ouroua, 2007. "Directly-Coupled Gas Turbine Permanent Magnet Generator Sets for Prime Power Generation on Board Electric Ships." In "IEEE Electric Ship Technologies Symposium," pp. 340–347. Arlington, Virginia, USA. doi: 10.1109/ESTS.2007.372108.

[99] A. Ouroua, J. Jackson, J. Beno, R. Thongam, and E. Schoeder, 2007. "Modeling and Simulation of Electric Ships' Power System Components and their Interaction." In "Summer Computer Simulation Conference," pp. 250–257. San Diego, CA, USA.

[100] "Internal Rolls-Royce comunication."

[101] C. Casarosa, F. Donatini, and A. Franco, 2004. "Thermoeconomic Optimization of Heat Recovery Steam Generators Operating Parameters for

Combined Plants." *Energy*, 29(3); pp. 389–414. doi:10.1016/S0360-5442(02)00078-6.

[102] G. Towler and R. Sinnott, 2012. *Chemical Engineering Design: Principles, Practice and Economics of Plant and Process Design*. Elsevier Science Ltd, 2nd ed.

[103] A. Traverso, A. F. Massardo, W. Cazzola, and G. Lagorio, 2004. "WIDGET-TEMP: A Novel Web-Based Approach for Thermoeconomic Analysis and Optimization of Conventional and Innovative Cycles." In "Proceedings of ASME Turbo Expo," Paper No. GT2004-54115, pp. 623–631. ASME, Viena, Austria. doi:10.1115/GT2004-54115.

[104] 2015. "The Annual Cost Index of Chemical Engineering Plant." *Chemical Engineering*.

[105] K. Deb, A. Pratap, S. Agarwal, and T. Meyarivan, 2002. "A Fast and Elitist Multiobjective Genetic Algorithm: NSGA-II." *IEEE Transactions on Evolutionary Computation*, 6(2); pp. 182–197. doi:10.1109/4235.996017.

[106] W. J. Marner and J. W. Suitor, 1983. "A Survey of Gas-Side Fouling in Industrial Heat-Transfer Rquipment." *NASA Report*.

[107] M. Asadi and R. H. Khoshkhoo, 2013. "Investigation into Fouling Factor in Compact Heat Rxchanger." *International Journal of Innovation and Applied Studies*, 2(3); pp. 238–249.

[108] H. Zarea, F. M. Kashkooli, A. M. Mehryan, M. R. Saffarian, and E. N. Beherghani, 2014. "Optimal Design of Plate-Fin Heat Hxchangers by a Bees Algorithm." *Applied Thermal Engineering*, 69; pp. 267–277. doi:10.1016/j.applthermaleng.2013.11.042.

[109] ESDU, 1988. "High-Fin Staggered Tube Banks: Heat Transfer and Pressure Drop for Turbulent Single Phase Gas Flow." *ESDU Data Items*, (Data Item No. 86022).

[110] G. Brighenti, P. L. Orts-Gonzalez, L. Sanchez, and P. K. Zachos, 2017. "Design Point Performance and Optimization of Humid Air Turbine Power Plants." *Applied Sciences*, 7(4). doi:10.3390/app7040413.

[111] W. L. Macmillan, 1974. *Development of a Module Type Computer Program for the Calculation of Gas Turbine Off Design Performance*. Phd thesis, Cranfield University, Cranfield, UK.

[112] P. Giannakakis, P. Laskaridis, T. Nikolaidis, and A. I. Kalfas, 2015. "Toward a Scalable Propeller Performance Map." *Journal of Propulsion and Power*, 31(4); pp. 1073–1082. doi:10.2514/1.B35498.

[113] V. Pachidis, P. Pilidis, L. Marinai, and I. Templalexis, 2007. "Towards a Full Two Dimensional Gas Turbine Performance Simulator." *The Aeronautical Journal*, 111(1121); pp. 433–442. doi:10.1017/S0001924000004693.

[114] Y. G. Li, L. Marinai, V. Pachidis, E. L. Gatto, and P. Pilidis, 2009. "Multiple-Point Adaptive Performance Simulation Tuned to Aeroengine Test-Bed Data." *Journal of Propulsion and Power*, 25(3); pp. 635–641. doi:10.2514/1.38823.

[115] A. Pellegrini, T. Nikolaidis, V. Pachidis, and S. Köhler, 2017. "On the Performance Simulation of Inter-Stage Turbine Teheat." *Applied Thermal Engineering*, 113; pp. 544–553. doi:10.1016/j.applthermaleng.2016.10.034.

[116] J. B. Young and R. C. Wilcock, 2002. "Modeling the Air-Cooled Gas Turbine: Part 2 - Coolant Flows and Losses." *Journal of Turbomachinery*, 124; pp. 214–221. doi:10.1115/1.1415038.

[117] ESDU, 1998. "Design and Performance Evaluation of Heat Exchangers: The Effectiveness–NTU Method Part 1." *ESDU Data Items*, (Data Item No. 98003).

[118] Wärtsilä, 2014. "Wärtsilä X92 Low-Speed Two-Stroke Diesel Engine Technical Information." URL https://cdn.wartsila.com/docs/default-source/product-files/engines/ls-x-engine/wartsila-o-e-ls-x92.pdf?sfvrsn=8c29e945{_}4

[119] Rolls Royce, 2016. "The MT30 Marine Gas Turbine." Tech. rep. URL https://www.rolls-royce.com/{~}/media/Files/R/Rolls-Royce/documents/customers/marine/rr-mt30-brochure-uk-2016.pdf

[120] A. Bejan, G. Tsatsaronis, and M. J. Moran, 1996. *Thermal Design and Optimization*. John Wiley & Sons, Inc., New York, USA.

[121] S. Barberis and A. Traverso, 2015. "Thermoeconomic Analysis of CSP Air-Steam Mixed Cycles." In "Proceedings of ASME Turbo Expo," Paper No. GT2015-42189. ASME, Montreal, Canada. doi:10.1115/GT2015-42189.

[122] M. Jonsson, 2003. *Advanced Power Cycles with Mixtures as the Working Fluid*. Phd thesis, Royal Institute of Technology, Stockholm, Sweden.

[123] K. D. Efird, 1975. "The Interrelation of Corrosion and Fouling for Metals in Sea Water." Tech. rep.

[124] L. Melo and T. Bott, 1997. "Biofouling in Water Systems." *Experimental Thermal and Fluid Science*, 14(4); pp. 375–381. doi:10.1016/S0894-1777(96)00139-2.

[125] A. Thomas and D. L. Hillis, 1989. "Biofouling and Corrosion Research for Marine Heat Exchangers." In "Proceedings OCEANS," pp. 38–41. doi:10.1109/OCEANS.1989.592807.

[126] C. G. Broyden, 1965. "A Class of Methods for Solving Nonlinear Simultaneous Equations." *Mathematics of Computation*, 19(92); pp. 577–593. doi:10.2307/2003941.

[127] S. Kakac and A. Pramuanjaroenkij, 2012. *Heat Exchangers: Selection, Rating, and Thermal Design*. CRC Press, Boca Raton, Florida, USA.

[128] C. Ezgi, N. Özbalta, and I. Girgin, 2014. "Thermohydraulic and Thermoeconomic Performance of a Marine Heat Exchanger on a Naval Surface Ship." *Applied Thermal Engineering*, 64; pp. 413–421. doi:10.1016/j.applthermaleng.2013.12.061.

[129] Y. Söhret, S. Ekici, Ö. Altunta, A. Hepbasli, and T. H. Karakoç, 2016. "Exergy as a Useful Tool for the Performance Assessment of Aircraft Gas Turbine Engines: A Key Review." *Progress in Aerospace Sciences*, 83; pp. 57–69. doi:10.1016/j.paerosci.2016.03.001.

[130] A. Kumari and Sanjay, 2015. "Investigation of Parameters Affecting Exergy and Emission Performance of Basic and Intercooled Gas Turbine Vycles." *Energy*, 90; pp. 525–536. doi:10.1016/j.energy.2015.07.084.

[131] M. Z. Sogut, E. Yalcin, and T. H. Karakoc, 2017. "Assessment of Degradation Effects for an Aircraft Engine Considering Exergy Analysis." *Energy*. doi:10.1016/j.energy.2017.03.093.

[132] C. T. Yucer, 2016. "Thermodynamic Analysis of the Part Load Performance for a Small Scale Gas Turbine Jet Engine by Using Exergy Analysis Method." *Energy*, 111; pp. 251–259. doi:10.1016/j.energy.2016.05.108.

[133] A. W. Date, 2011. *Analytic Combustion: With Thermodynamics, Chemical Kinetics and Mass Transfer*. Cambridge University Press, Cambridge, UK.

[134] TEMA, 1999. *Standards of the Tubular Exchanger Manufacturers Association*. Technical Comitee of the Tubular Exchnager Manufacturers Association, New York, USA, 8th ed.

[135] B. C. Pak, J. B. Braun, and E. A. Groll, 2003. "Impacts of Fouling and Cleaning on the Performance of Plate Fin and Spine Fin Heat Exchangers." *KSME international journal*, 17(11); pp. 1801–1811. doi: 10.1007/BF02983611.

[136] C. R. Bott, T. R., and Bemrose, 1983. "Particulate Fouling on the Gas- Side of Finned Tube Heat Exchangers." *Journal of Heat Transfer*, 105(February 1983); pp. 178–183. doi:10.1115/1.3245538.

[137] R. Kurz and K. Brun, 2001. "Degradation in Gas Turbine Systems." *Journal of Engineering for Gas Turbines and Power*, 123(1). doi:10.1115/1.1340629.

[138] R. Kurz, K. Brun, and M. Wollie, 2009. "Degradation Effects on Industrial Gas Turbines." *Journal of Engineering for Gas Turbines and Power*, 131(6). doi:10.1115/1.3097135.

[139] A. N. Lakshminarasimha, M. P. Boyce, and C. B. Meher-Homji, 1994. "Modeling and Analysis of Gas Turbine Performance Deterioration." *Journal of Engineering for Gas Turbines and Power*, 116(1); pp. 46–52. doi: 10.1115/1.2906808.

[140] A. Zwebek and P. Pilidis, 2003. "Degradation Effects on Combined Cycle Power Plant Performance – Part I: Gas Turbine Cycle Component Degradation Effects." *Journal of Engineering for Gas Turbines and Power*, 125(3); pp. 651–657. doi:10.1115/1.1519271.

[141] J. L. Bravo, J. Rocha, and J. Fair, 1985. "Mass Transfer in Gauze Packings." *Hydrocarbon Processing*, 64(1); pp. 91–95.

[142] J. L. Bravo, J. Rocha, and J. R. Fair, 1992. "Comprehensive Model for the Performance of Columns Containing Structured Packings." In "Institution of Chemical Engineers Symposium Series," vol. 1.

[143] V. Gesellschaft, 2010. "Calulation Methods for Thermophysical Properties." In "VDI Heat Atlas," chap. D1. Springer Science & Business Media, Berlin, Germany, 2nd ed. doi:10.1007/978-3-540-77877-6.

[144] ASME, 2010. "Section VIII Division 1 Rules for Construction of Pressure Vessels." *ASME Boiler and Pressure Vessel Code*. doi:10.1115/1.802191.ch21.

[145] A. Traverso and A. F. Massardo, 2005. "Optimal Design of Compact Recuperators for Microturbine Application." *Applied Thermal Engineering*, 25(14-15); pp. 2054–2071. doi:10.1016/j.applthermaleng.2005.01.015.

[146] V. Ganapathy, 2015. *Steam Generators and Waste Heat Boilers for Process and Plant Engineers*. CRC Press, Boca Raton, Florida, USA, 1st ed. doi:10.1201/b17519.

Publications

This appendix contains the publications produced by the author derived from the project's topic of research.

1. G. Brighenti, P. L. Orts-Gonzalez, L. Sanchez, and P. K. Zachos, 2017. "Design and Optimization of Humid Air Turbine Power Plants." *Applied Science*, 7(4). doi:10.3390/app7040413.

2. P. L. Orts-Gonzalez, P. K. Zachos, and G. D. Brighenti, 2018. "Techno-economic analysis of a reheated humid air turbine." *Applied Thermal Engineering*, 137; pp. 545554, doi: 10.1016/j.applthermaleng.2018.03.094.

applied sciences

MDPI

Article

Design Point Performance and Optimization of Humid Air Turbine Power Plants

Giovanni D. Brighenti *, Pau Lluis Orts-Gonzalez, Luis Sanchez-de-Leon and Pavlos K. Zachos

Propulsion Engineering Centre, School of Aerospace, Transport and Manufacturing, Cranfield University, Cranfield, Bedfordshire MK43 0AL, UK; p.ortsgonzalez@cranfield.ac.uk (P.L.O.-G.); luis.sanchezdeleon@upm.es (L.S.-d.-L.); p.zachos@cranfield.ac.uk (P.K.Z.)

* Correspondence: g.d.brighenti@cranfield.ac.uk; Tel.: +44-0-1234-75-4633

Academic Editor: Antonio Ficarella

Received: 30 January 2017; Accepted: 13 April 2017; Published: 20 April 2017

Abstract: With the recent drive towards higher thermal efficiencies and lower emission levels in the power generation market, advanced cycle power plants have become an increasingly appealing option. Among these systems, humid air turbines have been previously identified as promising candidates to deliver high efficiency and power output with notably low overall system volume, weight and emissions footprint. This paper investigates the performance of an advanced humid air turbine power cycle and aims to identify the dependencies between key cycle design variables, thermal performance, weight and cost by means of a parametric design optimization approach. Designs of the main heat exchangers are generated, aiming to ascertain the relationship between their technology level and the total weight and acquisition cost of them. The research outcomes show that the recuperator and the intercooler are the two components with the largest influence on the thermal efficiency and the total cost. The total weight of the power system is driven by the technology level of the recuperator and the economizer. Finally, the effectiveness of the aftercooler seems to have the greatest impact in reducing the total acquisition cost of the system with minimum penalty on its thermal efficiency.

Keywords: humid air turbine; power generation; design optimization

1. Introduction

Clean and cost effective power generation is a key factor to respond to the challenges arising nowadays in the power generation market. Thermal efficiency enhancements by advanced cycle power plants significantly impacts pollutant emissions and consequently cost of electricity. Therefore, it can be argued that advanced cycle plants with low environmental footprint increase their competiveness in a market dominated by increasingly stringent emission regulations. Techno-economic assessments of such technologies should be, therefore, undertaken to identify the economic viability of such systems.

Humid Air Turbine (HAT) or Evaporative Gas Turbine (EvGT) cycles were previously found to offer lower specific investment costs than combined-cycle gas turbines (CCGTs) and notably higher thermal efficiencies, especially in the range of small to medium-sized power plants [1,2]. Moreover, HAT cycles can also offer greater specific power (higher even than the specific power of the 'dry' gas turbines), faster start-up times (comparable to the typical start-up times of 'dry' gas turbine packages), potential to reduce even further the NOx emissions due to the presence of high levels of humidity within the combustion chamber of the gas turbine, better part-load performances, and low susceptibility to ambient conditions compared to the CCGTs [3].

Since the introduction of HAT cycles in the late 80s [4], the potential of these systems has been studied extensively. Chiesa et al. [5] performed a comparison of three humid cycles showing that the HAT cycle achieved the highest thermodynamic performance, enhancing the thermal efficiency more

than 10 percentage points (pp) compared to a simple cycle. The enhancement was mainly attributed to the reduction in the discharge losses and the recuperation of the heat rejected in the intercooler within the saturator. The authors also pointed that the thermal efficiency could be further increased if a reheater was placed. Lazzaretto and Segato [6,7] performed a thermodynamic optimization of a HAT cycle where they considered the heat exchanger network as a "black box" to be later optimized. The study established that the intercooling temperature for optimum thermal efficiency was the one minimizing the compression work, and that the pressure ratio does not affect the thermal efficiency but only the specific power. When optimizing the heat exchanger network independently, they discover that the best configuration only included one intercooler, one aftercooler, and one economizer. Ågren and Westermark analysed the potential of part-flow humidification whereby a percentage of the air flow bypasses the humidifier, showing that, in some cases, it can imply a lower initial investment and even higher cycle thermal efficiencies [8,9]. Moreover, Jonsson and Yan [1] presented a detailed economic analysis proving the advantages of part-flow humidification, as lower specific investment cost for a similar cost of electricity compared to the combined cycle or the fully humidifed version. They also proved, that for larger overall pressure ratios, the benefits of the humidification process increase. In addition, Thern et al. [10] tested the idea of including an aftercooler downstream the compressor, proving that the addition of this component boosts the performance of the whole plant by enhancing the amount of heat recovered in the humidifier. Further studies have been carried out on the part load performance of HAT cycles. Wang et al. [11] and Kim et al. [12] concluded that HAT systems are less susceptible to ambient conditions than simple cycle gas turbines. Takahashi et al. [13] showed that humid turbines may demonstrate a better part-load performance than combined cycles. Additionally, optimizations performed by Kavanagh et al. [14] and Moller et al. [15] showed that the variables that drive the cycle's thermal efficiency are the overall pressure ratio (OPR), the relative pressure ratio, and the recuperator effectiveness. Additionally, Nyberg and Thern [16] studied the influence of each of the heat exchangers in thermal efficiency and specific power of the cycle, proving that the intercooler and the recuperator are the components with the largest impact on the effieicny, and the economizer is the one that drives the most signcant increment in the specific work.

Although no HAT power plants are yet in commercial service, a few experimental facilities have been built [17–20] to demonstrate this concept in reduced-scale or even micro gas turbines and identify experimentally the potential of such systems in terms of performance, part-load operation and emissions. Only one full-scale 40 MW power plant has been built aiming to investigate potential commercialisation of such systems on the power generation field [21].

Although simple humid air turbine systems have been thorougly researched previously, no emhpasis was given on the identification of the maximum thermal efficiency potential of such system as highlighted by Chiesa et al. in [5] by means of a reheated humid cycle. As pointed out by Chiesa et al. [5], such a cycle may feature notably better performance relatively to a single burner system that may promote the exploitation of humid cycle power plants in applications where high thermal efficiency and high power-to-plant size rations are of importance. This paper presents the design and optimization of an advanced humid air turbine reheated power plant and a parametric analysis across a range of key design parameters. The relationship among the key design parameters of the main heat exchangers of the system and its thermal efficiency is established. Finally, design specifications of the key heat exchangers are produced enabling correlations between cycle efficiency and heat exchanger weight and acquisition cost.

2. Methodology

Figure 1 shows the layout of the HAT system studied herein. It comprises a dual-shaft gas generator with a free power turbine. Water absorption into the compressed air takes place in the saturator. The dry air entering the saturator is previously cooled down in the aftercooler, which increases the performance of the saturator tower as it permits to recover larger amounts of low-quality—i.e., low temperature—heat [10]. Once inside the tower, both heat and mass are

Appl. Sci. **2017**, *7*, 413 3 of 22

transferred from the stream of hot water circulating counter-currently into the air, increasing its temperature and mass flow. Due to the relatively low temperatures of the humid air exiting the saturator, the HAT cycle benefits from a recuperator that recovers the high-quality—i.e., high-temperature waste heat from the exhaust gases before streaming the humid air into the combustion chamber. An additional bypass is also present between the high-pressure compressor exit and the inlet of the recuperator, as suggested by Ågren and Westermark [8,9], so that a certain fraction of dry air can bypass the humidification process and is mixed with the rest of the humid air between the saturator and the recuperator inlet. The amount of air that bypasses the humidifier is represented by the parameter β, which represents the ratio of air flowing through the aftercooler and saturator to the inlet mass flow. Therefore, $\beta = 1$ when all the air goes through the aftercooler and saturator, whereas, for $\beta = 0$, all of the air bypasses them.

In this study, an open loop is used to feed water in the heat exchangers, on the assumption that a water source is available. The evaporation process in the saturator and an efficient droplet eliminator at the gas outlet of the saturator acts as a water-treatment device per se, allowing the use of non-demineralized water without undermining the life of the components.

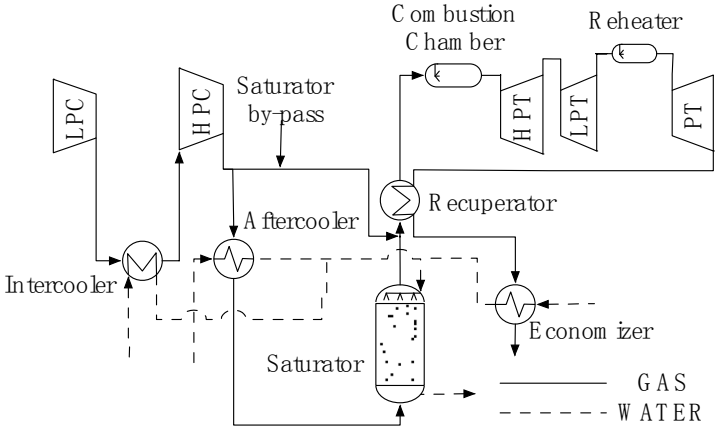

Figure 1. Schematic layout of the Humid Air Turbine.

The thermal performance of the system is resolved using Turbomatch© [22,23], an in-house 0D performance software developed at Cranfield University, with external modules for the heat exchangers and saturator performance, and blade cooling mass flow requirements calculations. For the design point performance prediction, the power output is set constant at 40 MW with no mechanical losses considered. In terms of fuel, Marine Diesel chemical properties were used for combustion calculations [24]. With regards to turbomachinery performance, a 90% polytropic efficiency is assumed for the compressors and the core turbines, whereas 92% is assumed for the power turbine, to reflect the current technology levels of these components. The turbine inlet temperature (TIT) at the outlet of the main combustion chamber as well as at the outlet of the reheater was set constant at 1600 K. Turbine cooling flows are calculated using the methodology proposed by Young and Wilcock [25]. This method accounts for the cooling requirement of the disks, and the stationary and rotating blades when cooled with internal convection and film cooling technology. Typical values for maximum metal temperature ($T_{m,max}$ = 1300 K), film cooling effectiveness (ε_f = 40%) and internal flow cooling efficiency (η_c = 70%) are used as discussed by Horlock et al. in [26]. Turbine cooling flows are extracted downstream of the high pressure compressor and upstream of the aftercooler.

The outlet conditions from all gas-water heat exchangers, namely the intercooler, the aftercooler and economizer, are resolved by imposing the effectiveness, which is viewed as the heat exchanger's technology level, ($\varepsilon = Q/Q_{max}$) and the heat capacity ratio ($C^* = C_{min}/C_{max}$) between the two streams, assuming that $C_w = C_{max}$.

Water condensation in the air stream is possible within the intercooler and aftercooler due to the high pressure and low temperature of the gas at the outlet of the heat exchangers ($T_{g,\,out} < T_{g,\,dew}$). In the economizer, condensation may also occur due to high humidity levels in the exhaust gas of the recuperator and the low temperature required at the economizer's exit. The latent heat of condensation of the water in the humid air varies the heat capacity of the gas C_g during condensation and generates a pinch point between the two streams within the heat exchanger (Figure 2). Therefore, this process is considered when simulating the performance of the heat exchangers.

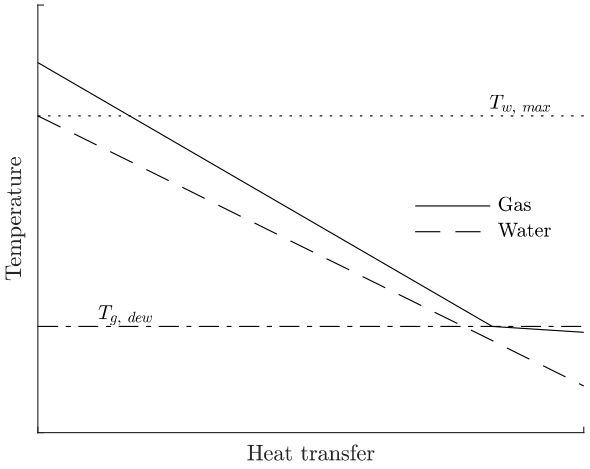

Figure 2. Heat transfer process in the Economizer.

Liquid water is injected into the saturator to facilitate the humidification process. The temperature of the water at the outlet of the heat exchangers is, therefore, limited by the water saturation temperature. A safety coefficient of 0.9 is introduced into the performance calculations to avoid any steaming in the saturator as follows:

$$T_{w,out} \leq T_{w,max} = T_{sat}(0.9 \times p_{SAT}), \tag{1}$$

where $T_{w,out}$ is the water temperature at the outlet of the heat exchangers, T_{sat} is the saturation temperature and p_{SAT} is the pressure in the saturator. When the water temperature at the outlet of the heat exchangers exceeds the limit temperature $T_{w,max,}$ a new value of C^* is calculated, overwriting the imposed value. In the recuperator, the inlet properties of both streams are defined; therefore, the outlet conditions of the two streams are calculated from the prescribed recuperator effectiveness. Total pressure losses of the heat exchanger are fixed at a target value of 5% in both sides of all heat exchangers as recommended previously by Kavanagh et al. [14] and Nyberg et al. [16].

The conditions at the outlet of the saturator are calculated by imposing the pinch point temperature difference between the operating line of the water and the saturation line. The saturator is modelled according to the approach discussed by Sanchez de Leon [27] and originally developed by Aramayo-Prudencio [28]. The detailed description of the thermodynamic model of the saturator and its validation against experimental data is provided in Appendix A.

The impact of the key heat exchanger design parameters on the cycle thermal efficiency, plant weight and cost is assessed via a parametric study. The heat exchanger technology level is represented by their effectiveness. In terms of saturator design, the pinch temperature difference between the operating and the saturated air enthalpy lines [28] is used as a design parameter, as it represents the driver for the heat and mass transfer process within the saturator.

Cycle analysis has shown that the overall pressure ratio (*OPR*) that maximizes the thermal efficiency for the imposed TIT of 1600 K is beyond the technology today available for stationary or

Appl. Sci. **2017**, *7*, 413

aero gas turbines ($OPR > 50$). Therefore, two values of OPR are investigated, namely 30 and 40, as representatives of a standard and an advanced compression system technologies currently available in the market.

The design envelopes of the above-mentioned variables are summarized in Table 1 and represent the range across which the parametric campaign was conducted for a total of 486 cycle designs.

Table 1. Range of parameters across which the parametric study was conducted.

Parameter		Units	Range
Intercooler, aftercooler, economizer effectiveness	$\varepsilon = Q/Q_{max}$	(-)	[0.75, 0.8, 0.95]
Recuperator effectiveness	$\varepsilon = Q/Q_{max}$	(-)	[0.8, 0.85, 0.9]
Saturator pinch temperature difference	ΔT_{ps}	(K)	[5, 10, 15]
Overall pressure ratio	OPR	(-)	[30, 40]

For each of the 486 cycles calculated, the rest of the design variables (heat capacity ratio of the water-air heat exchangers, relative pressure ratio, and saturator bypass) are optimized to maximize the thermal efficiency. This optimization is performed by means of the single objective genetic algorithm in MATLAB® (R2016a, MathWorks, Natick, MA, USA) [29]. The upper and lower bounds of these variables are reflected in Table 2. Therefore, the thermodynamic "design vector" comprises the effectiveness of the heat exchangers, the OPR and the humidifier pinch point as the free design variables, and the heat capacity ratios of the water-air heat exchangers, the relative pressure ratio and the saturator bypass as the optimized design variables.

Table 2. Heat exchanger design parameters and range specfication.

Design Variable		Range
Intercooler, Aftercooler, Economizer heat capacity ratio	$C^* = C_{min}/C_{max}$	[0.6–0.95]
Relative pressure ratio	$relPR = \log_{OPR} PR_{LPC}$	[0.25–0.75]
Saturator bypass	β	[0–1]

Detailed designs of the heat exchangers and the saturator tower are produced to estimate the weight and acquisition of these components. The geometries selected for the heat exchangers are: counter-current plate-fin for the intercooler and the aftercooler, multi-pass cross-flow plate-fin for the recuperator, and finned-tube for the economizer. Lastly, for the saturator, a structured packing-bed tower is selected. The models employed for the detailed design and optimization of these components and the correlations used to estimate the acquisition are summarized in Appendix B.

3. Results and Discussion

A number of cycles have been selected to describe the effect of the "design vector" on the performance, cost and size of the power plant. The heat exchanger "design vectors" of the selected cycles ($A \rightarrow G$) are shown in Table 3 and Figure 3. When referring to the cycles in the text, the overall pressure ratio is defined by the superscript L^{OPR} and the pinch temperature difference in the saturator by the subscript $L_{\Delta T_{ps}}$.

Table 3. Cycle nomenclature definition.

Parameter	*A*	*B*	*C*	*D*	*E*	*F*	*G*
ε_{IC} (-)	0.95	**0.85**	**0.75**	0.95	0.95	**0.75**	0.95
ε_{AC} (-)	0.95	**0.85**	**0.75**	**0.75**	0.95	0.95	0.95
ε_{EC} (-)	0.95	**0.85**	**0.75**	0.95	**0.75**	0.95	0.95
ε_{REC} (-)	0.90	**0.85**	**0.8**	0.90	0.90	0.90	**0.80**

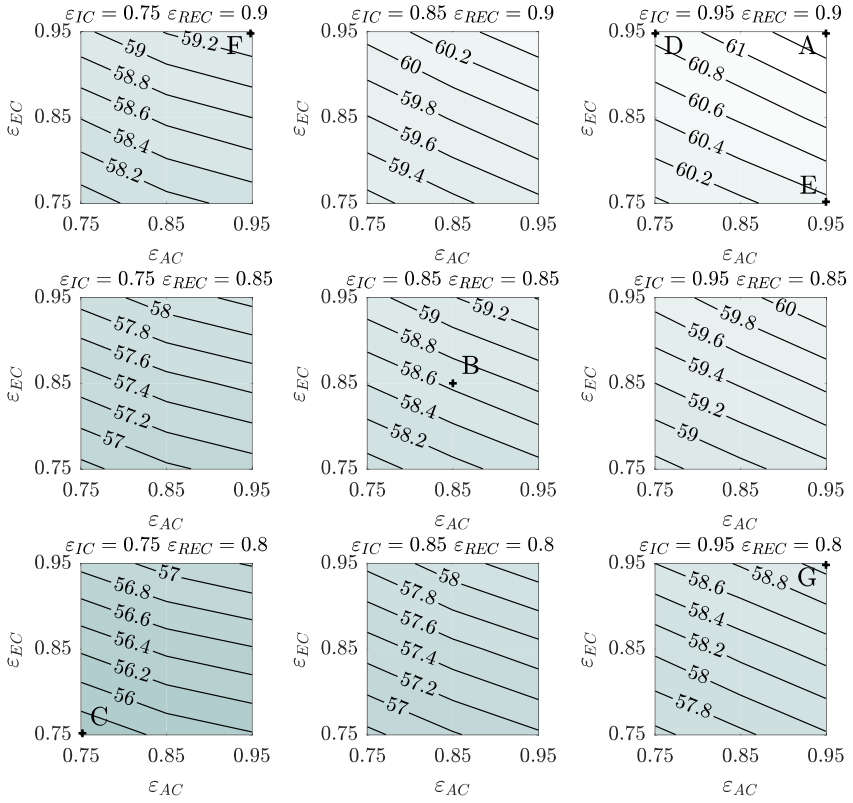

Figure 3. Cycle thermal efficiency across the design space as a function of the heat exchanger effectiveness—OPR = 40 & ΔT_{ps} = 5 K.

The outcomes of the parametric cycle performance studies are analyzed using cycle A_5^{40} as a reference, which represents the system with maximum thermal efficiency, maximum effectiveness of all heat exchangers, maximum OPR and minimum pinch temperature difference in the humidifier. The design vector of the baseline cycle as well as its performance metrics are shown in Table 4. All values in subsequent plots are normalized against the cycle with maximum thermal efficiency A_5^{40}.

Table 4. Design variables values of the baseline cycle A_5^{40} with maximum thermal efficiency.

Optimized Design Variable		Units	Value
Thermal efficiency	η_{HAT}	(%)	61.4
Overall pressure ratio	OPR	(-)	40
Relative pressure ratio	$relPR$	(-)	0.53
Intercooler effectiveness	ε_{IC}	(-)	0.95
Aftercooler effectiveness	ε_{AC}	(-)	0.95
Economizer effectiveness	ε_{EC}	(-)	0.95
Saturator pinch temperature difference	ΔT_{ps}	(K)	5
Recuperator effectiveness	ε_{REC}	(-)	0.9
Intercooler heat capacity ratio	C_{IC}^*	(-)	0.95
Aftercooler heat capacity ratio	C_{AC}^*	(-)	0.95
Economizer heat capacity ratio	C_{EC}^*	(-)	0.82
Saturator bypass	β	(-)	0.43
GT inlet gas mass flow	$\dot{m}_{g,GT\ inlet}$	(kg/s)	40.6

Appl. Sci. **2017**, *7*, 413

3.1. Impact of Heat Exchanger Effectiveness on Cycle Performance

The impact of heat exchanger effectiveness on the cycle thermal efficiency is shown in Figure 3, for constant *OPR* of 40 and pinch temperature difference in the saturator of 5 K. The *x*-axis and *y*-axis of the contour plots are, respectively, the aftercooler and economizer effectiveness, and the contour lines show the estimated cycle thermal efficiency. Moving vertically and horizontally through the contour plots, the effectiveness of the recuperator and intercooler vary respectively. Therefore, the top-right point of the top-right contour corresponds to the cycle A_5^{40} shown in Table 4.

In all contours with intercooler effectiveness of 0.75 (left column of contours in Figure 3), there is a change in in the variation rate of the thermal efficiency when the ε_{AC} falls below 0.85. This is due to the notably high value of aftercooler heat capacity ratio C^*_{AC} = 0.95 for aftercooler effectiveness of 0.95 and 0.85, which it decreases to C^*_{AC} = 0.64 when the effectiveness of the aftercooler is 0.75, in order for the outlet water temperature to remain within the limits imposed to avoid steaming in the saturator ($T_{w,out} = T_{sat}(0.9 \times p_{SAT})$).

The dependency between the thermal efficiency and the heat exchanger effectiveness remains linear when changing the effectiveness of all heat exchangers together. The comparison between cycles A_5^{40} and G_5^{40} highlights the impact of the recuperator effectiveness and results in a reduction of 2.28 pp in cycle thermal efficiency when recuperator effectiveness becomes 0.8 from 0.9. The impact of intercooler effectiveness is shown by comparing cycle A_5^{40} against F_5^{40}. A reduction in ε_{IC} from 0.95 to 0.75 causes a reduction of 2 pp in the cycle thermal efficiency. The impact of the aftercooler and economizer is shown by the comparison of the cycle A_5^{40} with the cycle D_5^{40}, and of A_5^{40} with the cycle E_5^{40}, with, respectively, a reduction of 0.48 pp and 1 pp on the thermal efficiency. The combined effect of the reduction in effectiveness of all the heat exchangers is shown by the comparison of the cycle A_5^{40} with the cycle B_5^{40} and C_5^{40} with, respectively, a drop of 2.7 pp and 5.5 pp in thermal efficiency.

Figure 4 shows the effect of the heat exchanger effectiveness on the absolute humidity at the inlet of the combustion chamber for constant values of *OPR* (40) and saturator pinch temperature difference (5 K). The maximum absolute humidity in the design space is 24.6%, which ensures stable combustion in a modern combustion chamber as discussed by Göke in [30].

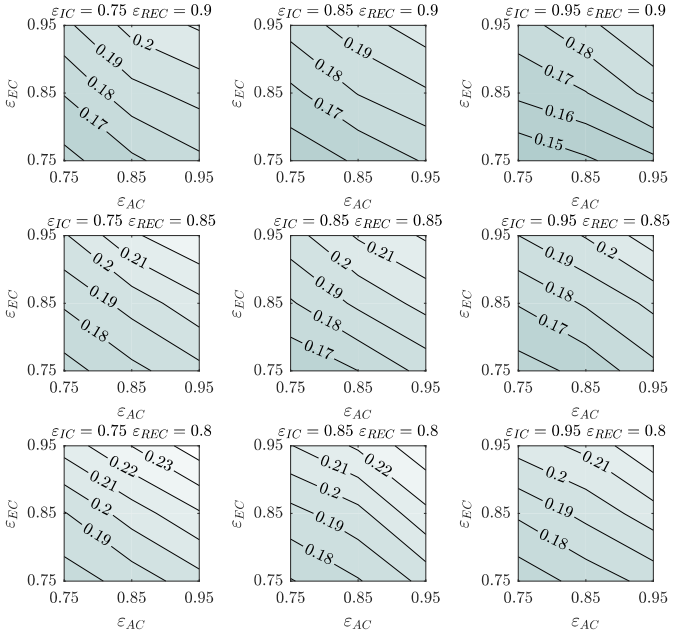

Figure 4. Absolute humidity at the inlet of the combustion chamber across the design space as a function of the heat exchanger effectiveness—*OPR* = 40 & ΔT_{ps} = 5 K.

The impact of heat exchanger effectiveness on the optimized saturator bypass ratio, on the consequent absolute humidity (ω) at the inlet of the combustion chamber and on cycle thermal efficiency is illustrated in Figure 5 for constant OPR = 40 and ΔT_{ps}= 5 K.

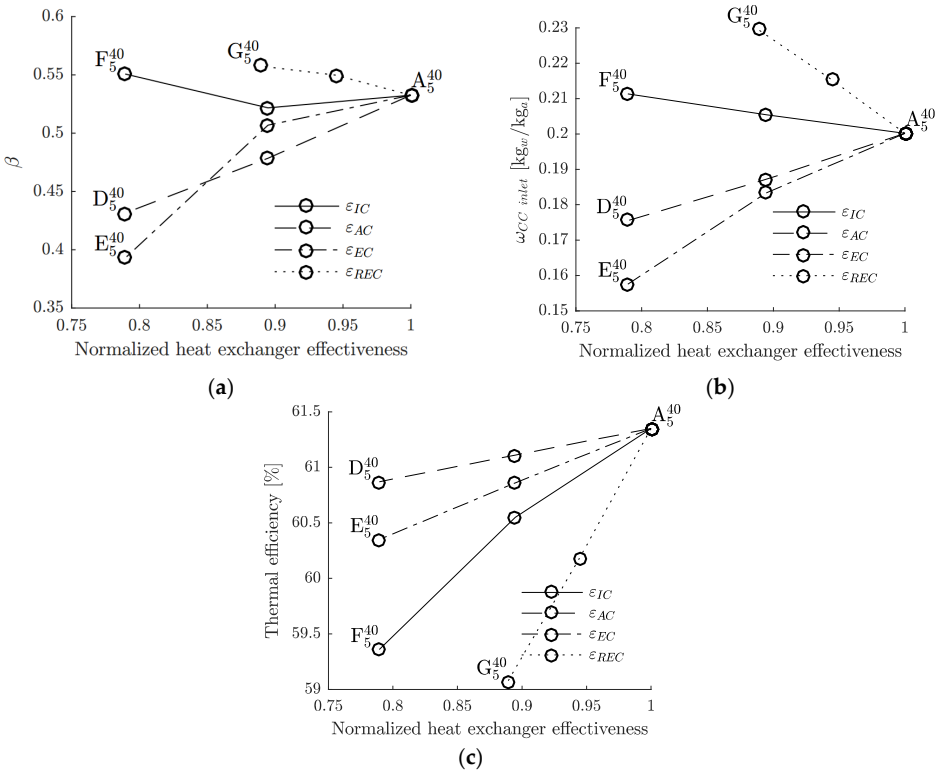

Figure 5. (**a**) normalized heat exchanger effectiveness vs. mass flow fraction through the saturator and aftercooler; (**b**) normalized heat exchanger effectiveness vs. absolute humidity at the inlet of the combustion chamber; and (**c**) normalized heat exchanger effectiveness vs. cycle thermal efficiency—OPR = 40 & ΔT_{ps} = 5 K.

The reduction in effectiveness of the aftercooler and economizer has an impact on the amount of heat and mass transfer that occurs in the saturator and, therefore, on the thermal efficiency of the cycle. For an aftercooler effectiveness of 0.75 ($A_5^{40} \rightarrow D_5^{40}$—see Figure 5), the water mass flow in the saturator is reduced by 0.5% while a 1.2% reduction is observed in its temperature ($C_{AC}^* = 0.95$ across the range). The temperature of the gas at the inlet of the saturator increases by 13.8%, reducing the temperature leap in the saturator and, therefore, the heat and mass transfer that occurs within the device. Hence, the fraction of gas that bypasses the saturator (β) decreases by 19% (Figure 5a) and the humidity at the inlet of the combustion chamber also decreases from 20% to 18% (Figure 5b). The reduction in heat recuperated at low temperature in the cycle, due to the aftercooler, affects the thermal efficiency of the cycle, with a 0.48 pp reduction between cycles A_5^{40} and D_5^{40} (Figure 5c).

When the economizer effectiveness reduces from 0.95 to 0.75 ($A_5^{40} \rightarrow E_5^{40}$—see Figure 5), the mass flow of the water heated in the heat exchanger falls by 22%, whereas the water outlet temperature falls only by 0.3%—i.e., C_{EC}^* increases. As for the aftercooler, the saturator bypass β decreases by 26% as shown in (Figure 5a) and the humidity at the inlet of the combustion chamber decreases from 20% to 15.7% (Figure 5b). This reduction in heat recuperated in the cycle at low temperature, as for the aftercooler, entails a decrease in thermal efficiency of 1 pp between cycles A_5^{40} and E_5^{40} (Figure 5c).

The effectiveness of the intercooler affects the amount of waste heat that is recuperated both at high and low temperatures within the cycle. When ε_{IC} becomes 0.75 from 0.95 ($A_5^{40} \rightarrow F_5^{40}$—see

Appl. Sci. **2017**, *7*, 413 9 of 22

Figure 5), the total amount of water injected in the saturator increases by 10% due to the increase of heat available in the gas at the inlet of the economizer—i.e., the temperature at the outlet of the recuperator on the hot side increases due to the increase in temperature of the gas at the inlet of the cold side. Therefore, the mass flow ratio of gas that bypasses the saturator decreases by 2% (Figure 5a) and the humidity at the inlet of the combustion chamber increases by 5% (Figure 5b). This highlights the importance of the intercooling process, since it not only reduces the compression work required but also the heat extracted from the gas between the two compressors is partly recovered in the saturator and not rejected entirely as in most common intercooled gas turbines. Thus, the reduction of the effectiveness of the intercooler from 0.95 to 0.75 entails a reduction of 2 pp in the cycle thermal efficiency ($A_5^{40} \rightarrow F_5^{40}$—see Figure 5c).

The recuperator is the heat exchanger whose effectiveness change has the most severe effects on the thermal efficiency of the cycle, with a reduction of 2.28 pp in thermal efficiency when it is reduced to 0.8 from 0.9 ($A_5^{40} \rightarrow G_5^{40}$—see Figure 5), due to the reduction of high quality heat recovery—i.e., heat recovery at high temperature—within the cycle. Nevertheless, this reduction in recuperator effectiveness results in higher enthalpy gas at the inlet of the economizer and entails 22% higher amount of heat transfer in the latter heat exchanger. Therefore, the water mass flow injected into the saturator increases by 10%, the mass flow ratio of gas that bypasses the saturator decreases—i.e., β increases by 4.7% as shown in Figure 5a—and the humidity at the inlet of the combustion chamber increases from 20% to 23% (Figure 5b).

Figure 6 shows the impact of the heat exchanger effectiveness on the heat transfer coefficient times the heat transfer area ($k \times A$) of each heat exchanger for constant *OPR* (40) and saturator pinch temperature difference (5 K). For similar inlet conditions, the variation in $k \times A$ of a heat exchanger is a useful parameter to evaluate the impact of the of the cycle "design vector" on the variation in size independently from the design choices in sizing the heat exchanger. Nonetheless, $k \times A$ should not be used to evaluate the differences in size between intercooler, aftercooler, economizer and recuperator due to the different inlet conditions of the two flows—i.e., different heat transfer coefficients. The values of $k \times A$ for each heat exchanger are normalized using the values of the reference cycle A_5^{40} which is reported in Table 5.

Table 5. $k \times A$ of the heat exchangers for the reference cycle A_5^{40} (see also Table 4).

Component	Units	$k \times A$ for Reference Cycle A_5^{40}
Intercooler	(kW/K)	545.5
Aftercooler	(kW/K)	267.7
Economizer	(kW/K)	389.1
Recuperator	(kW/K)	379.4

The heat exchangers that are mostly affected by the reduction in effectiveness are the intercooler and aftercooler, with a reduction of $k \times A$ respectively of 79% ($A_5^{40} \rightarrow F_5^{40}$—see Figure 6a) and of 82% ($A_5^{40} \rightarrow E_5^{40}$—see Figure 6b) in relative terms when reducing the effectiveness of the latter from 0.95 to 0.75.

The variation of effectiveness of a heat exchanger, however, has a knock-on effect on the $k \times A$ of the remaining heat exchangers. The aftercooler $k \times A$ is strongly affected by the variation of the intercooler and economizer effectiveness with a 38.5% and 22% reduction when reducing ε_{IC} and ε_{EC} become 0.75 from 0.95 ($A_5^{40} \rightarrow F_5^{40}$ in Figure 6a and $A_5^{40} \rightarrow D_5^{40}$ Figure 6c). In addition, the $k \times A$ of the economizer is strongly affected by the variation of the effectiveness of the recuperator ($A_5^{40} \rightarrow G_5^{40}$) with a reduction of 21%. No knock-on effect on the recuperator and intercooler $k \times A$ was found by effectiveness changes of the rest of the heat exchangers.

The increase of the saturator pinch temperature difference ΔT_{ps} from 5 K to 15 K ($A_5^{40} \rightarrow A_{15}^{40}$) has a linear effect on the thermal efficiency and on the absolute humidity of the air at the inlet of the combustion chamber (Figure 7a), with a reduction in thermal efficiency of 0.64 pp from the baseline

cycle. The $k \times A$ of all heat exchangers are not significantly affected by the pinch temperature difference in the saturator (Figure 7b) with a maximum increase of 4% in intercooler $k \times A$ for ΔT_{ps} = 15 K. The increases in $k \times A$ (cycle $A_5^{40} \rightarrow A_{15}^{40}$) are attributed to the 3.2% higher gas mass flow requirement to produce the prescribed power output of 40 MW triggered by the lower water content in the hot section of the power plant.

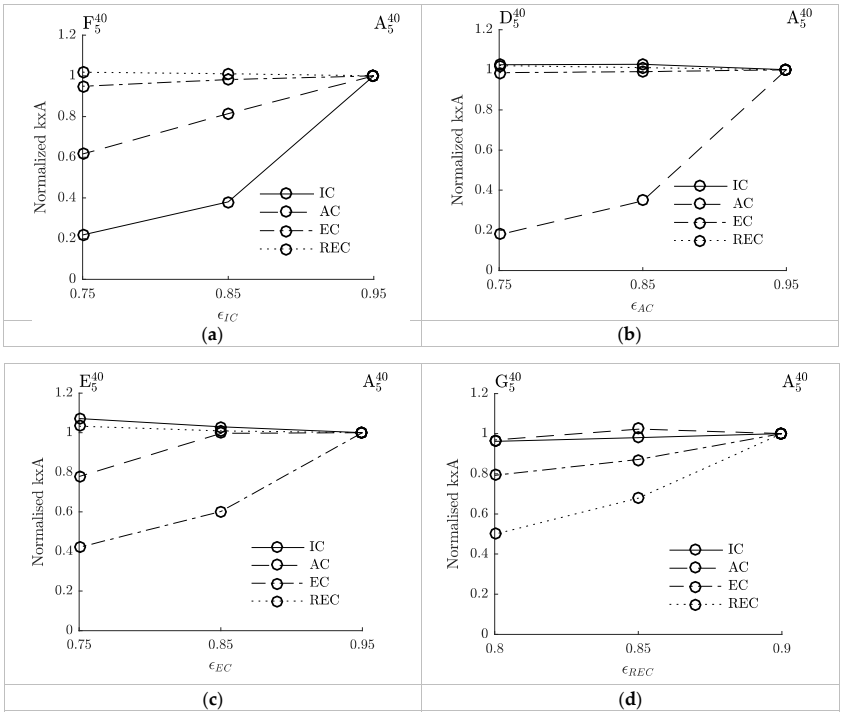

Figure 6. (**a**) normalized inverse total resistance, $k \times A$ of each heat exchanger vs. intercooler effectiveness ($A_5^{40} \rightarrow F_5^{40}$); (**b**) normalized $k \times A$ of each heat exchanger vs. aftercooler effectiveness ($A_5^{40} \rightarrow E_5^{40}$); (**c**) normalized $k \times A$ of each heat exchanger vs. economizer effectiveness ($A_5^{40} \rightarrow D_5^{40}$); and (**d**) normalized $k \times A$ of each heat exchanger vs. recuperator effectiveness ($A_5^{40} \rightarrow G_5^{40}$)—$OPR$ = 40 & ΔT_{ps} = 5 K.

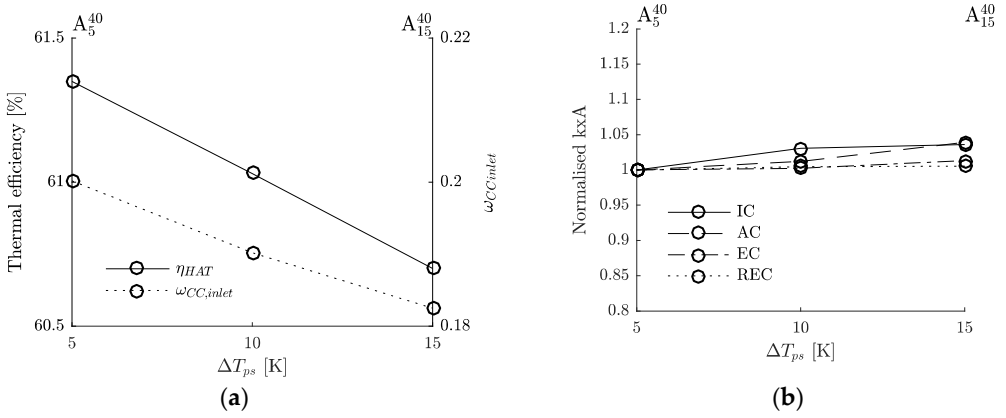

Figure 7. (**a**) saturator pinch temperature difference vs. cycle thermal efficiency and absolute humidity at the inlet of the combustion chamber ($A_5^{40} \rightarrow A_{15}^{40}$); (**b**) saturator pinch temperature difference vs. normalized $k \times A$ of each heat exchanger ($A_5^{40} \rightarrow A_{15}^{40}$)—OPR = 40 & ε_{IC} = 0.95 & ε_{AC} = 0.95 & ε_{EC} = 0.95 & ε_{REC} = 0.9.

Appl. Sci. **2017**, *7*, 413 11 of 22

3.2. Impact of Overall Pressure Ratio

The parametric design point performance analysis was conducted at an *OPR* of 30 that represents a typical technology level for current power generation applications. An optimum cycle configuration with thermal efficiency of 60.7% is achieved when reducing the overall pressure ratio from 40 to 30 ($A_5^{40} \rightarrow A_5^{30}$)—i.e., a reduction of 0.7 pp with regards to the baseline cycle with *OPR* = 40. The inlet gas mass flow to deliver the prescribed power output of 40 MW increases by 9.8%. This is achieved with the maximum specified effectiveness of all heat exchanger and minimum pinch temperature difference in the humidifier as shown in Table 6. The humidity levels at the inlet of the main burner is reduced by 10.2% while saturator bypass β increases by 4 pp when reducing the overall pressure ratio from 40 to 30. This is attributed to the lower water temperature at the outlet of the intercooler, aftercooler, economizer and the reduction in temperature of the gas at the outlet of the high pressure compressor.

Table 6. Design variables values of the baseline cycle A_5^{30} with maximum thermal efficiency.

Optimized Design Variable		Units	Value
Thermal efficiency	η_{HAT}	(%)	60.7
Overall pressure ratio	OPR	(-)	30
Relative pressure ratio	$relPR$	(-)	0.53
Intercooler effectiveness	ε_{IC}	(-)	0.95
Aftercooler effectiveness	ε_{AC}	(-)	0.95
Economizer effectiveness	ε_{EC}	(-)	0.95
Saturator pinch temperature difference	ΔT_{ps}	(K)	5
Recuperator effectiveness	ε_{REC}	(-)	0.9
Intercooler heat capacity ratio	C_{IC}^*	(-)	0.95
Aftercooler heat capacity ratio	C_{AC}^*	(-)	0.95
Economizer heat capacity ratio	C_{EC}^*	(-)	0.70
Saturator bypass	β	(-)	0.47
GT inlet gas mass flow	$\dot{m}_{g,GT\ inlet}$	(kg/s)	44.86

Although the reduction in overall pressure ratio implies cheaper and more compact turbomachinery, the decrease in specific power results in a 11.2% and 10.3% increase in $k \times A$ (Figure 8) of the intercooler and recuperator, respectively, whereas the aftercooler and economizer $k \times A$ decrease by approximately 4%. This yields more expensive designs of the intercooler and recuperator with an increase in acquisition cost index of, respectively, 25.6% and 7% (Figure 9).

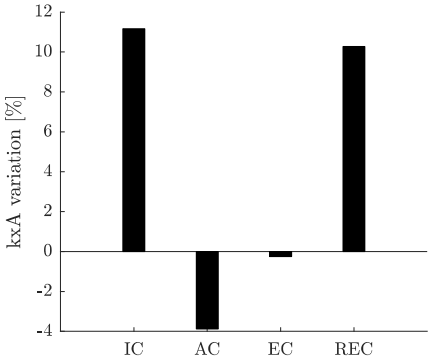

Figure 8. Variation of the $k \times A$ of the heat exchangers when varying the overall pressure ratio from 40 to 30 ($A_5^{40} \rightarrow A_5^{30}$)—$\Delta T_{ps}$ = 5 K, ε_{IC} = 0.95 & ε_{AC} = 0.95 & ε_{EC} = 0.95 & ε_{REC} = 0.9.

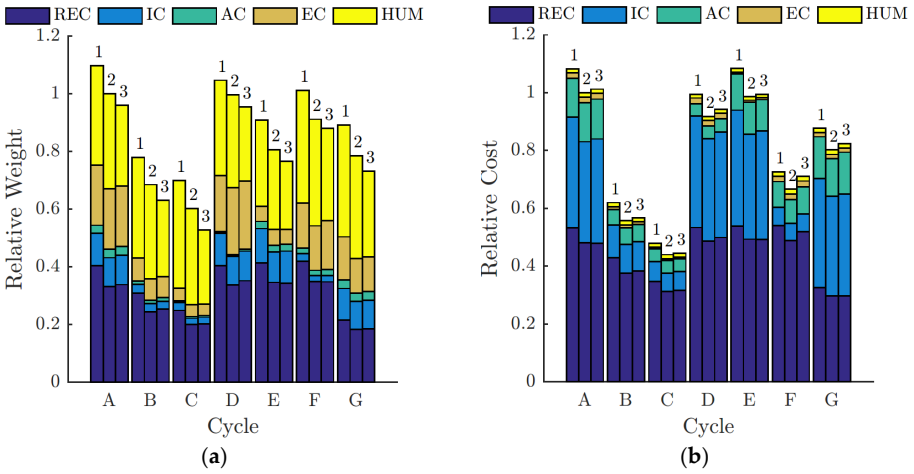

Figure 9. (**a**) break down of heat exchanger total relative weight; and (**b**) break down of heat exchanger total relative cost. (Bar 1) OPR = 30 & ΔT_{ps} = 5 K; (Bar 2) OPR = 40 & ΔT_{ps} = 5 K; (Bar 3) OPR = 40 & ΔT_{ps} = 15 K.

3.3. Heat Exchanger Size and Cost Analysis

The breakdown of the total weight and cost for the heat exchanger configurations are highlighted in Figure 9. Cycles *A*, *B*, and *C* (see Table 3) show the variation when the effectiveness of all heat exchangers vary together. On the other hand, cycles *D*, *E*, *F*, and *G* show the effect of reducing the technology level of one heat exchanger at a time. The reference cycle (A_5^{40}) has been used to normalize the weight and cost of the components. The total reference weight of all heat exchangers is estimated up to 47.76 tones, whereas the reference cost estimate is 4.2 m USD. These estimates are broadly in accordance with the cost estimates previously presented by Jonsson and Yan [1] for a power plant of 55.1 MW (3.8 m USD updated to 2015). It is important to highlight that the thermal efficiency achieved by the reference cycle (61.4%) is 11.9 pp higher than the one reported by Jonsson and Yan in [1], which partially justifies the discrepancy in the heat exchanger acquisition cost estimate.

For cycle A_5^{40}, the recuperator is the heaviest component—33.12% of the total weight—followed by the humidifier, the economizer, the intercooler, and finally the aftercooler—with relative contributions to the overall power plant weight of 33.01%, 20.96%, 9.98%, 2.94%, respectively. Although the economizer and the humidifier are among the heaviest components, their contribution to the overall cost of the system was found to be approximately 3% (Figure 9). In terms of heat exchanger cost, the recuperator is the most expensive heat exchanger—48.11% of the total cost, followed by the intercooler, the aftercooler, the economizer, and finally the saturator—with relative contributions to the overall cycle cost of 34.95%, 13.43%, 1.99%, and 1.52%, respectively.

Reducing the OPR from 40 to 30 increases the total weight across a range between 5% and 10% depending upon the cycle technology level (Figure 9a), and the total cost by 8% in all cases (Figure 9b). The observed increment in heat exchanger weight is primarily driven by the recuperator and the economizer due to the excess of available heat downstream the power turbine that needs to be managed by these two components whose size is further increased by the higher flow rate requirement of this low OPR cycle. As a result, the size increase of the recuperator primarily drives the increase in the estimated acquisition cost of the system. It is worth noting that when the OPR becomes 30 from 40, the humidifier is 7% less expensive, driven by the need for thinner shell walls. However, an increase in weight is observed as the required material for packing increases by 12% compared to the baseline case to facilitate the larger enthalpy flux. Finally, although the reduction of the OPR to 30 increases the weight and the cost of the components, it is associated with a reduction in the overall thermal efficiency of the system by 0.7 pp.

Appl. Sci. **2017**, *7*, 413

When the ΔT_{ps} becomes 15 K from 5 K, the size, and, consequently, the weight and cost of all the heat exchangers increases due to the demand of a higher mass flow to achieve the required power output. The saturator is the only component whose weight and cost reduce as it becomes shorter. Except for A_{15}^{40}, which increases its total weight compared with A_5^{40}, the reduction in the weight of the humidifier outbalances the increment in the weight of the heat exchangers, but not the increment in the cost. When the pinch point temperature is increased to 15 K, the total acquisition cost of the system marginally increases by around 3% while the thermal efficiency falls by approximately 0.45 pp.

The comparison of cycles A_5^{40}, B_5^{40}, and C_5^{40} (Figure 9), where the effectiveness of all the heat exchangers is reduced at the same time, shows the exponential relationship between the technology level of the components, and their weight and cost. When the effectiveness of the heat exchangers increases from 0.75 to 0.85 ($C_5^{40} \rightarrow B_5^{40}$), the total weight increases by 14% and the total cost by 28%. For a further effectiveness increase to 0.95 ($B_5^{40} \rightarrow A_5^{40}$), the weight rises by 46% and the cost by 80% with respect to the baseline cycle. On the other hand, the thermal efficiency shows a quasi-linear correlation with the cycle design parameters. From C_5^{40} to B_5^{40}, the efficiency rises by 2.8 pp, and from B_5^{40} to A_5^{40}, an increase of 2.7 pp is observed (Figure 3).

Considering each heat exchanger separately, between cycles A_5^{40} and C_5^{40}, the intercooler is the component that undergoes the largest variation in weight, manifesting a reduction of 77%. The economizer shows a reduction of 65% with regards to its reference cost, followed by the aftercooler with a reduction of 60%, and, finally, the recuperator with a reduction of 40%. On the other hand, the intercooler is the component that suffers the largest reduction in cost—82% of its reference cost, followed by the economizer, the aftercooler, and the recuperator—70%, 67%, and 35%, respectively. This demonstrates that the variations in the total weight of the heat exchangers and the variations in cost are linearly related, as the changes in cost are directly correlated with the variations in weight of each component.

Moreover, when comparing cycles D_5^{40}, E_5^{40}, F_5^{40}, and G_5^{40} with A_5^{40}, it can be seen that the reduction of the technology level of a heat exchanger has a knock-on effect on the remaining heat exchangers of the system (see Figure 9). The aftercooler is the heat exchanger that experiences the largest reduction in weight and cost—88% and 87%, respectively. In addition, both the weight and cost of the aftercooler are cut by 39% when the effectiveness of the intercooler is reduced from 0.95 to 0.75 ($A_5^{40} \rightarrow F_5^{40}$). However, both the weight and cost of the aftercooler are cut by 39% and 17%, respectively, when the effectiveness of the economizer is reduced from 0.95 to 0.75 ($A_5^{40} \rightarrow D_5^{40}$).

The weight and cost of the economizer is reduced by 43% and 14%, respectively, when the recuperator effectiveness is changed from 0.9 to 0.8 ($A_5^{40} \rightarrow G_5^{40}$). Hence, the design of the power plant must account for the impact of the technology level of one of the components on the design, cost, and weight of the remaining heat exchangers.

The overall system estimated acquisition cost and weight is shown in Figure 10 normalized against the baseline cycle A_5^{40} metrics. In terms of total weight, the change produced by the economizer and the recuperator—20% and 22% of the reference weight, respectively—is an order of magnitude higher than the changes produced by the intercooler, or the aftercooler—9%, and 1%, respectively. On the other hand, the changes produced by the intercooler, the recuperator, and the aftercooler—34%, 20%, and 8% of the reference cost, respectively—are one order of magnitude higher than the ones the economizer can create which is around 2%. In addition, from the contours illustrated in Figures 3 and 10b, it can be demonstrated that the most efficient way to reduce the total cost of the heat exchangers is to reduce the effectiveness of the aftercooler. The ratio of the percentage variation in cost to the variation in thermal efficiency $\Delta c(\%)/\Delta\eta(\%)$ is 17—i.e., the cost drops by 17% per percentage point drop of thermal efficiency, whereas, when reducing the effectiveness of the intercooler, recuperator and economizer, these ratios become 16, 9 and 1, respectively.

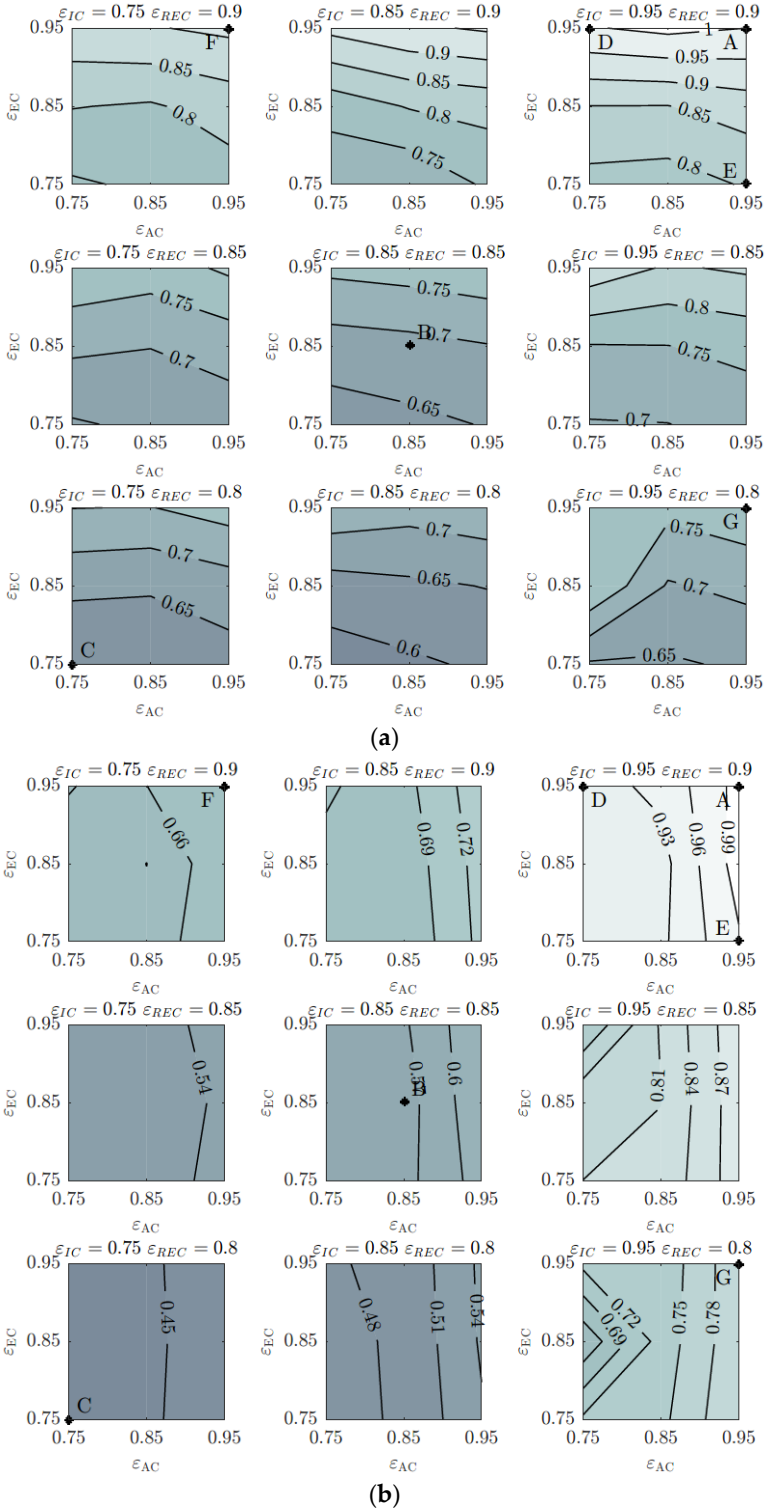

Figure 10. (**a**) heat exchanger total normalized weight and (**b**) total normalized acquisition cost index across the range of heat exchanger effectiveness for OPR = 40 & ΔT_{ps} = 5 K.

4. Conclusions

The parametric study of a humid air turbine system conducted in the current work has shown the high efficiency potential of this cycle across the design space, with a maximum thermal efficiency of 61.4%, achieved with maximum technology level of the heat exchangers and saturator, and maximum overall pressure ratio of at the gas generator. The absolute humidity at the inlet of the combustion chamber across the design space is within the limits for flame stability, never exceeding 0.25 kg_v/kg_a.

The final selection of the configuration of the power plant will depend on the levelized cost of the power production, which would require performing a full economic analysis. Depending on the market where the power plant is intended, an investment analysis should be conducted in order for the most appropriate candidate power system to be identified.

The parameter that was found to primarily drive the thermal efficiency is the intercooler and recuperator effectiveness. For a change in intercooler effectiveness from 0.95 to 0.75, the thermal efficiency falls by 2 pp, whereas, for the recuperator, a change from 0.9 to 0.8 causes a reduction in thermal efficiency of 2.28 pp. Cycle efficiency is not significantly affected by aftercooler and economizer effectiveness.

The parametric studies also showed that the technology level of each heat exchanger affects the thermal efficiency, total cost, and total weight of the power system differently: the recuperator was found to have the greatest impact on thermal efficiency, whereas the estimated acquisition cost is found to be mainly driven by the intercooler, while the total weight is mostly affected by the economizer and recuperator.

Overall pressure ratio was found to have great impact over the cycle metrics; when the OPR becomes 30 from 40, the total cost of the heat exchangers increases by 10%, total weight by 5% while thermal efficiency is penalized by 0.67 pp. On the other hand, an increase of the saturator's pinch temperature difference ΔT_{ps} to 15 K penalizes the thermal efficiency by 0.65 pp, while the full system's acquisition cost index was found to increase by 3%.

Overall, a typical design space of a complex humid air turbine power plant was systematically explored and the dependencies between key cycle parameters and component design including weight and acquisition cost were identified. The impact of heat exchanger effectiveness on cycle metrics was demonstrated, revealing their influence on thermal efficiency, cost and weight that was not previously known. The outcomes of this research constitute a step forward in understanding the performance of a complex power system across its design space and appreciating the potential of such systems for applications where high efficiency combined with low overall plant volume and weight are of importance.

Acknowledgments: This research program is financially supported by an Engineering and Physical Sciences Research Council (EPSRC) Industrial Cooperative Award in Science and Technology (I-CASE) Award and Rolls-Royce plc. (Bristol, UK) under the University Technology Centre in Aero System Design, Integration and Performance at Cranfield University (Cranfield, UK). The authors kindly thank Rolls-Royce plc. for permission to publish this work and for the technical support throughout the duration of the project.

Author Contributions: L.S.-d.-L. developed and implemented the heat exchanger and cycle design methodologies, G.D.B. developed the cycle thermal design and optimization platform, performed the simulations and analyzed the cycle performance data, P.L.O.-G. developed the heat exchanger detailed design and optimization framework, conducted the simulations and analyzed the design outcomes. P.K.Z. put together the manuscript.

Conflicts of Interest: The authors declare no conflict of interest.

Nomenclature

Symbols

C	kJ/K	Heat capacity
c	$	Cost
C^*	(-)	Heat capacity ratio
C_i	(-)	Weighting coefficient
d_t	m	Saturator packing bed diameter
F_i	(-)	Optimization fitness
h	kJ/kg	Specific enthalpy
h_t	m	Height of the packing bed of the saturator
H^+	MJ/kg	Enthalpy invariant
$k \times A$	kW/K	Overall heat transfer coefficient $\times$ Heat transfer area (Inverse of total resistance)
M^+	(-)	Flow invariant
p	MPa	Pressure
P	m	Perimeter
Q	MW	Heat transfer
SP	(-)	Selection parameter
T	K	Temperature
ΔT_{ps}	(-)	Saturator pinch temperature difference

Abbreviations

AC	Aftercooler
CC	Combustion chamber
CCGTs	Combined cycle gas turbines
EC	Economizer
EvGT	Evaporative gas turbine
GT	Gas turbine
HAT	Humid air turbine
IC	Intercooler
OPR	Overall pressure ratio
pp	Percentage point
REC	Recuperator
relPR	Relative pressure ratio
SAT	Saturator
TIT	Turbine inlet temperature

Subscripts

0	Pinch conditions
1	Bottom of the saturator
2	Top of the saturator
a	Dry air
dew	Dew
g	Gas
sat	Saturation
v	Vapor
w	Water

Appl. Sci. **2017**, *7*, 413 17 of 22

Greek Symbols

α	Weighting coefficient
β	Saturator bypass
ε	Effectiveness
ϕ	Relative humidity
ω	Absolute humidity

Appendix A. Humidifier Design

The methodology, discussed by Sanchez de Leon [27] and originally developed by Aramayo-Prudencio [28], defines the design point saturator performance using the inlet pressure and temperature of the two streams (water and dry air) at the inlet and the pinch temperature difference ΔT_{ps}. The pinch point temperature difference is defined as the minimum temperature difference between the operating line of the water and the saturated air enthalpy line across the saturator [28]. For this modelling process, the air–vapor mixture is treated as an ideal mixture of ideal gases, while the air at the outlet of the saturator is assumed to be fully saturated [9]. From the conservation of the dry air and water mass as well as conservation of energy two invariants of the system, (M^+, H^+) can be defined as:

$$\frac{m_w}{m_a} - \omega = M^+, \tag{A1}$$

$$h_a(T_g) + \omega\left[h_v(T_g) - h_w(T_w)\right] - M^+ h_w(T_w) = H^+. \tag{A2}$$

Under the assumption of ideal mixture of ideal gas, absolute humidity is defined as:

$$\omega = \frac{\Phi\, p_{sat}(T_g)}{p - \Phi\, \mathrm{p_{sat}}(T_g)}\,\frac{R_a}{R_v}. \tag{A3}$$

For the calculation of the saturated gas thermodynamic properties, the above-defined system of equations needs to be solved for three sections along the saturator as follows:

Station "0" corresponds to the pinch condition between the operating and saturated enthalpy lines of the saturator. The temperature difference between the two abovementioned lines is characteristic of the available technology level, which corresponds to the height of the saturation tower. The thermodynamic properties of the saturated gas (temperature T_0 and absolute humidity ω_0) in this section are the unknowns of the system. The relative humidity of the gas on the saturation line is $\Phi = 1$, and $T_{w,0}$ in the operating line is determined as $T_{w,0} = T_0 + \Delta T_{ps}$ once the pinch point temperature difference is defined; therefore, the invariant and absolute humidity equations can be rewritten as the following in agreement with [28] as follows:

$$\omega_0 - \frac{p_{sat}(T_0)}{p_1 - \Phi\, \mathrm{p_{sat}}(T_0)}\,\frac{R_a}{R_v} = 0, \tag{A4}$$

$$M^+ - \frac{cp_a}{cp_w} - \omega_0\left(\frac{cp_v - cp_w}{cp_w} + \frac{p_1}{p_1 - p_{sat}(T_0)}\,\frac{R_v}{cp_w}\left(\frac{h_{fg}(T_0)}{R_v\, T_0}\right)^2\right) = 0, \tag{A5}$$

$$H^+ - h_a(T_0) - \omega_0 h_{fg}(T_0) + \omega_0\left[h_w(T_0 + \Delta T_{ps}) - h_w(T_0)\right] + M^+ h_w(T_0 + \Delta T_{ps}) = 0. \tag{A6}$$

Station "1" corresponds to the bottom section of the saturator—i.e., air inlet/water outlet, for which the unknowns are the water temperature $T_{w,1}$ and the water mass flow $m_{w,1}$ whereas the gas properties are known. Therefore, the invariant equations can be written as follows:

$$M^+ + \omega_1 - \frac{m_{w,1}}{m_a} = 0, \tag{A7}$$

$$H^+ - h_a(T_{g,1}) - \omega_1 h_{fg}(T_{g,1}) + \omega_1\left[h_w(T_{w,1}) - h_w(T_{g,1})\right] + M^+ h_w(T_{w,1}) = 0. \tag{A8}$$

Station "2" corresponds to the top section of the saturator—i.e., water inlet/air outlet—for which the unknowns are the outlet gas conditions, namely temperature $T_{g,2}$ and absolute humidity ω_2, hence the gas mass flow. Air in this section is assumed to be saturated. The system of equations can be written as follows:

$$\omega_2 - \frac{p_{sat}(T_{g,2})}{p_1 - \Phi\, p_{\mathrm{sat}}(T_{g,2})} \frac{R_a}{R_v} = 0, \tag{A9}$$

$$M^+ + \omega_2 - \frac{m_{w,2}}{m_a} = 0, \tag{A10}$$

$$H^+ - h_a(T_{g,2}) - \omega_2 h_{fg}(T_{g,2}) + \omega_2\left[h_w(T_{w,2}) - h_w(T_{g,2})\right] + M^+ h_w(T_{w,2}) = 0. \tag{A11}$$

The equations of station "0" (Equations (A4)–(A6)) and station "2" (Equations (A9)–(A11)) form a system of six equations and six unknowns that resolve the pinch conditions (T_0, ω_0), the gas outlet conditions ($T_{g,2}$, ω_2), and the two invariants M^+ and H^+. Once the invariants are calculated, the equations of station "1" (Equations (A7) and (A8)) allow the solution for the water outlet conditions.

This model has been validated against experimental results of a HAT pilot cycle obtained by Lindquist et al. [17] and the maximum error in the outlet proprieties of the two streams is 1.5% as reported in Table A1.

Table A1. Validation of the saturator model against experimental data from Lindquist et al. [17].

Inlet/Input Conditions			Outlet Conditions				
Paremeter	**Units**	**Data**	**Parameter**	**Units**	**Model**	**Experimental Data**	**Discrepancy (%)**
$m_{g,1}$	(kg/s)	2.17	$m_{g,2}$	(kg/s)	2.5685	2.55	0.7
$T_{g,1}$	(K)	346.75	$T_{g,2}$	(K)	389.97	389.15	0.2
p_1	(bar)	7.88	ω_2	(-)	0.1837	-	-
$m_{w,2}$	(kg/s)	3.48	$m_{w,1}$	(kg/s)	3.0815	3.10	0.6
$T_{w,2}$	(K)	419.35	$T_{w,1}$	(K)	347.52	352.85	1.5
ΔT_{ps}	(K)	10.	-	-	-	-	-

Appendix B. Heat Exchanger Design

A counter-current plate-fin architecture was chosen for the intercooler and aftercooler design. For the airside, a serrated fin arrangement was selected based on its heat transfer and mechanical properties as discussed in [31]. On the waterside, stainless steel plain fins were employed to minimize pumping work, decrease the risk of fouling or passage blocking and avoid potential corrosion problems. The effectiveness-Number of Transfer Units (ε-NTU) method was followed to estimate the heat transfer area as described by Kays and London [32]. The number of transfer units was obtained by means of the correlations provided by the Engineering Society Data Unit (ESDU) in [33]. To obtain the main heat exchanger dimensions, the heat transfer coefficient of the airside was estimated using the expressions provided by Yang and Li [34]. For the waterside, the equations suggested in [35] were employed to evaluate the heat transfer coefficient for turbulent flow, and the equations in [36] were utilized for the laminar flow.

The recuperator is an air-air heat exchanger and, as such, a serrated-fin configuration was considered for both sides. In addition, the recuperator was arranged in a counter-current multi-pass cross-flow configuration. Due to the presence of the reheater, the maximum temperatures that the recuperator has to be able to stand can go up to 900 °C. Previous research by McDonald [37], Maziasz [38], and Min [39] has stated that Inconel 625 presents excellent creep resistance properties. Therefore, the passes with a temperature higher than 800 °C were assumed to be made of Inconel 625, whereas the rest of the heat exchanger material was assumed to be stainless steel. For the calculation of the heat transfer area, the ε-NTU method was followed [32]. The number of transfer units was obtained by means of the ESDU correlations [33] and the heat transfer coefficient was estimated with the equations purposed by Yang and Li [34].

Appl. Sci. **2017**, *7*, 413 19 of 22

In the economizer, up to 25% percent of the moisture in the air condenses during design point operation. Hence, to avoid issues associated with passage blocking due to the presence of contaminated air and water inside its passages, a mixture of finned-tube and plain-tube configuration was selected. The first part of the heat exchanger (dry part), where no condensation takes place, was designed using a finned-tube configuration. The later part (wet part), where the condensation begins to occur, was designed in plain-tube to ease the flow of the condensing moisture. The tubes are arranged in a counter-current multi-pass cross-flow configuration, with the air flowing over the tubes and the water through them in an effort to minimize passage blocking and fouling and ease maintenance procedures. The ε-NTU method [32] was followed to calculate the number of transfer units. Then, to calculate the heat transfer coefficient of the dry airside flow, the correlations given in the ESDU items [40] were utilized. However, in the wet part, the heat and mass transfer process was simulated following the model developed in [41]. The heat transfer coefficient of the water was evaluated as dictated in the ESDU items [35].

An index of the acquisition cost of the four heat exchangers specified above was estimated using heat transfer area based correlations. For the plate-fin geometries, the expressions proposed by Traverso and Massardo [42] were used. These correlations were originally derived for heat exchangers made of aluminum alloys; consequently, the material correction factors suggested by Towler and Sinnott [43] were applied to consider the different alloys employed. For the economizer, the correlation presented by Casarosa [44] was utilized for estimating its acquisition price. All cost estimates were updated to 2015 by means of the Chemical Engineering Plant Cost Index (CEPCI) [45].

For a prescribed thermodynamic "design vector" of the system, several different heat exchangers designs can be identified. A genetic algorithm based multi-objective optimization approach was applied to identify the individual that features the best compromise between cost and compactness [29]. The compactness was evaluated by means of the outlet perimeter, defined as the sum of the three main dimensions—i.e., height, length, and width. The result of each optimization was a Pareto front. In principle, any point within this Pareto front is an optimal candidate, and the balance between compactness and cost will depend on the considered application. To select the traded configuration from the Pareto front, a selection parameter SP (see Equation A12) of each configuration in the Pareto is calculated and finally the one with the lowest SP is selected. $F_i(x)$ represents the fitness of each individual in the Pareto—i.e., cost and perimeter, and α_i represents the weighting coefficients. These coefficients allow the designer to place more emphasis on any of the objectives when selecting the heat exchanger from the Pareto front. In the current case, their values were set to 0.5, in order to select the configuration that trades equally both objectives:

$$SP(x) = \sqrt{\sum_{i=0}^{i=n} \alpha_i \left(\frac{F_i(x)}{\max(F_i)} \right)^2}; \sum \alpha_i = 1. \quad \text{(A12)}$$

For the saturator design, a structured packing-bed tower was selected. For packing sizing, the models presented by Coulson and Richardson [46], and Aramayo-Prudencio and Young [47] were used. This method calculates the thermodynamic performance of the saturator tower using as input the geometrical data and the inlet conditions. Thus, it allows the derivation of the tower's key dimensions—i.e., the height and diameter of the packing—on a single iterative process, as the thermodynamic performance is defined by the cycle. The model was validated against experimental data presented by Lindquist et al. [17] and the results are presented in Table A2. The cost of the tower was calculated based on the shell weight and the packing volume. For the packing material a cost of 3800 USD/m^3 was assumed while a material cost of 8800 USD/ton was used for the vessel, both made in stainless steel based on [48]. To account for the costs of the droplet eliminators, water sprays, and the rest of subcomponents, an additional 14,000 USD was added on top of the baseline value of the saturator [48].

Table A2. Validation of tower packing height calculation against experimental data from Lindquist et al. [17].

Inlet/Input Conditions			Outlet Conditions				
Parameter	**Units**	**Data**	**Parameter**	**Units**	**Model**	**Experimental Data**	**Discrepancy (%)**
$m_{g,1}$	(kg/s)	2.17	$m_{g,2}$	(kg/s)	2.54	2.55	0.4
$T_{g,1}$	(K)	346.75	$T_{g,2}$	(K)	390.64	389.15	0.4
p_1	(bar)	7.88	ω_2	(-)	0.176	-	-
h_t	(m)	0.57	-	-	-	-	-
d_t	(m)	0.70	-	-	-	-	-
$m_{w,2}$	(kg/s)	3.48	$m_{w,1}$	(kg/s)	3.11	3.10	0.4
$T_{w,2}$	(K)	419.35	$T_{w,1}$	(K)	358.67	352.85	1.6

References

1. Jonsson, M.; Yan, J. Economic Assessment of Evaporative Gas Turbine Cycles With Optimized Part Flow Humidification Systems. In Proceedings of the ASME Turbo Expo, Atlanta, GA, USA, 16–19 June 2003.
2. Traverso, A.; Massardo, A.F. Thermoeconomic Analysis of Mixed Gas—Steam Cycles. *Appl. Therm. Eng.* **2002**, *22*, 1–21. [CrossRef]
3. Nakhamkin, M.; Swensen, E.; Wilson, J.M.; Gaul, G.; Polsky, M. The Cascaded Humidified Advanced Turbine (CHAT). *J. Eng. Gas Turbines Power* **1996**, *118*, 565–571. [CrossRef]
4. Rao, A.D. Process for Producing Power. U.S. Patent No. 4,829,763, 16 May 1989.
5. Chiesa, P.; Lozza, G.; Macchi, E.; Consonni, S. An Assessment of the Thermodynamic Performance of Mixed Gas-Steam Cycles Part B—Water-Injected and Hat Cycles. *J. Eng. Gas Turbines Power* **1995**, *117*, 499–508. [CrossRef]
6. Lazzaretto, A.; Segato, F. Thermodynamic Optimization of the HAT Cycle Plant Structure—Part I: Structure of the Heat Exchanger Network. *J. Eng. Gas Turbines Power* **2001**, *123*, 1–7. [CrossRef]
7. Lazzaretto, A.; Segato, F. Thermodynamic Optimization of the HAT Cycle Plant Structure—Part II: Structure of the Heat Exchanger Network. *J. Eng. Gas Turbines Power* **2001**, *123*, 8–16. [CrossRef]
8. Ågren, N.D.; Westermark, M.O.J. Design Study of Part-Flow Evaporative Gas Turbine Cycles: Performance and Equipment Sizing—Part I: Aeroderivative Core. *ASME J. Eng. Gas Turbines Power* **2003**, *125*, 201–215. [CrossRef]
9. Ågren, N.D.; Westermark, M.O.J. Design Study of Part-Flow Evaporative Gas Turbine Cycles: Performance and Equipment Sizing—Part II: Industrial Core. *ASME J. Eng. Gas Turbines Power* **2003**, *125*, 216–227. [CrossRef]
10. Thern, M. Theoretical and Experimental Evaluation of a Plate Heat Exchanger Aftercooler in an Evaporative Gas Turbine Cycle. In Proceedings of the ASME Turbo Expo, Atlanta, GA, USA, 16–19 June 2003.
11. Wang, B.; Zhang, S.; Xiao, Y. Steady State Off-Design Performance of Humid Air Turbine Cycle. In Proceedings of the ASME Turbo Expo, Montreal, QC, Canada, 14–17 May 2007.
12. Kim, T.S.; Song, C.H.; Ro, S.T.; Kauh, S.K. Influence of Ambient Condition on Thermodynamic Performance of the Humid Air Turbine Cycle. *Energy* **2000**, *25*, 313–324. [CrossRef]
13. Takahashi, T.; Nakao, Y.; Koda, E. Analysis and Evaluation about Advanced Humid Air Turbine System. *Chall. Power Eng. Environ.* **2007**, 341–344. [CrossRef]
14. Kavanagh, R.M.; Parks, G.T. A Systematic Comparison and Multi-Objective Optimization of Humid Power Cycles—Part I: Thermodynamics. *J. Eng. Gas Turbines Power* **2009**, *131*. [CrossRef]
15. Möller, B.F.; Obana, M.; Assadi, M.; Mitakakis, A. Optimisation of HAT-Cycles—With and without CO_2 Capture. In Proceedings of the ASME Turbo Expo, Viena, Austria, 14–17 June 2004.
16. Nyberg, B.; Thern, M. Thermodynamic studies of a HAT cycle and its components. *Appl. Energy* **2012**, *89*, 315–321. [CrossRef]
17. Lindquist, T.; Thern, M.; Torisson, T. Experimental and Theoretical Results of a Humidification Tower in an Evaporative Gas Turbine Cycle Pilot Plant. In Proceedings of the ASME Turbo Expo, Amsterdam, The Netherlands, 3–6 June 2002.

18. Araki, H.; Koganezawa, T.; Myouren, C.; Higuchi, S.; Takahashi, T.; Eta, T. Experimental and Analytical Study on the Operation Characteristics of the AHAT System. *ASME J. Eng. Gas Turbines Power* **2012**, *134*. [CrossRef]
19. Wei, C.; Zang, S. Experimental Investigation on the Off-Design Performance of a Small-Sized Humid Air Turbine Cycle. *Appl. Therm. Eng.* **2013**, *51*, 166–176. [CrossRef]
20. De Paepe, W.; Carrero, M.M.; Bram, S.; Parente, A.; Contino, F. Experimental Characterization of a T100 Micro Gas Turbine Converted to Full Humid Air Operation. *Energy Procedia* **2014**, *61*, 2083–2088. [CrossRef]
21. Yagi, M.; Araki, H.; Tagawa, H.; Koganezawa, T.; Myoren, C.; Takeda, T. Progress of the 40 MW-Class Advanced Humid Air Turbine Tests. *ASME J. Eng. Gas Turbines Power* **2013**, *135*. [CrossRef]
22. Li, Y.G.; Pilidis, P.; Newby, M.A. An Adaptation Approach for Gas Turbine Design-Point Performance Simulation. *J. Eng. Gas Turbines Power* **2006**, *128*, 789–795. [CrossRef]
23. Macmillan, W.L. *Development of a Module Type Computer Program for the Calculation of Gas Turbine off Design Performance*; Cranfield University: Cranfield, UK, 1974.
24. Goodger, E.M.; Ogaji, S.O.T. *Fuels and Combustion in Heat Engines*; Cranfield University Press: Cranfield, UK, 2011.
25. Young, J.B.; Wilcock, R.C. Modeling the Air-Cooled Gas Turbine: Part 2—Coolant Flows and Losses. *ASME J. Turbomach.* **2002**, *124*, 214–221. [CrossRef]
26. Horlock, J.H.; Watson, D.T.; Jones, T.V. Limitations on Gas Turbine Performance Imposed by Large Turbine Cooling Flows. *J. Eng. Gas Turbines Power* **2001**, *123*, 487. [CrossRef]
27. Sanchez, L. Advanced Gas-Turbine-Based Power Plants for Marine Commercial Applications. Ph.D. Thesis, Cranfield University, Cranfield, UK, 2014.
28. Aramayo-Prudencio, A.; Young, J.B. The Analysis and Design of Saturators for Power Generation Cycles: Part 1—Thermodynamics. In Proceedings of the ASME Turbo Expo, Atlanta, GA, USA, 16–19 June 2003.
29. Deb, K. *Multi-objective Optimization Using Evolutionary Algorithms*; John Wiley & Sons: New York, NY, USA, 2001.
30. Göke, S. Ultra Wet Combustion: An Experimental and Numerical Study. Ph.D. Thesis, Technische Universität, Berlin, Germany, 2012.
31. ESDU. Selection and Costing of Heat Exchangers. *ESDU Data Items*, 1 December 1994.
32. Kays, W.M.; London, A.L. *Compact Heat Exchangers*, 3rd ed.; Krieger Pub. Co.: New York, NY, USA, 1984.
33. ESDU. Design and Performance Evaluation of Heat Exchangers: The Effectiveness—NTU Method Part 3. *ESDU Data Items*, 1 July 1998.
34. Yang, Y.; Li, Y. General Prediction of the Thermal Hydraulic Performance for Plate-Fin Heat Exchanger with Offset Strip Fins. *Int. J. Heat Mass Transf.* **2014**, *78*, 860–870. [CrossRef]
35. ESDU. Heat Transfer Coefficients for Water or Steam in Plain Circular Tubes: Fully-Developed Turbulent Flow. *ESDU Data Items*, 1 November 1981.
36. ESDU. Forced convection heat transfer in straight tubes. Part 2: Laminar and transitional flow. *ESDU Data Items*, 1 November 2001.
37. McDonald, C.F. Recuperator Considerations for Future Higher Efficiency Microturbines. *Appl. Therm. Eng.* **2003**, *23*, 1463–1487. [CrossRef]
38. Maziasz, P.J.; Swindeman, R.W. Selecting and developing advanced alloys for creep-resistance for microturbine recuperator applications. *J. Eng. Gas Turbines Power* **2003**, *125*, 310–315. [CrossRef]
39. Min, J.K.; Jeong, J.H.; Ha, M.Y.; Kim, K.S. High temperature heat exchanger studies for applications to gas turbines. *Heat Mass Transf.* **2009**, *46*, 175–186. [CrossRef]
40. ESDU. High-Fin Staggered Tube Banks: Heat Transfer and Pressure Drop for Turbulent Single Phase Gas Flow. *ESDU Data Items*, 1 Jane 1988.
41. Gesellschaft, V. *VDI Heat Atlas*, 2nd ed.; Springer Science & Business Media: Berlin, Germany, 2010.
42. Traverso, A.; Massardo, A.F. Optimal Design of Compact Recuperators for Microturbine Application. *Appl. Therm. Eng.* **2005**, *25*, 2054–2071. [CrossRef]
43. Towler, G.P.; Sinnott, R.K. *Chemical Engineering Design: Principles, Practice and Economics of Plant and Process Design*, 2nd ed.; Butterworth-Heinemann: Oxford, UK, 2013.
44. Casarosa, C.; Donatini, F.; Franco, A. Thermoeconomic Optimization of Heat Recovery Steam Generators Operating Parameters for Combined Plants. *Energy* **2004**, *29*, 389–414. [CrossRef]
45. The Annual Cost Index of Chemical Engineering Plant. *Chem. Eng.* **2015**, *122*, 104.

46. Coulson, J.M.; Richardson, J.F.; Harker, J.H.; Backhurst, J.R. *Chemical Engineering: Particle Technology and Separation Process*, 5th ed.; Butterworth-Heinemann: Oxford, UK, 2002; Volume 2.
47. Aramayo-Prudencio, A.; Young, J.B. The Analysis and Design of Saturators for Power Generation Cycles: Part 2—Heat and Mass Transfer. In Proceedings of the ASME Turbo Expo, Atlanta, GA, USA, 16–19 June 2003.
48. Lindquist, T. Evaluation, Experience and Potential of Gas Turbine Based Cycles with Humidification. Ph.D. Thesis, Lund Institute of Technology, Lund, Sweden, 2002.

Applied Thermal Engineering 137 (2018) 545–554

Contents lists available at ScienceDirect

Applied Thermal Engineering

journal homepage: www.elsevier.com/locate/apthermeng

Research Paper

Techno-economic analysis of a reheated humid air turbine

Pau Lluis Orts-Gonzalez, Pavlos K. Zachos*, Giovanni D. Brighenti

Propulsion Engineering Centre, School of Aerospace, Transport and Manufacturing, Cranfield University, Cranfield MK43 0AL, Bedfordshire, United Kingdom

HIGHLIGHTS

- Economiser and recuperator dictate the economic metrics of a reheated humid air turbine system.
- Fuel and equipment purchase cost drive the average cost of the power produced by the system.
- Humid air turbine shows 14% higher thermal efficiency than a typical combined gas-steam plant.
- Humid air turbine show roughly 62% lower total purchasing cost than a combined gas-steam plant.

ARTICLE INFO

Keywords:
Humid air turbine
Evaporative gas turbine
Economic analysis
Power generation

ABSTRACT

The purpose of this paper is to identify the economic potential of a reheated humid air turbine system for power generation applications. A parametric analysis is performed to correlate the technology level of the system with the required cost of the electricity for economic viability. The effect of fluctuations of the main cost drivers is evaluated via an uncertainty analysis. The performance of the studied reheated humid air turbine is compared against previously studied humid configurations and well established gas-steam combined cycles. The fuel cost is found to be driving the cost of electricity. The uncertainty analysis also shows the dependency of the optimum cycle design parameters upon the market prices. The analysis reveals the capability of the reheated humid air turbine to be an economically viable option for the power generation sector featuring an estimated cost of electricity 2.2% lower than simpler humid cycles, and 28% lower than established combined cycles currently in service. The outcome of the work constitutes a step forward in the understanding of the economic performance of advanced complex cycles and proves the potential of such systems for applications where high efficiency and economic performance is jointly required.

1. Introduction

Over the past decades, thermal efficiency enhancements in gas turbine systems have been a key driver in the development of advanced power plant configurations. Advanced gas turbine configurations previously studied include steam injection, triple-pressure combined cycles, and humid air turbines [1–5]. Although combined gas-steam cycles are currently an established option in terms of thermal efficiency, several studies have postulated that humid air systems could also be attractive in the small to medium-size power generation market [5–10].

Humid Air Turbines (HAT) or Evaporative Gas Turbines (EvGT) were initially introduced by Rao in the late 80's [11]. Jonsson and Yan [9] performed a techno-economic comparison between HATs and combined cycles. This study proved the capability of the HATs to achieve a similar cost of electricity with a lower specific investment cost. Subsequent cost studies performed by Traverso and Massardo [12], and Kavanagh and Parks [10] showed that HATs are capable to achieve a lower cost of electricity that Combined Cycle Gas Turbines (CCGT), demonstrating the techno-economic potential of this advance cycle for the power generation market. The ability of the HAT systems to recuperate a notable part of the waste heat back into the cycle without the need of a bottoming cycle is the main driver of the observed competence against the CCGTs.

Pedemonte et al. [13,14] experimentally analysed the off-design performance of the air saturator. Wang et al. [15] and Kim et al. [7] studied the effect of the ambient conditions on the performance of the HAT. In both works, it was proved that as the ambient temperature increases the performance of the HAT is less penalised than the 'dry' gas turbines or the CCGTs. During warm days, the humid cycle is capable to evaporate a larger amount of water compensating the negative effect of a poorer compressor performance. In addition, Takashi et al. [16] concluded that humid air turbines show a better efficiency than CCGTs during part-load performance across a similar range of operation. In terms of emissions, Yagi et al. [17] reported that HAT NO_x emissions

* Corresponding author. Tel.: +44 (0) 1234 75 46 33.
E-mail addresses: p.ortsgonzalez@cranfield.ac.uk (P.L. Orts-Gonzalez), p.zachos@cranfield.ac.uk (P.K. Zachos).

https://doi.org/10.1016/j.applthermaleng.2018.03.094
Received 26 September 2017; Received in revised form 7 February 2018; Accepted 28 March 2018
Available online 30 March 2018

Nomenclature

Symbols

C_x	[J/K] Heat capacity
C^*	[-] heat capacity ratio
c_p	[J/kg K] specific heat capacity
COE	[$/kW h] cost of electricity
$\overline{COE}$	[$/kW h] average cost of electricity
H^+	[J/kg] enthalpy invariant
h	[J/kg] specific enthalpy
h_{fg}	[J/K] specific enthalpy of evaporation
M^+	[-] mass invariant
$\dot{m}$	[kg/s] mass flow
n	[years] years of life of the power plant
p	[Pa] pressure
p_{sat}	[Pa] saturation pressure
PEC	[$] purchase equipment cost
$\dot{Q}$	[W] heat rate
R_x	[J/kg K] specific gas constant
$SPEC$	[$/kW] specific purchase equipment cost
ΔT_{sp}	[K] saturator pinch point temperature difference
T	[K] temperature
t	[hours/year] hours of operation per year
T_{dew}	[K] wet bulb temperature
T_{sat}	[K] saturation temperature
$\dot{W}$	[W] plant power output

Abbreviations

AC	aftercooler
AE	annual expenses
CEPCI	chemical engineering plant cost index
DC	direct costs
EC	economiser
EvGT	evaporative gas turbine
FCI	fixed capital investment
HAT	humid air turbine
IC	intercooler
Int	interests
LNG	liquid natural gas
O&M	operation and maintenance
PFI	plant fixed investment
RC	recuperator
RHAT	reheated humid air turbine
SAT	saturator
TCI	Total Cost of Investment

Subscripts

a	dry air
$comb$	combustor
$comp$	compressor
fin	financing
g	humid air
gen	generator
HX	heat exchangers
i	operational year
in	inlet
ini	initial
max	maximum
min	minimum
out	outlet
v	vapour
w	water

Greek Symbols

η_{th}	thermal efficiency
ε	effectiveness
Ξ	[$] cost
ϕ	relative humidity
ω	water to air ratio

can be as low as roughly 10 ppm due to the high content of water within in the combustion chamber. Moreover, HAT systems are more compact power-units compared with 'dry' gas turbine packages and CCGT and present faster start-up times.

Although previous studies have focused on the performance capabilities of HAT systems, little effort has been invested to understand the full techno-economic potential of this cycle. Chiesa et al. [18] suggested that the addition of a reheater in the gas turbine would augment the thermal efficiency and specific work of the power plant. A reheated HAT system was previously studied by Brighenti et al. [19]. This work confirmed the potential of the reheated HAT configuration to achieve thermal efficiencies beyond the threshold of 60%. Nevertheless, no economic study of the reheated HAT system has been presented so far to identify the economic viability of such a system.

This paper presents a techno-economic analysis of a 40 MW class reheated humid air turbine power plant for power generation. A parametric design space exploration is performed to demonstrate the impact of the heat exchanger technology level on the economic metrics. An uncertainty analysis showing the impact of the main cost driver fluctuations on the cost of the electricity is also included. Finally, the economic performance of the investigated cycle is benchmarked against the performance achieved by high efficiency humid and combined cycle systems previously presented.

2. Methodology

2.1. Cycle configuration and modelling approach

The Reheated Humid Air Turbine (RHAT) analysed in this study, shown in Fig. 1, is based on the configuration previously presented by Brighenti et al. [19]. The cycle layout includes an aftercooler to augment the saturator performance as proposed by Thern et al. [20], an

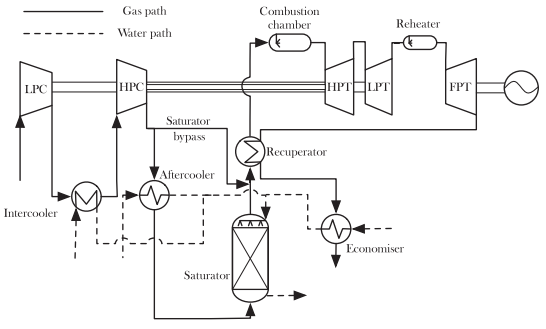

Fig. 1. Reheated humid air turbine system cycle layout.

intercooler to minimise the compression work, and an economiser to raise the temperature of the feeding water, as discussed by Nyberg and Thern [21]. A saturator bypass is included between the exit of the high pressure compressor and the inlet of the combustion chamber as suggested by Ågren and Westermark [22,23]. An open loop is used to feed water in the heat exchangers as previously discussed by Rosen [24].

The thermal performance of the system is simulated using a computational platform comprising modules that estimate the thermal behaviour of each component of the RHAT system. This platform has been previously described in detail by Brighenti et al. [19]. The performance of the gas turbine and the recuperator is calculated by Turbomatch© [25], a zero-dimensional, modular, component-based simulation framework developed at Cranfield University. The performance of the turbines and compressors are calculated using the polytropic expansion/compression relationships, the efficiency definitions, and the enthalpy balances. The performance of the combustor is estimated the enthalpy balance and the assumed efficiency of the burner. Details about the modelling approach for the main parts of the gas generator, i.e. compressors, turbines and burners, are shown by Walsh and Fletcher [26]. The performance calculation platform has been extensively validated in previous studies [27–30]. The performance of the saturator is calculated using the model based on mass and energy balance, in addition to mass and heat transfer equations, presented by Brighenti et al. [19]. This model has been also validated against experimental data provided by Lindquist et al. [31]. The key equations of the saturator performance calculation method adopted herein as well as the validation of the method is shown in Appendix A. The outlet conditions from all air-water heat exchangers and the recuperator unit are calculated using their imposed effectiveness and the energy balance equations as shown in Appendix B. The simulation platform also includes the calculation of the required turbine blade cooling flows, bled at the outlet of the high pressure compressor. The approach developed by Young and Wilcock in [32] has been employed for the estimation of the turbine cooling requirements.

The required parameters for the definition of the cycle are presented in Table 1, together with their assumed values. The bypass ratio, heat capacity ratio of the heat exchangers, and relative pressure ratio are optimised to maximise the thermal efficiency of the cycle, according to the model presented by Brighenti et al. [19]. The bypass ratio of the saturator is an optimised variable that varies across a range between 0 and 1, the relative pressure ratio from 0.25 to 0.75, and the air-water heat exchanger's heat capacity ratio from 0.3 to 0.95. The effectiveness of the heat exchangers is used as the technology level indicator of the cycle. The heat exchanger technology level scenarios analysed are shown in Table 2 and include a low, an average, and a high technology level case in terms of heat exchanger effectiveness. The optimised cycle parameters for each heat exchanger technology scenario are shown in Table 3.

Table 1
Cycle performance modelling assumptions.

Power output	40 MW
Turbine inlet temperature for both combustion chambers	1600 K
Overall pressure ratio	40
Compressor polytropic efficiency	0.90
Core turbine polytropic efficiency	0.90
Power turbine polytropic efficiency	0.92
Combustion chamber efficiency	0.99
Combustion chamber pressure loss	5%
Saturator pinch point	5 K
Saturator pressure loss	5%
Water-air heat exchangers air-side pressure loss	7.5%
Cold-side recuperator pressure loss	7.5%
Hot-side recuperator pressure loss	5%
Maximum allowed blade metal temperature	1300 K
Film cooling effectiveness	0.40
Internal flow cooling efficiency	0.70

Table 2
Heat exchanger effectiveness envelopes analysed.

Parameter	Technology level		
	Low	Average	High
Intercooler, Aftercooler, Economiser effectiveness	0.75	0.85	0.95
Recuperator effectiveness	0.8	0.85	0.90

Table 3
Optimised parameters for the studied cycle configurations.

Parameter		Technology level		
		Low	Average	High
Saturator bypass ratio	$\dot{m}_{g,AC}/\dot{m}_{g,HPC}$	0.46	0.41	0.53
Relative low pressure ratio	$\frac{\log PR_{LPC}}{\log OPR}$	0.57	0.53	0.53
Intercooler's heat capacity ratio	C_g/C_w	0.95	0.95	0.95
Aftercooler's heat capacity ratio	C_g/C_w	0.95	0.95	0.95
Economiser's heat capacity ratio	C_g/C_w	0.88	0.88	0.82

2.2. Cost analysis method

The economic analysis of the system relies on the Purchase Equipment Cost (PEC) as an economic metric to define the acquisition price. This comprises the cost of the gas generator including the power turbine ($\Xi_{bare\ GT}$), the packaging ($\Xi_{packaging}$), the electric generator (Ξ_{gen}), the saturator tower (Ξ_{SAT}), and the heat exchangers ($\sum \Xi_{HX}$), as shown in Eq. (1). The total price of the bare gas turbine includes the compressors, the turbines, the combustion chambers, and the ancillaries, as shown in Eq. (2). The acquisition cost of the turbomachinery and the electric generator are estimated using the correlations presented by Traverso et al. [33]. The cost of the compressors (Ξ_{comp}) and turbines (Ξ_{turb}) is based on the inlet mass flow, pressure ratio, inlet temperature and the assumed polytropic efficiency. The cost of the combustion (Ξ_{comb}) chamber is based on the outlet temperature, the temperature raise, and the relative pressure losses. The cost of the generator (Ξ_{gen}) is correlated with the power generated. The cost of the ancillaries ($\Xi_{ancillaries}$) is assumed to be 40% of the turbomachinery cost, and the cost of the packaging is estimated as 40% the cost of the previous two, as suggested by Kavanagh [10].

$$PEC = \Xi_{bare\ GT} + \Xi_{packaging} + \Xi_{gen} + \Xi_{SAT} + \sum \Xi_{HX} \quad (1)$$

$$\Xi_{bare\ GT} = \sum \Xi_{comp} + \sum \Xi_{turb} + \sum \Xi_{comb} + \Xi_{ancillaries} \quad (2)$$

The acquisition cost of the saturator is estimated based on the weight of the shell (8800 USD/ton) and the packing volume (3800 $/m^3), assuming that both are made in stainless steel as recommended by Lindquist in [34]. To account for the cost of the droplet eliminator, water sprays, and the rest of the subcomponents an additional $14,000 is added on top of the baseline cost [34]. The main dimensions of the saturator are calculated using the model presented by Brighenti et al. [19] (also in Appendix A of this paper) for a structured packing-bed configuration.

The intercooler, the aftercooler, and the recuperator are plate-fin counter-current cross-flow units, whereas the economiser is designed as a finned-tube counter-current cross-flow unit to avoid passage blocking as a consequence of water condensation, according to the configuration presented by Brighenti et al. [19]. The acquisition cost of the heat exchanger is estimated based on the heat transfer area using the correlations presented by the ESDU [35] for the plate-fin units, and by Casarosa [36] for the finned-tube units. The total heat transfer area of the heat exchangers is calculated using the effectiveness-Number of Transfer Units method developed by Kays and London [37]. Unit costs

Table 4
Economic assumptions for the calculation of the total cost of investment [40].

Total cost of investment	Fixed capital investment	Direct costs	Installation	20% of PEC
			Piping	10% of PEC
			Instruments and control systems	6% of PEC
			Electric equipment and materials	10% of PEC
			Land	5% of PEC
			Civil, structural, and architectural work	15% of PEC
			Service facilities	30% of PEC
		Indirect costs	Engineering and supervision	25% of PEC
			Construction	15% of DC
			Contingency	8% of all the above
	Other outlays		Startup	8% of FCI
			Working capital	15% of FCI
			Licensing, and research and development	7% of FCI

known from previous years are updated to 2015 prices using the Chemical Engineering Plant Cost Index (CEPCI) as described in [38]. The detailed heat exchanger geometry is specified using the methodology previously presented by Brighenti et al. [19].

In the absence of any detailed data about the infrastructure required, the Total Cost of Investment (TCI) is estimated based on the Purchasing Equipment Cost (PEC), the Direct Costs (DC), and the Fixed Capital Investment (FCI), as suggested by Bejan et al. [39]. The assumed values of these costs are based on the work published by Barberis et al. [40] and are represented in Table 4.

For a lifecycle economic analysis, the annual expenses during the plant economic life are required. These are estimated using the model proposed by Bejan et al. [39] which accounts for the payment of the Total Cost of Investment (TCI), the interest generated by the required loan (cost of financing), the taxes, the cost of fuel, and the Operation and Maintenance (O&M) costs to estimate the annual expenses (C_{AE_i}) as shown in Eq. (3). The TCI accounts for the plant's sub-system's costs including installation costs, the land acquistion costs, the construction of the access roads, etc. The loan's interests are derived from the credit required to pay off the TCI. In this study the loan is divided in three parts, a part paid with a common equity, other with debt, and the other with preferred stock. The fuel costs include the purchase of fuel required to operate the power plant, which is based on the power and efficiency of the plant. Finally, the O&M costs include the mantime required for normal operation of the power plant as well as the maintenance costs over the lifetime of the system including the costs for replacement parts. In this study, the O&M costs include a fixed part proportional to the PEC and a part proportional to the fuel used. Full details about the cost model can be seen in [39].

The assumed values to enable the cost study are presented in Table 5. The analysis is conducted in current dollars accounting for inflation and the assumptions made to support it rely on the economy of a developed country. A similar study using economic figures of an emerged economy might be able to identify the potential of such an advanced cycle system as part of the energy market in a developing country where high efficiency plants are also of critical importance.

Table 5
Assumptions for economic analysis.

Assumed starting year of the project	January 2015
Time until commissioning starts	1 year
Assumed plant commissioning time	2 years
Plant economic life	20 years
Plant life for tax purposes	10 years
Income tax rate	30%
Other taxes and insurances	2% of PFI
Real inflation	2.5%
Real inflation for the fuel	3.0%
Fraction funded by common equity	35%
Fraction funded by preferred stock	15%
Fraction funded by debt	50%
Interest rate of the common equity	6.5%
Interest rate of the preferred stock	6.0%
Interest rate of the debt	5.5%
Fuel price (LNG)	0.25 $/kg
O&M variable	2% of FCI
O&M fixed	0.83 $/kg of fuel
Availability	85%

The Cost of Electricity (COE) is calculated using Eq. (4). The COE_i represents the total cost of generating a kilowatt hour at year i and reflects the minimum sale price to recover the annual expenses. The COE varies during the book life of the power plant following the annual cost variation. As such, the average cost of electricity, $\overline{COE}$, for the book life is used as an economic index and is calculated as shown in Eq. (5). Average cost of electricity represents the total average cost of generating one kilowatt hour accounting for the annual expenses along the whole book life.

$$\Xi_{AE_i} = \Xi_{ini_i} + \Xi_{fin_i} + \Xi_{tax_i} + \Xi_{fuel_i} + \Xi_{O\&M_i} \tag{3}$$

$$COE_i = \frac{\Xi_{AE_i}}{t\dot{W}} \tag{4}$$

$$\overline{COE} = \frac{\sum_{i=1}^{n} C_{AE_i}}{nt\dot{W}} \tag{5}$$

3. Results and discussion

3.1. Effect of heat exchanger technology

The effect of the heat exchanger effectiveness on the thermal efficiency and the economic metrics of the power plant is presented in Fig. 2 for the three scenarios shown in Table 2. In this study the Specific Purchase Equipment Cost ($SPEC$) and the average cost of electricity ($\overline{COE}$) of the average technology scenario (heat exchanger effectiveness at 0.85 for all units, $SPEC$ = 334.06 $/kW, $\overline{COE}$ = 6.81 c$/kW h) have been used as reference to calculate relative changes. Fig. 2 shows that a

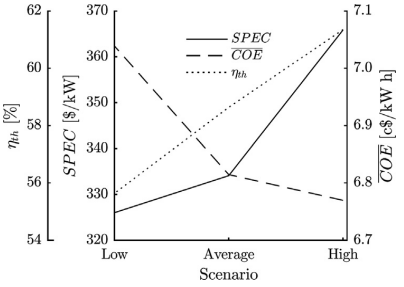

Fig. 2. Impact of the technology level of the heat exchangers on the $\overline{COE}$, $SPEC$, and η_{ih}.

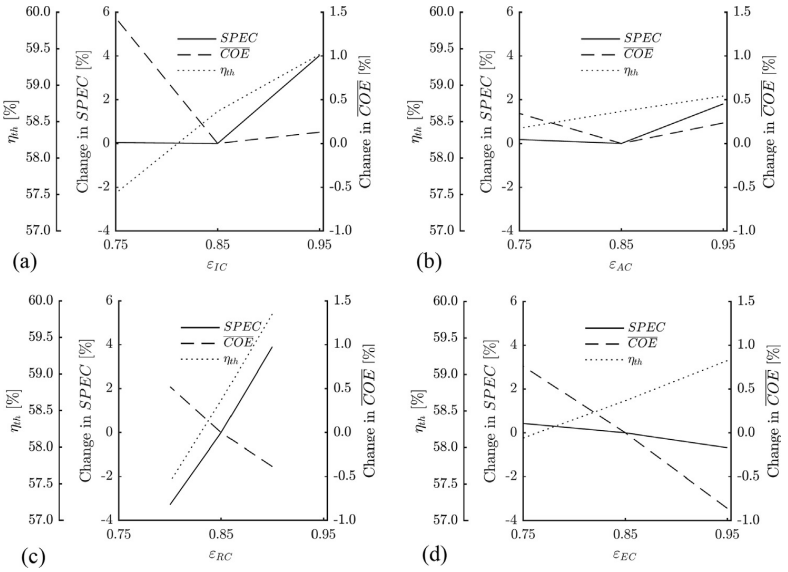

Fig. 3. (a) Effect of the intercooler, (b) effect of the aftercooler, (c) effect of the recuperator, (d) effect of the economiser effectiveness on η_{th} on $SPEC$ and on $\overline{COE}$.

reduction in the heat exchanger effectiveness from the average to the low technology level is associated with a 2.3% reduction in the Specific Purchasing Equipment Cost ($SPEC$), which when combined with the 3 percentage points (pp) loss in thermal efficiency yields to a 3% increase of the $\overline{COE}$. Improving the heat exchanger technology from the average to the high level scenario (see Table 2) yields to a more aggressive change in $SPEC$, which increases by 9.5% in this case. This increase combined with the improvement in thermal efficiency yields to a 1% reduction of the $\overline{COE}$ relative to its baseline value.

The impact of the effectiveness of each heat exchanger on the thermal efficiency, $SPEC$, and $\overline{COE}$ is shown in Fig. 3. The effectiveness of each heat exchanger varies across its specified design range, in order to identify its relative contribution to the overall economic metrics of the system, while the rest of the design variables are kept constant.

Fig. 3a shows that the reduction of the intercooler effectiveness from 0.85 to 0.75 causes an increase in the average cost of electricity by 1.46%. Although this reduction doesn't affect the purchasing costs of the unit, a notable penalty on its thermal efficiency is imposed, which drops by approximately 1 pp from 58.6%. Poor air humidification and the higher required compression work promoted by the less effective intercooling reduces the specific power of the plant causing an increase in size. Therefore, the lower acquisition cost of the less effective intercooler is compensated by the higher price of the rest of the units which keeps the $SPEC$ fairly constant. An intercooler effectiveness of 0.95 drives the system to more efficient but also to higher $SPEC$ configurations, which effectively cancel each other out leaving the average cost of electricity almost unaffected. The aftercooler shows broadly a similar behaviour as the intercooler (see Fig. 3b). However, the changes in $SPEC$ and thermal efficiency triggered by the increase in effectiveness are found to have a secondary effect on the predicted $\overline{COE}$. A 5 pp reduction in recuperator effectiveness (0.8 from 0.85, Fig. 3c) entails a 0.5% increase in the predicted $\overline{COE}$ due to the associated penalties in thermal efficiency (-1.34 pp) which are not compensated by the almost 4% reduction in $SPEC$. The driver behind the thermal efficiency deterioration is the reduced capacity of the system to exploit the waste heat. For a 5 pp increase in recuperator effectiveness (0.9 from 0.85), the thermal efficiency gain ($+1.18$ pp) out-competes the 4% increase in $SPEC$ yielding to 0.5% reduction in the $\overline{COE}$. Finally, the economiser is found to also drive the cost of electricity across a ± 1% zone for effectiveness values of 0.75 and 0.95 respectively. This change is primarily dominated by the increase in thermal efficiency of the system produced by a more effective unit.

Table 6
Heat exchanger effectiveness for minimum average cost of electricity ($\overline{COE}$).

ε_{IC}	[–]	0.85
ε_{AC}	[–]	0.85
ε_{RC}	[–]	0.90
ε_{EC}	[–]	0.95
η_{th}	[%]	60.33
$SPEC$	[$/kW]	345.33
$\overline{COE}$	[c$/kW h]	6.74

In conclusion, the analysis shows that the recuperator and the economiser primarily drive the cost metrics of the power plant, while the intercooler has a big impact on cost only for low effectiveness values. The parametric analysis enables the identification of the most cost-efficient system configuration. This features an intercooler and aftercooler effectiveness of 0.85, economiser effectiveness 0.95, and recuperator effectiveness 0.90 (see Table 6). The identified values of heat exchanger effectiveness that produce the cost optimum configuration balance the capacity of the cycle to recuperate heat directly against its capacity to exploit un-recuperated waste heat to raise humidity.

3.2. Uncertainty analysis

The total annual cost of the power plant operation depends on four key parameters: (i) fuel costs, (ii) purchase equipment costs (PEC), (iii)

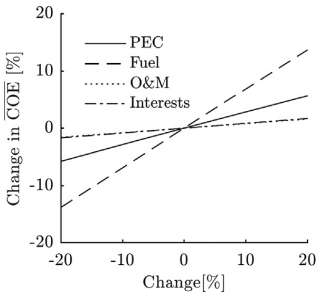

Fig. 4. $\overline{COE}$ sensitivities in cost drivers for the most cost efficient configuration.

interest rates over the loan period to pay off the initial investment, and (iv) operation and maintenance (O&M) costs. The nature of these cost elements is associated with an implicit uncertainty. Fuel prices may undergo severe fluctuations over time following global financial trends. Purchase cost estimates rely on correlations derived statistically from public domain data with an implicit standard deviation. The assumed interest rates may change significantly depending on the risk of the economic project, which is declared by the investor and heavily influenced by the current financial conditions. Finally, the O&M costs can vary across a wide range depending on the technology level of the equipment installed, the location of the power plant, operation mode, ambient conditions as well as other unforeseen circumstances which need to be accounted for as contingency. According to the above considerations, an imposed variation, across a range between −20% to +20%, is applied to each of the four parameters over the lifetime of the plant aiming to to assess the sensitivity of the average cost of electricity on these cost drivers. The selected uncertainty range is based on the expected error ranges derived from the calculation methods shown by Traverso et al. [33] and Bejan et al. [39] which justify that such a range is representative for the type of cost studies presented herein. The cycle configuration shown in Table 6 is used as reference to show the variations of the $\overline{COE}$. The reference values of interest rates, baseline fuel cost, and the O&M costs are the presented in Table 5, whereas the baseline purchase equipment cost (PEC) of $13,813,200 is derived from the *SPEC* provided in Table 6.

Fig. 4 shows the impact of the four parameters analysed on the $\overline{COE}$. The fuel cost is found to have the strongest influence in the $\overline{COE}$, showing a change of 0.75% per percentage point fuel cost variation. The PEC uncertainty causes small changes in the $\overline{COE}$, of the order of 0.25%, for each PEC percentage point variation. Variations in the O&M costs or the interest rates of the debts have minor effect, producing changes of only 0.05% per percentage point change (note that O&M and Interests lines are collapsing on top of each other in Fig. 4). Therefore, both lines appear overlapped in Fig. 4. The analysis reveals a linear correlation between any of the four cost drivers and the $\overline{COE}$. Therefore, such a study enables the impact of larger fluctuations of any of the four cost drivers by extrapolation using the data presented herein as reference.

The tile-plot shown in Fig. 5 identifies the exchange rates between all cost drivers across the design space. On each plot, the x-axis represents the percentage variation of the interest rates, and the y-axis the percentage variation of the O&M costs from the reference values shown in Table 5. Fuel cost variation from nominal values is shown in the major x-axis while uncertainty in PEC is shown in the major y-axis. The contour lines represent the percentage $\overline{COE}$ departure from the reference value (Table 6). Point A in Fig. 5 represents a pessimistic scenario whereby the variation of the four parameters is +20% with regards to their reference values. In that case, the $\overline{COE}$ is estimated to be around 23% higher with respect to the baseline case (point REF in Fig. 5). An optimistic scenario is represented by point B (bottom left corner in Fig. 5), where the variation for the four parameters is −20% in relation to their baseline values. This scenario shows a $\overline{COE}$ reduced by 22% compared to the baseline case (point Ref. in Fig. 5). In addition, as the PEC uncertainty decreases, the rate of change of the $\overline{COE}$ produced by the in interest rates and the O&M cost variations diminishes as these two parameters show strong dependence on purchasing costs. Finally, from Fig. 5 it becomes clear that increased relative fuel costs dictate a cost optimum system configuration with high technology level inter-cooler and recuperator (light grey regime $\varepsilon_{IC} = 0.95$, $\varepsilon_{RC} = 0.90$), which better exploits the waste heat within the power cycle. When the anticipated relative fuel costs drop, a low technology level system seems to also be viable ($\varepsilon_{IC} = 0.85$, $\varepsilon_{RC} = 0.85$, dark grey regime in Fig. 5), which combines low operating costs with low purchasing costs due to the relatively more compact size of these heat exchangers.

3.3. Comparison against other advanced cycles

In Table 7 the RHAT configuration shown in Table 6 is compared against the cost metrics of humid cycles previously reported by Kavanagh and Parks [10], and Traverso and Massardo [12]. A CCGT cycle [10] is also included for reference. The cost metrics of the current RHAT system are re-estimated under the assumptions of previous studies (Kavanagh et al. [10], Traverso and Massardo [12]) to enable comparison.

Table 7 shows that the RHAT system features 62% lower predicted cost of investment than an equivalent CCGT. As a result, the average cost of electricity ($\overline{COE}$) is reduced by 28%, also due to the RHAT's 14% higher thermal efficiency. Comparing against previous humid cycles, it is observed that the RHAT cycle features a 15% and roughly 8.5% lower *SPEC* than STIG and simpler HAT cycles respectively (Kavanagh and Parks [10]). The lower *SPEC* is a consequence of the higher specific power achieved by the RHAT (130% compared with the STIG and 38% compared with the HAT), as it reaches higher humidification ratios. As such, despite the additional combustion chamber and the requirement for advanced materials, the reduction in size of all the components, as a consequence of the higher specific power, enables a cost reduction that out-competes the above mentioned drawbacks. Nevertheless this reduction is not sufficiently large to achieve a lower *SPEC* than the TOP Humid Air Turbine [10], which does not require an intercooler, an aftercooler, or a humidifier. From Table 7 is also observed that the RHAT cycle out-competes the rest of the cycles in terms of thermal efficiency due to its increased capability to exploit waste heat and introduce humidity into the cycle. Finally, the enhanced thermal efficiency and the low purchasing costs of the RHAT system yield to a notably lower estimated average cost of electricity against the competitor systems with the $\overline{COE}$ reductions ranging from −28% against the CCGT plant [10] to roughly −2% against the humid air water injected system shown in [12].

4. Conclusions

In this paper, a techno-economic analysis of a reheated humid air turbine system is presented. Lifecycle cost analysis showed that the average cost of electricity is primarily driven by the effectiveness of the recuperator and economiser. These heat exchanger units represent the key components that manage the waste heat recuperation and humidity levels while they also dictate the size, hence the acquisition cost, of the power plant. Increasing the technology level of the recuperator and the

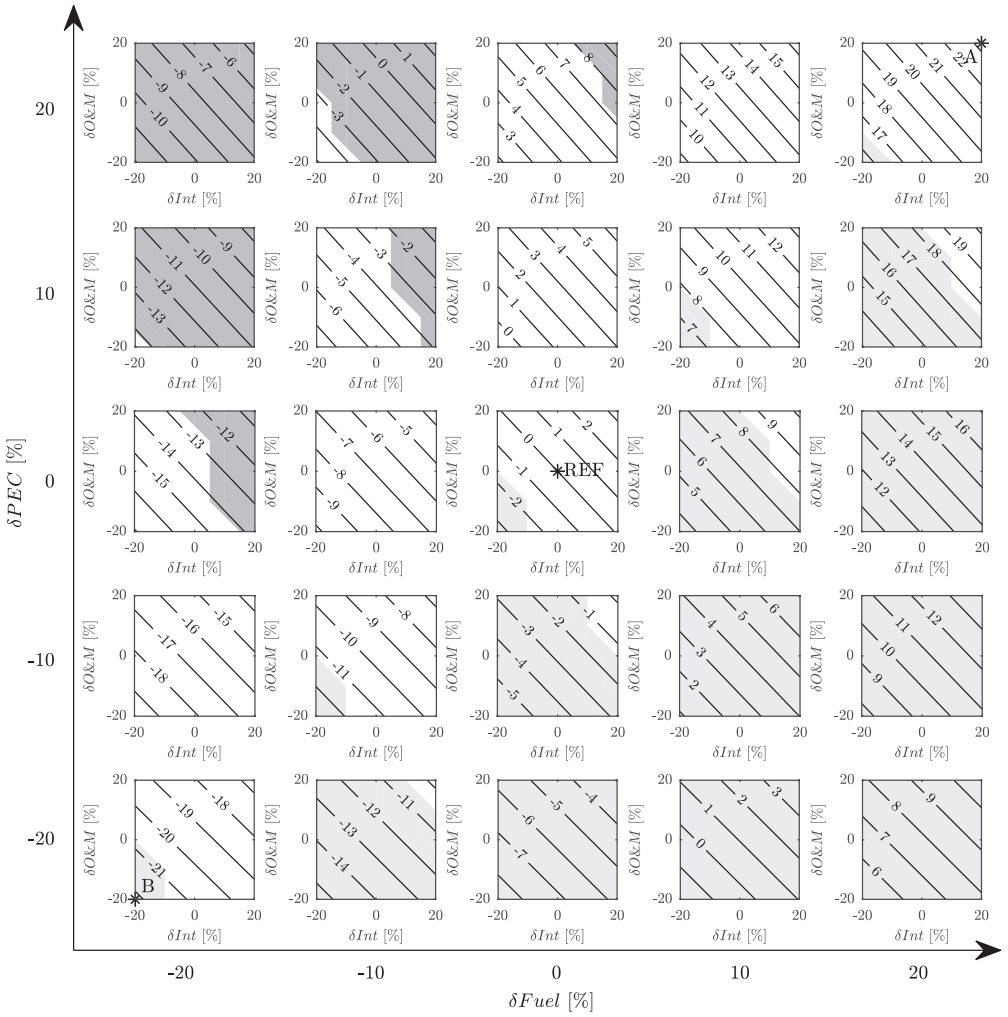

Fig. 5. Percentage mean cost of electricity variation from reference cycle. Cost optimum configuration in dark grey region $\varepsilon_{IC} = 0.85$, $\varepsilon_{AC} = 0.85$, $\varepsilon_{RC} = 0.85$, $\varepsilon_{EC} = 0.95$. Cost optimum configuration in blank region $\varepsilon_{IC} = 0.85$, $\varepsilon_{AC} = 0.85$, $\varepsilon_{RC} = 0.90$, $\varepsilon_{EC} = 0.95$. Cost optimum configuration in light grey region $\varepsilon_{IC} = 0.95$, $\varepsilon_{AC} = 0.85$, $\varepsilon_{RC} = 0.90$, $\varepsilon_{EC} = 0.95$.

Table 7
Comparison of reference reheated humid air turbine (Table 6) performance against previously reported advanced cycles.

Cycle	η_{th} [%]		*SPEC* [$/kW]		$\overline{COE}$ [c$/kW h]	
		RHAT		RHAT		RHAT
Steam injected cycle [10]	49.36	+22.2%	323	−14.9%	6.85	−26.4%
Gas-steam combined cycle [10]	53.00	+13.8%	720	−61.8%	7.00	−28.0%
Humid Air Turbine [10]	52.26	+15.4%	300	−8.3%	6.48	−22.2%
TOP Humid Air Turbine [10]	54.12	+11.5%	187	+47.0%	6.00	−16.0%
Humid Air Turbine [12]	51.74	+16.6%	n/a	n/a	4.21	−5.5%
Humid Air Water Injected Turbine [12]	50.04	+20.6%	n/a	n/a	4.07	−2.2%

economiser by 5 and 10 percentage units respectively yields to a reduction in the cost of the electricity of about 0.5% and 1% respectively.

The uncertainty study showed that possible variations in fuel costs and the uncertainty of the purchased equipment cost are the main parameters driving the fluctuations of the average cost of the electricity. The cost of electricity increases by 0.75% per percentage point of fuel price increase, and by 0.25% per percentage point rise in purchase equipment cost. Comparisons against previously reported studies

on combined and humid cycles show that the reheated humid air turbine features 61.8% lower purchasing costs than a typical CCGT. Moreover, due to its high efficiency (approximately 14% higher than a typical combined cycle), estimated average costs of electricity are approximately 30% lower than these of CCGT system.

Overall a detailed economic analysis of a reheated humid air turbine power plant intended for power generation has been performed in order to explore the potential of this configuration for power generation applications. The impact of the heat exchanger technology on the economic metrics was demonstrated, revealing their influence on the acquisition cost and in the $\overline{COE}$, which was not previously known. The outcome of the work constitutes a step forward in the understanding of the economic performance of advanced complex cycles and proves the potential of such systems for applications where high efficiency and economic performance is jointly required.

Acknowledgements

This research program is financially supported by an EPSRC Industrial CASE Award and Rolls-Royce plc. under the University Technology Centre in Aero System Design, Integration and Performance at Cranfield University. The authors kindly thank Rolls-Royce plc. for permission to publish this work. Due to confidentiality agreements with research collaborators, supporting data can only be made available upon reasonable request and with permission of the industrial collaborator. For data requests please contact the corresponding author.

Appendix A. Saturator tower performance calculation

The model for simulating the design performance of the saturator tower, previously presented by Brighenti et al. [19], relies on the inlet pressure, temperature, and mass flow of the two streams (dry air and water) and the pinch point temperature difference (ΔT_{ps}). The pinch point temperature difference is defined as the minimum temperature difference between the operating line of the water and the saturated air enthalpy line across the saturator [41]. For this modelling process, the air–vapour mixture is treated as an ideal mixture of ideal gases, while the air at the outlet of the saturator is assumed to be fully saturated [22]. From the conservation of the dry air and water mass as well as conservation of energy two invariants of the system (M^+, H^+) can be defined as:

$$\frac{\dot{m}_w}{\dot{m}_a} - \omega = M^+ \tag{6}$$

$$h_a@(T_g) + \omega[h_v@(T_g) - h_w@(T_w)] - M^+ h_w(T_w) = H^+ \tag{7}$$

Under the assumption of an ideal mixture of ideal gas, absolute humidity is defined as:

$$\omega = \frac{\phi\, p_{sat}@(T_g)}{p - \phi\, p_{sat}@(T_g)} \frac{R_a}{R_v}. \tag{8}$$

$\dot{m}$ represents the mass flows of the two streams, M^+ the mass invariant, $h_x@(T)$ the specific enthalpy evaluated at temperature T, p the pressure, ω the water to air ratio (defined as the amount of vapour in the air divided by the dry air $\dot{m}_v/\dot{m}_a$), H^+ the enthalpy invariant. $p_{sat}@(T_g)$ indicates the saturation pressure evaluated at the temperature of the gas. ϕ represents the relative humidity, R_x is the specific gas constant of each fluid, and the subscripts a, g, w, and v stand for dry air, humid air, water, and vapour respectively.

For the calculation of the saturated gas thermodynamic properties, the above-defined system of equations is solved at three sections along the saturator gas path. “Station 0” corresponds to the pinch point condition between the operating line and the saturated enthalpy line of the air. The temperature difference between the two above-mentioned lines is defined by ΔT_{ps}. Therefore, it is possible to approximate the water temperature as $T_w = \Delta T_{ps} + T_g$. “Station 1” corresponds to the bottom section of the tower, where the air inlet conditions are known. Last, “Station 2” corresponds to the top section of the saturator, where the water inlet conditions are known and the outlet air is assumed to be saturated. The equations Eq. (6)–(8) are evaluated and solved at “Station 0” and “Station 2”, which enables the calculation of the two invariants (M^+, H^+) and the conditions of the outlet gas. Once the invariants are known, the system of equations is evaluated at “Station 1”, which corresponds to the bottom section of the saturator, to calculate the conditions of the outlet water. Finally, the air outlet pressure is calculated assuming a 5% pressure loss of the inlet total pressure.

The saturator performance model was previously validated against experimental data obtained by Lindquist et al. [31] using the Lund HAT cycle demonstrator, as shown in Table 8.

Table 8
Validation of the saturator model against experimental data from Lindquist et al. [31].

Inlet/Input conditions			Outlet conditions				
Paremeter	Units	Data	Parameter	Units	Model	Experimental data	Discrepancy (%)
$m_{g,in}$	(kg/s)	2.17	$m_{g,out}$	(kg/s)	2.5685	2.55	0.7
$T_{g,in}$	(K)	346.75	$T_{g,out}$	(K)	389.97	389.15	0.2
p	(bar)	7.88	ω_{out}	(–)	0.1837	–	–
$m_{w,in}$	(kg/s)	3.48	$m_{w,out}$	(kg/s)	3.0815	3.10	0.6
$T_{w,in}$	(K)	419.35	$T_{w,out}$	(K)	347.52	352.85	1.5
ΔT_{ps}	(K)	10	–	–	–	–	–

The sizing model of the tower enables the estimation of the height and diameter of the saturator’s packing. The diameter is calculated following the correlation presented by Coulson and Richardson [42]. The pressure losses are set to 300 Pa/m and the maximum velocity is 60% of the flooding velocity to ensure stable operation and avoid water over-flood. The packing height is estimated based on a variation of the method previously proposed by Aramayo-Prudencio and Young [43]. This model enables the estimation of the saturator’s height from a given performance. The required inputs are: the characteristic dimensions of the packing-bed, the previously calculated diameter, an initial guess for the height, and the inlet conditions of both streams as inputs. The model iteratively calculates the humidifier’s performance based on the data provided and the initial guessed height, and compares the results with the humidifier thermodynamic data obtained from the cycle design. The packing height is determined

once the above-mentioned iteration reaches convergence.

Appendix B. Heat exchanger thermodynamic model

The outlet conditions from all air-water heat exchangers are calculated using the optimised heat capacity ratio (C^*), defined in Eq. (9), and the imposed effectiveness (ε), defined Eq. (10), where $\dot{Q}$ represents the heat rate. Gas mass flows are defined as part of the cycle analysis, whereas the heat exchanger water mass flows are calculated using the heat capacity ratio of the air and water streams, C^*, under the assumption that the water always presents the higher heat capacity ($C_w = C_{\max}$). As water condensation in the air stream is possible ($T_{g,out} < T_{g,dew}$), the latent heat of condensation of the water in the humid air causes variations in the heat capacity of the gas during the condensation process and generates a pinch point between the two streams within the heat exchanger (see Fig. 6).

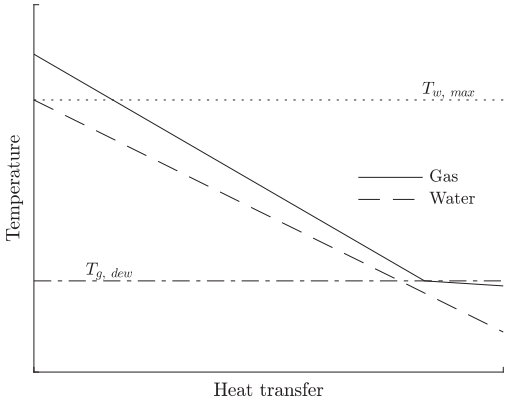

Fig. 6. Heat transfer process in air-water heat exchangers.

$$C^* = \frac{C_g}{C_w} \tag{9}$$

$$\varepsilon = \frac{\dot{Q}}{\dot{Q}_{\max}} \tag{10}$$

In order to calculate the heat exchanger outlet conditions and iterative scheme is used. The procedure begins by guessing the water mass flow. Then the maximum heat transferred ($\dot{Q}_{\max}$) is calculated as the minimum between Eq. (11) and Eq. (12). The subscripts *in* and *out* stand for inlet and outlet conditions respectively, $h@(T)$ is the specific enthalpy evaluated at temperature T and h_{fg} is the specific enthalpy of evaporation of the water.

$$\dot{Q}_{\max} = \dot{m}_{g,in} h_g@(T_{g,in}) - [\dot{m}_{g,out} h_g@(T_{w,in}) + (\dot{m}_{g,in} - \dot{m}_{g,out}) h_{fg}] \tag{11}$$

$$\dot{Q}_{\max} = \dot{m}_w h_w@(T_{g,in}) - \dot{m}_w h_w@(T_{w,in}) \tag{12}$$

Subsequently, the outlet gas and water temperatures are obtained from Eq. (13) and Eq. (14) respectively, where $\dot{Q}$ is obtained from Eq. (10).

$$\dot{Q} = \dot{m}_{g,in} h_g@(T_{g,in}) - [\dot{m}_{g,out} h_g@(T_{g,out}) + (\dot{m}_{g,in} - \dot{m}_{g,out}) h_{fg}] \tag{13}$$

$$\dot{Q} = \dot{m}_w h_w@(T_{w,out}) - \dot{m}_w h_w@(T_{w,in}) \tag{14}$$

The amount of condensed vapour is obtained from Eq. (15). $\omega_{sat}@(T_{g,out}, p_g)$ is the saturated water to air ratio evaluated at the outlet temperature of the gas and at the pressure of the gas. When $\omega_{sat} > \omega_{in}$ no condensation is taking place and the amount of water condensed is to zero.

$$\dot{m}_{g,in} - \dot{m}_{g,out} = \dot{m}_a(\omega_{in} - \omega_{out}) = \dot{m}_a[\omega_{in} - \omega_{sat}@(T_{g,out}, P_g)] \tag{15}$$

Once the outlet temperature of both flows is obtained, the heat capacity ratio of the air and water side is calculated from Eq. (16). $\Delta T_{x,dry}$ represents the temperature jump of the stream in the dry section, that is from the inlet of the gas up to the dew point. When no condensation occurs, $\Delta T_{x,dry}$ represents the temperature jump across the whole heat exchanger.

$$C_x = \frac{\dot{Q}}{\Delta T_{x,dry}} \tag{16}$$

Finally, a revised heat capacity ratio C^* is re-calculated using the values obtained from Eq. (16). In case that the calculated and the initial design values do not match, the water mass flow guess is revised and the process is repeated until convergence is reached.

The water is injected into the saturator at a liquid phase to facilitate the humidification process. The outlet temperature of the water is limited by the water saturation temperature evaluated at the saturator's pressure. A safety coefficient of 0.9 is introduced to avoid any steaming in the saturator, as shown in Eq. (17), where $T_{sat}@(0.9 p_{SAT})$ is the saturation temperature of the water evaluated at 0.9 the saturator's pressure. In case the condition was not satisfied, the water mass flow would be increased, a new heat capacity ratio is calculated which overwrites the initial value.

$$T_{w,out} \leqslant T_{w,\max} = T_{sat}@(0.9p_{SAT}) \quad (17)$$

In the recuperator, the inlet proprieties of both streams are defined. Therefore, the outlet conditions of the two streams are calculated with the definition of the effectiveness of the heat exchanger. The pressure losses of the heat exchangers are calculated analogously to the method used in the saturator since the pressure losses are imposed as a percentage on the inlet pressure.

References

[1] A.M. Bassily, Numerical cost optimization and irreversibility analysis of the triple-pressure reheat steam-air cooled GT commercial combined cycle power plants, Appl. Thermal Eng. 40 (2012) 145–160, http://dx.doi.org/10.1016/j.applthermaleng.2012.01.038.
[2] A.M. Bassily, Enhancing the efficiency and power of the triple-pressure reheat combined cycle by means of gas reheat, gas recuperation, and reduction of the irreversibility in the heat recovery steam generator, Appl. Energy 85 (12) (2008) 1141–1162, http://dx.doi.org/10.1016/j.apenergy.2008.02.017.
[3] S.K. Bakhshmand, R.K. Saray, K. Bahlouli, H. Eftekhari, A. Ebrahimi, Exergoeconomic analysis and optimization of a triple-pressure combined cycle plant using evolutionary algorithm, Energy 93 (2015) 555–567, http://dx.doi.org/10.1016/j.energy.2015.09.073.
[4] M. Jonsson, J. Yan, Humidified gas turbines—a review of proposed and implemented cycles, Energy 30 (7) (Jun. 2005) 1013–1078, http://dx.doi.org/10.1016/j.energy.2004.08.005.
[5] A. Rao, "Evaporative Gas Turbine (EvGT)/Humid Air Turbine (HAT) Cycles", Handbook of Clean Energy Systems, John Wiley & Sons Ltd, Chichester, UK, 2014.
[6] H. Araki, T. Koganezawa, C. Myouren, S. Higuchi, T. Takahashi, T. Eta, Experimental and Analytical study on the operation characteristics of the AHAT system, J. Eng. Gas Turbines Power 134 (2012), http://dx.doi.org/10.1115/1.4004732.
[7] T.S. Kim, C.H. Song, S.T. Ro, S.K. Kauh, Influence of ambient condition on thermodynamic performance of the humid air turbine cycle, Energy 25 (4) (Apr. 2000) 313–324, http://dx.doi.org/10.1016/S0360-5442(99)00074-2.
[8] M. Nakhamkin, E.C. Swensen, J.R. Scheibel, A. Cohn, CHAT Technology: an alternative approach to achieve advanced turbine systems efficiencies with present combustion turbine technology, ASME International Gas Turbine and Aeroengine Congress and Exhibition, Paper No. 98-GT-43, ASME, Stockholm, Sweden, Jun. 1998.
[9] M. Jonsson, J. Yan, Economic assessment of evaporative gas turbine cycles with optimized part flow humidification systems, in: Proceedings of ASME Turbo Expo, Paper No. GT2003-38009, ASME, Atlanta, Georgia, USA, 2003.
[10] R.M. Kavanagh, G.T. Parks, A systematic comparison and multi-objective optimization of humid power cycles—part II: economics, J. Eng. Gas Turbines Power 131 (2009), http://dx.doi.org/10.1115/1.3026562.
[11] A.D. Rao, Process for Producing Power, 1989.
[12] A. Traverso, A.F. Massardo, Thermoeconomic analysis of mixed gas-steam cycles, Appl. Thermal Eng. 22 (1) (Jan. 2002), http://dx.doi.org/10.1016/S1359-4311(01)00064-3.
[13] A.A. Pedemonte, A. Traverso, A.F. Massardo, Experimental analysis of pressurised humidification tower for humid air gas turbine cycles. part a: experimental campaign, Appl. Thermal Eng. 28 (2008) 1711–1725, http://dx.doi.org/10.1016/j.applthermaleng.2007.10.030.
[14] A.A. Pedemonte, A. Traverso, A.F. Massardo, Experimental analysis of pressurised humidification tower for humid air gas turbine cycles. Part B: correlation of experimental data, Appl. Thermal Eng. 28 (2008) 1711–1725, http://dx.doi.org/10.1016/j.applthermaleng.2007.10.030.
[15] B. Wang, S. Zhang, Y. Xiao, Steady state off-design performance of humid air turbine cycle, in: Proceedings of ASME Turbo Expo, Paper No. GT2007-27350, ASME, Montreal, Canada, 2007, pp. 139–149.
[16] T. Takahashi, Y. Nakao, E. Koda, Analysis and evaluation about advanced humid air turbine system, Challenges of Power Engineering and Environment, Springer Berlin Heidelberg, Berlin, Heidelberg, 2007, pp. 341–344.
[17] M. Yagi, H. Araki, H. Tagawa, T. Koganezawa, C. Myoren, T. Takeda, Progress of the 40 MW-class advanced humid air turbine tests, J. Eng. Gas Turbines Power 135 (11) (Sep. 2013), http://dx.doi.org/10.1115/1.4025037.
[18] P. Chiesa, G. Lozza, E. Macchi, S. Consonni, An assessment of the thermodynamic performance of mixed gas-steam cycles part B- water-injected and hat cycles, J. Eng. Gas Turbines Power 117 (3) (1995) 499–508, http://dx.doi.org/10.1115/1.2814122.
[19] G. Brighenti, P.L. Orts-Gonzalez, L. Sanchez, P.K. Zachos, Design point performance and optimization of humid air turbine power plants, Appl. Sci. 7 (4) (Apr. 2017), http://dx.doi.org/10.3390/app7040413.
[20] M. Thern, T. Lindquist, T. Torisson, Theoretical and experimental evaluation of a plate heat exchanger aftercooler in an evaporative gas turbine cycle, in: Proceedings of ASME Turbo Expo, Paper No. GT2003-38099, ASME, Atlanta, Georgia, USA, 2003, pp. 103–111.
[21] B. Nyberg, M. Thern, Thermodynamic studies of a HAT cycle and its components, Appl. Energy 89 (1) (2012) 315–321, http://dx.doi.org/10.1016/j.apenergy.2011.07.036.
[22] N.D. Ågren, M.O.J. Westermark, Design study of part-flow evaporative gas turbine cycles: performance and equipment sizing. Part II: industrial core, J. Eng. Gas Turbines Power 125 (2003) 216–227, http://dx.doi.org/10.1115/1.1476925.
[23] N.D. Ågren, M.O.J. Westermark, design study of part-flow evaporative gas turbine cycles: performance and equipment sizing. Part I: aeroderivative core, J. Eng. Gas Turbines Power 125 (2003) 201–215, http://dx.doi.org/10.1115/1.1476924.
[24] M. Rosen, Evaporative Cycles – in Theory and in Practise, PhD Thesis Lund Institute of Technology, Lund, Sweden, 2000.
[25] W.L. Macmillan, Development of a Module Type Computer Program for the Calculation of Gas Turbine Off Design Performance, PhD Thesis Cranfield University, Cranfield, UK, 1974.
[26] P.P. Walsh, P. Fletcher, Gas Turbine Performance, second ed., Blackwell Science Ltd, Oxford, UK, 2004.
[27] V. Pachidis, P. Pilidis, L. Marinai, I. Templalexis, Towards a full two dimensional gas turbine performance simulator, Aeronaut. J. 111 (1121) (Jul. 2007) 433–442, http://dx.doi.org/10.1017/S0001924000004693.
[28] Y.G. Li, L. Marinai, V. Pachidis, E.Lo Gatto, P. Pilidis, Multiple-point adaptive performance simulation tuned to aeroengine test-bed data, J. Propul. Power 25 (3) (2009) 635–641, http://dx.doi.org/10.2514/1.38823.
[29] P. Giannakakis, P. Laskaridis, T. Nikolaidis, A.I. Kalfas, Toward a scalable propeller performance map, J. Propul. Power 31 (4) (Jul. 2015) 1073–1082, http://dx.doi.org/10.2514/1.B35498.
[30] A. Pellegrini, T. Nikolaidis, V. Pachidis, S. Köhler, On the performance simulation of inter-stage turbine teheat, Appl. Thermal Eng. 113 (2017) 544–553, http://dx.doi.org/10.1016/j.applthermaleng.2016.10.034.
[31] T. Lindquist, M. Thern, T. Torisson, Experimental and theoretical results of a humidification tower in an evaporative gas turbine cycle pilot plant, in: Proceedings of ASME Turbo Expo, Paper No. GT2002-30127, ASME, Amsterdam, Netherlands, 2002, pp. 475–484.
[32] J.B. Young, R.C. Wilcock, Modeling the Air-cooled gas turbine: part 2 – coolant flows and losses, J. Turbomach. 124 (2002) 214–221, http://dx.doi.org/10.1115/1.1415038.
[33] A. Traverso, A.F. Massardo, W. Cazzola, G. Lagorio, WIDGET-TEMP: a novel web-based approach for thermoeconomic analysis and optimization of conventional and innovative cycles, in; Proceedings of ASME Turbo Expo, Paper No. GT2004-54115, ASME, Viena, Austria, 2004, pp. 623–631.
[34] T. Lindquist, Evaluation, Experience and Potential of Gas Turbine Based Cycles with Humidification, PhD Thesis Lund Institute of Technology, Lund, Sweden, 2002.
[35] ESDU, Selection and costing of heat exchangers, ESDU Data Items, No. Data Item No. 92013, 1994.
[36] C. Casarosa, F. Donatini, A. Franco, Thermoeconomic optimization of heat recovery steam generators operating parameters for combined plants, Energy 29 (3) (2004) 389–414, http://dx.doi.org/10.1016/S0360-5442(02)00078-6.
[37] W.M. Kays, A.L. London, Compact Heat Exchangers, third ed., Krieger Pub. Co, New York, USA, 1984.
[38] The Annual Cost Index of Chemical Engineering Plant, Chemical Engineering, 2015.
[39] A. Bejan, G. Tsatsaronis, M.J. Moran, Thermal Design and Optimization, John Wiley & Sons Inc, New York, USA, 1996.
[40] S. Barberis, A. Traverso, Thermoeconomic analysis of CSP air-steam mixed cycles, in: Proceedings of ASME Turbo Expo, Paper No. GT2015-42189, ASME, Montreal, Canada, Jun. 2015.
[41] A. Aramayo-Prudencio, J.B. Young, The analysis and design of saturators for power generation cycles: part 1 – thermodynamics, in: Proceedings of ASME Turbo Expo, Paper No. GT2003-38945, ASME, Atlanta, Georgia, USA, 2003, pp. 411–421.
[42] J.M. Coulson, J.F. Richardson, J.H. Harker, J.R. Backhurst, Chemical Engineering: Particle Technology and Separation Process, 5th ed., Butterworth-Heinemann, Oxford, UK, 2002.
[43] A. Aramayo-Prudencio, J.B. Young, The analysis and design of saturators for power generation cycles: part 2 – heat and mass transfer, in: Proceedings of ASME Turbo Expo, Paper No. GT2003-38946, ASME, Atlanta, Georgia, USA, 2003, pp. 423–432.

Summary presentation

This appendix contains a presentation summarising the most important findings.

Reheated Humid Air Turbine Techno-economic Analysis for Power Generation and Marine Propulsion Applications

Pau Lluis Orts-Gonzalez

Supervisor:
Pavlos Zachos

Viva Presentation

12th April 2018

www.cranfield.ac.uk

Contents

Background and motivation

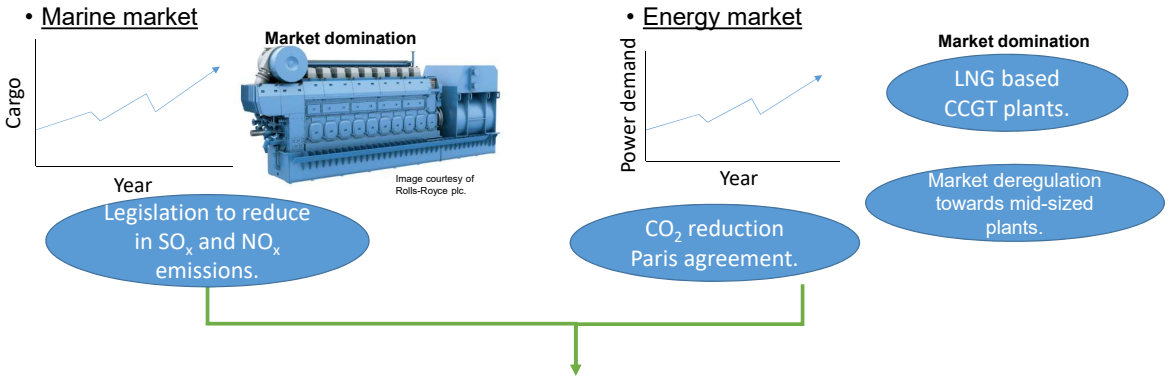

- Humid air turbines as possible solution
  - ➢High thermodynamic efficiency, 55%-64%.
  - ➢ Excellent off-design performance, 15% lower η_{th} than CCGT.
  - ➢No SO_x emissions, <10 ppm NO_x emissions.

Background and motivation (II)

Reheated humid air turbine.

Most efficient humid air turbine, maximum η_{th}= 64% (without cooling).

Open loop simplifies design. Suitable for marine and coastal applications.

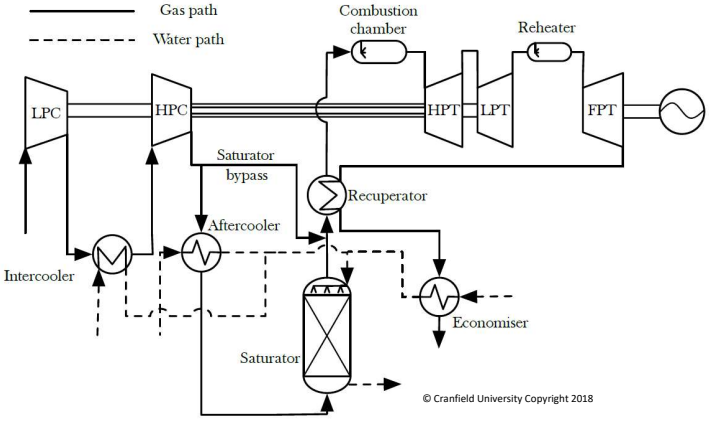

Contents

Aim

Quantify and assess the thermal and economic performance of reheated humid air turbine systems for marine and power generation applications.

Objectives

- Evaluate the thermal performance and power plant's designs across the design envelope.
- Compare efficiency and plant's designs against reference marine prime movers.
- Contrast the techno-economic performance of the cycle against reference power generation plants to prove its viability.
- Evaluate the effects of the component's degradation on the thermodynamic performance of the cycle.

Contents

Power plant design

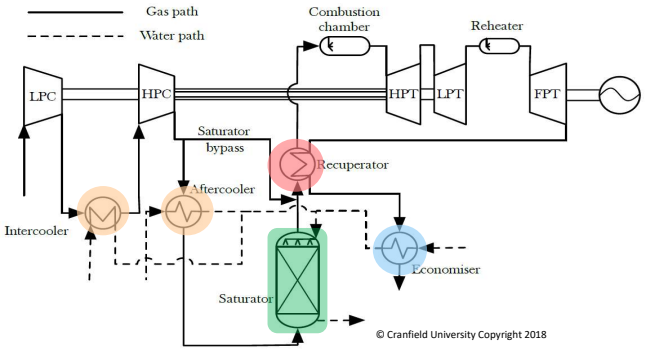

Heat exchanger	Geometry
Intercooler Aftercooler	• Plate-fin
Economiser	• Tube-fin
Recuperator	• Plate-fin
Humidifier	• Packing-bed

- Design assumptions

Power output	40 MW
Combustions chambers outlet temperature	1600 K

- Explored cycle design variables

$\varepsilon_{IC}, \varepsilon_{AC}, \varepsilon_{EC}$	0.75 , 0.85 , 0.95
ε_{REC}	0.8 , 0.85 , 0.9
ΔT_{sp}	5 K , 10 K , 15 K
OPR	30 , 40

Power plant design

Design flowchart

$\varepsilon_{IC}, \varepsilon_{AC}, \varepsilon_{EC}$	0.75 , 0.85 , 0.95
ε_{REC}	0.8 , 0.85 , 0.9
ΔT_{sp}	5 K , 10 K , 15 K
OPR	30 , 40

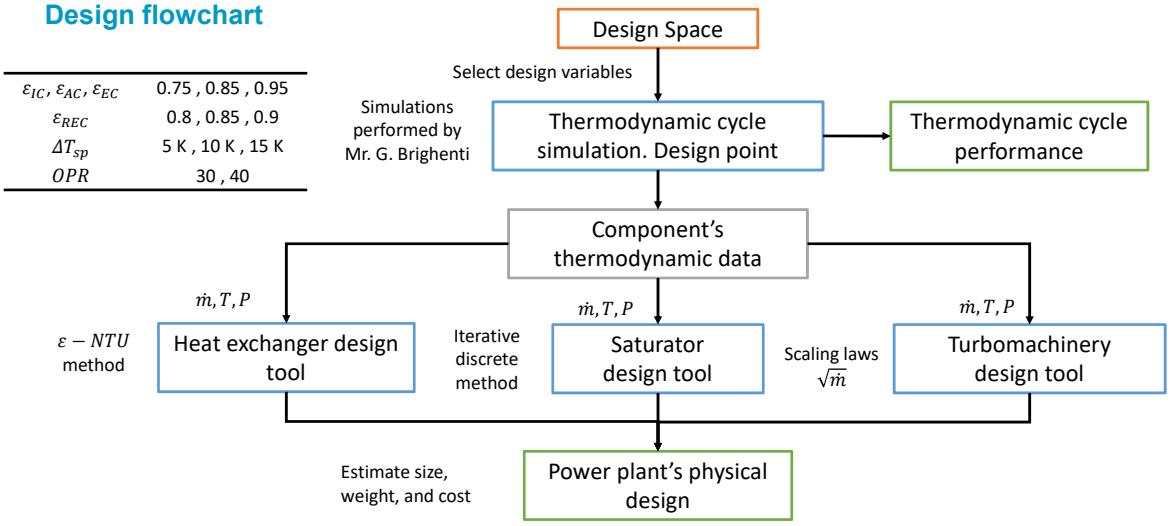

Power plant design

Mid technology reference cycle

Cycle design parameters

$\varepsilon_{IC}, \varepsilon_{AC}, \varepsilon_{EC}$	0.85
ε_{REC}	0.85
ΔT_{sp}	10 K
OPR	40
η_{th}	58.31%

Weight	Cost
43.86 t	$13,401,000

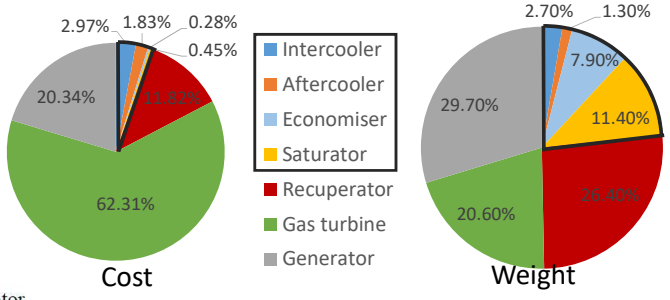

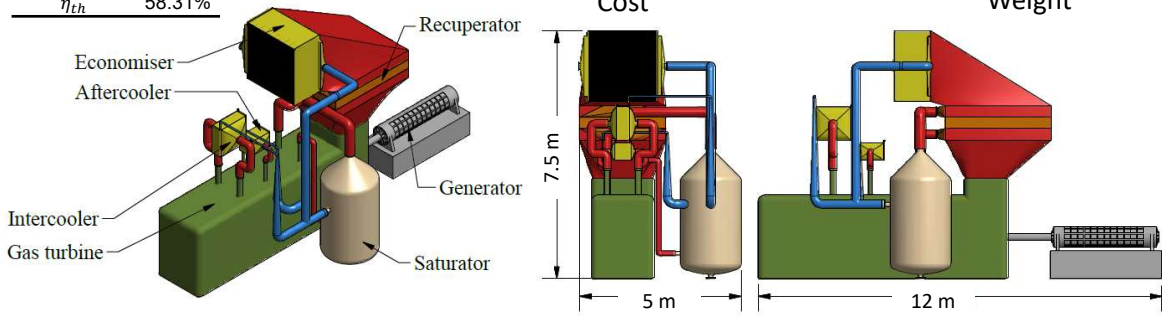

* Humidification system includes the intercooler, aftercooler, economiser, and saturator

Power plant design

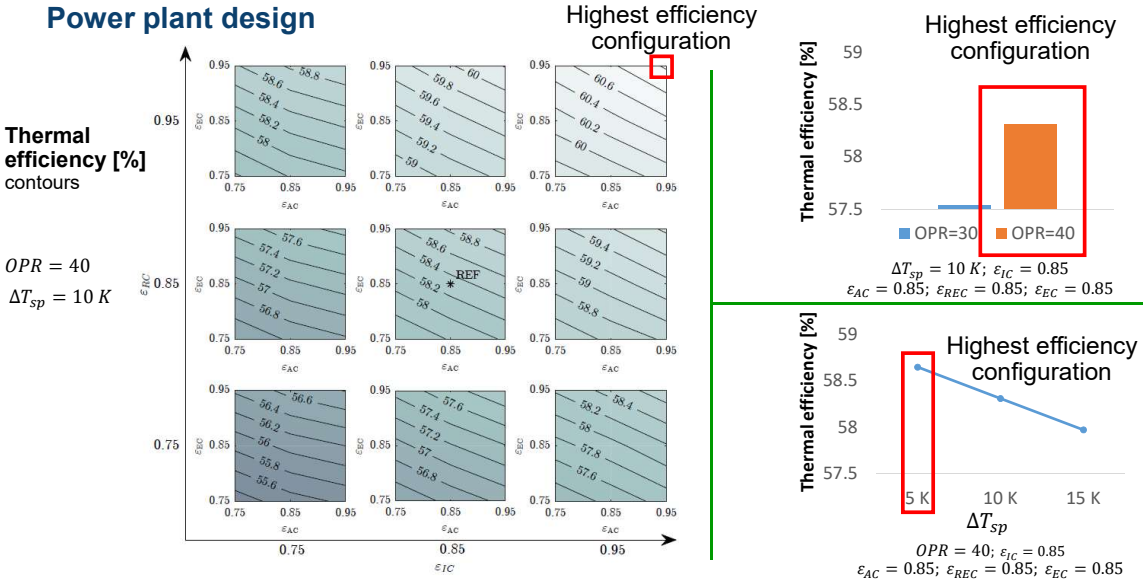

Power plant design

Comparison of power plant designs

	Baseline	Efficient	Low-priced	Light
OPR	40	40	40	40
ΔT_{sp}	10 K	5 K	5 K	5 K
ε_{IC}	0.85	0.95	0.75	0.85
ε_{AC}	0.85	0.95	0.75	0.75
ε_{EC}	0.85	0.95	0.95	0.75
ε_{REC}	0.85	0.90	0.80	0.80
η_{th}	58.31%	**61.35%**	58.86%	56.75%
SPEC [$/kW]	335	+9%	**-4%**	-3%
Weight [t]	43.9	+30%	-2%	**-11%**

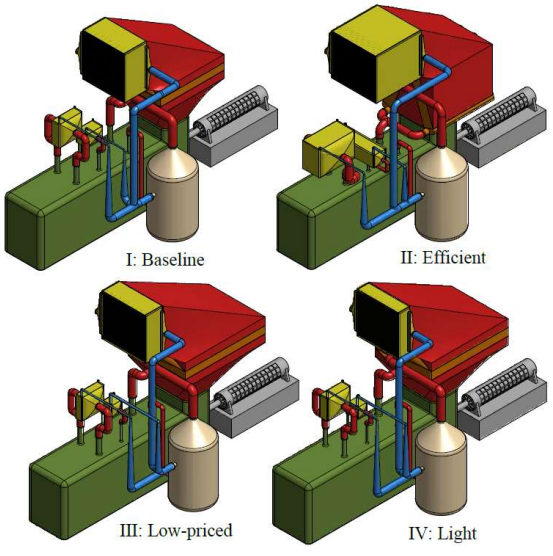

All figures have the same scale

Power plant design

Comparison against reference marine engines

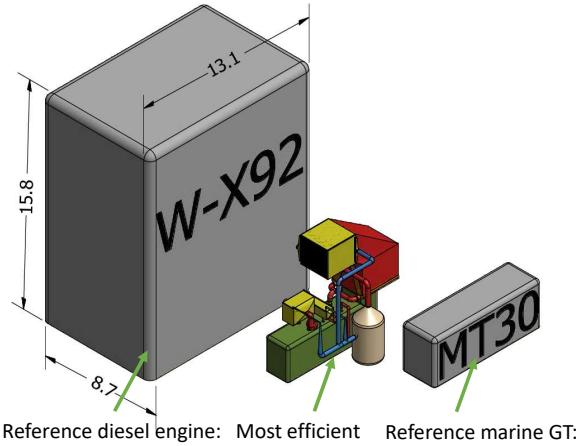

Reference diesel engine: Wärtsilä X92 [1]

Most efficient reheated humid air turbine

Reference marine GT: RR MT30 [2]

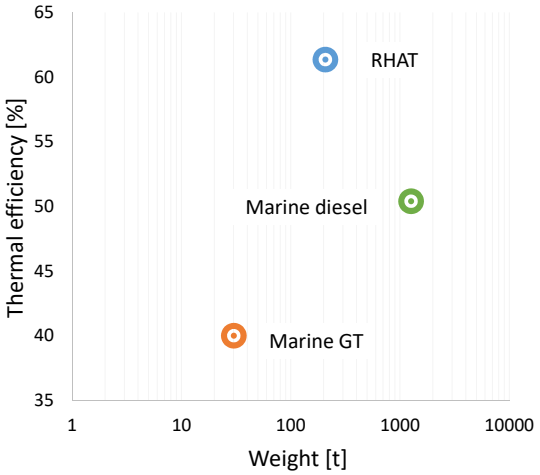

Packing and ancillaries assumed to be weight 80% of the Gas Turbine [2]

[1] "Wärtsilä X92 low-speed two-stroke diesel engine technical information" Available: https://cdn.wartsila.com/docs/default-source/product-files/engines/wartsila-low-speed-engines-technical-information-x92.pdf?sfvrsn=8c29e9f5_4 Visited on November 2017

[2] Rolls Royce, *The MT30 Marine Gas Turbine*, 2016.

Contents

Background and motivation

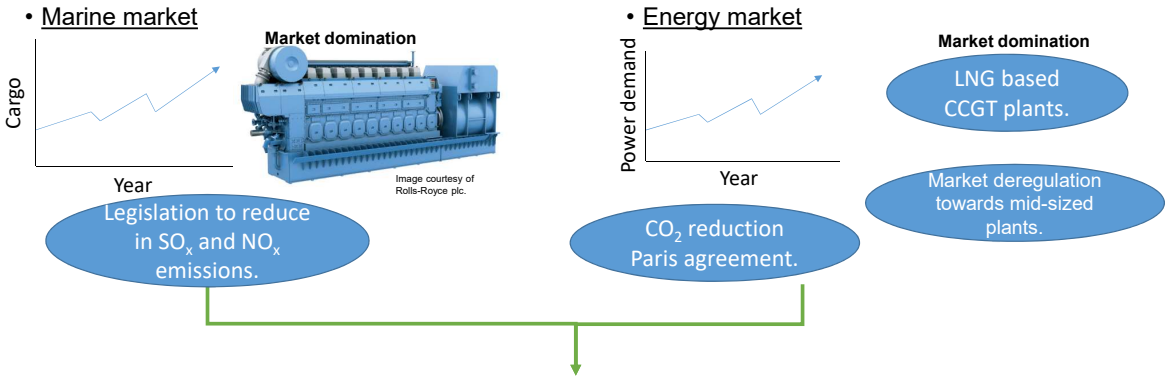

- Humid air turbines as possible solution
  - ➢High thermodynamic efficiency, 55%-64%.
  - ➢ Excellent off-design performance, 15% lower η_{th} than CCGT.
  - ➢No SO_x emissions, <10 ppm NO_x emissions.

Background and motivation (II)

Reheated humid air turbine.

Most efficient humid air turbine, maximum η_{th}= 64% (without cooling).

Open loop simplifies design. Suitable for marine and coastal applications.

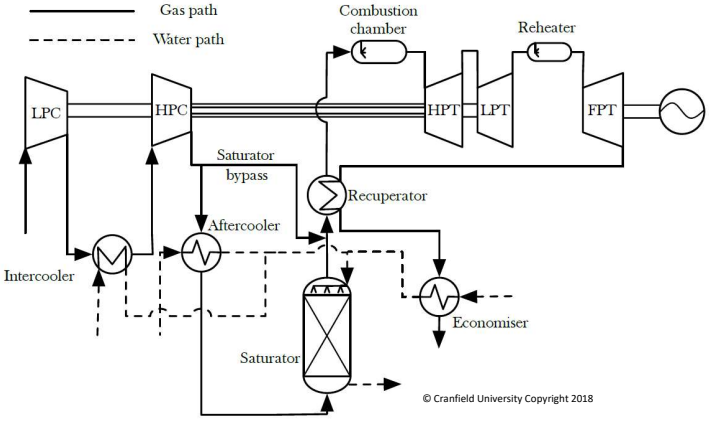

Economic analysis

- Analysis conducted to study the economic viability in energy market.
- Economic analysis based on the average cost of the electricity.

$$\overline{COE} = \frac{\sum_{i=1}^{n} C_{AE_i}}{n\, t\, \dot{W}}$$

- Cost of the electricity is based on the annual expenditures.

$$C_{AE_i} = C_{ini_i} + C_{fin_i} + C_{ta\ _i} + C_{fuel_i} + C_{O\&M_i}$$

- Design space exploration to analyse effect of cycle design variables and find most economic configuration.

$\varepsilon_{IC}, \varepsilon_{AC}, \varepsilon_{EC}$	0.75 , 0.85 , 0.95
ε_{REC}	0.8 , 0.85 , 0.9
ΔT_{sp}	5 K , 10 K , 15 K
OPR	30 , 40

Economic analysis

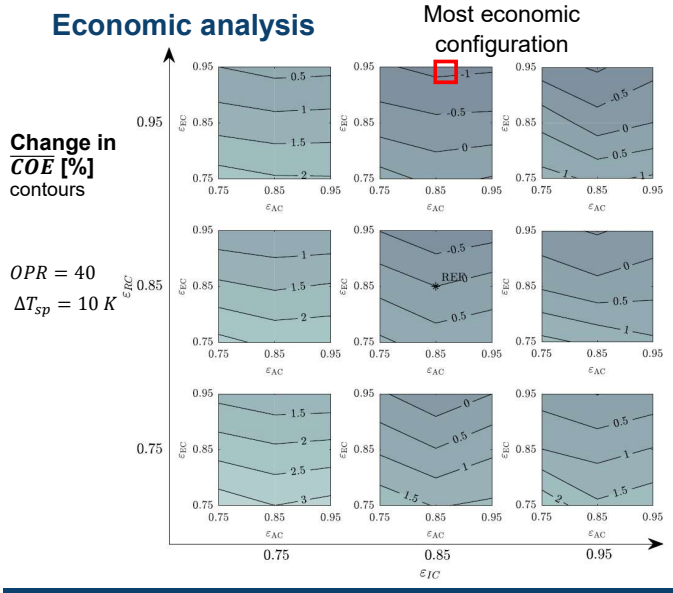

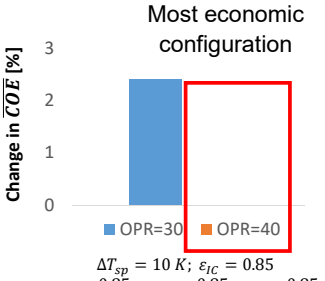

$\Delta T_{sp} = 10\ K;\ \varepsilon_{IC} = 0.85$
$\varepsilon_{AC} = 0.85;\ \varepsilon_{REC} = 0.85;\ \varepsilon_{EC} = 0.85$

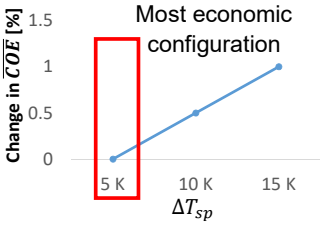

$OPR = 40;\ \varepsilon_{IC} = 0.85$
$\varepsilon_{AC} = 0.85;\ \varepsilon_{REC} = 0.85;\ \varepsilon_{EC} = 0.85$

Reference values:
$OPR = 40;\ \Delta T_{sp} = 10\ K;\ \varepsilon_{IC} = 0.85;\ \overline{COE} = 6.85\ c\$/kWh$
$\varepsilon_{AC} = 0.85;\ \varepsilon_{REC} = 0.85;\ \varepsilon_{EC} = 0.85;$

Economic analysis

Comparison against advanced power generation cycles*

Cycle	η_{th} [%]		$SPEC$ [$/kW]		$\overline{COE}$ [c$/kW]	
	Ref.	RHAT	Ref.	RHAT	Ref.	RHAT
Combined cycle [3]	**53.0**	**+14%**	**720**	**-62%**	**6.85**	**-28%**
Steam injection cycle [3]	49.3	+22%	323	-15%	6.85	-26%
Humid air turbine [3]	52.2	+15%	300	-8%	6.48	-22%
Humid air turbine [4]	51.7	+17%	n/a	n/a	4.21	-6%
Humid air water inject turbine [4]	50.0	+20%	n/a	n/a	4.07	-2%

- Reheated Humid Air Turbine offers significant lower acquisition cost compared to combined cycles.
- Reheated Humid Air Turbine stands as most economic power generation cycle.

[3] R. M. Kavanagh and G. Parks, 2009. \A Systematic Comparison and Multi-Objective Optimization of Humid Power CyclesPart II: Economics." Journal of Engineering for Gas Turbines and Power, 131. doi:10.1115/1.3026562.
[4] A. Traverso and A. F. Massardo, 2002. \Thermoeconomic Analysis of Mixed GasSteam Cycles." Applied Thermal Engineering, 22(1). doi:10.1016/S1359-4311(01)00064-3.

* The cost metrics are recalculated under the assumptions of the previous studies [3] and [4].

Contents

Component degradation

- Analysis conducted to quantify the impact of component deterioration on cycle performance.

- Component degradation includes:
  - ➢Heat exchanger fouling.
  - ➢Turbomachinery erosion.
  - ➢Turbomachinery fouling.

- Three design scenarios are analysed:

	High Tech	Mid Tech	Low Tech
$\varepsilon_{IC} = \varepsilon_{AC} = \varepsilon_{EC}$	0.95	0.85	0.75

$TET = 1600\ K, \quad OPR = 40, \quad \Delta T_{sat} = 5\ K, \quad \varepsilon_{REC} = 0.90$

- Heat exchanger fouling reduces heat transfer coefficient

$$\frac{1}{U_{foul}} = \frac{1}{U_{clean}} + R_{f,tot}$$

$$\frac{R_{f,tot}}{A_{HX,tot}} = \frac{R_{f,w}}{A_{HX,w}} + \frac{R_{f,a}}{A_{HX,a}}$$

$(\boldsymbol{R_{f,w}})_{Ref}$	$0.000\,2\ [\frac{m^2K}{W}]$
$(\boldsymbol{R_{f,a}})_{Ref}$	$0.000\,176\ [\frac{m^2K}{W}]$

$$DC = \frac{R_{f,tot}}{(R_{f,tot})_{Ref}}$$

- Turbomachinery degradation affects component flow capacity and efficiency

		Fouling	Erosion
Compressors	Flow capacity	-5%	-5%
	Efficiency	-2.5%	-2.5%
Turbines	Flow capacity	-5%	+5%
	Efficiency	-2.5%	-2.5%

- Simulations performed at constant TET.

Component degradation

- Intercooler main responsible of performance deterioration.

Effect of heat exchanger degradation,
Assuming fouling equal to reference value DC=1

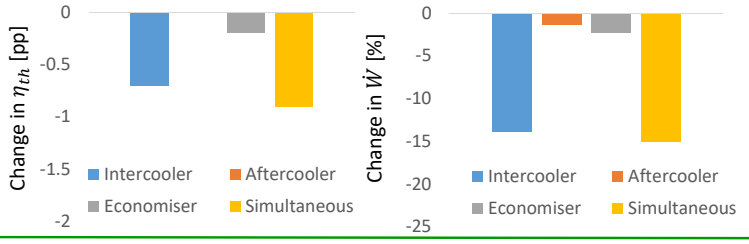

- Rising design ε from 0.75 to 0.85 reduces penalties a 40%.
- Rising design ε from 0.85 to 0.75 reduces penalties a 60%.

Effect of heat exchanger technology level,
Assuming fouling equal to reference value DC_{Sim}=1

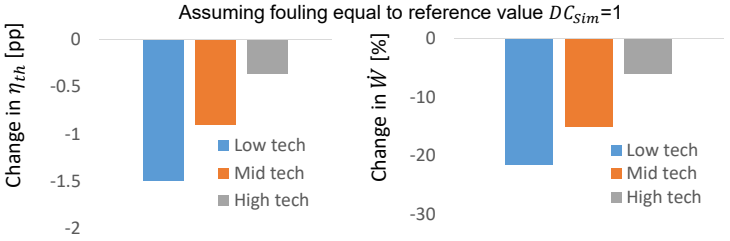

DC_{Sim} → Simultaneous degradation of 3 air-water heat exchangers

Component degradation

- Turbo. erosion largest impact on η_{th}. 40% larger than turbo. foul. 50% larger than HX deg.
- Turbo. fouling largest penalties on $\dot{W}$. 25% larger than HX deg. 55% larger than turbo. erosion

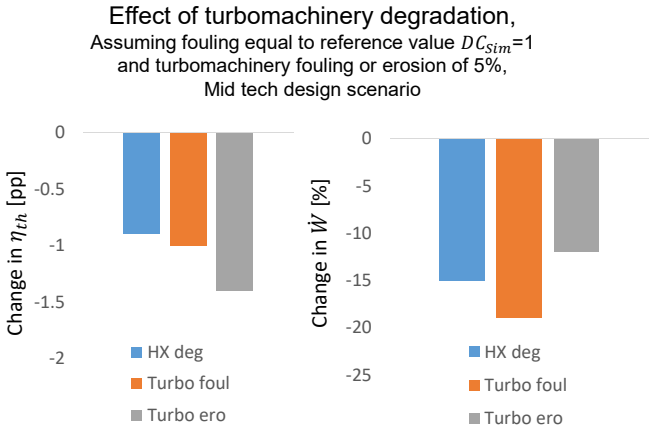

DC_{sim} → Simultaneous degradation of 3 air-water heat exchangers
HX deg → Heat exchanger degradation
T foul → Turbomachinery fouling, T ero → Turbomachinery erosion

Component degradation

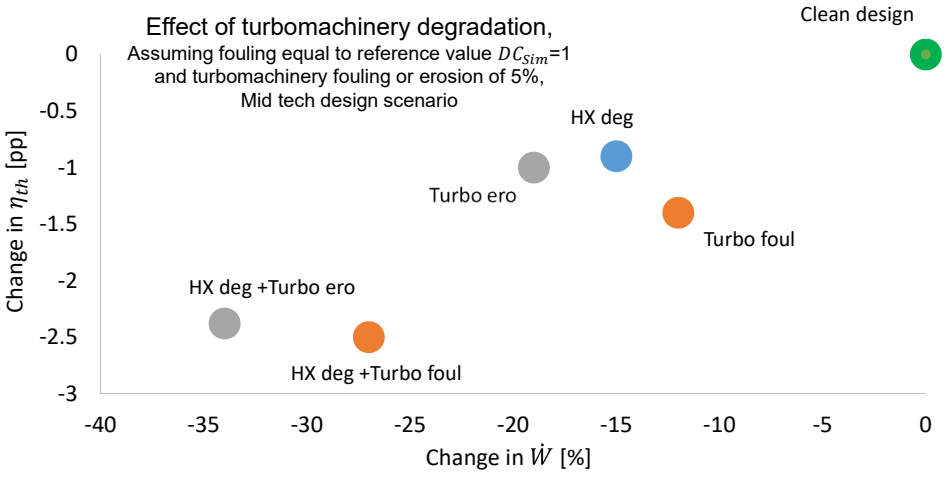

DC_{sim} → Simultaneous degradation of 3 air-water heat exchangers
HX deg → Heat exchanger degradation
T foul → Turbomachinery fouling, T ero → Turbomachinery erosion

Contents

- Background and motivation
- Aim and objectives
- Power plant design
- Economic analysis
- Component degradation
- Conclusions
- Dissemination

Conclusions

- Design space exploration proves feasibility of the cycle.
  - ➢Max η_{th}= 61.35%, SPEC= 366 $/kW, weight 57 tonnes.
- Reheated humid air turbine is
  - 11 pp more efficient, 84% lighter, 82% more compact

  than the reference marine diesel engines.
- Reheated humid air turbine is the most economic power plant for energy generation.
  - ➢28% more economic than combined cycle gas turbines.
  - ➢2-22% more economic than other humid air turbines.
- Intercooler degradation and turbomachinery degradation produce the largest penalties on performance.
  - ➢Intercooler degradation → $\Delta\eta_{th}$= -0.7 pp and $\Delta\dot{W}$= -13.9%.
  - ➢Impact reduces as design heat exchanger's effectiveness rises.
  - ➢Turbomachinery degradation → $\Delta\eta_{th}$= -1 to -1.4 pp and $\Delta\dot{W}$= -12 to -19 %.

Conclusions

Contribution to knowledge

- The research illustrates the promising thermodynamic performance of the reheated humid air turbine across its design space, while showing competitive acquisition costs.
- The outcomes prove the potential of the cycle to be employed in marine and power generation applications.
- Maintenance of the intercooler and the turbomachinery is of high importance as performance considerably drops with the degradation of these components.

- Overall this research constitutes a step forward in understanding the design and degraded performance of a new complex cycle across its design space, and appreciating its potential for marine and power generation applications.

Contents

Dissemination

1. Brighenti, G.; Orts-Gonzalez, P. L.; Sanchez, L.; Zachos, P. K., “Design Point Performance and Optimization of Humid Air Turbine Power Plants” *Applied Sciences*, Vol. 7, No. 4, Apr. 2017, doi: 10.3390/app7040413.

2. Orts-Gonzalez, P.L.; Brighenti, G.D.; Zachos, P.K. “Techno-economic analysis of a Reheated Humid Air Turbine” *Appl. Therm. Eng.,* Vol. 137, 30 March 2018, doi: ttps://doi.org/10.1016/j.applthermaleng.2018.03.094.

3. Brighenti, G.D.; Orts-Gonzalez, P.L.; Zachos, P.K. “Part-Load Performance Modelling of a Reheated Humid Air Turbine Power Cycle” *Appl. Therm. Eng.*

4. Orts-Gonzalez, P.L.; Brighenti, G.D.; Zachos, P.K. “The impact of heat exchanger degradation on the performance of a Humid Air Turbine system for power generation” *Appl. Therm. Eng.*

Cranfield University

Thank you
Any questions?

www.cranfield.ac.uk